

THE STRUCTURE, PETROLOGY AND GEOCHEMISTRY
OF THE TIBCHI YOUNGER GRANITE RING-
COMPLEX, NIGERIA

Echefu Cyriacus Ike

A Thesis Submitted for the Degree of PhD
at the
University of St Andrews



1979

Full metadata for this item is available in
St Andrews Research Repository
at:
<http://research-repository.st-andrews.ac.uk/>

Please use this identifier to cite or link to this item:
<http://hdl.handle.net/10023/15584>

This item is protected by original copyright

THE STRUCTURE, PETROLOGY AND GEOCHEMISTRY
OF THE TIBCHI YOUNGER GRANITE RING-COMPLEX, NIGERIA

by

ECHEFU CYRIACUS IKE

A thesis presented to the University of St. Andrews, in
application for the degree of Doctor of Philosophy.

September, 1979



ProQuest Number: 10170953

All rights reserved

INFORMATION TO ALL USERS

The quality of this reproduction is dependent upon the quality of the copy submitted.

In the unlikely event that the author did not send a complete manuscript and there are missing pages, these will be noted. Also, if material had to be removed, a note will indicate the deletion.



ProQuest 10170953

Published by ProQuest LLC (2017). Copyright of the Dissertation is held by the Author.

All rights reserved.

This work is protected against unauthorized copying under Title 17, United States Code
Microform Edition © ProQuest LLC.

ProQuest LLC.
789 East Eisenhower Parkway
P.O. Box 1346
Ann Arbor, MI 48106 – 1346

Th 9291

ABSTRACT

The 1:50,000 geological map of the Tibchi Complex presented is characterised by a closed elliptical ring-dyke framework hitherto unpredicted by pioneer workers. Major rock units comprise a basalt - potassic granite suite. The structural history of the Complex involved a central shield volcano, succeeded by a caldera and fluidised intra-caldera volcanism. The model proposed is on the principle of positive magma pressure during both caldera formation and ring-dyke intrusion. With ash-fall tuff and rhyolite lavas resting directly on the subsided basement block within the ring-fracture, the Tibchi Complex shows the first clear exposure of the Jurassic landscape to be recorded in Nigeria.

An olivine tholeiite - tholeiite - andesine basalt - trachyte sequence, and a microferrodiorite - microsyenite - granitic porphyries sequence are separately established but together appear to form a unified petrogenetic succession. The scarcity of modal plagioclase, and the low levels of calcium and magnesium, together with the extreme iron-enrichment, in the rocks, are accounted for. The petrology is complicated by various post-magmatic hydrothermal and metasomatic processes from which certain distinctive rock-types formed. These processes are described in full and explanations offered. Contact metamorphism previously unassociated with the Nigerian Younger Granites is recorded in a bifacial metamorphic aureole related to the biotite granite intrusion.

Joint-controlled greisen vein development and primary mineralisation are among the most extensive in the Nigerian Younger Granites.

Chemical analyses of fayalites, Ca-rich pyroxenes, amphiboles and a selection of biotites and chlorites show that these minerals approach very closely the iron end-members of their solid solution series. Two distinct but related pyroxene crystallisation trends are found in the porphyries. The 'granite porphyry pyroxene trend' involved a significant role of the acmite component in a way that suggests a modification of the 'quartz porphyry pyroxene trend' by increased oxygen fugacity. The presence of sufficient volatiles in the quartz porphyry magma was probably enough to account for the observed difference between the two trends. Pyroxene data on the whole indicate the Tibchi Complex to be of tholeiitic affinity, but with a mild alkalinity. Amphiboles are mostly postmagmatic in origin and define two divergent reaction series: a ferroactinolite - ferroedenite series, and a ferroactinolite - ferrorichterite - alkali amphibole series. The compositions of the amphiboles are predestined by the compositions of the pyroxenes from which they formed.

Despite the origin of the Tibchi rocks from basaltic liquids, the presence of large volumes of granitic rocks suggests extensive crustal anatexis as possible source of additional acid magma.

CERTIFICATE

I certify that Echefu C. Ike has been engaged in research for thirteen terms at the University of St. Andrews, that he has fulfilled the conditions of Ordinance No. 12 (St. Andrews) and Resolution of the University Court, 1967 No. 1, and that he is qualified to submit this thesis for the degree of Doctor of Philosophy.

I certify that the following thesis is based on the results of research carried out by me, that it is my own composition, and that it has not previously been presented for a higher degree.

To Eka, with love, for accommodating
the unkindly gesture of my spending
part of our honeymoon in the Tibchi
Complex.

CONTENTS

	Page No.
ABSTRACT	
CERTIFICATE	
LIST OF FIGURES	(v)
LIST OF PLATES	(viii)
LIST OF TABLES	(xiv)
CHAPTER 1. <u>INTRODUCTION</u>	
1.1 The Nigerian Younger Granites	2
1.2 The Tibchi Complex	4
CHAPTER 2. <u>FIELD GEOLOGY</u>	
2.1 Introduction	9
2.2 The Granitic Basement	9
2.3 The Volcanic Sequence	11
2.4 The Quartz Porphyries	16
2.5 The Granite Porphyry Ring-dyke and isolated minor dykes	23
2.6 The Central Biotite Granite Intrusion	30
2.7 Miscellaneous Rocks	38
CHAPTER 3. <u>THE VOLCANO-STRUCTURAL AND INTRUSIVE FEATURES OF THE TIBCHI COMPLEX</u>	
3.1 Introduction	43
3.2 Evidence for Surface Cauldron Subsidence and the formation of a Jurassic caldera in the Tibchi Complex	44
3.3 Pre-caldera Volcanism and the Probability of a Central Volcano	50
3.4 The Intra-caldera Volcanism: Fluidised Vents and a Quiescent Ring-dyke Intrusion	58
3.5 The Eccentricity of the Central Biotite Granite Pluton	63
3.6 Origin of Ring-complexes	65
3.7 Summary of Events in the Tibchi Complex	80

CHAPTER 4. <u>PETROGRAPHIC DESCRIPTION</u>	
4.1	Introduction 82
4.2	Lavas 83
4.3	Tuffs and Agglomerates 97
4.4	The Subvolcanic Rocks 116
4.5	Biotite granite and Microgranite 159
4.6	Miscellaneous rock types 175
CHAPTER 5. <u>MINERAL CHEMISTRY</u>	
5.1	Introduction 203
5.2	Fayalite 203
5.3	Pyroxenes 207
5.4	Amphiboles 229
5.5	Iron-titanium oxide minerals 249
5.6	Biotites and chlorites 257
CHAPTER 6. <u>WHOLE-ROCK MAJOR AND TRACE ELEMENT GEOCHEMISTRY</u>	
6.1	General 265
6.2	Analytical data 265
6.3	Chemical Variation Diagrams 267
	Rare earth element geochemistry 288
CHAPTER 7. <u>SUMMARY, CONCLUSIONS AND PETROGENESIS</u>	
7.1	Summary and conclusions 303
7.2	Petrogenesis 313
	LIST OF REFERENCES 318
	ACKNOWLEDGEMENT 332
	APPENDIX (a)-(q)

LIST OF FIGURES

		Page No.
<u>Figure 1</u>	Location map of the Tibchi Complex	1
<u>Figure 2.1</u>	Simplified geological map of the Tibchi Complex showing the major rock units and access	8
<u>Figure 2.5.3</u>	Post-emplacement faulting and displacement in a triplet set of minor granite porphyry dykes near the biotite granite margin, east of Kalato	27
<u>Figure 3.6.2</u>	Stress diagram to show supposed mode of formation of cone-sheets and ring-dykes	67
<u>Figure 3.6.4</u>	Diagrammatic representation of the structural evolution of the Tibchi Complex	75
<u>Figure 4.2LA</u>	Sample localities of the extrusive volcanic rocks referred to in the text	85
<u>Figure 4.4A</u>	Sample localities, quartz porphyries	117
<u>Figure 4.4L</u>	Sample localities, granite porphyry (ring-dyke and isolated minor dykes)	138
<u>Figure 4.5</u>	Sample localities of the biotite granite and microgranite referred to in the text	158
<u>Figure 4.6.2</u>	Sketch of the field relations and sample localities in the south-eastern over-saturated peralkaline suite	180
<u>Figure 5.3.3A</u>	Crystallisation trends of the Ca-rich pyroxenes, Tibchi Complex, plotted separately for different rocks/groups	212
<u>Figure 5.3.3B</u>	Crystallisation trends of the Ca-rich pyroxenes, Tibchi Complex, showing the general two-fold trend	213
<u>Figure 5.3.3C</u>	Plots of the Ca-rich pyroxenes, Tibchi Complex, in mole percent Mg (Diopside), Fe ²⁺ + Mn (Hedenbergite) and Na (Acmite)	214
<u>Figure 5.3.3D</u>	Comparison of the pyroxene trends of the Tibchi Complex with those of the Bushveld and Skaergaard intrusions, Thingmuli Volcano, and Pantellerites	224

<u>Figure 5.3.3E</u>	Comparison of published alkali pyroxene trends with those of the Tibchi Complex and the Skaergaard Intrusion	225
<u>Figure 5.4.2A</u>	Plot of $(Na+K)_A$ against $(8-Si)$ subdividing the calcic amphiboles analysed	234
<u>Figure 5.4.2B</u>	Plot of Na_B against $(Na+K)_A$ subdividing the sodic-calcic and alkali amphiboles analysed	235
<u>Figure 5.4.5A</u>	Plot of Ca against $(Na+K)$ for amphiboles of the Tibchi Complex, used to depict transitional trends	240
<u>Figure 5.4.5B</u>	Amphiboles of the Tibchi Complex plotted on the basis of alkali components and calcium	241
<u>Figure 5.5.2</u>	Plot of molecular compositions of analysed iron-titanium oxide minerals	250
<u>Figure 6.3.1A</u>	The Harker variation diagram for rocks of the Tibchi Complex	266
<u>Figure 6.3.2A</u>	Iron-enrichment ratio, $FeO + Fe_2O_3 / FeO + MgO$, plotted against SiO_2 (weight percent) for the Tibchi Complex and superimposed on the plots of Osborn's synthetic liquid, the Skaergaard Intrusion, the Cascade Series and the Thingmuli Volcano	270
<u>Figure 6.3.2B</u>	AFM diagram for rocks of the Tibchi Complex	271
<u>Figure 6.3.3A</u>	Plot of normative albite, orthoclase and quartz, for rocks of the Tibchi Complex	276
<u>Figure 6.3.3B</u>	Linear trends in porphyries, and biotite granites and microgranites	277
<u>Figure 6.3.3C</u>	Projections unto the anhydrous base of the tetrahedron $A_6-O_1-Q-H_2O$ illustrating vapour phase relations	278
<u>Figure 6.3.5A</u>	Comparison of the chondrite-normalised REE abundances of the Tibchi granite porphyry with those of the quartz syenite, Kila-Warji Complex	291
<u>Figure 6.3.5B</u>	Plot of chondrite-normalized REE abundances in quartz porphyries of the west-east traverse on logarithmic scale	292

<u>Figure 6.3.5C</u>	Plot of chondrite-normalised REE abundances in quartz porphyries of the west-east traverse on a linear scale	293
<u>Figure 6.3.5D</u>	Plot of chondrite-normalised REE abundances in selected rocks of the south-eastern suite	294

LIST OF PLATES

		<u>Page No.</u>
<u>Plate 2.6.2A</u>	'Contact foliation' in a rhyolite lava caused by later intrusion of biotite granite	31
<u>Plate 2.6.2B</u>	Veining of basalt by biotite granite	32
<u>Plate 2.6.3A</u>	Greisen vein swarm	32
<u>Plate 4.2A</u>	Hornblende in contact-metamorphosed basalt (T53)	91
<u>Plate 4.3A</u>	Ash-fall tuff showing layering	95
<u>Plate 4.3B</u>	Ash-fall tuff with cobble of basement	96
<u>Plate 4.3C</u>	Tri-radial shard. Poorly welded tuff (T126)	99
<u>Plate 4.3D</u>	Same as in Plate 4.3C magnified	99
<u>Plate 4.3E</u>	Tubular pumice vesicle or cell in poorly welded tuff (T126)	100
<u>Plate 4.3F</u>	Same as in Plate 4.3E, magnified, and in crossed polarised light, to show internal structure of the pumice cell, the axiolitic texture of wall, and the relatively coarse vapour-accelerated crystallisation in the interior	100
<u>Plate 4.3G</u>	Fiamme showing flame-like terminations, Lithic tuff (T114)	108
<u>Plate 4.3H</u>	Central cavity in large fiamme in Plate 4.3G magnified to show the nature of the vapour-phase crystallisation observed	108
<u>Plate 4.3K</u>	Three fiamme folded round the roundish edge of a lithic fragment during compaction against neighbouring lithic fragments. The fiamme apparently shows unlimited plasticity	109
<u>Plate 4.3L</u>	Away from crowded lithic fragments, distortion of fiamme (only moderately to slightly folded) is not usually great. Welded lapilli tuff (T116)	109
<u>Plate 4.3M</u>	Pseudo-flow texture produced by extreme compaction and welding in the crystal tuff matrix of the welded agglomerate (T125)	110

<u>Plate 4.3N</u>	Part of Plate 4.3M magnified to show the filamentous structure of drawn out shards and pumice fragments produced by extreme compaction and welding between crystal phenocrysts. A pseudo-flow structure between the two phenocrysts terminates in area of less compaction	110
<u>Plate 4.4B</u>	Two unaltered fayalite phenocrysts partially enclosed by K-feldspar. Fayalite ferrohedenbergite quartz porphyry (T105)	115
<u>Plate 4.4C</u>	A typical unaltered ferrohedenbergite. Fayalite ferrohedenbergite quartz porphyry (T105)	115
<u>Plate 4.4D</u>	Colour changes in altered quartz porphyries	
<u>Plate 4.4E</u>	Euhedral crystal of monazite, with laths of ferroedenite, granular and massive titanomagnetite and apatite needles on site of ferrohedenbergite hydrothermal degradation. Hydrothermally altered quartz porphyry (T169)	127
<u>Plate 4.4F</u>	Same as Plate 4.4E, crossed nicols	127
<u>Plate 4.4G</u>	Ferroedenite (E), Monazite (M) and Titanomagnetite (black) together occupy the site of degradation of a pre-existing calcic pyroxene or fayalite. Hydrothermally altered quartz porphyry (T169). Plane polarised light	128
<u>Plate 4.4H</u>	Titanomagnetite very often forms a complete or partial ring round other by-products of the hydrothermal degradation of calcic pyroxene or fayalite. Ferroedenite. Quartz porphyry (T169)	128
<u>Plate 4.4I</u>	Fayalite phenocryst with both ferrosichterite and riebeckite as products of hydrothermal alteration (T115)	133
<u>Plate 4.4J</u>	Pseudomorphs of spongy ferrosichterite after pyroxene and fayalite. Quartz porphyry T133	135
<u>Plate 4.4K</u>	Textural range in ferrosichterite. Quartz porphyry T133	135

<u>Plate 4.4M</u>	Pseudomorphs of sodic pyroxene after ferrohedenbergite. Hydrothermally altered granite porphyry ring-dyke	140
<u>Plate 4.4N</u>	Part of pseudomorph in Plate 4.4M magnified to show textural relationship between the sodic pyroxene and fringing amphibole	140
<u>Plate 4.4NX</u>	Colour variation in samples from the granite porphyry ring-dyke caused by hydrothermal modification	opposite page 139
<u>Plate 4.4P</u>	Perthite phenocryst pseudomorphed by siderophyllite. Metasomatically altered granite porphyry dyke	144
<u>Plate 4.4R</u>	A portion of a siderophyllite pseudomorph magnified to show pockets containing genthelvite, quartz and opaque iron oxide	144
<u>Plate 4.4T</u>	Pocket in Plate 4.4R magnified	146
<u>Plate 4.4W</u>	Same as Plate 4.4T crossed nicols	146
<u>Plate 4.4X</u>	Fayalite ferroaugite microferrodiorite enclave in porphyry	149
<u>Plate 4.4Y</u>	Similar enclave as in Plate 4.4X	149
<u>Plate 4.4Z</u>	Similar enclave as in Plate 4.4X showing ferroaugite interstitial to plagioclase	150
<u>Plate 4.4Z(i)</u>	Part of enclave in Plate 4.4Z magnified and in plane light to show zig-zag habit of ferroaugite	150
<u>Plate 4.4Z(ii)</u>	Fayalite crystals in a protracted interstitial crystallisation relative to earlier plagioclase	151
<u>Plate 4.4Z(iii)</u>	Fayalite as discrete but later grains	151
<u>Plate 4.4.2A</u>	Skeletal pyroxenes nucleated along the rays of spherulitic intergrowths	153
<u>Plate 4.4.2B</u>	Same as in Plate 4.4.2A, crossed polarised light. Spherulites consist of anti-rapakivi plagioclase	153
<u>Plate 4.4.2C</u>	Skeletal pyroxenes	154
<u>Plate 4.4.2D</u>	Anti-rapakivi plagioclase in Plate 4.4.2C, magnified	154

<u>Plate 4.4.2E</u>	Abundance of apatite needles in microsyenite enclaves	155
<u>Plate 4.4.2F</u>	Ferrohedenbergite microsyenite enclave in granite porphyry ring-dyke (T5)	155
<u>Plate 4.5A</u>	Plagioclase mantled by microperthite in biotite granite	161
<u>Plate 4.5B</u>	Inclusions of discrete plagioclase in microperthite in same rock as Plate 4.5A	161
<u>Plate 4.5E</u>	Coalescence of vein texture in perthite into patches, through coarsening of ex-solved phase. Mineralised biotite granite (T138), Kogo hill	162
<u>Plate 4.5F</u>	Textural evidence (?) for the replacement origin of 'mantling' of plagioclase by alkali feldspar. Mineralised biotite granite (T138), Kogo hill	162
<u>Plate 4.5G</u>	Transitional stage in the replacement of reddish-brown biotite by calcite and muscovite. Mineralised biotite granite (T70)	166
<u>Plate 4.5H</u>	Consumation of replacement of reddish-brown biotite by calcite and muscovite. Mineralised biotite granite (T70), Kogo hill	166
<u>Plate 4.5J</u>	Calcite accompanied by muscovite completely pseudomorphs a congregation of biotite flakes. Mineralised biotite granite (T70), Kogo hill	167
<u>Plate 4.5K</u>	Rod-like crystals of calcite nucleated round the margins of a fluorite inclusion in biotite undergoing progressive replacement by calcite. Mineralised biotite granite (T70), Kogo hill	167
<u>Plate 4.6.1A</u>	General texture of the chlorite microcline porphyry (T41) with cross-hatch twinned microcline phenocryst in centre	174
<u>Plate 4.6.1B</u>	Part of the microcline phenocryst in Plate 4.6.1A magnified, to show overgrowth from original crystal boundary into the groundmass and the abundance of minute inclusions	174

<u>Plate 4.6A</u>	Lobate and serrated grain boundaries between adjacent perthites in Aegirine-augite ferrichterite syenite (T34C), and braided perthitic texture (top left) is common	181
<u>Plate 4.6AT</u>	The metasomatic transition in the over-saturated peralkaline syenites as seen in hand specimen	opposite page 184
<u>Plate 4.6B</u>	General texture of Aegirine-augite ferrichterite syenite T34C	181
<u>Plate 4.6C</u>	Granoblastic polygonal texture in Amphibole potash syenite (T34)	182
<u>Plate 4.6D</u>	Interstitial role of amphibole in Amphibole potash syenite (T34) displayed. Amphibole traces the granoblastic polygonal texture of the rock, thus showing its late stage crystallisation during the metasomatic textural re-equilibration	182
<u>Plate 4.6E</u>	Arfvedsonite in peculiar stellate habit. Sodic granite (T173)	183
<u>Plate 4.6F</u>	Intergrown magnetite-haematite replacing amphibole during the potassic phase of metasomatism. Potassic syenite (T34)	183
<u>Plate 4.6G</u>	Antiperthite texture in anti-perthite biotite granite (T34B)	189
<u>Plate 4.6H</u>	Textural evidence for the subsolidus origin of the biotite in biotite granite (T34BB)	189
<u>Plate 4.6J</u>	Biotite preferentially crystallises along healed fracture	
<u>Plate 4.6K</u>	Replacement perthitic texture in fine-grained biotite granite (T34BB)	195
<u>Plate 4.6L</u>	Textural relationship between adjoining perthites of the fine-grained biotite granite T34BB	195
<u>Plate 4.6M</u>	Green biotite with dactylitic outgrowths which selectively replace the K-phase of surrounding perthites. Biotite is post-exsolution. Fine-grained biotite granite (T34BB)	196

<u>Plate 4.6N</u>	Magnification of part of a biotite crystal in Plate 4.6F, showing detailed textural relationship between the biotite and perthite at an advanced stage of selective replacement of the K-phase in the perthite by the biotite	196
<u>Plate 4.6P</u>	Zoned plagioclase showing orientation of inclusions parallel to the albite twinning in the outer zone. Metasomatically altered 'basement screen' (T35)	199
<u>Plate 4.6PA</u>	Metasomatically altered 'basement screen' hand specimens showing gradational textural changes	opposite page 198
<u>Plate 4.6Q</u>	Cross-cutting veins of hastingsite in metasomatically altered 'basement screen'	199

LIST OF TABLES

		Page No.
<u>Table 2.3.2</u>	Stratigraphical Succession of the Extrusive Volcanic Rocks	12
<u>Table 5.2</u>	Fayalite analyses	204
<u>Table 5.3A</u>	Representative ferroaugite analyses	209
<u>Table 5.3B</u>	Representative ferrohedenbergite analyses	210
<u>Table 5.4A</u>	Representative analyses of calcic and sodic-calcic amphiboles	230
<u>Table 5.4B</u>	Analyses of sodic pyroxenes and alkali amphiboles	231
<u>Table 5.5</u>	Representative analyses of iron-titanium oxide minerals	248
<u>Table 5.6</u>	Analyses of selected biotites and chlorites	258
<u>Table 6A</u>	Whole-rock major and trace element analyses of basement and extrusive volcanic rocks	261
<u>Table 6B</u>	Whole-rock major and trace element analyses of the porphyries	262
<u>Table 6C</u>	Whole-rock major and trace element analyses of samples from the biotite granite pluton	263
<u>Table 6D</u>	Whole rock-major and trace element analyses of miscellaneous rocks	264
<u>Table 6.3.5</u>	Rare-earth element data for selected rocks of the Tibchi Complex	290
<u>Table 4.5</u>	Modal analyses of representative biotite granites	Appendix
	X-ray data on alkali feldspars from the Tibchi Complex	Appendix
	Additional analytical data on rock-forming minerals	Appendix

THE NIGERIAN YOUNGER GRANITE PROVINCE

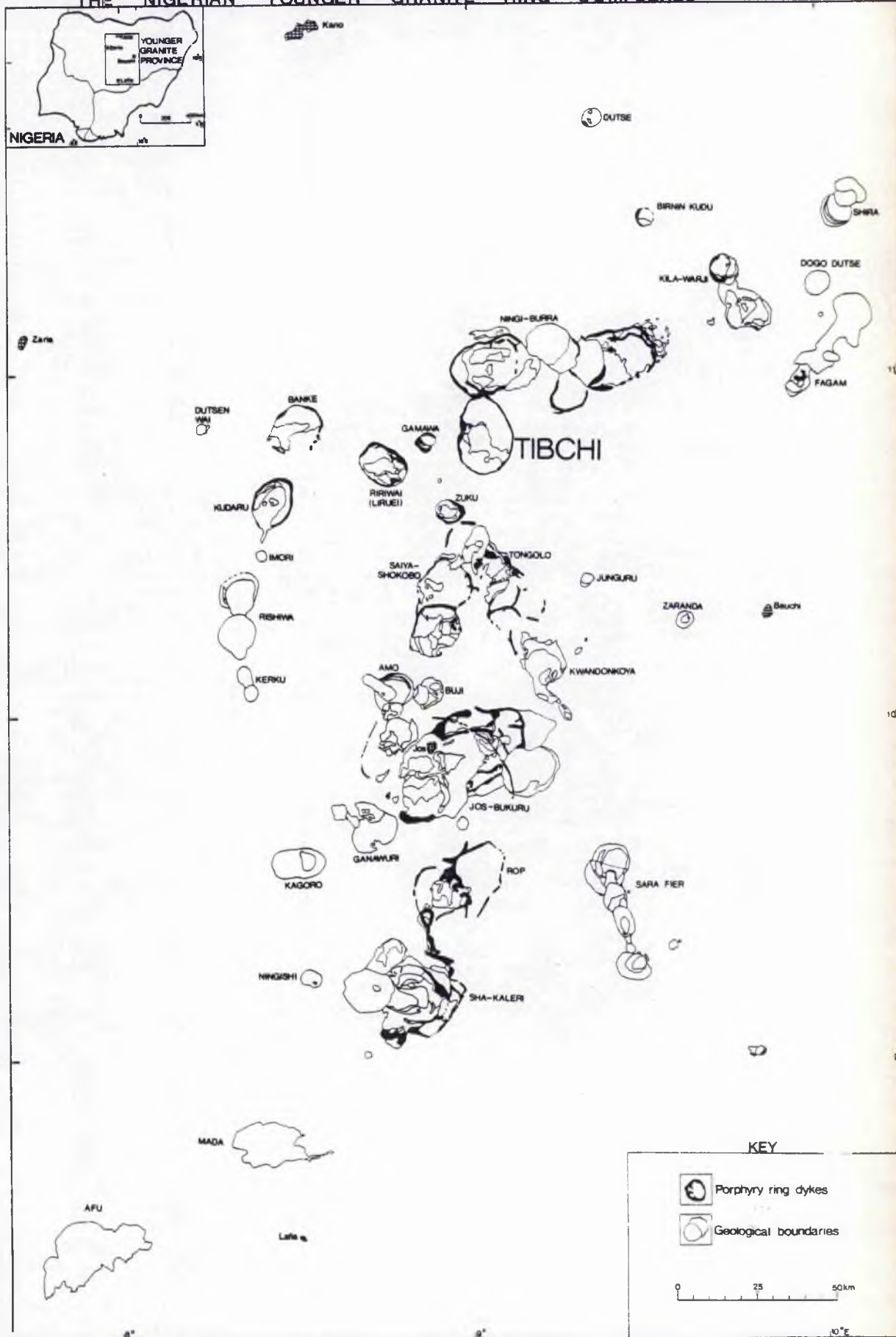


Figure 1 Location map of the Tibchi Complex.

CHAPTER 1
INTRODUCTION

1.1 The Nigerian Younger Granites

The Nigerian Younger Granite province comprises over forty individual anorogenic ring-complexes, one of which is the Tibchi Complex. These complexes range in size from less than 2 square kilometres up to 1500 square kilometres and occupy a north-south zone, about 300 kilometres wide, in the north-central part of Nigeria (Figure 1). It is now established (Black, 1963) that the above zone extends northwards across the national frontiers to link with a petrologically similar but older group of ring-complexes in Niger.

A progressive north-south age trend for these complexes from Niger to Nigeria has been proposed, indicating that magmatism commenced in the early Silurian times in the Air region of Niger and apparently ceased in the southern extremity of the Nigerian province in the late Jurassic period (Bowden *et al.*, 1976). The Nigerian province alone ranges from Upper Triassic to Lower Jurassic.

By about the first quarter of this century, almost all individual ring-complexes now known in the Nigerian province, had been discovered and mapped in outline. The importance of mineralisation was also recognised and the interest generated then has grown over the years. By the mid-nineteen-sixties, ring-complexes belonging mainly to the Jos Plateau area had been mapped in detail and some of them geochemically studied. Detailed chemical studies of the rock-forming minerals were confined to the amphiboles and to a small extent Na-rich pyroxenes

and micas. Details of the above studies and the general features of the Nigerian Younger Granite province including distribution of individual complexes, structural features, principal rock-types, and summary of the chemical characteristics of the province, may be found in Jacobson et al., 1958; Macleod et al., 1971; and Buchanan et al., 1971. Turner (1972, 1973, 1976) has also reviewed in detail the existing information on the tectonic setting, structure and petrology of the province.

Since the mid-nineteen sixties research interests in the province have diversified. Geophysical measurements (Ajakaiye, 1968, 1970, 1974), radiometric dating (van Breemen and Bowden, 1973; van Breemen et al., 1975; Bowden et al., 1976), rare-earth element studies (Aleksiyev, 1970; Bowden and Whitley, 1974; Moyes, 1979; Bowden et al., in press), feldspar studies (Badejoko, 1977; Martin and Bowden, in preparation), and mineralisation (Abaa, 1976; Kinnaird, 1977; Bowden and Jones, 1978; Bowden and Kinnaird, 1978) demonstrate the current trend of approach to the problems of the Nigerian Younger Granite magmatism. In the same period, geological maps and descriptions of three complexes have appeared in the literature (Turner, 1968; Oyawoye, 1968; Turner and Bowden, 1979). Other complexes such as Afu, Mada, Kagoro, Rishua, Fagam, Tibchi (this study) and others still remain known only in outline.

A lot has been achieved over the years. However data on mineral chemistry are conspicuously scarce, especially with respect to certain mineral species like fayalite, Ca-rich pyroxenes and iron-titanium oxides. In igneous petrology these minerals play important individual and collective roles which to date have hardly been exploited by previous workers. It is desirable

also to correlate structural, petrological, and mineralo-chemical data in individual ring-complexes in order to impose the necessary constraints on the interpretation of results. Such information will make a significant contribution to the overall interpretation of the problems of the Nigerian Younger Granite magmatism.

1.2 The Tibchi Complex

1.2.1 Present study

The work carried out is a detailed study of the little-known Tibchi Complex. The aim was to map the Complex and to study its geology with respect to structure, petrology and geochemistry. Emphasis on the geochemical studies is placed on the mineral chemistry of fayalite, Ca-rich pyroxenes and amphiboles. It is hoped that successful correlation of the structural, petrological and chemical features should provide a sound basis on which future work in other complexes can be carried out.

1.2.2 Previous work

Between 1919 and 1934 when the then newly established Geological Survey of Nigeria undertook to discover and map in outline all occurrences of Younger Granite complexes in Nigeria, the Tibchi Complex, then called the Tibchi-Yeli Hills, was recognised and appeared for the first time in an outline map of the Northern Tinfields of Bauchi Province (Falconer and Raeburn, 1923). Brief descriptions were given of the rock types found.

Between 1941 and 1951 three internal reports concerning mineralisation, were written for the Geological Survey of Nigeria;

the first on wolfram occurrence in the Kalato-Kogo area (Tattam, 1941), the second on some primary mineralisation at Yeli and Kogo (Rockingham, 1950), and the third a preliminary report on the Kogo lode (Rockingham, 1951). Haag (1943), reviewing wolfram occurrence in Nigeria, reported on the Tibchi area. A private report on the economic potentiality of the Kalato area as a tinstone producer was written by Dempster (1956).

Rb-Sr age determination on a biotite microgranite (T15) from the Tibchi Complex, by J.N. Bennett and M.O. Rahman (pers. comm.), gave 175 ± 3 m.y. (Lower Jurassic).

1.2.3 Location and access

The location of the Tibchi Complex in the Nigerian Younger Granite province is shown in Figure 1 and access in Figure 2.1.

1.2.4 Mapping and map-preparation

The mapping of the Tibchi Complex was continued from November 1975 to July 1976 during a period which corresponds broadly with the dry season in the northern part of Nigeria.

Generally exposure is good and contacts among the principal rock units are direct and well defined, although in some cases this may be an over-generalisation.

The mapping was carried out using aerial photographs with an approximate scale of 1:40,000 taken in November-December 1971. The map was drawn using an unpublished 1:50,000 planimetric map of the Tibchi area (obtained from the contiguous Sheets 126 Ririwai and 127 Kalato of the Geological Survey of Nigeria), as a base. With the aid of a Hilger and Watts SB100 Radial Line

Plotter of the Department of Geography, St. Andrews University, it was possible to transfer geological boundaries directly from pairs of air photographs to the base map accurately.

Cartography and final production of the 1:50,000 geological map were also done by the writer, using draughting equipment in the Department of Geology, University of St. Andrews.

1.2.5 Physiography and drainage

Topographically the Tibchi Complex is conspicuous relative to the surrounding basement, in the central area occupied by the biotite granite, and in the western and eastern arcs of the peripheral granite porphyry ring-dyke. This is virtually the form in which the Complex appears in the existing outline map (Falconer and Raeburn, 1923). Details of the topographical form of the Complex may be found in the three cross-sections of the 1:50,000 geological map accompanying this work.

In summary, the Younger Granite rocks in the Complex form a central area of high ground, with radial drainage and marginal basins within the peripheral ring-dyke. The Tibchi Complex provides headwaters for two regional river systems - the River Kano in the west and the River Bunga in the east. The watershed between the two river systems is located along a linear tract between Yarda Gungume and Rafin Dinya in the north-east, running south-westerly between Kogo and Mai Lafia, to the area west of Kalato. Here the watershed turns south-easterly towards Old Nukusum.

1.2.6 Climate and vegetation

The Nigerian climate is tropical, with two well-marked seasons - a dry season and a rainy season. In the latitude

of the Tibchi Complex the dry season occurs between November and April followed by the rainy season from May to October. All the rain that falls in the Tibchi area is almost, if not entirely, during the rainy season, with an average of about 112cm (44 ins) in the year. During the rainy season the 'savannah' (grassland) vegetation flourishes. Normal bush may be quite thick in places at this time, consisting mainly of tall grass and scattered shrubs. Rivers and streams are recharged and roads may become flooded where intersected by river and stream courses and these may impair access to the Complex. In the dry season dry conditions return.

Average maximum and minimum temperatures in the Tibchi area are about 31°C (87°F) and 18°C(64°F) respectively. There is sunshine and warmth all the year round. The months of November to February correspond approximately to the 'harmattan' period when the North-East Trade Winds begin to blow southward into the country from the Sahara belt. At this period it is generally cooler than normal and less humid, with air-borne dust causing poor visibility at intervals during the day.

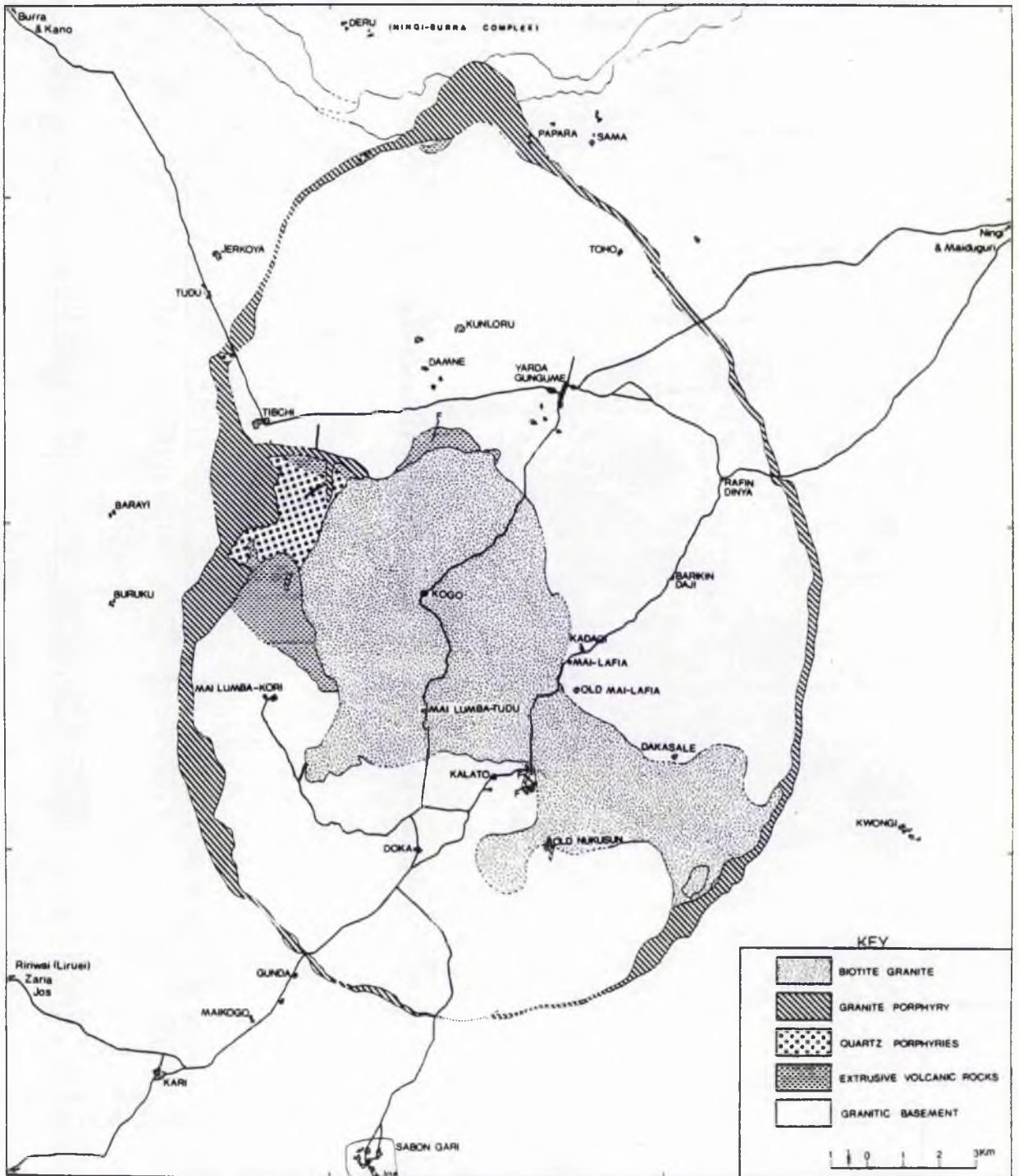


Figure 2.1 Simplified geological map of the Tibchi Complex, showing the major rock units and access.

CHAPTER 2

FIELD GEOLOGY

2.1 Introduction

This chapter consists of a field description of the principal rock units of the Tibchi Complex, based on the new 1:50,000 geological map of the Complex (in pocket). Description follows the chronological order: the granitic basement, the extrusive volcanic rocks, the quartz porphyries, the granite porphyry ring-dyke and isolated dykes, and the central biotite granite (Figure 2.1). A number of minor rock types have been found to be distinctive from within members of the above major rock units. These have been grouped together as 'miscellaneous rocks'.

2.2 The Granitic Basement

2.2.1 Distribution

The basement rocks occur both as an outer envelope to the peripheral granite porphyry ring-dyke, and as a rock unit enclosed within the ring-dyke itself. The basement enclosed within the ring-dyke, hereafter called the 'enclosed basement', is observed to be in virtually continuous contact with the inner perimeter of the dyke, except in the north-west and south-east. In the latter two places the ring-dyke makes direct contact with the volcanic rocks and the central granite, respectively. In surface area the enclosed basement occupies 226 square kilometres, of the total 344.5 square kilometres, of all exposed rocks within the ring-dyke.

2.2.2 Lithology

The basement rocks associated with the Tibchi Complex belong to the group commonly known as the 'Older Granites'. Chronologically, the Older Granites are the youngest members of the basement superstructure in Nigeria. Macleod et al. (1971) have given a comprehensive account of the basement geology of the Younger Granite province, with particular reference, however, to the Jos Plateau area. Relevant parts of the above account are found to be generally applicable to the basement rocks of the Tibchi Complex especially in terms of regional field relations and lithological sub-divisions of the 'Older Granites'. Strictly, the 'Older Granite' basement of the Tibchi Complex consists of adamellites. These adamellites have been differentiated, in the enclosed basement (see 1:50,000 geological map), into a coarse-grained porphyritic hornblende biotite Older Granite in the west, and a fine- to medium-grained biotite (muscovite) leucogranite in the east, both delineated by an approximately north-south boundary. The above divisions are based on the classifications of Macleod et al. (op. cit.). A sparsely porphyritic variety of the coarse-grained Older Granite outcrops in a small area south of Mai Lumba-Kori.

2.2.3 Relative age

Macleod et al. (1971) discovered in the Jos Plateau area that the fine- to medium-grained biotite and biotite (muscovite) leucogranites of the Older Granite basement are usually "elongated bodies with approximately meridional trend" The meridional trend of the boundary between the coarse-grained and fine- to medium-grained types in the Tibchi Complex may have been dictated by the later intrusion of the fine-grained phase

into an earlier coarse-grained phase. This is consistent with the relative age between the two phases suggested by Macleod et al. (op. cit.).

2.3 The Volcanic Sequence

2.3.1 General

The volcanic sequence consists essentially of extrusive volcanic rocks. These are preserved in two principal localities: south-west of Yarda Gungume, in the north-central area; and north of Mai Lumba-Kori, in the west. Members of the sequence near Yarda Gungume generally strike east-west, while those close to Mai Lumba-Kori generally strike north-ward. The intervening area between the two sectors is occupied by the quartz porphyries in which a few remnant 'caps' of crystal tuffs occur. In the extreme north, near the Ningi-Burra Complex, a 'tongue' of crystal tuff is also preserved within the Tibchi ring-dyke framework.

Criteria for classification of the pyroclastic rocks are based on Ross and Smith (1961). Size classification of volcanic fragmental materials in terms of 'block', 'lapilli', and 'ash' are those of Wentworth and Williams (1932) and Blyth (1940), except that all sizes below 4mm are regarded as 'ash' in this study. The term 'rhyolite agglomerate' is used here to designate an agglomerate whose fabric is composed entirely of rounded, fragmental, and apparently 'plastic' blocks of rhyolite (perhaps in near-consolidation state prior to pyroclasis), welded strongly in the absence of a tuff matrix, possibly as a vent phenomenon. Wherever the term 'ignimbrite' is used in this study, the definition of Macdonald (1972) is implied, thus

TABLE 2.3.2

Stratigraphical Succession of the Extrusive Volcanic Rocks

----- Quartz Porphyries -----	
12. Welded crystal tuff (2)	40-50% phenocryst
11. Welded agglomerate with crystal tuff matrix	40-50% phenocryst in matrix
10. Welded crystal tuff (1)	20-30% phenocryst. Lithic fragments up to 30-20% in places.
9. Welded lithic tuff	Less than 10% phenocryst. Lithic fragments much more important.
8. Welded lapilli tuff	Intercalated with at least two (but very thin) basalt flows.
7. Rhyolite agglomerate	(see text)
6. Interbedded agglomerate, and basalt	(Poorly exposed)
5. Bedded flow trachyte	
4. Basalt	
3. Poorly welded tuff	Leucocratic and devoid of mafic minerals.
2. Rhyolite lavas and minor siliceous feeder dykes	
1. Ash-fall tuffs	

Older Granite Basement

the term is synonymous with ash-flow tuffs and includes both welded and non-welded types. Classification according to degree of welding assumes that the possibility of shards and pumice fragments being resistant to compaction and flattening during welding is small, and hence follows the method of Mansfield and Ross (1935): In non-welded tuffs the original forms of the shards and pumice fragments remain unmodified; in poorly welded tuffs there is flattening but without obliteration of the characteristic shard structure; and in very strongly welded tuffs there is extreme flattening (and folding round the edges of lithic fragments and phenocrysts).

2.3.2 The stratigraphical succession

The stratigraphical succession of the volcanic rocks may be found in the 1:50,000 geological map but is reproduced in Table 2.3.2. The succession presented is probably self-explanatory in terms of the rock types encountered in the field as well as chronology.

The maximum exposed vertical (not stratigraphical) thickness of the entire extrusive sequence is found in the Mai Lumba-Kori sector (ref. O-P line of cross-section, 1:50,000 geological map). Here the crystal tuff (1) caps the sequence at a topographical height of 1013 metres above sea level or 229 metres above the general basement level; the true thickness being approximately 450 metres, taking into account the general inclination towards the centre. The latter is thought to represent the minimum thickness before erosion.

In the Mai Lumba-Kori sector, the bottom of the extrusive sequence is occupied by rhyolite lava lying directly on Older Granite basement. Several stream courses run perpendicularly

to the strike of the volcanic pile and expose the underlying basement in several places. Narrow dykes of rhyolite, sometimes up to one metre wide, are observed to cut through the basement, apparently as feeders to the lavas. In the Yarda Gungume sector, the rhyolite lava lies directly on the basement as an easterly semi-circular mass. In the northern part of the main sequence the rhyolite lava is observed to be underlain by ash-fall tuff. Some roundish inclusions up to 15 x 11 millimetres in size are found in the ash-fall tuff and have been identified microscopically as belonging to basement lithology. These inclusions are surrounded by thin brownish coating suggestive of subaerial exposure and oxidation prior to incorporation into the ash-fall tuff. There are also isolated grains of quartz, rounded off in outline. The above inclusions and rounded quartz grains are interpreted as non-pyroclastic in origin (see Chapter 4) and probably represent alluvial or eluvial material lying on the basement surface prior to deposition of the ash-fall tuff. The total thickness of the ash-fall tuff is probably less than 0.5m. Based on the field relationship between the rhyolites and basement on the one hand, and the ash-fall tuff and the basement on the other, it is apparent that the Tibchi Complex provides the first clear exposure of the Jurassic land surface to be recorded in Nigeria.

2.3.3 Inward dip and the tilted floor of the volcanic sequence

In the Mai Lumba-Kori sector in the west, the volcanic rocks are observed to have a general northerly strike, and a general easterly dip towards the centre of the Complex. Those in the Yarda Gungume sector in the north have an east-west strike and

a general southerly dip towards the centre of the Complex.

The above two modes of inclination towards the same centre perhaps represent relics of an originally centripetal inward dip phenomenon with a focus in the vicinity of the present location of Kogo village.

Within the general inward dip in each sector, a progressively decreasing angle of dip is observed towards the interior of the Complex. In the Mai Lumba-Kori sector, for example, the following angles were measured, towards the central granite:

1) Younging 2) Towards Centre	Dip (in degrees)	Strike (in degrees)	Rock type measured
↑	d) Sub-horizontal	north-south	Crystal tuff (1)
	c) 032	340	Lithic tuff
	b) 045	309	Bedded trachyte
	a) 056	190	Poorly welded tuff

As can be seen by reference to the stratigraphical succession, the dips displayed above decreased not only from periphery to centre of Complex but also from older to younger rocks.

The floor of the volcanic sequence is considered to be essentially the surface of the enclosed basement. Although there appears to be a radial distribution of dip about a centre among the volcanic rocks, the Mai Lumba-Kori group demonstrates in addition, that the basement floor on which it rests, is probably tilted in the north-west direction. Along the general northerly strike of the above group, there is a step-wise disposition of topography corresponding to successively younger rock units (see

geological map), all pitching an echelon towards the north-west. For example the base of the crystal tuff (1) is at an elevation of about 945 metres (3145ft) isograde in the south-east end of the sequence and at about 710 metres (2700ft) in the north-west, signifying a drop of about 235 metres within a distance of about 2 kilometres, and a gradient of about 1 in 10. Since all units are displaced, if there was subsidence, it is reasonable to assume that the subsidence was not everywhere equal.

2.4 The Quartz Porphyries

2.4.1 General

The term quartz porphyry is a most uncertain term in the literature, especially in contradistinction to granite porphyry. In the Glossary of Geology of the American Geological Institute (Gary et al., 1974), quartz porphyry is defined as "A porphyritic extrusive or hypabyssal rock containing phenocrysts of quartz and alkali feldspar (usually orthoclase) in a microcrystalline or cryptocrystalline groundmass; a rhyolite.", and adds, "European petrologists called pre-Tertiary and Tertiary extrusive equivalents of granite 'quartz porphyry' and post-Tertiary equivalents, 'rhyolite' (Streckeison, 1967, p.189). Syn: quartz felsite."

From the above, quartz porphyry is synonymous with rhyolite in America and quartz felsite in Britain. Granite porphyry is defined by the A.G.I. Glossary as "A hypabyssal rock differing from a quartz porphyry by the occasional presence of mica, amphibole, or pyroxene phenocrysts in a medium- to fine-grained groundmass."

None of the above definitions can be applied successfully to the Nigerian Younger Granite province without qualification.

The current usage of these terms in the Nigerian literature does not preclude the occurrence of mafic phenocrysts in quartz porphyries (eg. Jacobson et al., 1958; Macleod et al., 1971; Jacobson and Macleod, 1977); in fact mafic minerals are often used to distinguish the different varieties of quartz porphyries as well as granite porphyries. Some authors (e.g. Turner, 1976; Turner and Bowden, 1979) distinguish between a 'granite porphyry' and a 'porphyry', each qualified by its characteristic mafic assemblage, the 'porphyry' being in detailed description the quartz porphyry of previous authors.

2.4.2 Definition and delimitation of terminology

Although the bulk chemistry (assuming the absence of hydrothermal activity) between the quartz porphyries and granite porphyries in Nigeria, may be found to be identical, petrographically the two rock types are distinctive. It is the petrographical distinction that forms the basis for separating the quartz porphyries from the granite porphyries in this study. Support for this division will be seen later in subsequent chapters.

In the Tibchi Complex the above petrographical difference lies principally in the texture, and in the unaltered rocks, on the number of phases of characteristic high temperature minerals present. The difference in the number of high temperature minerals will be shown later to be related to the difference in time and mode of emplacement, between the quartz porphyries and the granite porphyries. Macleod et al. (1971) adequately summarised the relationships: "A distinctive sub-group" of the porphyries "is the quartz fayalite porphyries, forming for

example the great ring-dyke at Kudaru and small plugs cutting rhyolite at Buji, Jere-Sanga and Liruei. These rocks occur as the last stage in the volcanic phase of activity and are transitional between the microcrystalline cauldron rhyolites* and the granite porphyries, both texturally and in time and mode of occurrence."

For detailed petrographical descriptions, the reader is referred to Chapter 4. Below is a brief summary of the textural characteristics of each of the two porphyry types and the mineralogical character of unaltered samples, as observed in the Tibchi Complex.

In the quartz porphyry, the phenocrysts (principally alkali feldspar and quartz) would not usually exceed 7x3 millimetres maximum grain size, and are characteristically fragmental in appearance. In the latter respect, the quartz porphyry tends towards the crystal tuffs. In fact there is field evidence that the quartz porphyry may be partly extrusive; its extrusive equivalent being often difficult to distinguish from the crystal tuff. The mafic assemblage in the unaltered quartz porphyry consists of fresh fayalite and Ca-rich pyroxene (ferroaugite-ferrohedenbergite series), without co-existing amphiboles.

On the other hand, the granite porphyry consists of relatively large phenocrysts, reaching 18x11 millimetres in some cases (50mm length has been recorded in Rop by Jacobson et al., 1958). The feldspar phenocrysts show a diagnostic synneusis

*The 'cauldron rhyolites' correspond to the late rhyolites of Jacobson et al. (1958) and the Crystal tuff (2), this study. These are essentially caldera filling ignimbrites, rather rhyolite-looking but strongly welded. They are thought to have been fed into the caldera by quartz porphyries.

which is absent in the quartz porphyries. Amphiboles are absent in the unaltered granite porphyry, fayalite also cannot be optically identified even if it may be present as a relict phase in the form of iddingsite etc. Thus Ca-rich pyroxene is observed to be the only stable mafic phase present. The implications of these observations are treated in Chapter 3. The disappearance of fayalite as a stable phase in the granite porphyry is consistent with the earlier observation of Macleod et al. (1971) that, "The degree of reaction which the fayalite and hedenbergite have undergone can be correlated with the rapidity of chilling of the intrusions and the amount of volatiles present during the later stages of crystallisation. The quartz pyroxene-fayalite porphyries, where reaction relationships are minimal, have apparently chilled rapidly." In contrast the more slowly cooled granite porphyries show "a preponderance of the later members of the reaction series."

Summary The quartz porphyry, in the Tibchi context, may be defined as the porphyritic extrusive or hypabyssal rock containing phenocrysts of quartz and alkali feldspar in a microcrystalline or cryptocrystalline groundmass, but showing a varying degree of ignimbritic texture, and with fayalite and pyroxene as the only mafic phases in unaltered samples. The granite porphyry differs from the above by being exclusively hypabyssal and by possession of glomeroporphyritic texture, and only pyroxene as the stable mafic phase, in unaltered samples.

2.4.3 The Tibchi Quartz Porphyries

The quartz porphyries of the Tibchi Complex occur as one

main unit south of Tibchi Village and between the Mai Lumba-Kori and Yarda Gungume sectors of the extrusive volcanic rocks. There are also two separate minor occurrences within the granite porphyry ring-dyke in the north-west.

The quartz porphyries of the main unit are truncated in the west by the peripheral granite porphyry ring-dyke and in the east by the central biotite granite. It is observed that, while the quartz porphyries nearest the ring-dyke remain unaltered, a varied degree of hydrothermal alteration has occurred in all areas on the flanks of the biotite granite, with the alteration apparently increasing in intensity towards the biotite granite contact.

Closely spaced traverse and random sampling in the field, over the entire area of the main quartz porphyry unit, has made it possible to draw lithological boundaries based on degrees of hydrothermal alteration. These boundaries are obviously transitional. The lithological descriptions below consist of two parts: firstly, the 'pristine' rocks and secondly, the hydrothermally altered rocks.

The Pristine Quartz Porphyries The word 'pristine' is a relative term used here to designate all the quartz porphyries which can be shown to have been unaffected by the hydrothermal alteration referred to above. The character of the pristine rocks can thus be shown to be related to the original magmatic crystallisation.

The pristine quartz porphyries comprise the two separate minor inclusions in the granite porphyry ring-dyke, in the north-west; and that portion of the main unit nearest the

ring-dyke in the west; all as shown in the 1:50,000 geological map and Figure 4.4A (Chapter 4). Detailed petrographical descriptions are given in Chapter 4. Characteristically the pristine rocks are green in colour, although it is possible to find those with only minor alteration being essentially green also. This observation only emphasizes the transitional nature of the boundaries allocated in the map.

The hydrothermally altered Quartz Porphyries A broad zone of incompletely altered rocks is shown, in the geological map, adjacent to the pristine rock of the main unit. This zone is amphibole-bearing. In it also fayalite and Ca-rich pyroxenes appear unstable and are mantled by amphiboles. Along the biotite granite contact alteration is observed to be complete, with the absence of fayalite and pyroxene and the presence of amphibole phases only. However only the portion of the completely altered zone characterised by one amphibole phase (ferrorichterite) has been shown in the geological map. Elsewhere more than one amphibole may be found. Detailed petrographical descriptions have been given in Chapter 4 for all the lithological variants.

The clearest field indication of hydrothermal alteration in the quartz porphyries is an obvious change in colour. This colour change occurs first as blotches of light blue or grey on the normally green rock. The blotches increase in size and the new colour eventually assumes dominance over the initial green colour as one approaches the biotite granite contact. Along this contact lithological variants are found with totally blue or grey colours. The control for the final colour observed

will be shown later to be dependent on the nature of the starting (pristine) rock; and more than one pristine rock has been identified (see Chapter 4). Also, the colour of the final rock can be correlated with the type of amphibole assemblage present and ultimately with the composition of the Ca-rich pyroxene from which the new amphiboles have formed. The transition affects not only the mafic minerals, but also the feldspars and the texture of the groundmass. Electron microprobe analyses of the mafic phases as well as X-ray analyses of the feldspars have been used to monitor the progressive changes; these changes have been correlated with petrographic observations. Rare-earth element concentrations in the various samples have also been determined (Moyes, 1979). Results of the above analyses have been presented and discussed elsewhere in this study, with the aim of characterising the observed hydrothermal alteration.

2.4.4 Inclusions and relative age

The quartz porphyries are characterised in some places by a phenomenal proportion of xenoliths. These xenoliths which range from basalts to rhyolites, are fragmental in form. However, certain microferrodiorite and microsyenite inclusions observed have distinctive irregular and diffuse borders, and are shown subsequently to be cognate enclaves genetically related to the porphyries.

From the foregoing, it is inferred that the quartz porphyries were preceded in time, not only by members of the extrusive volcanic succession already described earlier, but also by certain primitive rock types not represented at the

present erosion level. Inclusions of the quartz porphyries are found in the granite porphyry and the latter also intrude the former through apophyses of the ring-dyke (ref. 1:50,000 map). It is therefore inferred that the quartz porphyries were emplaced earlier than the granite porphyry. The truncation of the quartz porphyries by the biotite granite clearly shows that the biotite granite was emplaced later than the former.

2.5 The Granite Porphyry Ring-dyke and isolated dykes

2.5.1 General features of the ring-dyke

In plan, the Tibchi Complex is defined by a peripheral granite porphyry ring-dyke which is elliptical in shape and almost symmetrically disposed north-south along its major axis. This major axis is 27.3 kilometres long while the minor (east-west) axis is 17.4 kilometres. The ring-dyke encloses all other rock units, and a large area of Older Granite basement, within its perimeter of 81.7 kilometres, and defines a total surface area of 344.5 square kilometres for the Complex.

The ring-dyke is virtually continuous in outcrop although as a topographical feature it is occasionally transgressed by the drainage systems radiating outwards from the central granite intrusion. Topographically, the dyke is most prominent in its western and eastern arcs; hitherto these arcs were the only features known of the peripheral ring structure. The ring-dyke attains its maximum thickness of about 2 kilometres in the west (south of Tibchi village), and in the north at the border with the Burra Massif, the most westerly unit of the Ningi-Burra Complex.

Photogeological interpretation of the ring-dyke is in

favour of an almost vertical inclination in most places. In the western arc where the ring-dyke is associated with basement rocks preserved on the outside margin of the dyke, the actual field impression is also that the ring-dyke has an approximately vertical dip. In the north and west, a vertical dip may be inferred as unlikely from the relatively extreme width of the dyke in these places, although it is hard to decide whether the inclination is outward or inward. Also, it may be observed in most places, especially in the west, that while the outside margin of the ring-dyke remains fairly regular in curvature, the inside margin shows a less regular form and in some cases actually protrudes into the interior of the Complex. The regular outside margin is interpreted to indicate lack of deviation of the dyke by changes in topography, indirectly suggesting a vertical dip; the irregular inside margin is interpreted to be due to varying degrees of development of apophyses directed towards the enclosed basement block. If subsidence of the enclosed basement block occurred, the chances of protruberances of the ring-dyke extending into this fractured central block than to the outside rigid basement wall-rock, would be greater. Indeed the well formed, repeatedly branching apophysis of the ring-dyke, south of Tibchi village, provides a good illustration of the above hypothesis and is described later. In the south, near the Sabon Gari road intersection, a cross-cutting cliff face shows the ring-dyke literally sandwiched in the basement, with both its outside and inside margins exposed. The dyke is less than 30 metres here. Field measurements give a strike of 120° - 125° and dip of 87° - 90° (towards the centre of the Complex) for the outside margin. Additional evidence on

the ring-dyke's inclination comes from a consideration of the general structure of the Complex. Marginal uptilting of the extrusive volcanic units preserved may indicate (see Chapter 3) that an inward dip, with depth, of the ring-dyke may be assumed. In summary, it seems certain that at the present level of erosion, the ring-dyke may be considered to be generally vertical but that in detail it may have, with depth, an inward-dipping tendency.

2.5.2 Contact relations

Since all granite porphyries may strictly be regarded as chilled to some extent, the 'chilling' described below refers to an additional effect related only to the contact zones of the granite porphyry ring-dyke.

Chilling of the granite porphyry along the ring-fracture has been observed against basement wall rocks, and it is found to occur most frequently where the ring-dyke, or its apophysis, is very thin. The chilling does not appear to cause any appreciable diminution of the usual size range of the constituent phenocrysts, nor of the phenocryst to groundmass ratio. Changes are apparent only in the groundmass. The normal groundmass of the unaltered granite porphyry is greenish-grey in colour, but black in the chilled borders of the ring-dyke, signifying that the groundmass is finer in grain size in the chilled rock.

Shearing and brecciation of the basement rocks has been observed alongside the southern arc of the ring-dyke. Here the dyke is very much reduced in size and possesses chilled borders. The large feldspar phenocrysts of the coarse grained porphyritic basement rock (with feldspar phenocrysts up to 3cm)

are crushed along multiple fault planes parallel to the ring-dyke margin. These fault planes are only a few centimetres or less apart and the shearing leads to elongated lenses of sliced feldspar megacrysts.

A black, fine-grained, rhyolite-looking 'flinty' rock, about one metre maximum width, has also been found between the outside margin of the narrow southern ring-dyke and the adjacent basement, near the Sabon Gari road intersection. A cliff face exposure as well as good outcrop surface enable the 'flinty' rock to be seen in three-dimensions and studied in detail. Vertically it is sandwiched between the ring-dyke and the basement but shows no abrasive relationships with the ring-dyke. On the outcrop surface it retains its position between the two rock units above but gradually pinches out in thickness over a distance of less than one kilometre. Since this 'flinty' rock is not treated further in petrographic descriptions (Chapter 4), reference may be made here to its microscopic features.

Microscopically the 'flinty' rock shows layering parallel to the ring-dyke contact and there appears to have been simply a comminution and induration of the constituent particles, with no evidence of magmatic textures. The crystal fragments consist of microcline, perthite, plagioclase and quartz. The number of quartz grains that show undulose extinction is relatively small. But bulk chemical composition places the 'flinty' rock clearly in the field of basement rocks.

The above rock may have been formed either by fluidisation along the ring fracture, prior to the granite porphyry ring-dyke intrusion, or by cataclasis associated with ring-faulting. The arguments are presented in Chapter 3. However, origin as

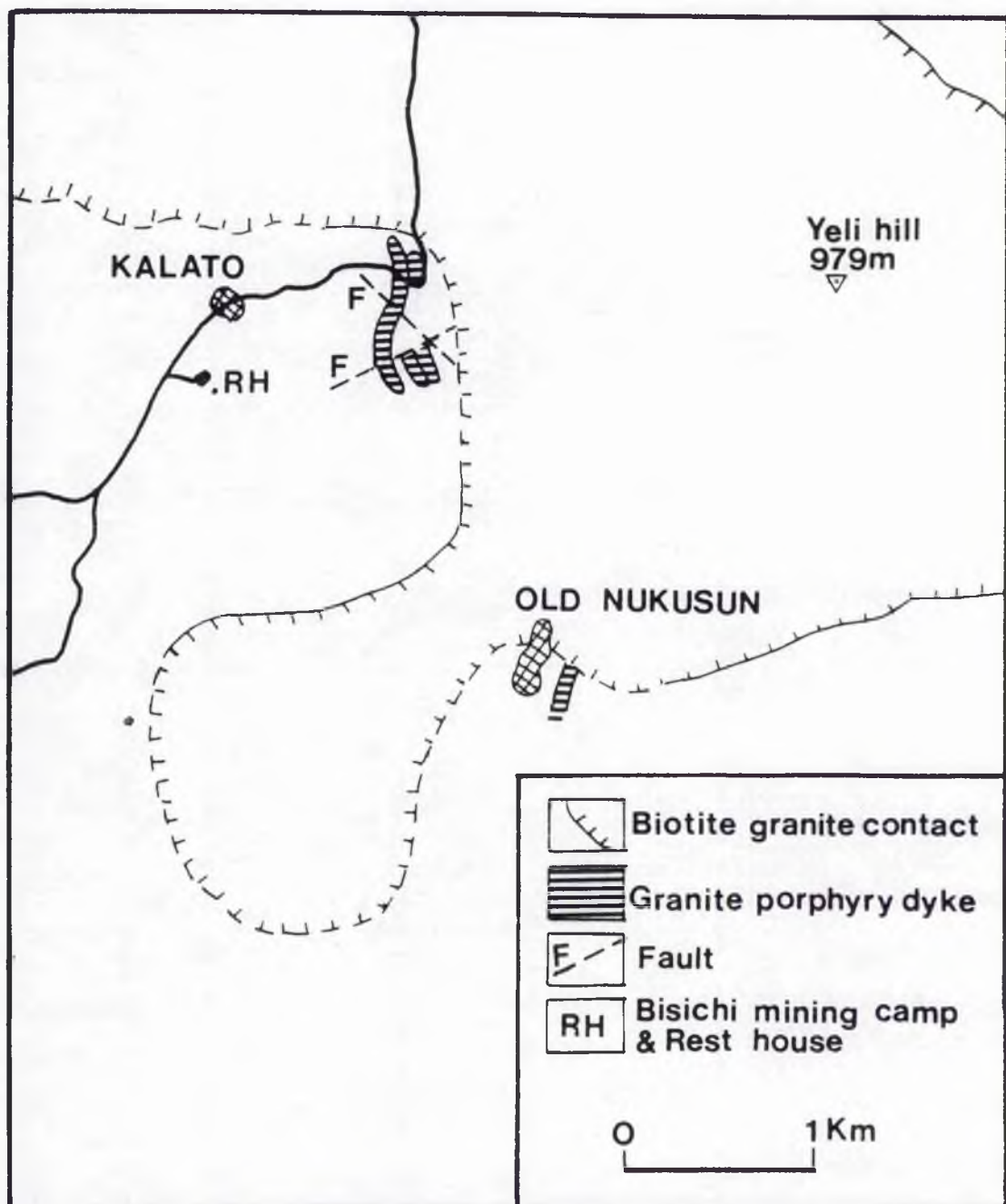


Figure 2.5.3 Post-emplacment faulting and displacement in a triplet set of minor granite porphyry dykes near the biotite granite margin, east of Kalato.

a 'flinty crush rock' (ref. Clough et al., 1909) associated with ring-faulting is favoured.

2.5.3 Apophysis of the ring-dyke and radial (?) dykes of granite porphyry

In the west, south of Tibchi village, the granite porphyry ring-dyke has an apophysis which penetrates the interior of the Complex. This offshoot is about 250 metres wide and follows the boundary between the basement and the main quartz porphyry unit. It repeatedly divides in its terminal region, with the subsidiary branches penetrating the quartz porphyries.

The ability of the ring-dyke to penetrate the enclosed basement much more readily than the (external) basement envelope is clearly demonstrated above. The implications are discussed in Chapter 3.

In the south-central area of the Complex there are three localities where small granite porphyry dykes outcrop. South of Mai Lumba-Kori and at Nukusun, single dykes occur, each cut by the central biotite granite. The occurrence east of Kalato, however, consists of a triplet set of dykes which have undergone post-emplacement faulting and displacement thought to be related to the adjacent biotite granite intrusion (Figure 2.5.3).

The above minor dykes are identical in lithology to the main granite porphyry ring-dyke and perhaps represent an originally larger group of radial dykes emplaced contemporaneously with the ring-dyke.

2.5.4 Lithological variations

A lithological variation has been observed round the perimeter of the granite porphyry ring-dyke as follows:

In the western, northern and eastern arcs of the ring-dyke, the granite porphyry can be described as belonging to the pristine lithology formed at the time of magmatic emplacement of the ring-dyke. Mineralogically hydrous phases are absent in the pristine rock, as described earlier in this chapter. The southern and south-eastern arcs of the ring-dyke, however, constitute a zone of localised variation with a marked presence of late amphiboles and sodic pyroxenes, and the complete absence of the initial high temperature mafic phases found in the pristine rock.

The above lithological variations are thought to be due to hydrothermal changes caused by the later intrusion of the biotite granite. In the south-east arc where the biotite granite/granite porphyry ring-dyke contact is exposed, the change in the lithology of the granite porphyry can be clearly observed. Details of the structural relationships envisaged, are shown in the cross-sections of the 1:50,000 geological map and Figure 4.4L (Chapter 3), while petrographical descriptions of all the lithological variants may be found in Chapter 4.

2.5.5 Relative age

Xenoliths of volcanic and subvolcanic rocks are found in the granite porphyry ring-dyke. These include the large quartz porphyry units in the north-west arc of the dyke. Xenoliths show fragmental forms and clear-cut boundaries with the host rock. There are also microferrodiorite and microsyenite inclusions whose boundaries with the host dyke rock are diffuse and irregular. These are shown (later) to be genetically related to the quartz, and granite porphyries and are for convenience referred to as 'cognate enclaves'. Obviously these

enclaves represent rocks earlier than the granite porphyry in time, in addition to the earlier extrusive volcanic rocks and quartz porphyries. However, the ring-dyke and its apophysis as well as the contemporaneous isolated dykes described, are partially or completely truncated by the biotite granite intrusion. Thus the granite porphyry ring-dyke and related dykes are clearly older than the biotite granite but later than all the other rock units of the Complex.

2.6 The Central Biotite Granite Intrusion

2.6.1 General

The biotite granite outcrops within the peripheral ring-dyke as an elongate unit. In the western part of the Complex it cuts the volcanic rocks and quartz porphyries and forms a circle of hills centred around Kogo area. From this area the granite outcrop tapers south-easterly across the Complex until the intrusion partially truncates the granite porphyry ring-dyke in the south-east. The biotite granite is thus in contact with the enclosed basement for most of its exposed total expanse. The above contact with the basement is, especially in the southern sector, characteristically sinuous in plan. The biotite granite is medium-grained and generally pinkish in colour. Detailed petrographical description is given in Chapter 4.

2.6.2 Contact relations

Five areas of biotite microgranite have been mapped along the margins of the intrusion. Contact between the microgranite and the main intrusion is gradational. While pinkish microgranites may be found, the majority are whitish in colour. In

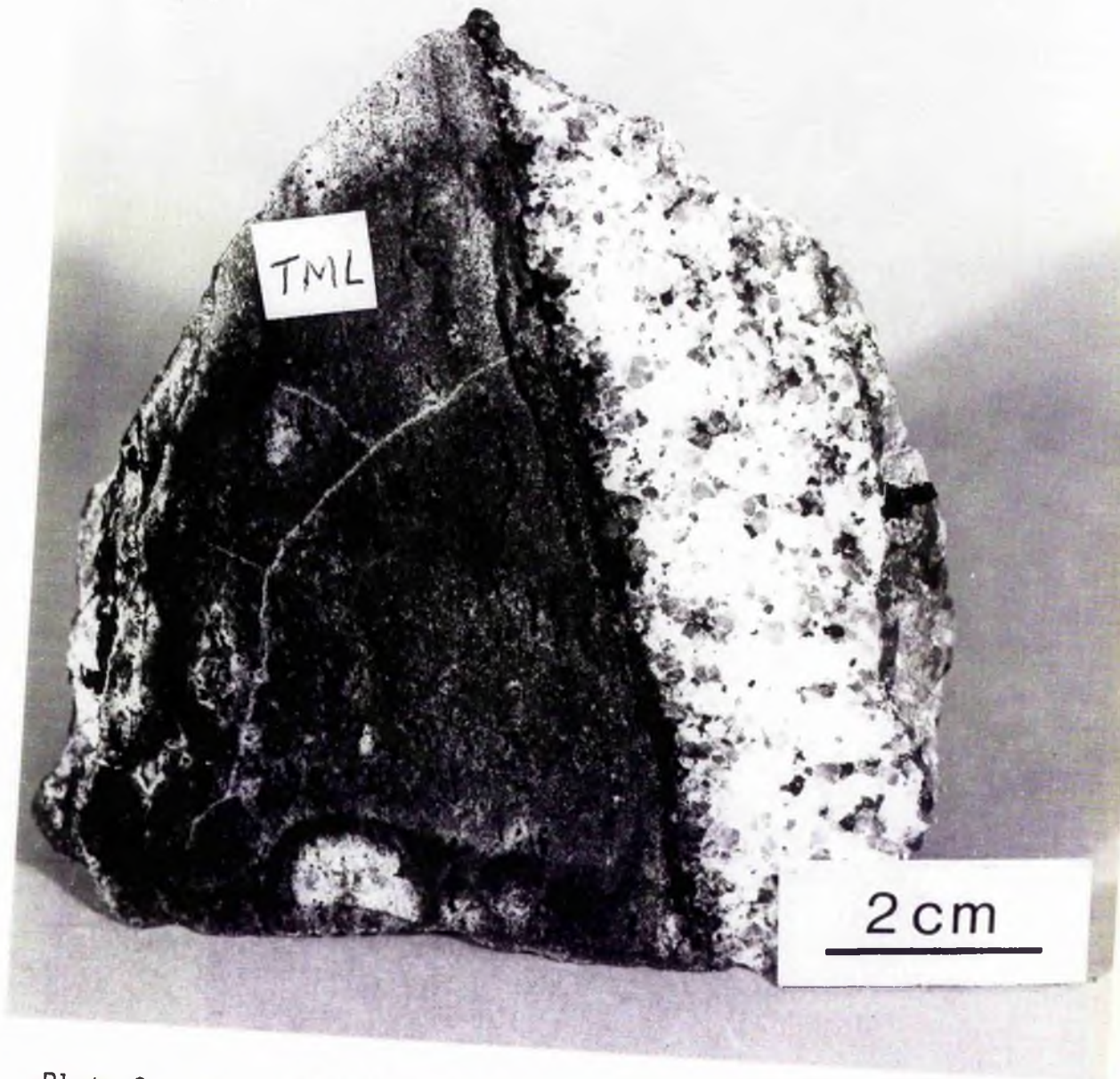


Plate 2.6.2A 'Contact foliation' in a rhyolite lava (dark grey) apparently caused by the later intrusion of the biotite granite (white).

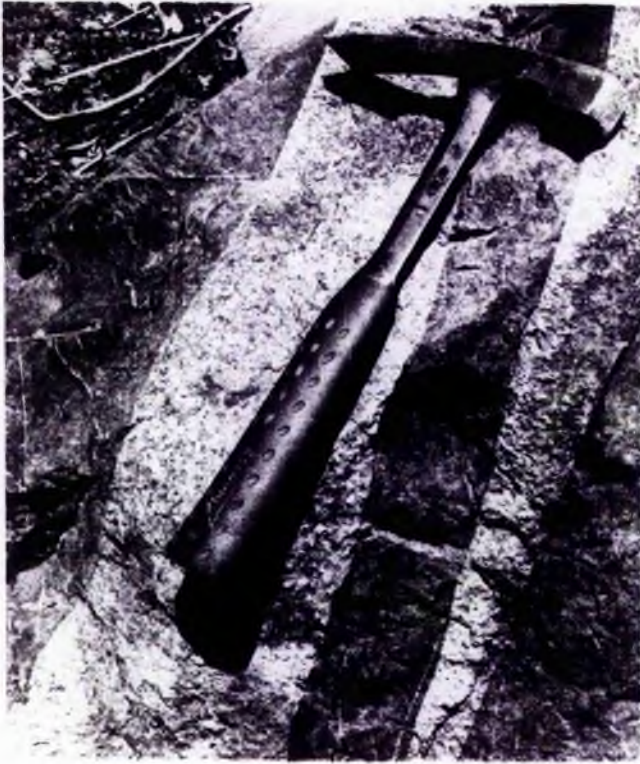


Plate 2.6.2B Veining of basalt (dark grey) by biotite granite

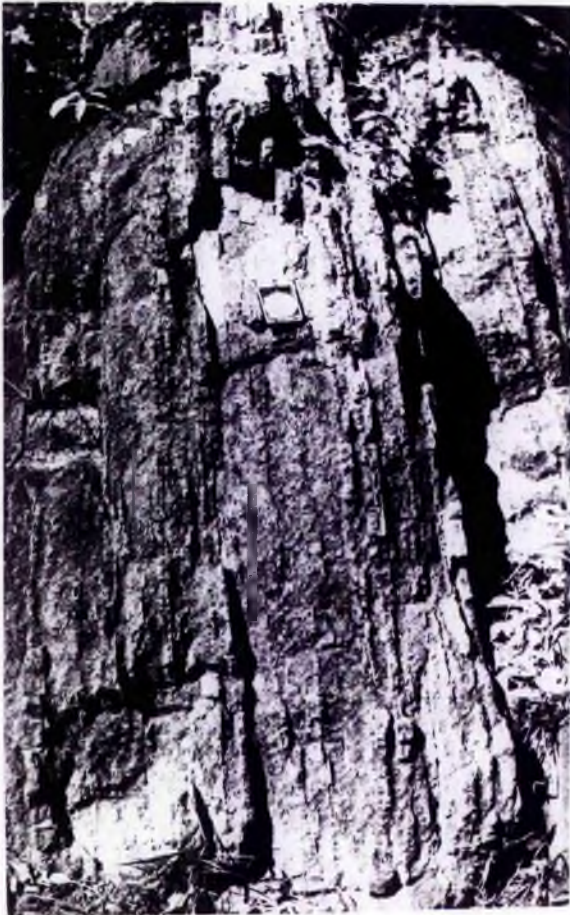


Plate 2.6.3A Greisen vein swarm, Tibchi Complex.

detail, the marginal microgranite facies, as the above may be called, is observed to be nearly always present round the entire contact of the main intrusion with the basement. Thus only the relatively large units have been shown on the geological map. In contrast, no occurrence of the biotite microgranite has been found along the contact between the biotite granite intrusion and the volcanic rocks or porphyries. It may be noted that it is these volcanic rocks and porphyries that show the most intense and extensive alteration along the biotite granite contact. A central area near Kogo is occupied by biotite microgranite. The contact of the latter with the main mass of the intrusion is gradational. Remnants of the microgranite can be seen to cap some of the biotite granite hills encircling the Kogo area, indicating the sheet-like form of the original microgranite facies as a roof to the main granite.

The biotite granite contact with the extrusive rhyolite in the Mai Lumba-Kori area shows that the intrusion has caused recrystallisation in the rhyolite and more importantly has caused a new mineral orientation to develop parallel to the contact (Plate 2.6.2A). The contact zone is very sharp but devoid of chilled borders and any pegmatitic development. On a smooth wet surface of an oriented hand specimen or a large thin section, black elongated streaks occur parallel to the line of contact. These black laminations, in detail, consist of aggregates of mica in parallel or semi-parallel alignment. This alignment is most probably due to a stress field originating from the biotite granite intrusion. The outer limit of this field was not investigated but another sample of a rhyolite agglomerate further north and some metres away from the line of

contact bears a similar imprint. This phenomenon is hereafter referred to as 'contact foliation'.

Veining of pre-existing rocks by the biotite granite intrusion has been observed in three localities, two in the extrusive volcanic series and one in the basement Older Granite. The extrusive rocks veined are: the basal rhyolite of the Mai Lumba-Kori sector, and the basalt of the Yarda Gungume group. The biotite granite penetrates these rocks by finger-like extensions ranging from less than 3cm wide to 6cm or more (Plate 2.6.2B). The rhyolite is at the same time recrystallised thoroughly while the basalt is strongly contact-metamorphosed, but there is hardly any mechanical mixing relationship between the veining granite and these rhyolite and basalt lavas.

An apparent incorporation of Older Granite basement is found in the area of the microgranite facies of the pluton south-east of Mai Lumba Kori. Here 'slicing' is parallel to the contact, resulting in incorporation of basement material by the biotite granite. A zone of hybridisation, up to about 30cm or more in places is formed by what appears to be a mechanical mixing of the two rock types.

Contact zone adjacent to the Older Granite basement is not only characterised by chilled borders of the biotite granite, but also by a thin, discontinuous, string of pegmatite. A conspicuous feature of the pegmatite development is its "doublet" character: the formation of two sets, one related to the biotite granite and the other to the basement Older Granite, parallel to each other and to the line of contact between them. Usually each set consists of one to several minor stringlets, the

stringlets on the biotite granite side are distinguished by their pinkish alkali feldspars while those on the Older Granite basement side have whitish feldspars. The colours of the feldspars correspond to the general colours of the feldspars in the respective rock types, hence the doublet effect of the pegmatites can be very distinct in the field. Pegmatite feldspars are larger on the basement side, than on the biotite granite side, of the contact. In the former, they may exceed 15x8cm in size and rarely up to 20x12cm; in the latter, they are much less. The contact of the biotite granite with the granite porphyry ring-dyke in the extreme south-east is marked by pegmatite knots also but without the 'doublet' effect described above. The contact of the biotite granite intrusion with the volcanic rocks and the quartz porphyries is devoid of pegmatites. Apart from marginal pegmatites, there are scarcely any pegmatites found in the main body of the biotite granite intrusion. At the summit of the Yeli hill, however, thin strips of pegmatites are observed to mark off, at intervals of a few metres, horizontal sheets of granite. This summit facies of the biotite granite is about 50% finer grained than the main rock, and whitish in colour owing to the nature of the feldspars present. The pegmatites found here are considered to be analogous to the pegmatite facies described earlier for the biotite granite margins.

Displacement of a triplet set of small granite porphyry dykes has been observed at the biotite granite contact, near Kalato (Figure 2.5.3). The dykes have been displaced by a set of complementary faults, as plotted in the figure above. The brecciation, shearing and incipient mylonitisation associated

with the displacement are well preserved in the field.

Contact metamorphism is observed to have taken place in the basalt lavas adjacent to the biotite granite contact. The metamorphic effects are witnessed as far as up to 1.6 kilometres from the exposed margin of the granite intrusion. A bifacial paragenesis has been optically established namely, an albite epidote hornfels facies in the outer part of the aureole, and a hornblende hornfels facies nearer the granite contact. The hydrothermal alteration of the quartz porphyries, and the devitrification and recrystallisation of the acid lavas and tuffs have already been mentioned in connection with the biotite granite contact effects. Details of the contact metamorphism, hydrothermal alteration, devitrification and recrystallisation may be found under petrographic descriptions (Chapter 4) of the respective rock types. Lastly it may be mentioned that along the contact zone of the biotite granite also, the enclosed basement rocks consisting of hastingsite biotite (muscovite), adamellites are found to be thoroughly recrystallised, with brown biotite appearing as the only mafic phase. This reaction in the basement is not discussed further.

2.6.3 Greisen vein development and mineralisation

Greisen vein development and mineralisation in the Tibchi Complex are probably comparable only to the most extensive occurrence elsewhere in the Nigerian Younger Granite province. The economic potential of the greisen veins, particularly the great Kogo Lode, and mineralisation in general, including primary and alluvial, in the Complex, had pre-occupied previous workers.

In the geological mapping (this study), effort has been

made to locate as many of the greisen veins as could be represented within the working scale of the map.

The greisen veins are concentrated in the biotite granite; occurrence of these veins in the basement rocks adjacent to the biotite granite, can be shown to be related to biotite granite underlying the basement rocks in the relevant marginal zones. This is particularly evident in the southern parts of the Complex where the biotite granite can be seen to disappear beneath the basement cover, at low angles. The envisaged general relationship between the basement 'roof' and the biotite granite intrusion, is shown in the cross-sections of the 1:50,000 geological map. At the biotite granite margins, greisen veins are observed to pass through to the basement, undeviated; so also from the main biotite granite to its microgranite facies.

Generally, greisen veins of the Tibchi Complex are seen to occur as single or multiple veins. Single veins are usually thin and are found to be of little economic importance. The multiple veins, on the other hand, are much more important in terms of overall size and economic mineralisation. Multiple veins may occur either as unidirectional, or anastomosing, swarms. Unidirectional swarms consist of parallel to sub-parallel veins forming a mass of limited lateral extent; often the juxtaposition may be so tight that to a first approximation the contiguous mass may be regarded as one entity. Figure 2.6.3A illustrates the above phenomenon at the stage where individual veins may still be discernible. Larger greisen veins, such as the Kogo Lode, may have originated in the above fashion.

Joint control appears to have been a dominant feature in the observed form and distribution of the greisen veins. This is clearly evident from the 1:50,000 geological map. Even in the case of anastomosing patterns it is found, as in the basement rocks east of Kalato village, that the existing joint pattern is equally complicated. However, joint control is probably not a rule (Rockingham, 1951).

The Kogo Lode is specifically labelled on the geological map. It is a system of mineralised greisen veins consisting of one main trunk and some subsidiary branches. The main trunk is more than one kilometre long and up to 14 metres wide (Rockingham, 1951). Reports on this lode are contained in the list of references.

The following minerals occur in the Complex:
Cassiterite, Sphalerite, Wolfram, Pyrite, Arsenopyrite, Chalcopyrite, Chalcanthite, Native Copper, Molybdenite, Galena, and Siderite.

2.6.4 Relative age

A few xenoliths of extrusive volcanic rocks are found in the biotite granite, especially close to the contact with the above rocks. Occasionally xenoliths of basement rocks have also been found, but usually such xenoliths are more evident in thin section. However, the biotite granite is observed to cut all the other major rock units of the Complex, and was thus clearly the last to be emplaced.

2.7 Miscellaneous Rocks

2.7.1 The chlorite microcline porphyry dyke

This is a narrow dyke situated in the Older Granite basement south-east of Tibchi village (ref. 1:50,000 geological map). It is oriented north-south, and is about 750 metres long and 10 metres wide. Its contact with the basement is clear and sharp. Occasionally inclusions of basement can be seen in the dyke, as thin slices parallel to the line of contact.

At its southern extremity the dyke is truncated by apophysis of the granite porphyry ring-dyke. This apophysis is seen to be chilled against both the adjacent basement and the chlorite microcline dyke. A cross-cutting stream course exposure in the far north of the chlorite microcline dyke shows that the latter is essentially vertical in attitude.

The observation that the granite porphyry ring-dyke apophysis cuts and chills against the dyke described above, indicates that the latter is post-dated by the ring-dyke and related minor dykes.

In hand specimen the chlorite microcline dyke rock has a distinctive grey colour and can be readily distinguished from the granite porphyry. Detailed petrographical descriptions are given in Chapter 4. The unusual feature of the chlorite microcline dyke, however, is the presence of microcline as phenocrysts in an apparently rapidly crystallised hypabyssal intrusion. The microcline is unusually fresh even in hand specimen. Other peculiarities of both the microcline phenocrysts and the chlorite (which is seen as the only mafic phase) are described in Chapter 4.

2.7.2 The south-eastern suite of oversaturated and under-saturated peralkaline and peraluminous rocks

In the south-eastern part of the Complex, where the biotite granite makes contact with the ring dyke, a roughly rectangular body of biotite granite about 1x0.5 kilometres in size, stands out topographically distinct from the general level of the main intrusion. The above rectangular mass forms a ridge rising to a crest of about 75 metres, and its rock is a distinctly whitish medium-grained biotite* granite which contrasts with the pinkish, though medium-grained, rock of the main biotite granite intrusion. About two-thirds of the way up to the northern part of the ridge, a fine- to medium-grained variety of biotite* granite appears, in apparently horizontal sheet position. This latter rock is characteristically 'stained' by the presence of haematite and possesses several healed fractures and cross-cutting black veins (Plate 4.6J). Samples from the above rectangular ridge of biotite granite, including the fine- to medium-grained biotite granite, show unusual petrographic character relative to the main intrusion. Especially important is the presence of metamorphic textures. One analysed sample shows that the ridge may be composed of a peralkaline, acmite-normative anti-perthite biotite granite.

At the crest of the ridge, towards the northern extremity, is a linear zone about 50x30 metres, of mostly syenitic peralkaline rocks. This linear zone strikes roughly parallel to the long axis of the ridge. There appears to be an overlapping zonation of the component units as sketched diagrammatically in Figure 4.6.2. The following rock types have been

* Strictly, siderophyllite in composition.

sampled:

- (a) Aegirine-augite ferrichterite syenite (sodic) - white
- (b) Arfvedsonite syenite (potassic) - pink
- (c) Arfvedsonite haematite syenite - red .

At the contact between the aegirine-augite ferrichterite syenite and the peralkaline biotite granite (the main ridge-rock), is a white arfvedsonite granite (sodic). At the contact between the amphibole syenite and the peralkaline biotite granite is a biotite arfvedsonite granite.

Detailed petrographical descriptions of the above rocks are given in Chapter 4. The unusual character of these peralkaline syenitic rocks and their associated contact modifications are evident firstly in their metamorphic textures (as described in Chapter 4) and secondly in their chemistry (Chapter 6). Evidence from these and other sources in this study suggest possible metasomatic origins for the observed textures and chemistry.

At the contact of the biotite granite with the granite porphyry ring-dyke, near the suite of peralkaline granites and syenites described above, is a 'screen' of 'basement' rock about 400x100 metres in size. This rock has a dark green colour and is characterised by a coarse porphyritic texture transitional to aphanitic modifications, in some cases even within the same large hand specimen. The porphyritic texture is due to the presence of magacrysts of sodic plagioclase. The absence of quartz is conspicuous in this rock which, besides its dark green colour would at a glance be regarded as of basement lithology. The dark green colour is due to the pervasive presence of hastingsitic amphibole as the only mafic

phase. Chemically the rock is undersaturated, nepheline-normative and peraluminous; such a rock with sodic plagioclase as phenocryst and amphibole as the only mafic phase, is hitherto undocumented in the Nigerian Younger Granite province.

CHAPTER 3
THE VOLCANO-STRUCTURAL AND INTRUSIVE
FEATURES OF THE TIBCHI RING-COMPLEX

3.1 Introduction

In this chapter attempt is made to reconstruct the volcano-structural and intrusive history of the Tibchi Complex on the basis of important relict features preserved in the field geology and on the basis of established criteria documented in other areas of ring-complex development.

Ring-complexes are expressions of near-surface magmatism which can either be of calc-alkaline or alkaline lineage. The calc-alkaline lineage is usually connected with orogenic belts, the ring-complexes being documented as belonging to the post-orogenic stages of magmatism. The alkaline lineage is, on the other hand, found in anorogenic areas. Without prejudice to the remote implications of plate tectonics, the common characteristic features of ring-complexes in post-orogenic and anorogenic areas appear to justify the unified approach to ring-complex development adopted by previous workers. Clough et al. (1909) working in the calc-alkaline post-Caledonian Glen Coe Complex favourably compared the latter to the modern 'alkali' anorogenic Askja Caldera in Iceland, while Pitcher (1978) found the ring-complex development in the 'alkali' anorogenic Younger Granite province of Nigeria comparable to that in the calc-alkali post-orogenic stages of the Coastal Batholith of Peru. Therefore it is obvious that emphasis is placed on the structural evolution of the ring-complexes during near-surface magmatism, irrespective of rock association. This is the view adopted in this chapter.

The second part of the chapter deals with the origin of ring-complexes associated with caldera formation, with special referenceto the Tibchi Complex. Specifically the mechanism of surface cauldron subsidence and ring-dyke intrusion are considered, beginning with a critical review of important propositions since 1909 and ending with a simple model for the Tibchi Complex, that most satisfies the observed field relations.

3.2 Evidence for surface cauldron subsidence and the formation of a Jurassic caldera in the Tibchi Complex

Evidence for subsidence of the central block within the surface area defined by the present peripheral dyke of the Tibchi Complex may be summarised as follows:-

- (a) If the ring-dyke intruded along a ring-fracture, then the observed completeness of the ring-dyke through 360° of the ellipse, would be presumed to indicate that the ring-fracture was virtually complete in outline. Subterranean support for the central block would clearly be under enormous strain and the likelihood of continued support is doubtful in the light of withdrawal of magma through intrusion along the fracture itself.
- (b) The occurrence of the 'flinty crush rock', and the presence of other evidence of shearing of the basement rocks, along the ring fracture, have been observed.
- (c) The preservation of extrusive volcanic rocks within the ring-dyke but not outside, can best be explained by preferential subsidence of the enclosed block on which the preserved volcanic rocks initially rested.
- (d) That the extrusive rocks preserved are found to lie

directly on the enclosed basement's surface, suggests that the volcanic rocks had been initially laid on a basement surface undergoing erosion rather than having been deposited in a major tectonic depression or landmass undergoing sedimentary deposition.

(e) The apparent centripetal dips of the extrusive volcanic rocks suggest a sagging of the subsided volcanic pile. This is more likely if it is admissible that deposition was initially on a landmass undergoing erosion rather than deposition.

In a broad sense, the presently exposed surface of the enclosed basement does, from the foregoing, represent the exhumed Jurassic land surface which was intersected by the initial ring-fracture. Thus a surface cauldron subsidence inextricably associated with a caldera as its surface expression, is preserved in the Tibchi Complex at the present level of erosion. A caldera of that time cannot be expected to be wholly preserved today. Instead, what is seen in the field and recorded in the geological map, is merely a level in the denudation history of a caldera/ring-dyke association, at which the base of the subsided volcanic pile is exposed relative to the ring-fracture (ring-dyke) framework.

Two ways by which the amount of subsidence can be estimated are: from the thickness of the extrusive volcanic rocks within the subsided central block, and from the difference in elevation between definite stratigraphic levels such as sedimentary units or the contact between the basement and volcanic rocks within, and outside, the ring-structure. The lack of sedimentary units in the basement rocks, and the absence of volcanic rocks outside the ring-dyke, render the

second method impracticable. On the first method, the maximum vertical thickness of the volcanic rocks preserved, can be obtained by projecting the maximum elevation of the extrusive rocks to the base of the 'saucer' shaped structure formed by the centripetal dips (in the O-P line of cross-sections: 1:50,000 geological map). This gives an approximate value of 600m, which however must be regarded as the minimum down-throw, in view of subsequent erosion.

3.2.1 Discussion

The term 'cauldron subsidence' often used unqualified, has created an unnecessary doubt in parts of the literature. The doubt stems from lack of recognition of the long established existence of two different kinds of cauldron subsidence. Surface cauldron subsidence (Clough et al., 1909) essentially involves ring-faulting associated with fractures which can be shown to have intersected the pre-existing land surface. On the principle of surface cauldron subsidence, ring-complex development is necessarily associated with (surface) calderas. Subterranean cauldron subsidence (Clough et al., 1909; Richey, 1928), on the other hand, is based on the principle that a complete ring-fault could develop below the ground surface; a cross-fracture forming the roof of an initial ring-fracture could separate the central block which then becomes free to subside into the magma chamber. A classical example is the Mourne Mountains of Northern Ireland (Richey, 1928).

Having made the above distinction clear, further reference to subterranean cauldron subsidence will not be made, since it is obviously inapplicable to the Tibchi case.

Apart from the classic Glen Coe example, surface cauldron

subsidence has been well documented in the following ring-complexes:- Ossipee Mountains of the White Mountain Magma Series (Kingsley, 1931), the Baerum, Glitrevann, Sande, and Drammen Cauldrons* in the Oslo Region of Norway (Oftedahl, 1953). In Nigeria, the following complexes are believed to be associated with surface cauldron subsidence:- Ririwai (Jacobson et al., 1958), Banke (Jacobson and Macleod, 1977) and Ningi-Burra (Turner and Bowden, 1979). The only British Tertiary igneous complex confidently ascribed to surface cauldron subsidence is Centre 1, Mull, which Richey (1932) considered to have "originated through a ring-fissure having extended to the surface".

The chief criteria employed by the different workers above in establishing the case of surface cauldron subsidence in their respective ring-complexes, may be summarised briefly as follows:

(1) Evidence for loss of stratigraphical height in the central block enclosed within the ring-structure is given in one of two ways (sometimes both). Extrusive volcanic rocks preserved inside the ring-fracture but not outside is generally quoted. In exceptional cases such as in the Baerum Cauldron, extrusive rocks are found both inside and outside the ring-structure and it is observed that the thickness outside is much reduced. It appears to be only time dependent for the outside extrusive rocks to be completely obliterated by erosion while those within the ring-structure still remain preserved.

* Oftedahl defined in his text the term 'cauldron' as simply connoting that the subsided area was not connected with "an active volcano or a volcanic explosion", otherwise the term is synonymous with surface cauldron subsidence unit.

Depending on the type of basement involved, (and this needs to be partly at least sedimentary), displacements in the stratigraphical column of the basement rocks may be recorded within the down faulted central block relative to the column outside the ring-fracture as in Glen Coe and the Oslo Cauldrons. In these cases, it is observed that within the ring-fault upper units are brought into juxtaposition with lower members outside the ring, and boundaries of outcrop between any given pair of units is usually shifted around within the cauldron.

(2) Marginal uptilting of the volcanic sequence preserved within the ring-structure gives rise to a 'bowl' or 'saucer' structure in cross-section. Vertical and overturned effects have been observed against the ring-fault in Glen Coe (Clough et al., 1909). Occasionally resurgent doming by subsequent central intrusion could cause a reversed outward tilt in some parts of the original 'bowl' as in the Sande Cauldron (Oftedahl, 1953), Ririwai Complex (Jacobson et al., 1958) and Centre 6, Ningi-Burra Complex (Turner and Bowden, 1979). Marginal uptilting is not, however, found to be universal, nor does it need to be always centripetal. Tilting en masse has been observed in some complexes. In the Baerum Cauldron, cited earlier, marginal uptilting is found to be absent and Oftedahl (1953) interpreted this to indicate subsidence along vertical ring-faults. The principle behind marginal uptilting and 'bowl' structure in cross-section is subsidence guided by ring-faults whose dip change gradually inward with depth (Oftedahl, 1953). The possibility, however, remains that in some cases the apparent sagging may be due to deposition of the volcanic rocks on originally inward-dipping surfaces.

(3) Mechanical evidence of faulting is considered extremely important by most workers and is seen along the line of the fault, or alongside ring-intrusion (if any) in the form of cataclastic brecciation, crushing and mylonitization. One problem is distinguishing the so-called 'crush-rocks' from normal rhyolite or rhyolitic tuff exploring the same ring-fracture. The historical example is the "flinty crush-rock" of Glen Coe Complex (Clough et al., 1909), thought to be the final product of intense shearing caused by ring-faulting. The rock has a characteristic 'flinty lustre', dark colour, frequent, but not consistent, flow banding which is more pronounced in thin section and an extremely comminuted texture that reveals only "the beginnings of a crystalline structure" in its groundmass. Reynolds (1956), Hardie (1963), Roberts (1963), and Taubeneck (1967) have individually come to the conclusion that the so-called "flinty crush-rock" of Glen Coe was indeed essentially pyroclastic rather than cataclastic, and produced by fluidisation in vents located along the fault after cataclasm had taken place. The lack of pronounced strain shadows in the quartz fragments was also considered a negative evidence for cataclastic origin of the crush-rock.

The Tibchi "crush-rock" described in Chapter 2, in many ways resembles the Glen Coe example above. Although like the latter, there may be insufficient amount of strain shadows in the quartz fragments, the latter intrusion of the granite porphyry ring-dyke may have had a reverse effect on these quartz fragments through reheating, although it may be difficult to explain this in detail owing to the very fine grain size involved. However what appears to be overwhelming evidence of the source of the Tibchi crush-rock is the nature of the bulk

chemical composition; this places the rock clearly in the field of the basement rocks. Perhaps the best possible explanation is that the crush-rock was derived from the basement through intense grinding. Until the thermal effect of the latter intrusion of the granite porphyry ring-dyke on the crush-rock is fully investigated, the question of insufficient strain shadows in quartz fragments must be kept at a low profile.

3.2.2 Conclusion

The three most important criteria documented in well established cases elsewhere, of surface cauldron subsidence, are met in the observed field geology of the Tibchi Complex (Chapter 2). Clearly there is a strong case for the above type of subsidence.

In the use of basement stratigraphical displacement for estimating the amount of down-throw, an over-riding precondition seems to be that the basement be in part at least, sedimentary. Hence in New Hampshire, and Nigeria, as well as parts of the British Tertiary province, where basement is mostly or entirely granitic, surface cauldron down-throw will have to remain a matter of conjecture.

3.3 Pre-caldera Volcanism and the Probability of a Central Volcano

3.3.1 Distinguishing between the pre-caldera and intra-caldera phases of volcanism in the Tibchi Complex and adjoining complexes.

Most of the work so far done in the Nigerian Younger Granite province has been concentrated in the southern sector, especially in the Jos Plateau area. In this southern sector

subterranean cauldron subsidence has been repeatedly proposed (Jacobson et al., 1958; Turner, 1962). This proposition in principle precludes caldera formation.

However, surface cauldron subsidence has been proposed for each of the northern complexes so far studied (except Kударu) namely, Ririwai (Jacobson et al., 1958), Banke (Jacobson and Macleod, 1977), Ningi-Burra (Turner and Bowden, 1979) and Tibchi (this study). The Ningi-Burra Complex is indeed a chain of several calderas displaced westward with migration of the magmatic centre. In Kударu, Bain (1934) found no evidence for any kind of cauldron subsidence, surface or subterranean.

Turner's (1976) "erosion level" explanation for the discrepancy in apparent structural disposition between the southern and northern ring-complexes is pertinent here. In the south, deeper level of erosion reveals multiple intrusions. In the north however, details of volcanic succession can be seen owing to higher levels of erosion and it is possible therefore to distinguish between relationships of volcanic rocks.

Distinguishing between pre-caldera and intra-caldera volcanism thus appears to be a matter for consideration in the northern group of complexes. Incidentally these spread around the Tibchi Complex and give great confidence that the evolutionary history of the respective calderas were essentially similar. In the brief review below, adjoining complexes are given priority in presentation, with Tibchi last.

According to Jacobson and Macleod (1977) the volcanic rocks of the Banke Complex consist of two disproportionate groups namely "Early rhyolites" and pyroclastic rocks inter-

calated with minor basalt lavas; and "Late rhyolite as dykes and surface cauldrons". The first group is comparatively thin and confined to a limited exposure at the base of the southern escarpment of an enormous plateau formed by the late group. The authors are in no doubt that the late rhyolite, as they called it, which is practically homogeneous "both laterally and vertically", and at least 600m thick preserved over an expanse of about 10x6 kilometres is a "large-scale" outpouring into a caldera, tending to fill it up, hence the plateau topography of today. "Banke provides one of the best examples in the province of wholesale surface cauldron subsidence and the accompanying upwelling of large volumes of virtually homogeneous lava" (Jacobson and Macleod, 1977). This so called late rhyolite is indeed a crystal-rich ignimbrite (crystal tuff, this study), and as adequately expressed by the above writers, is the "extrusive equivalents of the quartz-pyroxene-fayalite-porphyrries that form the ring-intrusion at Kudaru and the large volcanic plug of Dutsen Shetu at Liruei".

Turner and Bowden (1979) have been most categorical about the temporal relationships among the volcanic rocks associated with the individual calderas of the six migratory centres of the Ningi-Burra Complex. Each subsequent centre followed the same sequence of stages: the pre-caldera, the caldera-forming, and the post-caldera stages. The pre-caldera rocks consist of the same varied assemblage as in other complexes reviewed here, of tuffs, agglomerates, rhyolites and minor basic and intermediate lavas. In the caldera-forming stage, intra-caldera rocks are characterised by the accumulation of thick crystal-rich ignimbrites and the emplacement of a granite porphyry ring-dyke. A "porphyry" described as "part of the ash-flow material which

consolidated in the ring fissures...." (called 'quartz porphyry' in this study and by previous workers, ref. Chapter 2) links the crystal rich ignimbrites with the granite porphyry ring-dyke, the latter two being a constant feature of the various centres. A post-caldera stage of volcanism is speculated although the authors considered that the lateral shift in magmatic centres would have made post-caldera renewal of volcanism at the same site, unlikely.

In the Ririwai Complex the situation is not very clear. Jacobson et al. (1958) have separated the volcanic rocks into two groups: "Early rhyolites, tuffs and agglomerates" and "Late rhyolites and intrusion breccias". Descriptions of the late rhyolites above are consistent with those of the crystal-rich ignimbrites (or crystal tuffs) in Turner and Bowden (1979) and this study. However the late group in Ririwai is described as being subordinate in a real extent to the early group and is restricted to a swarm of dykes and irregular bodies intrusive into the early group. The relation of these early and late groups to the event of caldera formation does not appear to be conclusively known. Jacobson et al. (1958) believe that all volcanic activity was subsequent to the "ring-fracturing and block subsidence which led to the formation of a large caldera", thus precluding any incidence of pre-caldera volcanism. Later Jacobson and Macleod (1977) however, stated differently: "... there is strong evidence to suggest that the volcanism was initiated by the development of a series of arcuate vents around the peripheral ring-fracture. In the following stage, it seems likely that a large caldera may have formed, inside which the bulk of the lavas accumulated". This represents a modification

of the earlier concept, with a distinction drawn between pre-caldera and intra-caldera eruptions as found in other complexes.

In the Tibchi Complex, the bottom of the volcanic sequence consists of a varied assemblage of tuffs, rhyolites and agglomerates, with minor basalt lavas and trachyte intercalated with them. This group conforms with the pre-caldera group as seen above for other complexes. At the top of the series are crystal-rich ignimbrites or crystal tuffs and an agglomerate with crystal-tuff matrix. This group corresponds to the intra-caldera group of other complexes.

From the foregoing general review emerge the following points: There appears to be everywhere in the complexes concerned, two definite groups of volcanic rocks which can be correlated with their equivalents elsewhere as 'pre-caldera' and 'intra-caldera'. The pre-caldera group,

a) consists mostly of rhyolitic (i.e. acid) tuffs and agglomerates. Lavas, *sensu stricto*, are subordinate in abundance.

b) is variable in crystal content compared with the intra-caldera group, but mostly crystal-poor.

c) is undoubtedly a composite product of vent eruptions although the nature of these vents is not yet properly investigated in most of these complexes.

The intra-caldera group,

a) consists almost exclusively of crystal-rich ignimbrites (crystal-tuffs) whose strong welding provides a homogeneity that is akin to that normally associated with (porphyritic) rhyolite lavas, hence this usual misnomer, 'late rhyolites',

b) is typically massive both laterally and vertically, and

c) may be intrusive as well as extrusive, hence the usual link in the field with quartz porphyry feeders from which it is sometimes inseparable.

In the Tibchi Complex both the pre-caldera and intra-caldera groups are well preserved. The stratigraphical disconformity between the two groups is obvious from the geological map. Secondly the marginal uptilting of individual volcanic units resulting in the 'bowl' structure already discussed, is more apparent in the pre-caldera group than in the intra-caldera group. The uppermost member of the intra-caldera group, namely the crystal tuff (2), is found to be sub-horizontal in attitude contrasting with the well defined dips of earlier units. These structural aspects of the distinction between the pre-caldera and intra-caldera groups, apparently neglected or unrecognised, are in this study emphasized.

3.3.2 The probability of a central volcano

Reference to the stratigraphical succession of the volcanic rocks of the Tibchi Complex shows:

1) that the earliest extrusive volcanic rock was pyroclastic, namely an ash-fall tuff;

2) that a mixed composition appears to be significantly important in the basal part of the sequence which, in the light of discussions in the previous section, can be confidently called the pre-caldera group;

3) that nevertheless in the pre-caldera group (as indeed throughout the sequence as a whole) pyroclastic rocks far outweigh all lavas (basic, intermediate and acid) put together.

It is therefore inferred that the pre-caldera volcanism was violent, with mainly pyroclastic products. The nature and

mixed composition of the rocks shows that such a suite of rocks could only be produced from vent eruptions dominated by explosions.

There are two alternative loci to these vents, judging from the apparent concentric distribution of the rocks: either along the present ring-dyke position or in a position central to the ring-complex.

From detailed studies of inclusions found round the perimeter of the granite porphyry ring-dyke, it was apparent that the order of intrusion along the ring-fracture was probably as follows (in decreasing age): microferrodiorite, microsyenite, quartz porphyry and lastly the present granite porphyry. A few xenoliths of early tuffs and lavas were also found. These already extruded rocks are believed to have been incorporated by the granite porphyry ring-dyke when the latter intruded the base of the subsided volcanic pile.

Volcanic vents of the explosive type located along ring-fractures have been recorded in Mull and Slieve Gullion Complexes (Bailey et al., 1924; Richey, 1932). Characteristically these vents contain remnants of the agglomerates, within the subsequent ring-dyke intrusion. No agglomerates have been found in the ring-dyke of the Tibchi Complex. Yet agglomerates form a dominant proportion of the pre-caldera sequence. It is therefore concluded that vents related to these agglomerates and associated tuffs, were not located along the peripheral ring-fracture.

The other alternative locus for the vent eruptions is in the form of a central volcano. The principal focus of this volcano is thought to be in the vicinity of the present Kogo village.

The ash-fall tuff which marks the base of the stratigraphical succession is believed to represent the earliest eruption of the proposed central volcano. Xenoliths of this ash-fall tuff have been found in the crystal-tuff of the post-caldera succession located in the extreme north of the Complex, and in the quartz porphyry in the western extremity of the Complex also. Both of these sample localities are separated from the type locality (south-west of Yarda Gungume, around the central area of the Complex) by distances of about 8km and 6km respectively, and are adjacent to the ring-dyke in each case. The expanse of the volcano is evidently therefore at least the surface area marked out by the present ring-dyke but there is every reason to believe that it probably exceeded this limit. Rhyolite lavas succeeded the ash-fall tuff in time. Where these early lavas lie directly on the basement, narrow rhyolite feeder dykes varying from 0.5 to 1.0 metre wide and persisting for reasonable distances, have been found subjacent to the lavas. These minor dykes are perhaps subsidiary feeders issuing at high angles from the central vent of the volcano.

During the subsequent surface cauldron subsidence, the initial volcanic edifice must have collapsed and caused inversion of the topography. However, the inter-lithological relationships such as age sequence, thickness of individual beds, distribution about a common vent locus, and minor feeder dykes were all apparently preserved. On the other hand, the initial morphological form of the volcano cannot be reconstructed with the same degree of confidence. Judging from the thinness of the individual units, it is reasonable to envisage a shield volcano analogous to those described in Tibesti (Vincent, 1970).

3.4 The Intra-caldera Volcanism: Fluidised Vents and a Quiescent Ring-dyke Intrusion

3.4.1 Fluidised Vents

The role of the central volcano most probably ceased before ring-fracturing and the commencement of surface cauldron subsidence, if the required stress distribution for the observed pattern of ring-fracture was to be achieved (see subsequent model). The collapse and caldera formation was probably not a sudden drop-down process, but considering the 360° of the ellipse described by the ring-structure, it must have been completed as a continuous process and within a relatively limited period of time. Any form of subterranean support for the otherwise 'free' subsiding block was unlikely to have held out too long before yielding further to the enormous load pressure.

However, it appears logical that once the ring-fracture formed, gas streaming must have ensued and re-established its major role in the new volcanism as it had done in the pre-caldera regime. This new role is thought to be in the form of fluidisation along vents located in, and conforming with, the ring-fracture and also located in positions branching off from the ring-fracture into the subsiding central block. This distribution pattern is based on the observed positions of rock bodies and inclusions considered to be feeders to the intra-caldera extrusive rocks. It is however in no way assumed or implied that fluidisation took place equally all round the ring-fracture. The contrary was most probably the case.

The inference of fluidisation is based primarily on the observed texture and field character of the intra-caldera rocks (feeders and extrusive products inclusive). The intra-caldera extrusive rocks are represented by the crystal-rich ignimbrites

(crystal tuffs) while their feeders are the quartz porphyries, as concluded in the preceding section. The relationship between the two is evident in the field both in Tibchi, and in neighbouring complexes as shown previously. The large bodies and smaller inclusions of quartz porphyries found (Chapter 2) in the present granite porphyry ring-dyke are interpreted as remnants of pre-existing quartz porphyry feeders in the ring-fracture displaced by the de-gassed granite porphyry magma which moved up behind the fluidised quartz porphyry system.

The fluidisation vents in the initial stages must have been confined to the width of the ring-fault zone. The full phase of the fluidisation process appears to have reached maturity with expansion in the width of the vents. Such expansion is likely to be guided by breaks, near the ring-fracture, of the subsiding central block, causing bulging or buttressing into bodies like the observed stock-like main quartz porphyry unit south of Tibchi village. The enlarged vents were apparently capable of massive outpouring of the crystal-rich ignimbrites into the adjacent caldera trough.

Fluidisation was originally an industrial flowage principle for the transportation of solids suspended in a gas (Matheson et al., 1949). This concept was, however, later applied as a geological process (Reynold, 1954) for the dispersal of ash-flow materials. In summary fluidisation means that a mass of fine solid particles agitated by increasingly greater velocity of gas becomes, at a critical stage, entrained in a spontaneous upward movement of a gas stream through the mass. The particles suspended in the gas medium can therefore move like a "fluid", the mass having been "fluidised" by the gas.

Tazieff (1970) discussed the fluidisation mechanism of producing ignimbrites "...normal ignimbrites would result from the outpouring of supervesiculated pyromagma already fragmented by the coalescence of bubbles; in other words as a 'fluidised' ash flow, or as an 'aerosol' of hot gases carrying ashes in suspension (these ashes being merely shreds of septa of pumice bubbles resulting from the coalescence of the bubbles) and blebs of pumice in which vesicles did not inflate to coalescence. The extremely low aerosol viscosity allows this suspension to be spread very far from the eruptive vent, even over flat country". Earlier it was mentioned that in the new intra-caldera volcanism of the Tibchi Complex, gases simply resumed the major role they had played in the pre-caldera stage, although now channelled through the ring-fracture vents rather than through the central (volcano) vent. The distinction between the pyroclasis of fluidised vents and the central volcano is among other things that the fluidised vents do not produce ash-fall tuffs (Tazieff, 1970); these can only be produced by the paroxysmal (sudden and violent) explosion characteristic of central vents. This is because fluidisation implies lowering of viscosity and increase in fluidity. These two complementary aspects preclude paroxysm. Tazieff's (1970) comment is pertinent: "The ignimbrite aerosol would result from a balance between the inner pressure of gas vesicles and the litho-atmospheric one; such an equilibrium would allow bubbles to expand to complete coalescence and formation of a gaseous continuum, but would not give explosions violent enough to hurl the liquid and solid particles up into the cold air by 'vulcanian' or 'pelean' type of explosions. The aerosol so

engendered is poured out in a comparatively quiet way and spread over the surroundings".

The term 'ignimbrite' as used by Tazieff above is synonymous with ash flow tuff, its deposition from 'flow' rather than 'air-borne lapilli' is emphasized, as well as the presence of an ignimbrite of the characteristic shards and fiamme. The fluidisation mechanism fully accounts for certain peculiar characters of the intra-caldera crystal tuffs namely, their massive appearance in the field - involving great thicknesses such as have been observed in the Banke and Ningi-Burra Complexes, and their great homogeneity both laterally and vertically. The above two characteristics are due to their lava-like outpourings which had led in the past to the misnomer of "late rhyolites" in some complexes by previous workers. The consistently high crystal content of the intra-caldera crystal tuffs from complex to complex, probably indicates that they could only be erupted after a certain degree of crystallization had been attained in the subvolcanic magma chamber. This degree corresponds to the stage at which the critical amount of gaseous pressure, required for fluidisation to take place, has been attained (increasing crystallization leading to increasing vesiculation of gas).

3.4.2 The ring-dyke intrusion

Apparently, by the time the granite porphyry finally welled up as the pervasive occupant of the ring-fracture, the magma had most probably been de-gassed. Already, an overwhelming stream of gas must have been spent in the preceding fluidisation associated with the quartz porphyries and their

intra-caldera crystal tuff products. Hence the granite porphyry intrusion is believed to have been quiescent, as revealed in the observed euhedral, essentially non-fragmental form of its phenocrysts, and the synneusis of its feldspars.

Presence of xenoliths of extrusive volcanic rocks in the granite porphyry ring-dyke, suggests that the ring-dyke continued to move upward beyond the base of the subsided volcanic pile and thus beyond the base of the caldera.

The intrusive relationship between the granite porphyry magma and the preceding quartz porphyry, within the ring-fracture, may be viewed in two different ways. Firstly it is possible that the de-gassed granite porphyry magma simply moved up behind the still-active fluidised quartz porphyry system. If this was so, then it would be difficult to explain, without implying liquid segregation, the presence of quartz porphyry inclusions having definite boundaries, in the host granite porphyry ring-dyke. Liquid segregation is unlikely in two rocks that are chemically essentially the same. Alternatively it may be proposed that part of the fluidised quartz porphyry system chilled in the ring-fracture conduit ahead of the up-coming de-gassed granite porphyry magma. The latter was probably able, while still liquid, to surpass the level at which the preceding quartz porphyry system chilled, perhaps as a result of less loss of heat (since country wall rocks, fracture zone etc. were already heated up through the previous fluidisation regime). If that was so, then disruption of the chilled quartz porphyry through some form of fracture-controlled stoping would explain more satisfactorily the observed well defined nature of the xenoliths of quartz porphyry

in the granite porphyry ring-dyke. Piecemeal stoping in ring-dykes is well established (eg. Billings, 1943, 1945; Oftedahl, 1953; Chapman, 1976).

It is very likely that in the Tibchi Complex, subsidence of the central block continued however briefly, even after the chilling of the quartz porphyry feeders in the ring-fracture conduit. This late subsidence would be favoured by the late granite porphyry intrusion, on a magma-release principle, enabling further intrusion of the granite porphyry to displace the weakened or brecciated quartz porphyries by some form of stoping.

The exterior margin of the granite porphyry ring-dyke is relatively regular and is interpreted to be a feature of the principal control by the ring-fracture, relative to the basement envelope, of the granite porphyry intrusion. However the interior margin is characterised by protuberances and apophyses directed into the central block. The apophysis south of Tibchi Village branches repeatedly inside the central block in a manner that suggests a follow-up of a fracture system. This secondary controlling fracture system is thought to represent collapse features of the subsided central block. In all cases therefore the ring-dyke and its apophyses prove to be structurally controlled so that in general it may be concluded that the ring-dyke intrusion was by fracture-controlled stoping along the primary ring-fracture and secondary fractures in the subsided central block.

3.5 The Eccentricity of the Central Biotite Granite Pluton

The 'central' biotite granite intrusion does not, at

least at the present erosion level, occupy a truly central position within the peripheral ring-dyke framework. Hence in its north-west end an arc of volcanic rocks separate the granite margin from the western arc of the ring-dyke, while in the south-east the granite partially truncates the ring-dyke itself.

The very steep dip of the granite margin near the volcanic rocks in the west suggests that the pluton may be stock-like. The north-eastern flank of the granite, from Yarda Gungume area to Kadagi is topographically high, perhaps suggesting at least a moderate angle of inclination of the margin of about 50° to 60° outward. From Old Mai-Lafia to the eastern arc of the ring-dyke, however, the margin of the granite describes broad loops; these may indicate a much lower angle than above, probably 30° to 40° outward.

In the south-east of the Complex the attitude of the granite to the ring-dyke is not quite definite. However the partial truncation of the ring-dyke here could be inferred to be due to an inclination of the granite margin to the latter, with a possibility of actually transgressing the boundary of the Complex as defined by the ring-dyke.

In the south near Mai Lumba-Kori, the microgranite marginal facies in contact with basement has a measured inclination outward of 56° . Around Kalato area and Old Nudusun, the margin of the pluton outcrops as contorted loops south-easterly to the eastern ring-dyke. The contact west of Old Nukusun is clearly sub-horizontal and the intervening basement between Kalato and Old Nukusun has been demonstrated, in one of the cross-sections of the geological map, to be essentially a sub-horizontal roof cap.

The occurrence of greisen veins in the enclosed basement within the southern sector of the Complex had earlier been attributed to a shallow subjacent biotite granite roof, an assumption supported by the above paragraph. Towards and near the southern arc of the ring-dyke, dolerite dykes in the basement have developed large spherulites of actinolitic amphibole, up to 8 centimetres in diameter probably from a subjacent biotite granite contact metamorphism. No other source of similar effect can be reasonably adduced. The hydrothermal alteration of the ring-dyke within the latter's southern and south-eastern zone is attributed to subjacent biotite granite in this zone.

In summary, various clues in field geology collectively enable the proposition to be made that the biotite granite intrusion is eccentric relative to the centre of the ring-structure, and is displaced to the south-south-east.

3.6 Origin of Ring-complexes

3.6.1 The theory of cauldron subsidence

Cauldron subsidence is the brain-child of Clough et al., (1909) and was postulated in the type-complex of Glen Coe. The principal concept is essentially an interpretation of field observation, which has since become a theory de facto and may be stated very simply: that a continuous ring-fracture intersecting the ground surface results in a crater of subsidence. The origin of the ring-fracture, the mechanism of the subsidence and the usually accompanying ring-intrusion have remained since 1909 perennial problems of theoretical importance. Stated as above the subsidence was qualified as surface cauldron

subsidence. In considering the late Cruachan Granite that intruded the foundered Glen Coe cauldron, Clough and coworkers also came to a second conclusion that was later to become equally important: that it is possible for the ring-fracture not to intersect the surface but to remain fully developed underground. In that case, the ring-fracture is expected to extend downward to the magma chamber thus isolating a central block which subsides, creating a potential void. This 'void' is filled spontaneously with ascending magma in the geometrical shape of the ring-fracture. This phenomenon was distinguished from the first and called subterranean cauldron subsidence. Although their evidence for surface cauldron subsidence was, and still remains, unsurpassed, their ideas on subterranean subsidence were at that time at best speculative.

Du Toit (1920) found evidence for 'a bell-jar' hypabyssal intrusion in South Africa which was interpreted on the basis of subterranean cauldron subsidence of an enclosed paraboloidal block, but in fact it was Richey (1928) who substantiated and established this subterranean type conclusively, in the Eastern Mourne Granites. Till this day, in the Mournes "one is left with little choice but to accept the classic concept of subterranean cauldron subsidence" (Taubeneck, 1967). Two types of cauldron subsidence are thus unquestionably distinguished, based essentially on the same theory of a central block set free to subside by a ring-fracture, one on the surface, the other underground.

3.6.2 Anderson's dynamic theory of cone-sheets and ring-dykes

Anderson (in Bailey et al., 1924) evolved a dynamic theory for the formation of cone-sheets and ring-dykes which may be

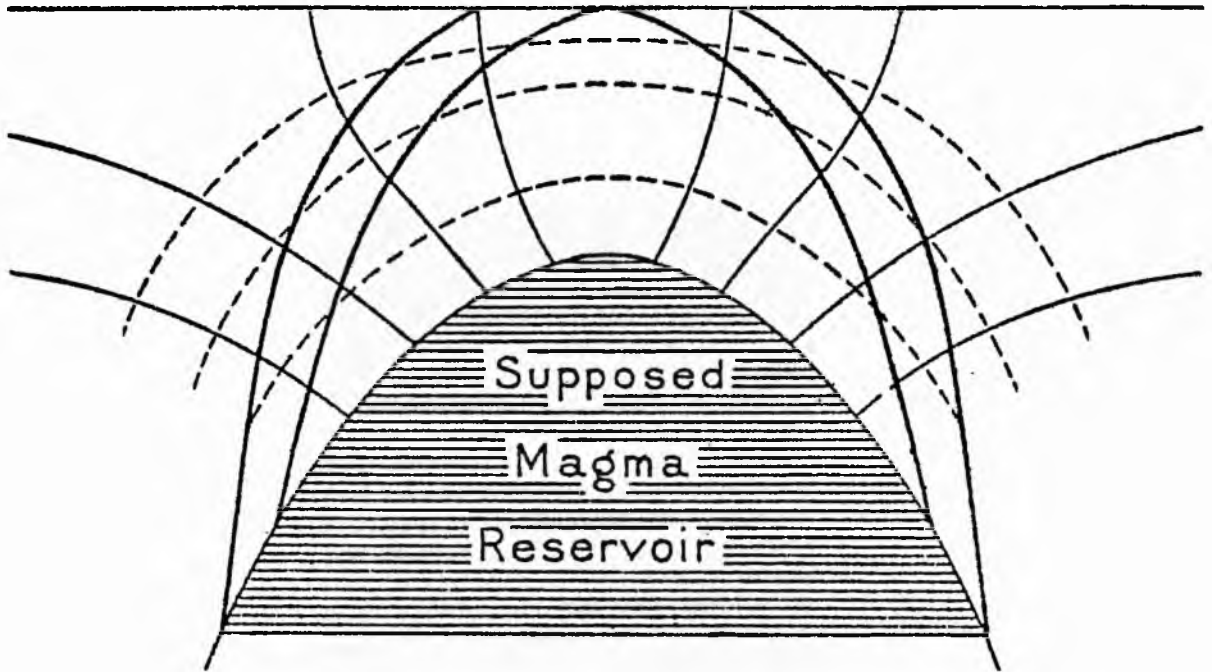


Figure 3.6.2 Stress diagram to show supposed mode of formation of cone-sheets and ring-dykes (Anderson, in Bailey et al., 1924). Thick solid lines represent shear fracture surfaces (referred to in text).

summarised as follows:-

One of the assumptions is that the initial ground surface be taken as horizontal, without any volcanic edifice. A paraboloidal magma chamber is also assumed to exist several kilometres deep. The specific gravity of the magma is assumed to be equal to that of the host rock but the magma has enough pressure to enable it to rise to the surface in the event of an outlet. Prevailing vertical and horizontal pressures in the crust surrounding the magma are assumed to be the same everywhere. Under these conditions no fractures of any kind could form.

If the magma chamber were to acquire a new and increasing pressure a system of pressure surfaces simulating the geometrical shape of the magma chamber would be superimposed on the overlying crust (Figure 3.6.2). A complementary system of tension surfaces which are conical near the top of the magma chamber and spreading outwards therefrom, is developed simultaneously and orthogonally to the pressure surfaces. If magma pressure continued to rise, these tension surfaces would develop into tensile fractures along which magma would intrude, forming cone-sheets.

If on the other hand, the magma pressure decreased dramatically below the initial value, a reversed situation would occur: a system of pressure surfaces would form in the position of the conical fractures (previously designated for cone-sheet intrusion) and an orthogonal system of tension surfaces would in turn simulate the shape of the magma chamber. Actual fractures, however, would form not as tensile but as shear fractures on account of which these

fracture pathways would become inclined to the tension surfaces as shown, giving outward dipping ring-dykes, once the central free block has subsided and a potential void is created and quickly filled by magma.

Three points are worthy of note from the theory:

- 1) that ring-dykes must necessarily have outward dipping contacts,
- 2) that if the ring-fractures formed closed cross-sections, subterranean cauldron subsidence would result, accompanied by upwelling of magma to fill the space so created,
- 3) that if the fractures intersected the surface, surface cauldron subsidence would form with ring-dykes dipping outward as low as 30° or less.

3.6.3 Anderson's dilemma and present problems

Two of the points raised in the last paragraph do not conform with present field knowledge. First, the general impression of the attitude of ring-dykes in Anderson's time, though vague, was that of outward dip. Reynolds (1956) took the protagonists of outward dipping ring-dykes to task and concluded that they lacked proper knowledge of the situation owing to insufficient data and therefore "lack of evidence as to the three-dimensional form" of the ring-dykes which were often referred to. Taubeneck (1967) commented from a personal field review that "no unequivocal example of an outward-dipping ring fracture is to be found" in the three areas below although "they may be seen in the Mourne Mountains". As Anderson had based his theory on Mull, Ardnamurchan and Slieve Gullion, there is no doubt that the theory was in serious jeopardy. Billings (1943, 1945) concluded from the data of several generations of workers in the New Hampshire area, that the dips of ring-

fractures and ring-dykes are essentially vertical. Oftedahl's (1953) extensive work on the cauldrons of the Oslo region led him to conclude that the ring-faults and -dykes were inward-dipping. The classic Glen Coe Complex also had vertical ring-faults (Clough et al., 1909). As Reynolds finally concluded, "The fact that many ring-dykes are essentially vertical at the present denudation level, however, possibly implies that the dip of the cone-shaped faults steepens upwards".

Anderson (1936) recognised the inadequacy of his theory to account for vertical or steep inclinations when he stated that "The steeply dipping outer margins of granite stocks may in general have been initiated as ring-fractures, but the present theory does not give an explanation of these, which can be regarded as complete".

Anderson's greatest dilemma is expressed in his own words and this is the problem of the present day, "A difficulty of another type is involved in the explanation of surface subsidences. The ring-fracture directions (of the stress fields analysed) flatten upwards and if such a fracture were initiated close to the surface its angle of dip would be only about 25° . The fault which bounds the Glen Coe subsidence was, however, originally vertical. It may have originated at some depth and gradually extended upwards. In doing so it must have retained its original direction, but it must be admitted that the dynamics of the (surface cauldron subsidence) process has not been worked out" (underlining and brackets, the present writer's).

Details of stress analyses are beyond the scope of the present consideration, but mention must be made of Robson and

Barr (1964) and Roberts (1970) who both attempted to establish criteria for brittle failure in the vicinity of the magma body in an attempt to account for the formation of cone-sheets and ring-dykes. Both arrived at the same conclusion that magma pressure and the prevailing regional stress in the crust were together responsible for both the type of faulting or fracture and the form of the minor intrusive body. Robson and Barr apparently did not take into consideration the hydrostatic pressure of the magma, and so their set of criteria were rejected by Roberts together with their conclusion that ring-dykes occupy tensile fractures whereas cone-sheets intrude shear fractures. In rejecting the above conclusion Roberts inherited Anderson's problem of inward dipping ring-dykes. He briefly mentioned it, simply stating that whether ring-dykes were outward dipping or inward was only directly related to a spherical and cylindrical shape, respectively, of the magma body. But he did not proceed to demonstrate the stress pattern. He also erroneously emphasized that "Most, if not all, ring-dykes are associated with the cauldron subsidence of a central block bounded by a ring-fracture. Stopping on any scale is, therefore, unlikely to be an important mechanism of emplacement" (1970, p.323). This view runs contrary to field evidence, as Billings (1943) summarizes in his review of field data: "The importance of piecemeal stopping in the formation of ring-dykes was realized by New Hampshire field geologists during the years 1931 to 1934. J.E. Richey, who has had more experience with the ring-dykes of Scotland than anyone else had already realized the possible importance of piecemeal stopping (1932, pp.99 and 132)". Fracture-controlled stopping has already been shown for the Tibchi ring-dyke and piecemeal stopping was shown for the Oslo Region cauldrons

by Oftedahl (1953). The fact is probably that the mathematically inclined stress analysts have insufficient field control, and that the evidence for ring-dyke stoping shown by field geologists are complicated by other factors not allowed for during stress analyses.

3.6.4 Origin of ring-complexes associated with caldera formation with special reference to the Tibchi Ring-complex

The problem of the origin of ring-complexes associated with caldera formation (ie. with surface cauldron subsidence) is essentially the problem of inward dipping ring-faults (and ring-dykes) being associated with subaerial collapse of the central block. Based on the old rules both seem incompatible because the inward dipping cone fractures demonstrated by Anderson (in Bailey et al., 1924, and Anderson, 1936) were produced by increased magma pressure and upward rather than downward tendency of movement of the central block. At the same time field evidence is overwhelmingly committed to foundering of the central block bounded by inward dipping peripheral ring-faults. And as shown in the previous section, stress analysts could not reconcile the two facts, almost surely because of limited field knowledge, so that most often they ended up with a short-fall from the field criteria.

With respect to calderas, there is a general agreement as shown by Williams (1941) as to their normal formation by collapse.

Reynolds (1956) has discussed the two hypotheses pertinent to caldera formation in which inward dipping ring-fractures are implied, namely Escher's (1929) Gas Coring hypothesis and van Bemmelen's (1939) Collapsed Dome hypothesis. Escher's is

based on experimental work while van Bemmelen's is based on geological observation. The principles of van Bemmelen's hypothesis appear to be more compatible with field evidence from the Tibchi Complex, than those of Escher's.

van Bemmelen's hypothesis is based on studies of the origin of one of the largest known calderas - the Tertiary caldera of Lake Toba in North-West Sumatra, Indonesia. Lake Toba from which it takes its name is situated in it and only partly covers the huge caldera which measures 50x20 km (compared with 27x17 km of Tibchi) that is, about twice as elongated in plan as the Tibchi Complex.

A reconstruction by van Bemmelen (1939) shows that the earliest event was tectonic, with up-doming of the overlying crustal rocks. The 'diapiric' action is thought to have been caused by a great accumulation of highly energised gases pushing ahead of the magma. The up-doming was followed by the development of tensile fractures accompanied by volcanism and caldera formation. Initial volcanism was paroxysmal with mainly acid pyroclastic products. The volcanism associated with caldera formation produced "ignimbrites and pumice" most likely corresponding to the definition of ignimbrites as produced by fluidisation (Tazieff, 1970), and as described for the Tibchi caldera formation. Because the caldera formation was associated with the regime of volcanism, van Bemmelen attributed the collapse to loss of support arising from eruption.

Williams (1941) adapted van Bemmelen's hypothesis and attributed subsidence to loss of support due to the creation of actual or potential void in the magma chamber, resulting from eruption and sub-surface intrusion of magma, thus evacuating

the magma chamber, partly at least. Prior to subsidence therefore, a negative magma pressure is expected or at least a cessation of any prevailing magma pressure, in order to create a void or potential void situation. This is equivalent to total acceptance of Anderson's (1936) stress distribution for ring-dyke formation which should automatically give outward dipping ring-fractures. It has already been shown earlier, as accepted by Anderson himself, that while this could explain underground cauldron subsidence characterised by outward dipping ring-fractures, it is incapable of explaining surface cauldron subsidence and caldera formation and the question of inward dipping ring-fractures. On this ground, Reynolds (1956) thought that Williams' brand of collapse hypothesis, which has since won popularity among text-books, should no longer be tenable .

Throughout the two episodes of volcanism and caldera collapse magma pressure should remain positive despite any reductions that may arise as eruption begins. This is the principle favoured in this study. It is based on van Bemmelen's studies and explained on the additional principle of fluidisation by Reynolds (1956) on the following main points:

1) Initial doming and cone-fracture formation. A ring-dyke could form as a master cone-fracture by positively increased magma pressure rather than by reduced magma pressure or potential void situation;

2) The "fluidisation of erupted materials";

3) The loss of support resulting in caldera formation by collapse of the central area.

The model presented below for the Tibchi Complex is based on the above framework drawn up by Reynolds (op.cit.) but

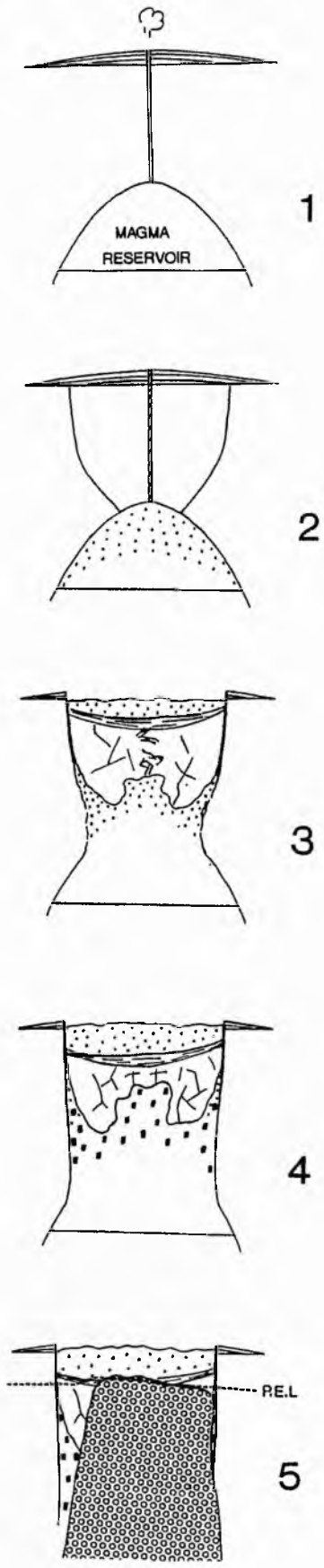


Figure 3.6.4 Diagrammatic representation of the structural evolution of the Tibchi Complex. Numbers correspond to stages described in the text. Shaded areas are as follows: Continuous lines = extrusive products of the central volcano; after subsidence (Stage 3) lines are shown as discontinuous. Dotted area in Stage 2 = Gas-charged magma; in Stage 3 symbol includes intra-caldera ignimbrites. Area with solid rectangles = Gas-poor magma; circles = biotite granite magma. P.E.L. = Present erosion level.

with further adaptations to suit field observations from Tibchi (see also Figure 3.6.4).

Stage 1

There was an initial gas build up as the ascending magma approached high level conditions. Up-doming of the country rocks may have taken place although all evidence is now lost through erosion or cannot be observed even in relict form because of the granitic nature of the country rocks and the absence of sedimentary formations. Paroxysmal eruptions culminated in the development of a central shield volcano, with a central vent which formed in place of an initial set of cone-fractures. The mathematical basis of this assumption was manifested in Anderson's (1936, p.148) stress analyses for cone-fractures although it was unacceptable to him as practicable owing to lack of field data support: "A further consequence of the particular solution corresponding to the point push remains to be discussed. If the cone-sheet tensions on any horizontal level are examined in the table (of principal tensions and pressures) they are seen always to be large, and sometimes to reach their maximum, where $x=0$; that is, directly above the centre of the cauldron. This does not however correspond with reality. The sheets of any particular system occupy a belt one or two miles in width. The central area is often obscured by later ring-dykes, which make observation difficult." Observation is only made difficult but not impossible. Field evidence for a central volcano as the first superstructure in Tibchi has already been given. The central vent was most probably effectively sealed by the extrusion of a highly viscous rock type such as the rhyolite agglomerate

(see geological map and stratigraphical succession of the volcanic rocks, Chapter 2) which marked the end of this stage and set up the conditions for the second stage.

Stage 2

Reconstitution of the magma by replenishment of supplies while the magma chamber remained effectively sealed at its relatively near-surface position resulted in two circumstances mutually related:

a) a second gas build-up resulting from new supplies and also from

b) continued crystallisation in which crystal to magma ratio was increasing up to 20-50% (inferred from modal analyses of crystal to groundmass in the resultant crystal-rich rocks).

The new gas build-up behaved as in Stage 1 and presumably began to up-dome the volcanic edifice and the intervening crustal layer. But because of the presence of the existing volcano directly above the magma chamber position, it would appear that the volcano's load pressure, would bear against central updoming or reopening of the already welded volcanic neck. Further increase in magma pressure would therefore result in a peripheral strain concentration to form a master cone-fracture which was apparently complete as a ring-fracture. The shape of this ring-fracture would be ultimately controlled by a combination of the overhead load distribution due to the volcano and the shape of the magma chamber below.

Stage 3

Availability of outlet for the gases and gas-charged magma resulted in fluidisation along the ring-fracture with the extrusion of the second batch of erupted material. Subsidence of the central block began as soon as magma began to be

discharged. On the other hand if at any stage the central block was absolutely free, its load pressure was bound to aid the fluidisation process and expel portions of the magma. Owing to the conical form of the ring-fracture it is to be expected that the central block would not always be free to subside because of the obstructive inward dipping basal regions. However, fluidisation of the walls of the ring-fracture has the ability of widening the base of the cone, the widening effect being greatest at the re-entrant basal region in contact with the magma chamber. This enables the initially conical central block to subside. The products of fluidisation were crystal-rich ash-flow tuffs which formed the intra-caldera unit.

Stage 4

The feeders to the crystal-rich ash-flow tuffs, frozen in the ring-dyke or stock position, correspond to the quartz porphyries. Quartz porphyry stocks observed in most occurrences in marginal positions close to the ring-dyke, in the Nigerian province, as here in Tibchi, may thus be regarded as ring-fracture fluidisation offshoots. Fluidisation waned as the magma became depleted in gas. Gas-poor magma welled its way up along the same ring-fracture, in the normal process of igneous intrusion, after the cessation of fluidisation but while magma pressure remained positive. Final subsidence caused brecciation of the frozen quartz porphyry located in the ring-fracture conduit. The gas-poor magma corresponds to the present granite porphyry ring-dyke; it was able to displace the 'frozen' quartz porphyries in the ring-fracture by some form of stoping. Remnants of the quartz porphyries are still

preserved in the granite porphyry, now seen as a complete explorer of the ring-fracture.

Stage 5

The granite porphyry was a forerunner of the ensuing plutonic phase of intrusion. A central stock of biotite granite was emplaced as a final episode. The mechanism of its intrusion was by piecemeal stoping through the collapsed basement of the central block. Perhaps a small westward tilt of the central block during subsidence was responsible for the eastward eccentric position of the central biotite granite pluton relative to the centre of the ring-complex.

One of the observations to be made from the above model is that it is quite feasible for ring-dykes to form without necessarily involving appreciable subsidence of the central block because ring-fracturing is shown to precede subsidence. If therefore the initial fluidised feeders froze in the ring-fracture conduit even before the central block had subsided enough to leave its imprint, a ring-dyke was already formed irrespective of any, or further, subsidence. In the Kudaru Complex, Nigeria, Bain (1934) found no evidence for cauldron subsidence and ascribed the peripheral ring-dyke to cone-fracturing. The ring-dyke rock is the quartz porphyry which has been shown in the model to correspond to the 'frozen' fluidised feeders of the Tibchi Complex. Quartz porphyries in ring-dyke position and stocks are identical from complex to complex in the neighbourhood of the Tibchi Complex, and it seems reasonable therefore to believe that their role was identical in each ring-complex.

Secondly a point of probable petrogenetic importance: a comparison between the 'non-subsided' Kudaru Complex and the

'fully subsided' Tibchi Complex shows that riebeckite granite is present almost to the exclusion of biotite granite as the central stock and vice versa in the Tibchi Complex.

A model for the formation of ring-dykes by cone-fracturing and subsidence has been proposed by Chapman (1966, 1976) but his model, as he has expressed categorically, differs from that of Reynolds (1956) and by deduction that of van Bemmelen (1939), on both of which the Tibchi Model is here based. Above all the Tibchi Model is different in the involvement of the central shield volcano as a precursor to the caldera formation, based not on general consideration but on evidence available from Tibchi.

3.7 Summary of Events in the Tibchi Complex

The earliest igneous activity was violent and eruptive, with mainly pyroclastic products. The composition and distribution of the extrusive volcanic rocks suggest the existence of a central shield volcano with a principal focus in the vicinity of Kogo (about the centre of the ring-complex). Its total expanse most probably extended beyond the circumference of the present peripheral ring-dyke. At a critical stage in this early volcanic era, the country rocks were fractured in an elliptical shape, apparently complete in perimeter and intersecting the then Jurassic land-surface.

Collapse of the central block was inevitable. The down-faulting produced a centripetal dip phenomenon in the extrusive sequence attributed to a progressive downward convergence of the initial ring-fracture.

The beginning of fluidisation along the ring-fracture and the commencement of collapse of the central block were

essentially contemporaneous. Caldera formation was thus attended by intra-caldera volcanism. The quartz porphyries were feeders to the caldera-filling ash-flow crystal tuffs. The granite porphyry magma moving behind the fluidised quartz porphyry system in the ring-fracture, was essentially de-gassed and by sheer retention of heat, surpassed the level at which the preceding quartz porphyry magma had chilled at the cessation of fluidisation.

Subsidence contemporaneous with the granite porphyry intrusion caused weakening of the ring-fracture conduit and brecciation of the chilled quartz porphyry feeders. Through pervasive fracture-controlled stoping the granite porphyry magma displaced the quartz porphyries from the ring-fracture, leaving only a few remnants, exploiting the ring-fault to the full, while also penetrating secondary fractures in the central subsided block.

The cycle ended with the intrusion of a central, though eventually eccentric intrusion of biotite granite that pierced through the bottom of the subsided volcanic pile, causing widespread contact-metamorphism, hydrothermal alteration and re-crystallisation.

CHAPTER 4PETROGRAPHIC DESCRIPTION4.1 Introduction

In comparison with the majority of the Nigerian Younger Granite Complexes, the Tibchi Complex is perhaps one of the simplest in terms of the occurrence and distribution of major rock units. In detail, however, the occurrence and distribution of minor rock types in the Complex is found to be complicated. Most of these minor rock types can be shown to represent subsolidus derivatives of rocks which belong to the normal magmatic sequence in the Complex. In a few cases, almost all clues are lost presumably through extreme modification of the initial rock. Field descriptions (Chapter 2) and structural interpretation of the Complex (Chapter 3) strike a note on the possible effect of later intrusions (especially the central biotite granite) on earlier volcanic and subvolcanic rocks, through observed pervasive contact metamorphism, hydrothermal alteration and recrystallisation.

In the following petrographic description, effort is made to 'preserve' the initial (magmatic) character of the rocks while still giving detailed descriptions of the relevant subsolidus modifications. The intention is part of a general aim, in the long-term, to draw up separate but related 'magmatic' and 'post-magmatic' models in the context of an overall petrogenetic history of the Complex.

The range in mineralogy is extensive. The majority of the rock-forming minerals found have been analysed using the electron microprobe. The analytical data provide additional insight into the evolutionary process of the rocks at both

magmatic and postmagmatic stages, and are therefore separately treated under Mineral Chemistry (Chapter 5). The nomenclature adopted for all minerals in the present chapter are those specified under each mineral group, in Chapter 5.

4.2 Lavas

4.2.1 Rhyolites

The rhyolites are generally porphyritic (with less than 20 percent phenocrysts), and grey in colour when fresh. Of minor occurrence is a type that weathers to bright shades of red and orange colours marking the oxidised zones, and petrographically characterised as follows:- In hand specimen only phenocrysts of quartz are apparent and these may be up to 2.5 millimetres across. In thin section aggregates of greenish-brown biotite crystals cluster in groups and as scattered minute crystals in the groundmass.

The dominant rhyolite type shows a dull colour zoning during weathering. Phenocrysts of quartz and alkali feldspar occur as tiny specks just visible to the unaided eye. The groundmass is generally recrystallised and consists mainly of alkali feldspar and quartz. Biotite produced during recrystallisation is dark greenish-brown, α = pale greenish-yellow, β = γ = dark greenish-brown.

Minor rhyolite dykes (less than one metre maximum width) cutting through the basement, and related to the rhyolite lavas (Chapter 2), consist of a black rock characterised by large quartz phenocrysts up to 9x5 millimetres in size. These quartz phenocrysts and any xenoliths of basement in the rock, are generally round in shape and the quartz constantly shows undulose extinction.

4.2.2 Basalts

General All the basalts found in the Tibchi Complex show pilotaxitic textures typical of subaerial flows, and can be divided into two groups on the basis of plagioclase crystallisation history. In the non-plagiophyric group only one generation of plagioclase occurs whereas in the plagiophyric group two or more plagioclase generations may be found, one being the groundmass phase while the other(s) represent(s) the phenocryst phase(s). By measurement of the composition of the plagioclase, wherever possible, in each of the basalt flows belonging to the two groups above, it has been possible to monitor the magmatic evolution of the basalt lavas and to determine at which stage the non-plagiophyric liquids were 'tapped' from the main reservoir while the latter continued to evolve through the plagiophyric series. In both the non-plagiophyric and plagiophyric series, however, augite occurs constantly in the fresh unaltered rock as microphenocrysts.

Later, a separate description is given of the contact metamorphism of basalts within the biotite granite metamorphic aureole, as outlined in Chapter 2.

It has been possible to use plagioclase compositions in consideration of the magmatic evolution of the basalts because only in extreme cases of contact metamorphism has the plagioclase been affected seriously, and in this case only when the granite actually veins the basalt. Veining of the basalt was fortunately very localised.

In all cases plagioclase composition has been measured optically by the symmetrical extinction method of Michel Lévy (Heinrich, 1965), the values obtained are thus only approximate.

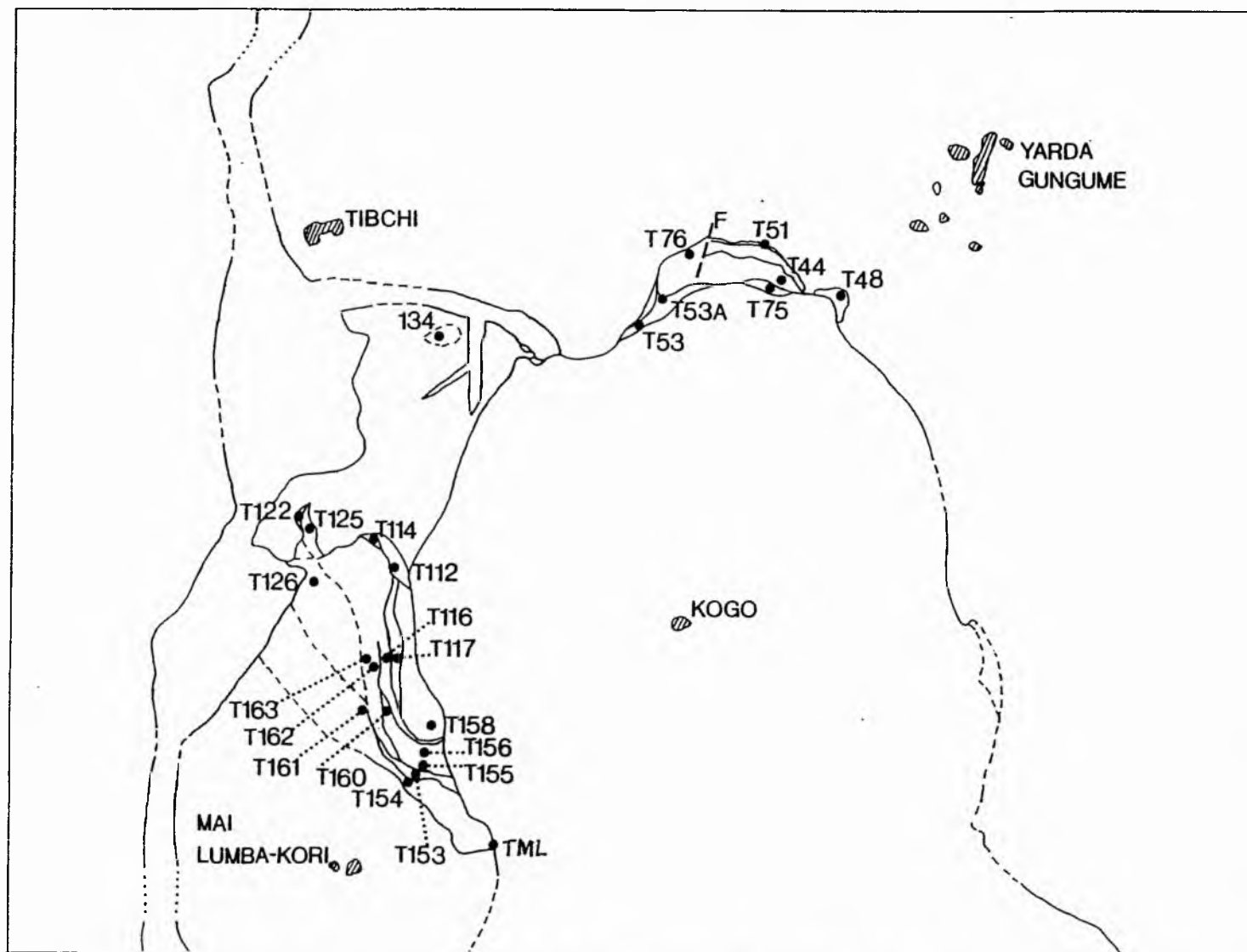


Figure 4.21A. Sample localities of the extrusive volcanic rocks, referred to in the text. For key to geological units, see 1:50,000 map.

(a) Non-plagiophyric basalts The magmatic petrographic features of the non-plagiophyric basalts are best represented in the unaltered rock (T122 locality) north of Mai Lumba-Kori and about 1.7 kilometres from the exposed biotite granite margin (Figure 4.2LA). A representative sample is characterised as follows:

Hand specimen description The rock is very dark in colour and lacks the subdued greenish tint normally found in most of the metamorphically affected basalts.

Microscopic features Essential minerals are plagioclase (An_{53}), augite, and opaque iron oxide. Accessory minerals consist chiefly of apatite.

Augite microphenocrysts are light brown in plane light and measure up to 2.3×1.1 millimetres in size. These microphenocrysts optically enclose plagioclase laths and have the following optical properties: moderate birefringence, with maximum interference colours in the lower 2nd Order; length-slow; maximum extinction angle $\gamma \wedge c = 47.6^\circ$.

Plagioclase laths do not normally exceed 0.35×0.05 millimetres in size, and together with augite form the groundmass. Groundmass augite is sometimes greenish in plane light.

Chronologically the last of all basalts found in the Complex is the non-plagiophyric andesine basalt (T53A). Its essential minerals consist of andesine (An_{41}), opaque iron oxide and augite. Accessory minerals consist mainly of apatite, with some fine-grained epidote. Opaque iron oxide makes up to 20 percent by volume of the rock and is subordinate only to plagioclase.

(b) Plagiophyric basalts These are separable into four

individual flows which, however, have not been delineated in the geological map. When arranged in their stratigraphical order and by means of their representative samples, they fall into a sequence (in order of decreasing age) as follows:

T53, T75B, T162, T163.

The first two form the basalt unit of the Yarda Gungume sequence and are in direct contact with the biotite granite, hence they are strongly metamorphosed (see later). The second two are successive intercalations in the welded lapilli tuff in the Mai Lumba-Kori sequence. T162 is strongly metamorphosed and is described later. T163 is the least altered of all the plagiophyric members and its petrographic description below may therefore be broadly representative of the plagiophyric series:

Hand specimen description Two generations of plagioclase phenocrysts can be distinguished: an earlier phase very sparsely distributed and in size up to 10 millimetres across and perhaps over; and a later phase more easily found and up to 4x2 millimetres in size. Each generation is characteristically rounded off in outline.

Microscopic features Essential minerals are as described earlier for the non-plagiophyric basalt (T122). The augite phenocrysts also have similar ophitic texture with plagioclase laths and similar optical properties. However a blue-green actinolitic amphibole partly replaces the augite.

Plagioclase phenocrysts occur either in single crystals or in synneusis. They are zoned, with the peripheral zone having a smaller extinction angle than the core. The core of the second generation of phenocrysts gave a labradorite composition of An_{54} . The rim is thus less calcic than An_{54} . No suitable grains were found for measurement among the first

generation phenocrysts.

Groundmass plagioclase laths are of the order of 0.19x0.05 millimetres and less, in size, and of andesine composition An_{40} .

The augite sometimes assumes a green tint which may be due to a deuteric alteration to chlorite or amphibole, or to a contact-metamorphic effect, as the rock lies in the outer zone of the biotite granite aureole.

A similar plagiophyric basalt (T75B) has two generations of plagioclase. Although no suitable grains were found for measurement among the first generation phenocrysts, the second gave a composition of An_{50} .

In summary, it is observed that in the non-plagiophyric series two plagioclase compositions are represented - An_{53} in the earlier, and An_{41} in the later, basalt lavas. In the plagiophyric series three compositions corresponding to two phenocryst generations and one groundmass phase, are observed - An_{54} , An_{50} (phenocrysts), An_{40} (groundmass).

Magmatic evolution of the basalt series

From the plagioclase compositions obtained, it appears reasonable to suggest that the plagiophyric lavas evolved through a series of intermediate stages probably involving changing conditions in pressure and temperature, in a relatively longer time span. The evolution, as registered in the plagioclase phenocrysts, is consistent with the expected trend, under magmatic conditions, for an ascending basalt liquid.

It is highly probable that the early non-plagiophyric basalt flow (T122) was 'tapped' from the above basalt magma at the earliest stages and extruded quickly to the surface

while the magma continued to evolve. Although it may have been possible that this process of partial magma withdrawal was repeated in the later stages, the andesine basalt T53A represents the most evolved fraction of the initial liquid, within the basalt range of composition.

4.2.3 Trachyte

In the field trachyte shows a very striking and consistent bedding ranging in thickness from less than one centimetre to three centimetres. The bedding plane is often accentuated by the late crystallisation in them of a yellow microcrystalline epidote. In parts where the above bedding is absent, the rock is almost indistinguishable from the aphyric basalt lavas.

Hand specimen description A smooth surface, preferably wetted or varnished, reveals the otherwise obscure porphyritic character of the rock. Felsic phenocrysts (see later) occur as faint irregular masses up to 3 to 4 millimetres across.

Microscopic features The essential minerals consist of alkali feldspar and plagioclase, while accessory minerals include opaque iron oxides and apatite, and traces of quartz.

Alkali feldspar is a cryptoperthite and occurs as the only phenocryst phase as well as a groundmass constituent. As phenocryst, it poikilitically encloses disoriented laths of plagioclase. The poikilitic habit of the phenocryst is thought to be responsible for the irregular shape of the latter as observed macroscopically.

The groundmass generally shows a taxitic texture, with preferred orientation of andesine plagioclase (An_{32}) parallel to the bedding.

4.2.4 Contact-metamorphism of the basic and intermediate lavas

The thermal history of the central biotite granite's contact-metamorphic effect and the nature of the aureole are best preserved among the basalt lavas of the (north-central) Yarda Gungume sequence of the extrusive volcanic rocks. These basalts, comprising about four flows, are cut directly by the biotite granite. At the present level of exposure, the lateral distance from the biotite granite margin to the outermost part of the basalt sequence is about 400 metres.

Traverse sampling from the granite contact outward across the basalt unit indicates varying degrees of contact metamorphic effects and makes possible a broad two-fold division of the aureole into outer and inner zones.

Elsewhere in the Mai Lumba-Kori sector in the west, the basalts are not in direct contact with the biotite granite but are about 500 to 700 metres or more away. Some of these basalts are also affected and according to the two-fold division above, these all fall into the outer zone of the aureole.

Three localities individually and together illustrate the full range of the observed contact-metamorphic process: one locality each in the outer and inner zones, and a third locality in the inner zone in which biotite granite actually veins the basalt. These are described separately and progressively, beginning with the outer zone.

The Outer Zone The type-locality is found in the Mai Lumba-Kori sector, where two successive lava flows represented by T162 and T163 (Figure 4.2.LA) are intercalated in acid pyroclastic rocks and exposed nearer and farther from the direction of the granite, respectively. In the farther (T163) basalt



Plate 4.2.A Hornblende in contact-metamorphosed basalt (T53). Note decussate arrangement of hornblende. Hornblende-hornfels facies. Plane polarised light.

exposure, a blue-green actinolitic amphibole with traces of chlorite partly replaces the augite. Elsewhere in the peripheral part of this zone this amphibole also fills any available cracks in the rock and significant epidote begins to appear. In the nearer (T162) basalt which represents the inward part of the outer zone, the mafic phase is almost completely converted to the actinolitic amphibole which forms wisps and needles in the groundmass and in-situ plate-like forms within relict poikilitic masses (after initial pyroxenes). Optical properties of the actinolite include: pleochroism α = pale yellow, β = yellowish green, γ = pale blue-green, $\gamma > \beta > \alpha$; moderate birefringence, maximum interference colours lower 2nd Order; length-slow, $\gamma \wedge c = 17^\circ$. Elsewhere in this part of the outer zone epidote spreads as interconnecting chains. (The appearance of epidote at each stage appears to be directly dependent on the calcic character of the individual basalt flow.)

According to the classifications of Turner and Verhoogen (1960) and Winkler (1965), the new mineral paragenesis of the outer zone comprising actinolite, epidote (and chlorite) represents the albite-epidote hornfels facies, which also corresponds broadly to the muscovite-hornfels facies of Sobolev and co-workers (Reverdatto et al., 1970).

The Inner Zone The type-locality for the inner zone is located in the Yarda Gungume sector and at the biotite granite contact (T53, Figure 4.2.LA). The most obvious petrographic feature of the rock is the presence, in thin section, of the pervasive crystallisation of a green hornblende to the complete exclusion of the initial augite (the hornblende being assumed to have formed from the augite). The hornblende forms monomineralic 'mats', with decussate metamorphic texture (Plate 4.2A).

Isolated crystals have subhedral to euhedral habits. The freshness of the amphibole can be seen not only from its homogeneous body colour, but also from its sharply defined crystal boundaries and cleavage traces. The amphibole attains a maximum individual size of the order of 0.19×0.06 millimetres. Its optical properties include: pleochroism, $\alpha =$ light yellow, $\beta =$ yellowish-green, $\gamma =$ green, $\gamma > \beta > \alpha$; moderate birefringence, with maximum interference colours in the lower 2nd Order; length-slow, $\gamma \wedge c = 25^\circ$.

The other minerals associated with the amphiboles are concentration of globular aggregates of epidote, opaque iron oxide and apatite. It may be noted that up till this stage polysynthetically twinned plagioclase remains apparently a stable phase.

Veining of basalt by granite In this situation it is observed that instead of hornblende, as above, a greenish-brown biotite of much finer size than the hornblende, is pervasively formed, and characteristically nucleated around the opaque iron oxides. Instead of the polysynthetically twinned plagioclase, there is a homogeneous feldspar.

Harker (1974) noted that any appreciable recrystallisation of the feldspar in the basalt during contact metamorphism was a step ahead of the amphibole stage; during the latter stage the plagioclase was usually stable (as noted above). In Harker's (op.cit.) case also, the biotite (similarly brown) succeeded the hornblende as the dominant mafic phase.

The fine-grained size of the iron-ore would appear to suggest that they may have recrystallised. If that was so, then the biotite/recrystallised plagioclase/recrystallised iron ore paragenesis which marks the highest grade of contact

metamorphism obtainable in a basic rock aureole of a granite intrusion (Harker, 1974; Reverdatto et al., 1970) has been obtained. And it belongs, together with the other basalts at the granite contact characterised by the green hornblende described earlier, to the hornblende hornfels facies of Turner and Verhoogen (1960) and Winkler (1965), which is equivalent to the amphibole hornfels facies of Sobolev and co-workers (Reverdatto et al., 1970).

Discussion A bifacial contact aureole, as described above contains not only the highest grade of metamorphism, but also the maximum number of facies obtainable in a basic rock intruded by a granite (Harker, 1974; Reverdatto et al., 1970). The Tibchi granite metamorphism therefore belongs to Reverdatto's (1970) Type 3 - the bifacial 'Tanohata' type.*

Contact metamorphism can be shown to be dependent on: the magma temperature and composition, the initial temperature of the country rocks, and the depth of the intrusive rock. The occurrence of the hornfels-type of contact metamorphism is a low pressure, near surface, phenomenon limited to less than 2-3 kilobars pressure and 8-10 kilometres depth (Reverdatto et al., 1970). This condition can be assumed for Tibchi. It can also be assumed that the prevailing temperatures in the Tibchi basalts were less than "the kinetic limits of contact-metamorphism" (below which contact metamorphism will normally not take place without extraneous heat supply, given as 300-400°C by Fyfe et al. (1958) but increased to 400-500°C by Reverdatto et al. (1970). Thus magma temperature and

* From a well-known contact metamorphic zonation developed near the granitic pluton at Tanohata, Japan.



Plate 4.3A Ash-fall tuff showing layering. Succession of coarse, medium and fine layers is cyclic and each cycle may be representative of ash from one pulse of volcanic explosion. Large thin section, 10cm long, crossed polarised light.

x



y

Plate 4.3B Ash-fall tuff with cobble of basement (B). The vein-like body along XY axis is a later intrusion. Large thin section, 8cm long, crossed polarised light.

composition become the decisive factors. Using experimental data on stability relations of relevant minerals normally associated with contact metamorphic aureoles and analytical data from natural minerals, Reverdatto et al. (1970) estimated that the temperature for the attainment of the hornblende hornfels facies (amphibole-hornfels facies) at shallow depth in rocks in direct contact with intrusive granites is about 500 to 600°C. This temperature is consistent with the temperature range at which the Tibchi biotite granite solidus must have been.

The actual dimensions of the aureole were not given in the description earlier owing to complications introduced by considerations of possible three-dimensional irregularities in the form of the subjacent granite beyond the exposed contacts. It was believed to be more important to consider instead the quality of the metamorphic grade attained and the maximum number of facies developed in the aureole as a means of characterising the observed contact-metamorphic effects.

4.3 Tuffs and Agglomerates

4.3.1 Ash-fall tuff

Hand specimen description The ash-fall tuff has an overall grey colour. In detail, however, it is observed that the tuff consists of a parallel alternation of coarser-grained grey, and finer-grained dark-grey, layers. This layering is frequent and thin; within a section about 10 centimetres thick, nine layers ranging from less than 5, up to 10 millimetres thick each, have been observed.

Microscopic features Layering is even more conspicuous in thin section (Plate 4.3A), and together with the fragmental

nature of the constituent particles, forms the most important microscopic features observed in this rock.

Sorting is prominent and appears to be responsible for the regular gradation from coarse to medium to fine layers, observed in several thin sections to be cyclic. Each cycle consisting of the three successive layers above is thought to represent a single fall of ash (and by inference, a single pulse of volcanic explosion).

The composition of the fragments presents a mixed mineralogy. Feldspar fragments consist of cross-hatched microcline, polysynthetically twinned plagioclase, crypto- and micropertthites. Mafic minerals are not important and consist of extremely fine aggregates of colourless mica.

The extreme hardness of the ash-fall tuff is thought to result from subsequent induration.

Cobbles of basement and alluvial detritus in ash-fall tuff

Some roundish inclusions of basement lithology and isolated grains of quartz also rounded in outline (Plate 4.3B), are found in the ash-fall tuff. These have been described in Chapter 2. Their conspicuously rounded outline contrasts strongly with the characteristically angular fragments of the main ash-fall fabric, and are therefore interpreted to be non-pyroclastic in origin.

4.3.2 Poorly welded tuff

Hand specimen description This rock has a distinctive white colour and a crude eutaxitic texture portrayed by sub-parallel alignment of moderately flattened pumice fragments. These pumice fragments are light brown in colour and occur as lenses generally less than 15 millimetres long. Fragmental

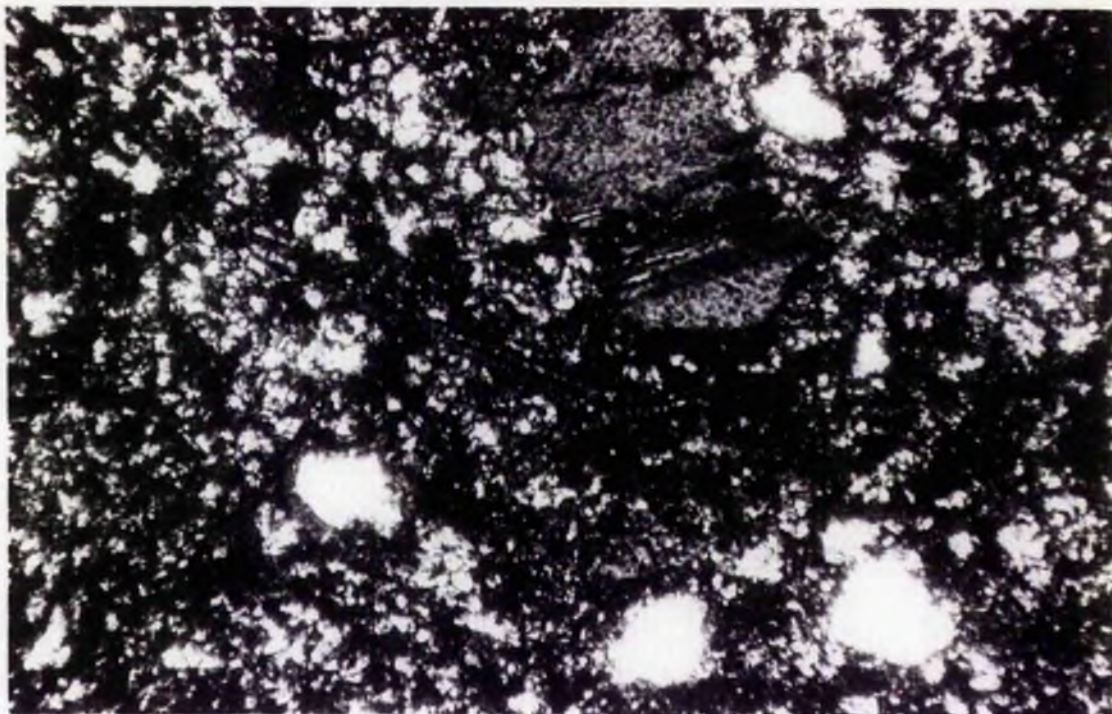


Plate 4.3C Tri-radial shard. Poorly welded tuff (T126) crossed polarised.

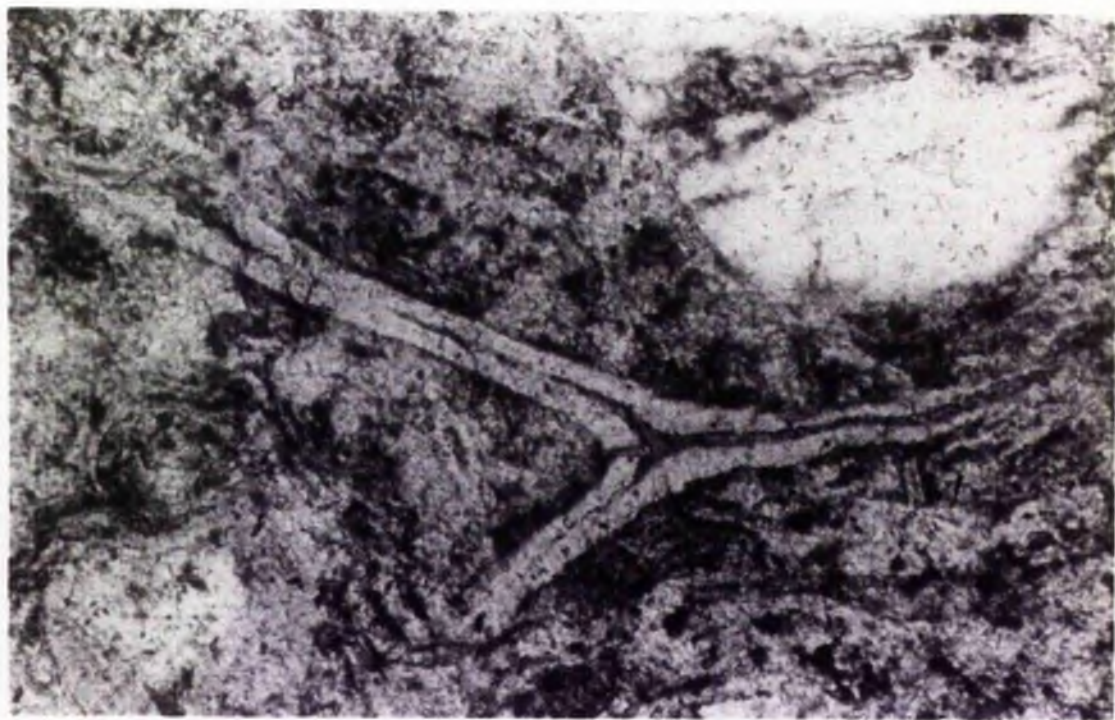


Plate 4.3D Same as in Plate 4.3C, magnified. The white dense wall of the shard consists of axiolitic intergrowth of -cristobalite and alkali feldspar. Plane polarised light.

2mm

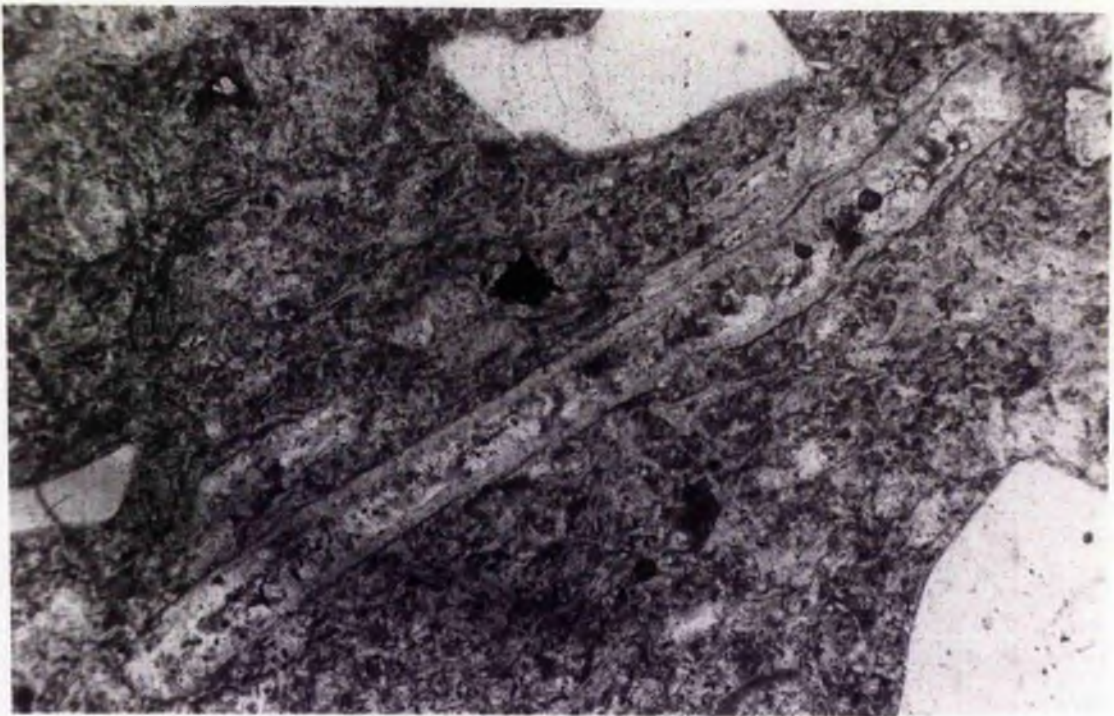


Plate 4.3E Tubular pumice vesicle or cell in poorly welded tuff (T126). Section is cut parallel to direction of compaction and welding, hence the (crude) alignment of shards parallel to the tubular pumice cell. Plane polarised light.



Plate 4.3F Same as in Plate 4.3E, magnified, and in crossed polarised light, to show internal structure of the pumice cell. Note axialitic texture of wall and the relatively coarse vapour-accelerated crystallisation in the interior.

1mm

phenocrysts of quartz are very conspicuous but alkali feldspars have generally been replaced by kaolinite. Lithic fragments up to 10 millimetres are interspersed in the rock.

Microscopic features Alkali feldspar and quartz occur as fragmental phenocrysts while the groundmass consists mainly of glass-shards.

Modal analysis gives a phenocryst content of 21 percent by volume, with alkali feldspar twice as abundant as quartz. Both the feldspar and quartz are of comparable size and generally less than 5x3 millimetres.

The groundmass consists of lenticular glass-shards of various shapes among which are found: Y-shaped shards (Plates 4.3C and D); double branching (bow-tie shaped) shards, perhaps representing two contiguous Y-shaped shards; multiple-branching shards; lunate or U-shaped shards; and O-shaped shards.

The walls of the shards are characterised by axiolitic intergrowth of α -cristobalite and alkali feldspar, resulting from devitrification (Ross and Smith, 1961). The cristobalite-bearing, axiolitic wall optically shows (this study) a consistent negative relief relative to the groundmass and to crystalline phases within the central parts of the shard or pumice. This negative relief is most probably due to the presence of the α -cristobalite since X-ray studies of Ross and Smith (op.cit.) preclude the presence of other SiO_2 -polymorphs in axiolites.

The internal structure of the eutaxitic pumice lenses in the poorly welded tuff shows elongated, tubular and parallel vesicles or cells. In the large lenses, these vesicles are partially collapsed and their dense walls devitrify to spherulites while the lumen of each vesicle devitrifies to a relatively coarser and granular crystalline assemblage.

The elongated tubular structure of individual vesicles or cells of rhyolite pumice was originally described by Lacroix (1930) and was contrasted with those of trachytic and phonolitic pumice which are more or less spherical. Of special interest therefore is the occurrence in the poorly welded tuff of isolated, apparently uncollapsed, pumice vesicles or cells (Plates 4.3E and 4.3F). Those measured range from 2.25x0.13 millimetres to 1x0.19 millimetres in size. At the end of some of them, septa of contiguous cells can be seen. The various peculiar shapes of the shards described earlier namely Y-, double Y-, lunate and O-shaped types, can be shown to represent various parts of disrupted pumice cells such as shown in Plates 4.3E and 4.3F.

4.3.3 Welded lithic tuff

Hand specimen description The rock is characterised by the preponderance of lithic fragments of assorted colours mostly different shades of grey and black, corresponding to earlier volcanic rocks in the stratigraphical succession (Chapter 2).

The groundmass is dark blue/green in colour and in it fragmental phenocrysts of alkali feldspar and quartz are sparsely distributed. The groundmass shows a streaky structure produced by contortions of pumice fragments around lithic fragments during extreme compaction and welding. This contorted foliation contrasts with the unfoliated fabric in the poorly welded tuff described earlier. Another point of contrast is that in this strongly welded rock the large pumice fragments are dark in colour (compared to brown in the poorly welded tuff). These pumice fragments show 'flamme-like'

terminations identical to the classical 'fiamme' (Ross and Smith, 1961). The term 'fiamme' is used hereafter to describe such pumice fragments.

Internal structure of the fiamme A special thin section was cut to show the internal structure of the largest fiamme recorded in the welded lithic tuff. This fiamme measures 33x6 millimetres, and has a central cavity of 1.8x0.5 millimetres elongate and parallel to the length of the fiamme (Plate 4.3G). All the solid areas surrounding the central cavity are believed to have been produced by the collapse of the initial pumice and the strong compaction and welding of the parallel glass walls of individual vesicles or cells.

Devitrification of the dense body of the fiamme has resulted in two zones of spherulites, the zonation being parallel to the long axis of the fiamme. In the outer zone the spherulites are compact, with cryptocrystalline rays, and are about 0.08 mm in diameter. In the inner zone, the spherulites have coarsened and consist of microscopically recognisable rays.

Within the central cavity there is a vapour-phase crystallisation of discrete euhedral crystals of quartz, homogeneous alkali feldspar and a few polysynthetically twinned albite (Plate 4.3H). The largest crystal size is attained by quartz (0.27mm long). Every other space within the cavity is filled by massive fluorite, with small amounts of intergrown magnetite-haematite (microprobe analysis, Table 5.5, Chapter 5). In the central cavities of some other fiamme, the intervening space among euhedral crystals is filled by fluorite and/or green mica (microprobe analysis, Table 5.6, Chapter 5). The green mica is found to be of the same composition as the green mica crystallising as long fibres along the rays of spherulites within the

dense part of the fiamme and in the general groundmass as scattered irregular crystals. Clearly, this mica is a devitrification product, if the spherulites are of devitrification origin.

Most of the fiamme studied have shown the same mineralogical assemblage as described above. However, in one locality (T117), the mafic mineral is a blue amphibole instead of a mica. The amphibole crystallises along the rays of spherulites in the dense walls of the fiamme and in isolated pockets in the central mid-line. In the latter case the amphibole is prismatic and is accompanied by granular quartz and alkali feldspar. The amphibole is pleochroic, γ = yellowish-green, $\alpha = \beta$ = deep blue, $\alpha = \beta > \gamma$; length-fast. The amphibole was not chemically analysed but is thought to be probably arfvedsonite.

4.3.4 Welded crystal tuff (1)

Hand specimen description This rock is dark grey to black in colour and is porphyritic, with fragmental phenocrysts of alkali feldspar and quartz. These phenocrysts, making up 20-30 percent by volume of the rock, do not generally exceed 3 millimetres across. In the field it is the comparatively high phenocryst that distinguishes this rock from those described earlier. However lithic fragments are common and may sometimes be comparable in proportion to the crystal content. In one variant of the rock (T134, ref. Figure 4.2.2) a eutaxitic alignment of fiamme can be seen on a smooth surface. These fiamme are very much elongated, up to 40x2 millimetres and wavy along their length, as a result of compaction against phenocrysts. A second variant (T158) is so strongly welded that the individual

fiamme cannot be distinguished macroscopically.

Microscopic features In the T134 variant of the rock the groundmass is partially recrystallised resulting in only the larger fiamme being recognisable and even these are coarsely devitrified. The recrystallisation in the groundmass has caused precipitation of fine-grained crystals of reddish-brown and green biotite. Clusters of relatively coarser crystals of biotite, co-existing in patches with opaque iron oxide, probably represent recrystallised earlier mafic minerals.

Microscopic evidence for strong welding is better preserved in the T158 variant. The groundmass shows partial isotropism and numerous lenticular shards and laminated fiamme have been observed folded round the edges of lithic fragments and phenocrysts. Following devitrification in some of the fiamme, a greenish biotite crystallises in flakes in the central midline, together with granular quartz and alkali feldspar.

Generally accessory minerals consist of opaque iron oxide and fluorite both of which are associated with clusters of biotite in the recrystallised variant. Lithic fragments consist of earlier volcanic rocks shown in the stratigraphical succession.

4.3.5 Welded crystal tuff (2)

The welded crystal tuff (2) differs from the welded crystal tuff (1) described earlier in having a much lower lithic fragment content, which is often negligible in places, and in having a higher proportion of phenocryst content (40-50 percent by volume). Mineralogically also the welded crystal tuff (2) is found to contain the full range of the major mafic mineral groups: ferrohedenbergite, (relict) fayalite, amphibole and

biotite. The welded crystal tuff (2) is in terms of crystal content and mineralogy thought to be directly transitional to the fayalite ferrohedenbergite quartz porphyry group. This concept has been described and discussed in Chapters 2 and 3.

Hand specimen description When fresh, the welded crystal tuff (2) is characterised by whitish alkali feldspar phenocrysts (up to 5mm long) and are, together with associated quartz, characteristically fragmental in shape. Incipient oxidation produces a purple-coloured rock, but when extensively re-crystallised the rock is rather grey.

Microscopic features Evidence for very strong welding is displayed in thin section by the high degree of compaction of the shards and fiamme against (solid) crystal and lithic fragments giving rise to apparent flow textures. The obsidian-like groundmass is mostly isotropic but can be seen in plane light to consist of the thread-like, contorted shards and fiamme, whose forms may be due to the effect of extreme welding (Ross and Smith, 1961).

Although alkali feldspar and quartz are the principal phenocrysts, ferrohedenbergite and relict fayalite are also found. A well-formed phenocryst of ferrohedenbergite, 1.5x0.5mm in size, consists of islands of fresh green, pleochroic pyroxene separated from each other by a meshwork of yellowish-brown alteration product. Further, a bluish-green amphibole optically similar to the ferrichterites of the quartz porphyries, partially replaces both the pyroxene and its alteration product. The replacement amphibole occurs as a mass of minute prismatic aggregates and is also found dispersed in the groundmass in extremely fine aggregates.

Massive recrystallisation observed in the grey-coloured variant has completely destroyed the initial texture of the groundmass. The shards and pumice fragments are replaced by relatively coarse granular quartz and alkali feldspar. These are associated with new greenish-brown biotite in clusters, presumed to have formed from original pyroxene and fayalite phenocrysts. However only ghostly relics of the very large fiamme can be used to definitely relate this rock to the crystal tuff rather than to a porphyritic rhyolite lava.

The massive recrystallisation is attributed to the nearby biotite granite since it increases in intensity nearer the latter intrusion. Further away from the biotite granite a green siderophyllite mica (Table 5.6, Chapter 5) replaces alkali feldspar phenocrysts, in the crystal tuff, in characteristic spherulitic masses.

4.3.6 Welded lapilli tuff

Hand specimen description In this rock lapilli constitute over 75 percent by volume of the rock. The assortment of lapilli consisting essentially of pre-existing tuffs and lavas, presents a multi-coloured assemblage on a smooth surface. Some are brown and apparently homogeneous, others are orange-brown and mottled; these two groups appear to represent rocks already subaerially oxidised or partially weathered prior to incorporation into the present tuff magma, however certain grey and black aphanitic rocks, some porphyritic, are much more common.

Microscopic features All the assorted lapilli are welded together by a tuff matrix. The role of solid fragments on the compaction and distortion of pumice fragments and shards during

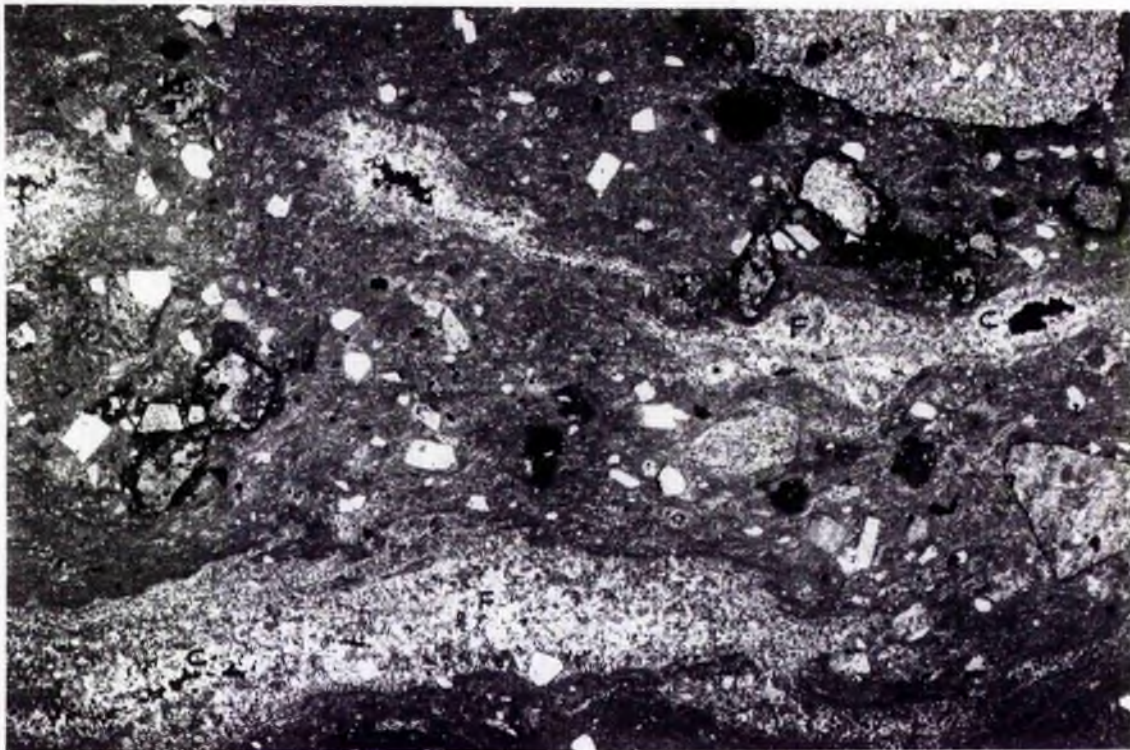


Plate 4.3G Fiamme (F) showing flame-like terminations, Lithic tuff (T114). Note elongate central cavities (C) parallel to the length of the fiamme. The cavity in bottom left is magnified in Plate 4.3H. Whole thin section, 3.2 centimetres long, crossed polarised light.

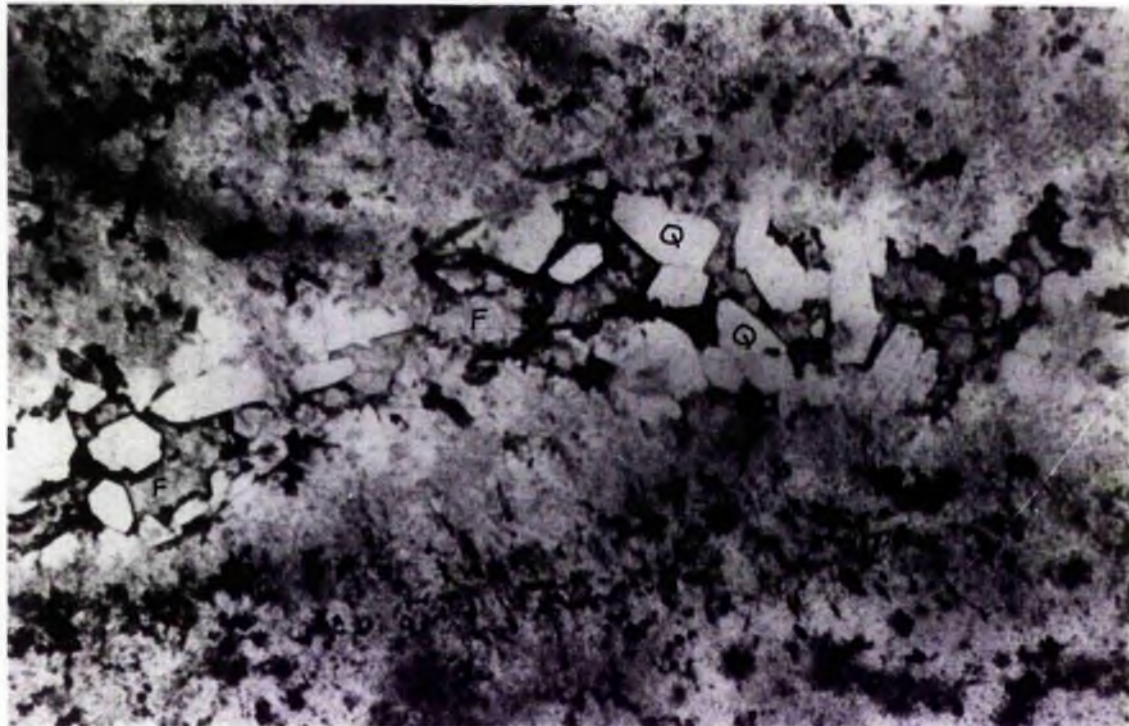


Plate 4.3H Central cavity in large fiamme in Plate 4.3G magnified to show the nature of the vapour-phase crystallisation observed (see text). Q = quartz, F = fluorite, Black = intergrown magnetite-haematite and green mica. Plane polarised light.



Plate 4.3K Three fiamme folded round the roundish edge of a lithic fragment during compaction against neighbouring lithic fragments. The fiamme apparently show unlimited plasticity. Welded lapilli tuff (T116). Plane polarised light.



Plate 4.3L Away from crowded lithic fragments, distortion of fiamme (only moderately to slightly folded) is not usually great. Welded lapilli tuff (T116). Plane polarised light.

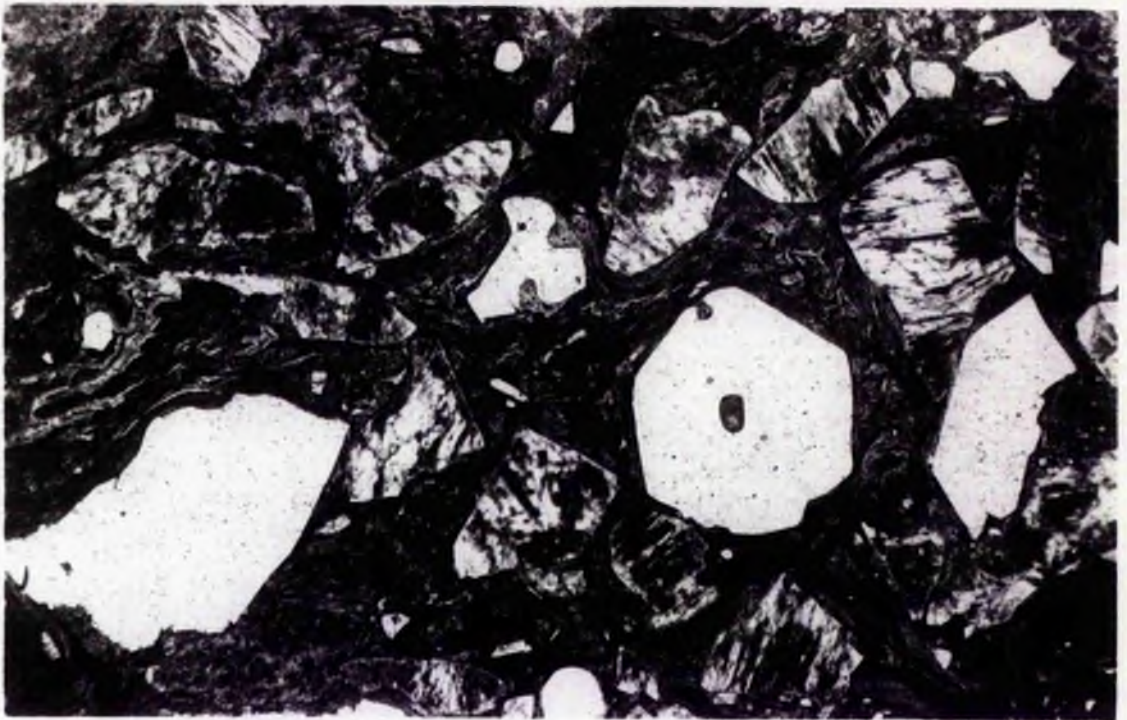


Plate 4.3M Pseudo-flow texture produced by extreme compaction and welding in the crystal tuff matrix of the welded agglomerate (T125). Plane polarised light.

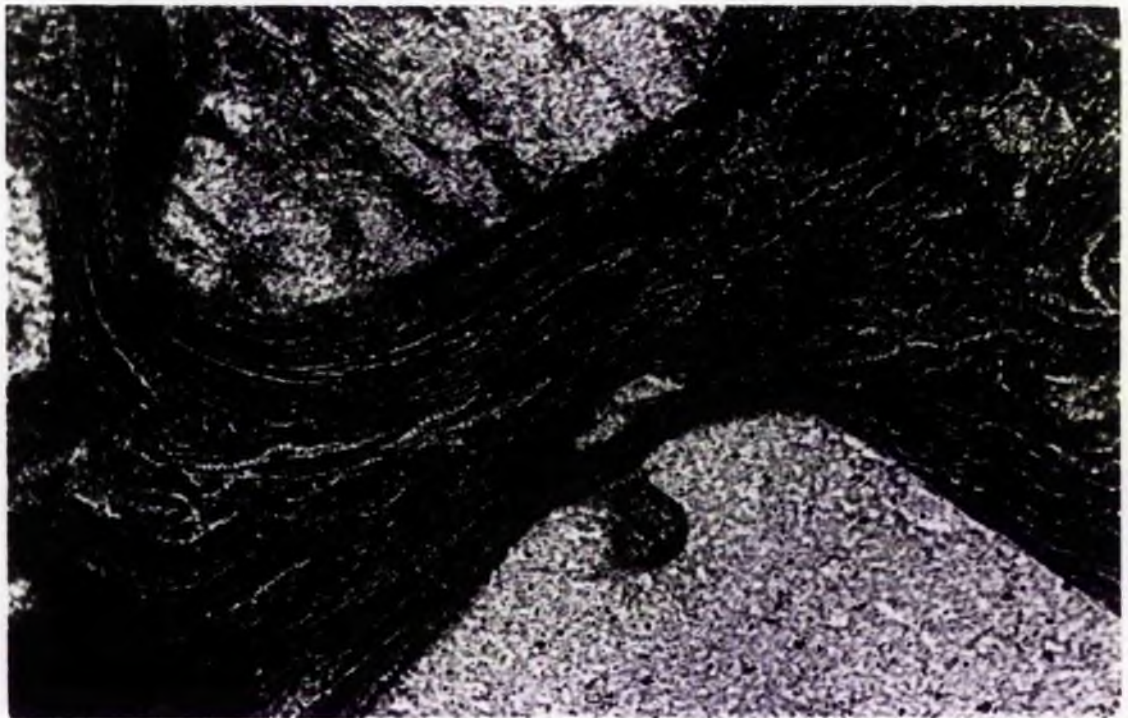


Plate 4.3N Part of Plate 4.3M magnified to show the filamentous structure of drawn out shards and pumice fragments produced by extreme compaction and welding between crystal phenocrysts. A pseudo-flow structure between the two phenocrysts terminates in area of less compaction (top right). Plane polarised light.

the consolidation of the lapilli tuff (and the welded tuff in general) is strikingly demonstrated in Plates 4.3K and 4.3L. Plasticity of these glass fragments is apparently unlimited during the period of consolidation.

Near the biotite granite contact, quartz veins up to 0.75mm wide, but generally less, have been observed to cut through both the tuff matrix and the lithic fragments. Partial recrystallisation of the groundmass is visible in high magnification. Scattered irregular masses, and sometimes small elongate prisms, of ferroedenite are formed in the groundmass of the tuff and in only one species of the lithic fragments namely those of the rhyolite agglomerate lithology. In the trachyte lithic fragments epidote crystallises instead of ferroedenite. In lithic fragments of the early rhyolite lavas there are hardly any appreciable mineralogical changes. Epidote also crystallises in the tuff matrix itself. Optical properties of the ferroedenite recorded include: Pleochroism, $\gamma = \beta = \text{green}$, $\alpha = \text{yellow}$; length-slow, $\gamma \wedge c = 21.6^\circ$; maximum interference colour, first order yellow.

Discussion If temperature and pressure near the biotite granite contact can be assumed to be approximately constant within the dimensions of a single thin section, then the observed differences in the appearance of epidote and/or ferroedenite can be reasonably assumed to be dependent on bulk chemical composition of the individual rock types found as lithic fragments. It had been mentioned in descriptions of the basalts earlier that contact metamorphism of different flows within the same contact zone preferentially produced epidote in some flows only, the earlier flows being characteristically liable to the formation of epidote than the latter flows.

Therefore it is possible that some essential elements varying with the evolution of the series may be important, most probably calcium and iron. In the present lapilli tuff a further complication may be introduced by the state of oxidation of the various extrusive rock types prior to incorporation into the lapilli tuff and therefore prior to subsequent thermal effect within the biotite granite aureole. Perhaps a more detailed investigation will be required for a satisfactory explanation to be reached.

4.3.7 Agglomerates

As stated in Chapter 2, there are three agglomerates in the stratigraphical succession namely, Interbedded agglomerate and basalt; Rhyolite agglomerate; and Welded agglomerate with crystal tuff matrix. The first named is poorly exposed and could not be sampled fresh. It is therefore not discussed further in this section. The descriptions below refer only to the rhyolite agglomerate and the welded agglomerate with crystal tuff matrix.

Rhyolite agglomerate This consists of two rhyolite components, a porphyritic rhyolite and an aphyric rhyolite, both intermingled with each other so that blocks and particles of one may be found in the other and vice versa. Also interfingering of both lavas is common.

The porphyritic rhyolite component is black in colour with phenocrysts of whitish alkali feldspar and quartz, both roundish in shape though occasionally angular, especially the feldspar which is mostly cryptoperthitic. Near the biotite granite contact, the feldspar undergoes a partial alteration to minute aggregate of colourless mica. The groundmass is interspersed

with two generations of opaque iron oxide, but predominantly consists of quartz and alkali feldspar.

The aphyric rhyolite component has a grey colour. In thin section its groundmass is homogeneously fine-grained.

Elsewhere, in the sample locality T160, the rock becomes very complex in lithology. Both the porphyritic rhyolite phase (T156) and the aphyric-porphyritic phase (T155) are seen as lithic fragments in an apparently new aphyric rhyolite whose phenocrysts are conspicuously shattered although no ash flow structures such as shards and pumice fragments could be identified. This host rhyolite is thought to be a second lava phase accompanied by pyroclasis. This second lava phase is observed to be bedded, with individual beds from less than 30cm to several centimetres thick. Blocks of pre-existing rocks are rounded and up to 25cm across.

The rhyolite agglomerate is thought to have been derived from the foregoing components by an initially erupting porphyritic phase being intermingled with a second aphyric phase or vice versa, by explosive action in a confined space, possibly a volcanic conduit or upper part of the magma chamber, thus permitting a repetition of the same process as many times as possible. Alternatively, a low pressure fractionation in a shallow granitic magma chamber could cause the separation and floatation of felsic crystalline phases capable, at some stage, of literally choking the magma conduit. The resulting sudden explosive ejection could cause a mixing of the two porphyritic and aphyric components.

Welded agglomerate with crystal tuff matrix The welded agglomerate with crystal tuff matrix is, as its title portrays, essentially a crystal tuff with 40-50 percent phenocrysts, but

with blocks of lithic fragments as a dominant component of the rock as a whole. Some of the blocks are rounded, others are angular. The most striking feature of this rock, however, is in the apparent "flow texture" seen in its matrix in thin section. Inspection under high magnification, however, reveals that these 'flow lines' are indeed extremely laminated but discontinuous, collapsed pumice fragments and drawn out, filamentous shard lenticles (Plates 4.3M and N). This texture is therefore produced by extreme compaction and welding. Ross and Smith (1961) have pointed out that "silicic flow rocks nearly always show flow banding. This means that if linear elements in unmetamorphosed rock extend over several feet the rock almost surely is not a welded tuff". It is observed that within the same thin section the flow laminations in the matrix terminate. Surely this is a welded tuff, as the termination is too abrupt for a flow rhyolite. As these pseudo-flow effects are most prominent between closely spaced lithic blocks and phenocrysts, it is believed, as in the welded lapilli tuff previously described, that the presence of solid particles supplements actual load pressure in causing extreme compaction during welding. Gibson and Tazieff (1967) have pointed out that the low viscosity associated with peralkaline ignimbrites could be responsible for intense flattening and welding observed even in thin units. Evidence from the lapilli tuff and the welded agglomerates above indicate that the presence of solid (crystal or lithic) fragment could supplement actual load pressure during compaction and welding even in ignimbrites not particularly peralkaline. However the ignimbrites of the Tibchi Complex are peralkaline (see Chapter 5).

2 mm

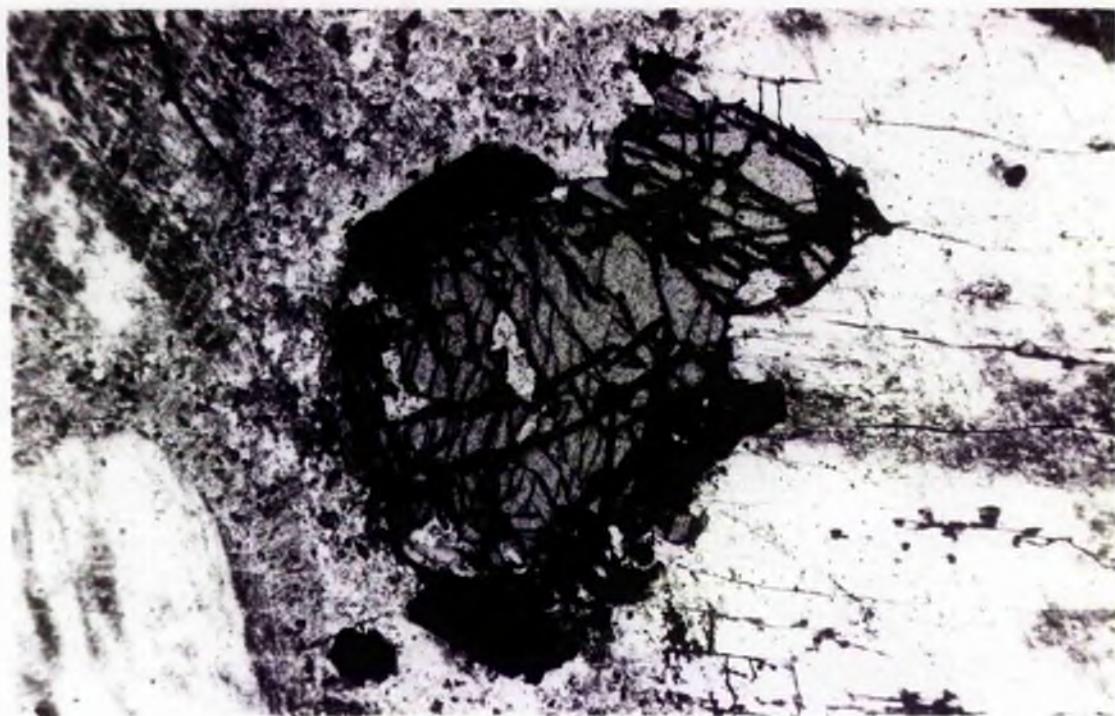


Plate 4.4B Two unaltered fayalite phenocrysts partially enclosed by K-feldspar (right, white). Black = ilmenite. Fayalite ferrohedenbergite quartz porphyry (T105). Plane polarised light.

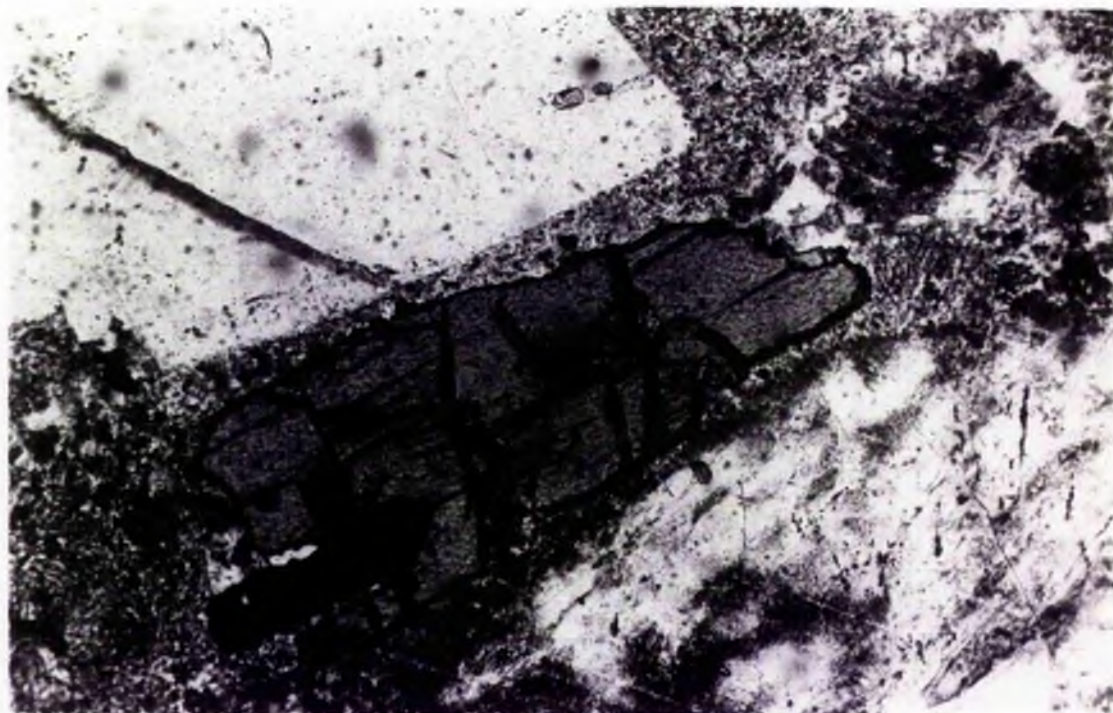


Plate 4.4C A typical unaltered ferrohedenbergite. Black prism = ilmenite. Fayalite ferrohedenbergite quartz porphyry (T105).

1 mm

4.4 The Subvolcanic Rocks

4.4.1 General

For convenience the quartz, and granite, porphyries are grouped together in this section. The term 'pristine' as used for some rocks of the two porphyry groups here, has already been fully explained in Chapter 2; it may be assumed to be synonymous with 'unaltered' but with special reference to what is eventually shown in this study to be subsolidus modifications of initially magmatically crystallised rocks.

In the following descriptions, pristine rocks have been described separately from the hydrothermally altered variations, in each of the two porphyry groups above. The most important, and common, aspect of the pristine rocks of the two porphyries, is found in the occurrence in them of a Ca-rich clinopyroxene series in continuous compositional variation. It must be emphasized that this variation is of magmatic origin, and that the above clinopyroxene series is found to be the key to the magmatic history of the granitoid rocks in the Complex (Chapter 5).

With regard to the hydrothermally altered rocks, it is the purpose in the relevant parts of this section to demonstrate the textural and mineralogical sequence of changes and of special interest is the transition from the clinopyroxene series and fayalite (Plates 4.4C and B) to their characteristic late amphibole species.

4.4.2 The pristine quartz porphyries

Two variants of the pristine quartz porphyries (Figure 4.4A), based principally on the mineralogy of the clinopyroxenes, have been distinguished:-

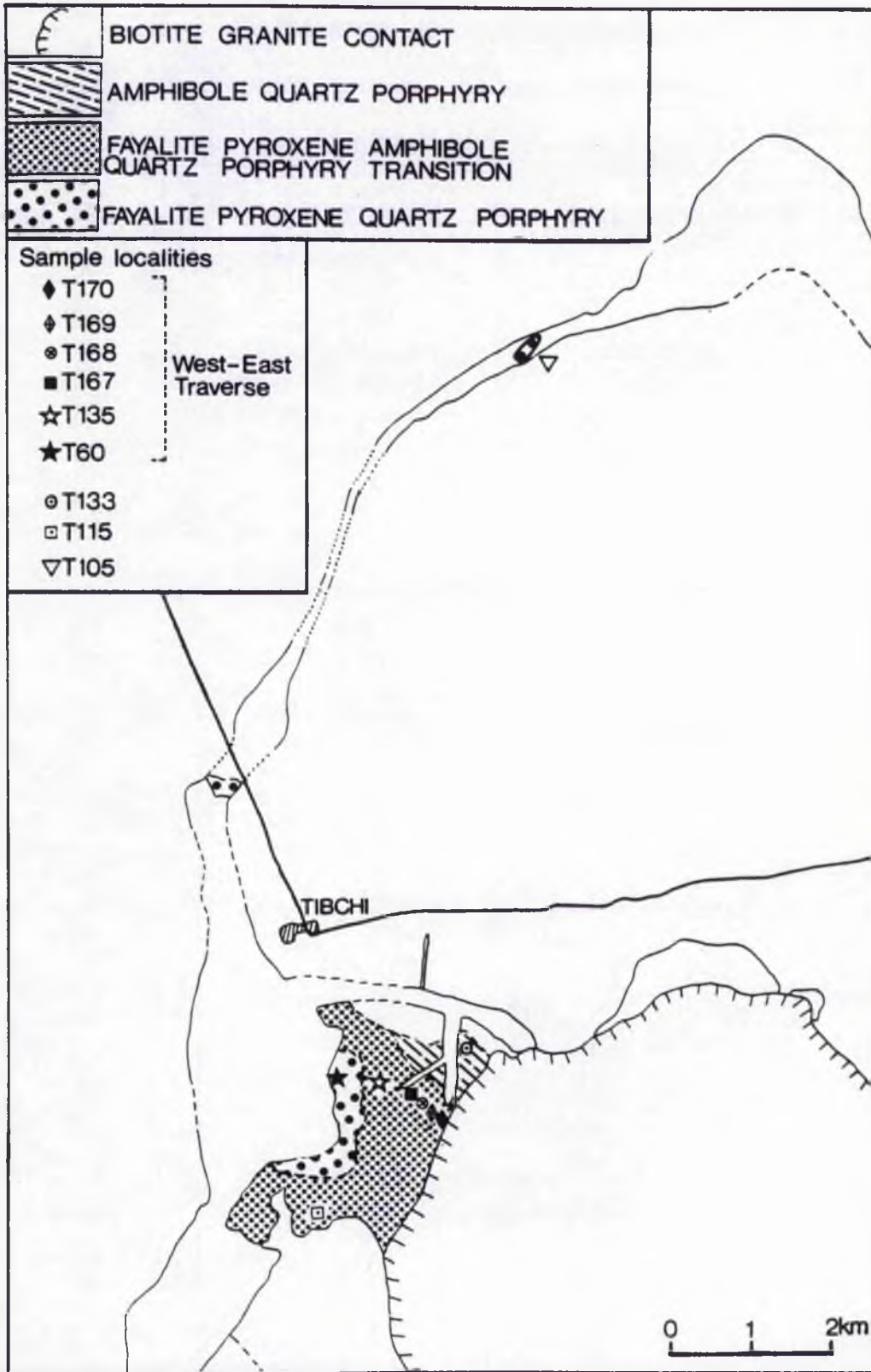


Figure 4.4.A Sample localities, quartz porphyries.

- (1) A fayalite ferroaugite ferrohedenbergite variant (T60); and
- (2) A fayalite ferrohedenbergite variant (T105).

These two are separately characterised as follows:

(1) Fayalite ferroaugite ferrohedenbergite quartz porphyry (T60)

Hand specimen description The rock is dark green in colour and porphyritic. The phenocrysts consist of green coloured alkali feldspar, quartz, pyroxene and fayalite. Maximum phenocryst sizes recorded are 7x3mm (feldspar), 5x3mm (quartz), 2x0.75mm (pyroxene) and 1.13x0.75mm (fayalite). The phenocrysts are often fragmental especially the feldspars while some of the quartz crystals retain their bypyramidal habit. The groundmass is microcrystalline. The occurrence of xenoliths of earlier extrusive volcanic rocks mainly fine-grained lavas and tuffs, is common. A group of cognate enclaves which occur both in the quartz porphyries and in the granite porphyry ring-dyke, is described separately.

Microscopic features T60 has a phenocryst content of 42 percent, compared with a range for all quartz porphyries of 40-50 percent, by volume.

The greenish feldspars are clear and transparent. They are however often rimmed by brown turbid areas which also penetrate the phenocryst through cracks and cleavage planes. In the extreme cases it is possible to find phenocrysts which are largely brown and turbid, with cores or isolated remnants of clear zones. Microperthitic exsolution albite may be visible in minute enclaves within the brown turbid zones. From detailed X-ray* studies it has been found that the green transparent

* Analyst: Prof. R.F. Martin

feldspars correspond compositionally to orthoclase. On the other hand the brown and turbid zones sometimes with exsolved albite, consist of a three-phase assemblage of a dominant orthoclase component with subordinate amounts of intermediate microcline ($\Delta = 0.59$), and low albite.

Feldspar phenocrysts especially, and occasionally quartz, show conspicuous overgrowth along their crystal margins. This overgrowth occurs even in fragmental phenocrysts, suggesting that the overgrowth took place after the fragmentation (intrusion and emplacement) stage of the rock. As the overgrowth itself is in continuity with the groundmass, it is inferred that the overgrowth was contemporaneous with the groundmass crystallisation.

Quartz phenocrysts show both bi-pyramidal and roundish forms in unbroken phenocrysts. Groundmass crystals apparently enclosed in the quartz phenocrysts or 'embaying' the latter, have been observed (see later discussion).

The pyroxenes consist of ferroaugite and ferrohedenbergite in continuous compositional variation, as revealed from electron microprobe analyses. Both pyroxene phases are green in colour and difficult to distinguish from each other optically. But from the analytical data it appears that the ferroaugite is substantially subordinate in abundance to the ferrohedenbergite. Normal zoning has been chemically, sometimes optically, observed in both phases. The typical pyroxene form is prismatic but often showing imperfections such as roundish ends and irregular outlines; these grade to sievy skeletal crystals. These irregularities are regarded as quenched textures in early phenocryst development, a view supported by the fact that the skeletal crystals analysed gave ferroaugite compositions rather than ferrohedenbergite. The normal pyroxene prismatic cleavage

may be complicated by heavy body fractures in a manner almost analogous to those characteristic of the fayalite phenocrysts. This tendency in the pyroxenes is correlated with the fragmentation and fracturing in other mineral species and is believed to be due to the fluidised emplacement mechanism of the quartz porphyries. The pyroxenes show no appreciable pleochroism. Birefringence is moderate in both pyroxenes but appears to be slightly higher, in analysed crystals, in the ferrohedenbergite than the ferroaugite. The maximum interference colour recorded in 2nd Order green, $\gamma_{\Lambda c} = 49.9^\circ$. In crystals showing normal zoning, the ferrohedenbergitic rim has a larger extinction angle than the ferroaugitic core by up to 5° . Although both pyroxenes occur as phenocrysts, the groundmass phase seems to be composed of ferrohedenbergite only. The pyroxenes are characteristically associated with ilmenite.

Fayalite forms 0.5 percent by volume of the rock. It is pale yellow in colour and often elliptical in outline though sometimes also equidimensional. Fayalite is characteristically heavily fractured. Less severely fractured crystals may show ill-defined cleavage parallel to the long axis. Birefringence is strong with respect to the ferrohedenbergite pyroxene which often mantles it; maximum interference colour recorded is 3rd Order green. The mantle of pyroxene consists usually of a row of small anhedral to subhedral crystals. The fayalite is altered in varying degrees to pale greenish antigorite or bowlingite and to various shades of red and orange corresponding to iddingsite. Average end member composition obtained from electron microprobe analyses of fayalite in the T60 rock is $Fa_{97.3}$.

The microcrystalline groundmass displays in some places

devitrification textures, mainly spherulites in different stages of coarsening. Elsewhere the groundmass consists of a finely crystalline assemblage of alkali feldspar, quartz, ferrohedenbergite and accessory minerals.

The chief accessory mineral is iron oxide. When enclosed in pyroxene or fayalite phenocrysts, the iron oxide composition (from microprobe analyses) corresponds to ilmenite whereas in the groundmass it is found to be ferrian ilmenite. Apatite is also associated with the mafic phenocrysts as long needles.

Groundmass crystals apparently enclosed in the quartz phenocrysts or 'embaying' the latter are considered to represent later crystallisation of groundmass in voids or an irregular margins of quenched skeletal quartz phenocrysts. The alternative explanation is perhaps a resorption phenomenon of early quartz crystals by the groundmass, but it is doubtful that any real compositional difference existed between phenocryst and groundmass phases of quartz. On the other hand the occurrence of skeletal crystals (as in pyroxenes) is found to be common in the rock.

(2) Fayalite ferrohedenbergite quartz porphyry (T105)

This rock is also green in colour and texturally similar to T60. The main points of difference are as follows:-

The phenocryst content is more in T105, reaching 50 percent by volume of the rock.

The feldspar phenocrysts in T105 are more easily distinguishable in hand specimen apparently because of the more common occurrence of turbid brown rims round cores of clear orthoclase cryptoperthites. The turbid rims appear white in colour macroscopically and mark out individual feldspar

phenocrysts.

The most important point of difference is the occurrence in T105 of only one pyroxene phase namely ferrohedenbergite to the exclusion of ferroaugite, as verified by microprobe analysis. Zoning in T105 is optically more definite, with a yellowish core of ferrohedenbergite and a bright green rim tending towards sodian ferrohedenbergite (up to 0.9 percent Na_2O). Colour zoning in T60 is poorly displayed.

In the above differences can be found, various lines of evidence to suggest that T105 is a more evolved rock than T60. These two pristine rocks must not be regarded as the only magmatic representatives of the quartz porphyry suite prior to hydrothermal alteration. They only illustrate the evolutionary sequence that may have been emplaced; in fact analytical data on pyroxenes (Chapter 5) clearly indicate that the quartz porphyries evolved beyond the T105 stage to a final stage (T115) which is not preserved entirely in its pristine form anymore. It is perhaps possible now to review the hydrothermally altered rocks against a background of a continuously varying bulk and mineral composition in the rocks involved.

4.4.3 Petrographical changes in the hydrothermal alteration of the quartz porphyries

The complications in the field relations of the quartz porphyries are summarised below in order that the field control and method of study adopted for the above changes, may be understood:-

(a) The biotite granite is the only 'plutonic' phase of intrusion in the Tibchi Complex, and it truncates the main quartz porphyry suite over a distance of two kilometres.

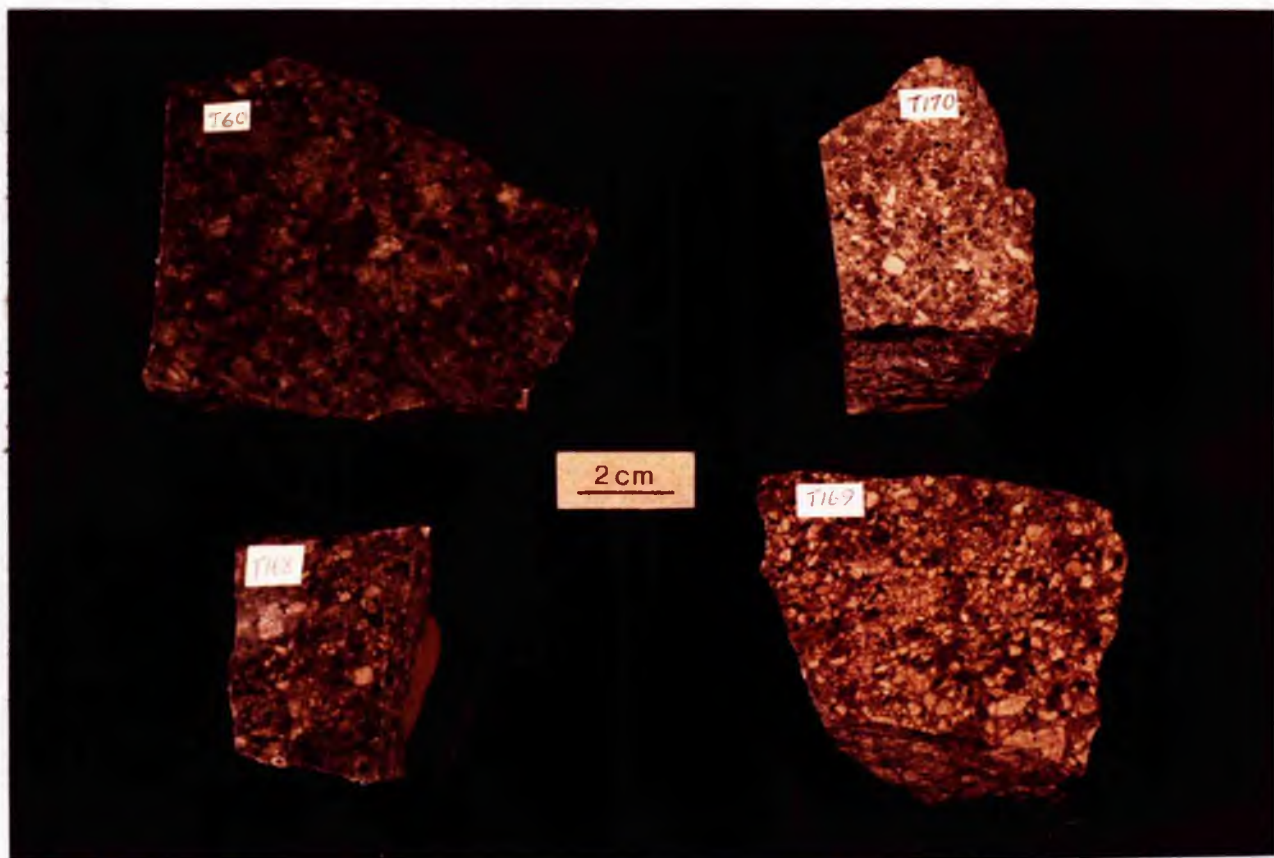


Plate 4.4D Colour changes in the hydrothermal alteration of the quartz porphyries (see text).

(b) The fluidisation mechanism of emplacement of the quartz porphyries is capable of rapid ejection of different parts of an evolving magma into an apparently homogeneous mass.

(c) There is an observed general tendency for increase in degree of hydrothermal alteration of the quartz porphyries, as the biotite granite is approached.

(d) Complete alteration of the quartz porphyries has been observed only along the biotite granite contact, yet these completely altered rocks do not have the same lithology.

As a result of the above complications, an effective model for the observed changes can only be achieved through combination of a well selected field control in sampling, and a suitable record of the possible range in pristine rock types involved despite the apparent homogeneity of the rock mass in the field.

Field control Sampling consisted of a west-east traverse (Figure 4.4A), from the pristine rock T60 in the west, through the transitional quartz porphyries, to the boundary with the biotite granite in the east, in the following order of sample localities:

T60, T135, T167, T168, T169, T170

Two localities outside this traverse which are of special importance are T115 south of the traverse and T133 north of it.

Record of possible range of pristine rocks involved In addition to obtaining petrographic and chemical data from pyroxenes of the two pristine rocks described earlier, these data have also been obtained from remnant pyroxenes in the partially altered rocks.

The West-East Traverse

T135

In the hand specimen, there is practically no significant change in the rock at this stage.

Microscopically, however, a ferrorichterite amphibole appears as small reticulate crystals sparsely distributed in the groundmass and sometimes also mantling phenocrysts of ferrohedenbergite.

The clinopyroxene is olive green in colour and slightly pleochroic to yellowish green, especially in the central areas of the phenocryst. Electron microprobe analyses show a reversed compositional zoning (Table 5.3B, Chapter 5), with a sodian ferrohedenbergite core and a ferrohedenbergite rim.

X-ray studies of the alkali feldspars also indicate that a similar reverse situation as above exists, between the groundmass and phenocryst feldspars, with respect to structural state, and composition of the K-phase in the perthite. The phenocrysts consist of intermediate microcline with a triclinicity (Δ) of 0.71. This represents a substantial degree of Al/Si ordering. On the other hand the groundmass feldspars consist of (monoclinic) orthoclase. In addition the orthoclase of the groundmass is purer than the microcline of the phenocrysts in terms of K-phase composition; this relationship should be the reverse if these feldspars were initially in equilibrium.

T167

Macroscopic changes are first observed in this locality. The alteration appears as light blue blotches pervading the green colour of the rock. In some places these blotches have increased, eventually coalescing to become the dominant phase. The initial green areas however usually persist as isolated irregular patches within the new invading blue phase.

Microscopically the occurrence of amphibole replacing initial mafic phases is, with respect to the form and degree of nucleation, comparable to the situation discussed in the preceding section (T135).

The structural state of the feldspars is however different. In T167 both the phenocryst and groundmass feldspars are orthoclase cryptoperthite, with identical degree of purity, and disorder, of the K-phase in the perthite.

T168

Hand specimens from here are homogeneously brownish in colour.

Microscopically, fayalite phenocrysts are heavily encased in antigorite which is pleochroic from pale yellow to green. The pyroxene present is a pale brown-green ferrohedenbergite. It is faintly pleochroic: γ = pale brown-green; $\beta = \alpha$ = pale greenish-yellow. $\gamma > \beta = \alpha$. The pyroxene phenocrysts are intensely altered. Microprobe analyses give only occasional ferroedenite amphibole compositions from the complicated series of poorly crystallised intermediate alteration products.

The phenocryst and groundmass phases of the feldspars consist of orthoclase with approximately the same K-phase composition in the perthite.

Turbidity in the feldspars in T135, T167 and T168 especially with respect to the groundmass phase, is much more than was observed in T60, and may be described as very intense. In these rocks there has not been any appreciable recrystallisation of the groundmass but coarsened spherulites can be seen to varying extents. However from T169 to T170 turbidity in the groundmass feldspars undergoes a dramatic change as the groundmass also changes in texture and composition.

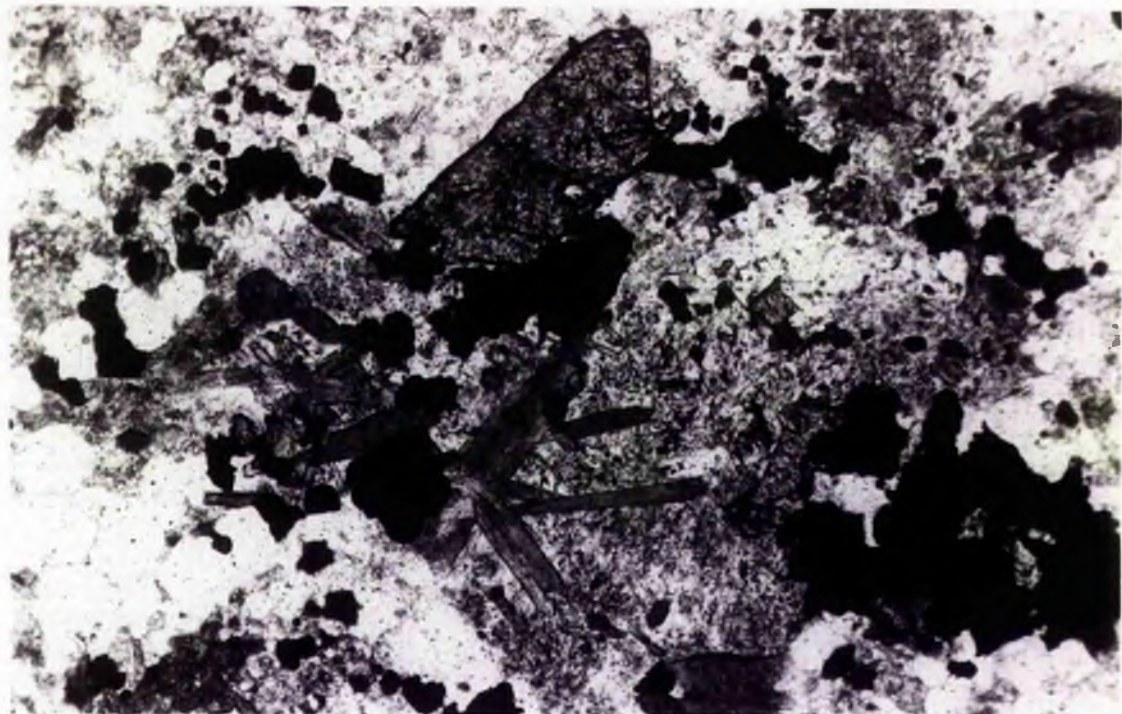


Plate 4.4E Euhedral crystal of monazite (M), with laths of ferroedenite (E), granular and massive titanomagnetite (black), and apatite needles (colourless, especially left hand side) on site of ferrohedenbergite hydrothermal degradation. Hydrothermally altered quartz porphyry (T169). Plane polarised light.



Plate 4.4F Same as Plate 4.4E, crossed nicols. Note the extinction angle of monazite megacryst, and the ferroedenite lath below it (no.E in Plate 4.4E), also in extinction.

1 mm

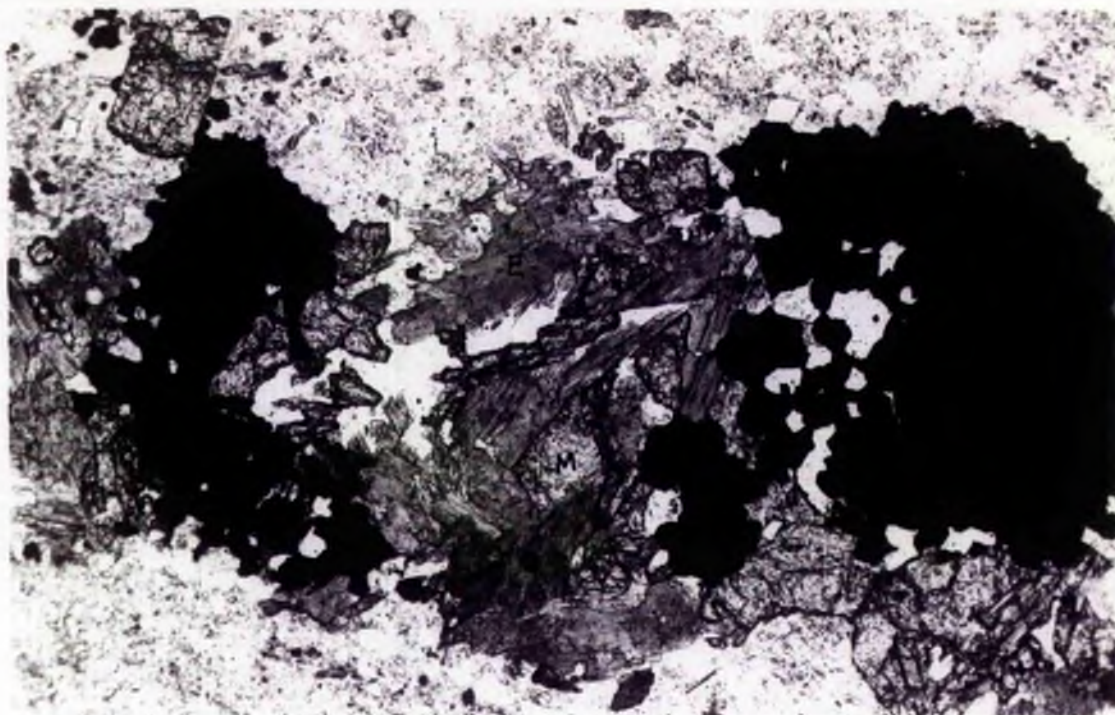


Plate 4.4G Ferroedenite (E), Monazite (M) and Titanomagnetite (black) together occupy the site of degradation of a pre-existing calcic pyroxene or fayalite. Hydrothermally altered quartz porphyry (T169). Plane polarised light.

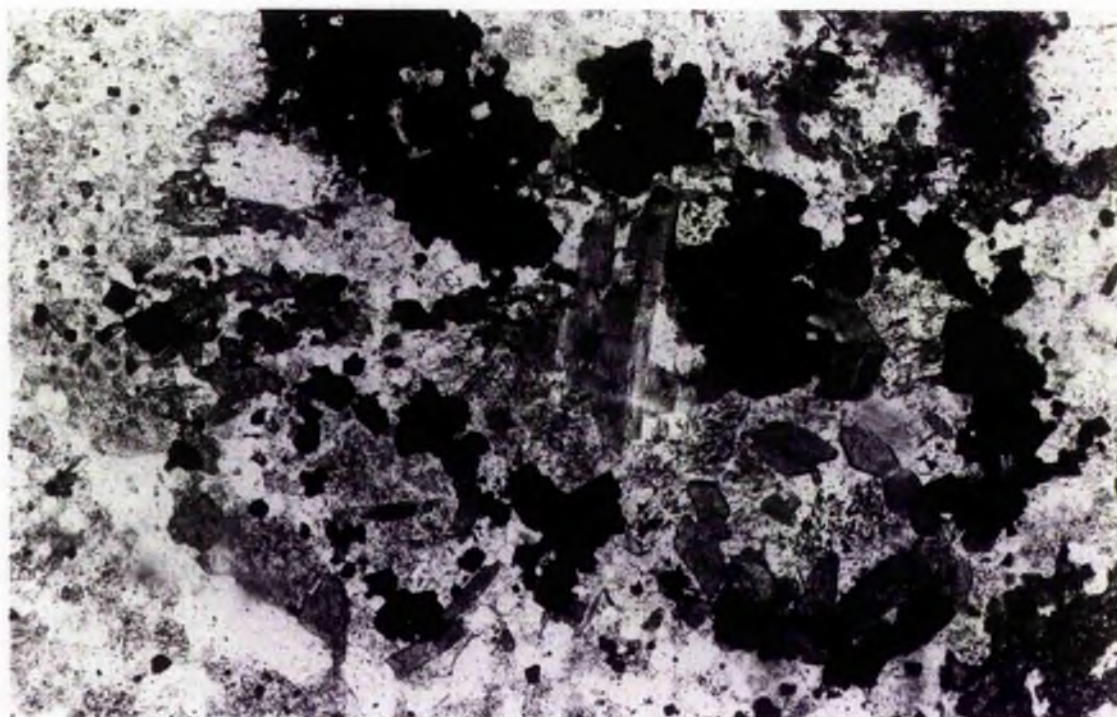


Plate 4.4H Titanomagnetite very often forms a complete or partial ring round other by-products of the hydrothermal degradation of calcic pyroxene or fayalite. Ferroedenite may be seen as laths or in good amphibole basal section in lower right corner. Quartz porphyry (T169). Plane polarised light.

1 mm

T169

In hand specimen the rock here is lighter in colour than that in the T168 locality, being light brown-grey (Plate 4.4D).

Microscopically, the dominant mafic phase in T169 is the amphibole, rather than the clinopyroxene. The amphibole consists of a well formed light turquoise-coloured ferroedenite and an unstable-looking ferroactinolite. The ferroedenite crystallises as slender prisms or laths (Plates 4.4E and 4.4F). These laths, often up to 0.38mm long, are usually congregated on sites of pre-existing pyroxenes. Co-existing by-products of the pyroxene replacement are granular crystals of titanomagnetite which are sometimes precipitated in such a way that they form a ring round a central congregation of ferroedenite laths (Plates 4.4G and 4.4H). Two other minerals found on the site of replacement are monazite and zircon. Monazite crystals up to 0.26mm long have been observed and the mineral itself could be strikingly abundant in some places. When ferroedenite forms plat-like crystals or tends to be massive, it invariably pseudomorphs pyroxene phenocrysts, with fluorite filling interstices.

Pyroxene is scarce. When found it occurs as 'islands' in the central areas of large altered phenocrysts. However these 'islands' show good optical and chemical characteristics. They are pale brown in colour and chemically have the most calcic composition found in the whole quartz porphyry suite.

Optical properties of the ferroedenite include: strong pleochroism, γ = light turquoise, β = green, α = yellow;

$\gamma > \beta > \alpha$; length-slow; birefringence moderate, maximum interference colour 1st Order red, body colour possibly masks interference colours; maximum extinction angle $\gamma \wedge c = 23^\circ$.

Feldspar phenocrysts still remain within the range of orthoclase, but in detail show evidence for a greater degree of Al/Si ordering than in T167 and T168.

The groundmass is appreciably recrystallised, with discrete crystals of albite in the recrystallised areas. The turbidity of the groundmass feldspars so far recorded to be very intense in all the three preceding localities, is almost cleared here in T169. This may be a consequence of the recrystallisation of the groundmass. On the other hand, while turbidity diminishes in the groundmass, the feldspar phenocrysts become even more turbid and almost completely brown.

T170

In hand specimen, this rock is the most light coloured of all the quartz porphyries. It is cream in colour, with pinkish-white alkali feldspar phenocrysts.

Microscopically, it is observed that there is a complete absence of pyroxene and fayalite. Instead there are two phases of amphibole crystallisation, namely ferrorichterite and ferroactinolite.

The ferrorichterite phase crystallises in multicrystalline aggregates of short euhedral prisms, and are associated with granular titanomagnetite. Ferrorichterite crystals and titanomagnetite grains located in one congregation appear to have been formed from the complete degradation of one pre-existing pyroxene or fayalite phenocryst. Optical properties of the ferrorichterite include: strong pleochroism, α = yellow, β = black, γ = dark greenish blue $\beta > \gamma > \alpha$. Birefringence is moderate, maximum interference colour is 1st Order yellow, but appears to have been masked by the strong absorption.

In orientations parallel to the c-axis its crystals show anomalous extinction. Ferrorichterite is also found in the groundmass as small scattered crystals.

The ferroactinolite forms large elongate crystals - these being pseudomorphs after initial pyroxene phenocrysts. The fibrous cleavage in the new amphibole pseudomorph gives it a pseudo-asbestiform habit in crushed rock samples. Separates from the crushed rock are distinctively greenish in colour and dull in appearance. Individual crystals look like bundles of discrete fibres cemented by a whitish substance (ref. Chapter 5, 5.4.6, equation (1)).

The above form of the ferroactinolite is an expression of the instability in the mineral; this instability being also seen in thin section by the lack of freshness in appearance. This contrasts strongly with the freshness of the ferrorichterite multicrystalline aggregates which have well defined crystal outlines and cleavage traces, uniform body colour and the absence of incipient alteration. Chemically the electron microprobe analyses of both the ferrorichterite and the ferroactinolite show a continuous compositional variation between the two.

Exsolution in the feldspars has reached the stage where enclaves of polysynthetically twinned albite can be readily distinguished in the perthite. Boundaries of individual feldspar phenocrysts cannot be distinguished, in plane light, from the general groundmass. Hitherto the brownish turbidity in the feldspar phenocrysts and that in the groundmass had always varied, with the groundmass being well defined. The Al/Si ordering of the feldspars here is the maximum obtained along the traverse, with phenocrysts giving a triclinicity (Δ) of 0.74, corresponding to intermediate microcline. The groundmass

is conspicuously re-crystallised, with discrete crystals of albite being abundant.

Important hydrothermal alteration localities outside the west-east traverse: T115 and T133 quartz porphyries

T115 is partially, while T133 is completely, altered, with the latter having a mineral assemblage and textures different from those obtained at the culmination (in T170) of the alteration observed along the west-east traverse.

T115 The rock is greyish-blue in hand specimen.

Microscopically, the three-phase assemblage of fayalite, pyroxene and secondary amphibole, is particularly well displayed.

The pyroxene is a zoned ferrohedenbergite, with a sharp colour contrast between a pale greenish-yellow non-pleochroic core of ferrohedenbergite and a bright green rim of sodian ferrohedenbergite which is pleochroic. Pleochroism in the rim is as follows: $\alpha = \beta =$ olive-green, $\gamma =$ yellowish-green. $\alpha = \beta > \gamma$. Difference in average extinction angles $\gamma \wedge c$ between the cores (45°) and the rims (60°) gives an average of 15° . Microprobe analyses of the pyroxenes give ferrohedenbergite compositions which plot in the most evolved field for the quartz porphyries (Chapter 5).

Fayalite occurring in T115 is also shown from microprobe analyses to be the most evolved of all in the quartz porphyry suite, with average fayalite end-member composition of $Fa_{99.3}$.

The pyroxene and fayalite phenocrysts are mantled by reticulate ferrichterite amphibole. The amphibole replaces some of the smaller mafic phenocrysts completely forming whole 'sponges' or massive cores with 'spongy' rims. All components of the new amphibole, whether wholly or partially spongy, are

2 mm



Plate 4.4.I Fayalite phenocryst rimmed by amphibole (dark).
Along most of its rim the alteration results in ferrichterite
but around titanomagnetite inclusions (?) within the fayalite,
alteration produces riebeckite. Hydrothermally altered quartz
porphyry (T115). Plane polarised light.

are observed to be in optical continuity. The ferrorichterite is dark green in plane light and strongly pleochroic from pale brownish-yellow to dark bluish-green. Birefringence is often masked by its strong colour absorption and the amphibole is also length-slow.

There is a localised crystallisation of secondary riebeckite around the titanomagnetite found in fayalite phenocrysts (Plate 4.4I). The riebeckite has a distinctive indigo-blue colour. The localised crystallisation of riebeckite around inclusions of titanomagnetite inside fayalite phenocrysts has also been recorded elsewhere in the quartz porphyry transition series (eg. in T167). On the periphery of the fayalite, or along its fracture planes, ferrorichterite however remains the dominant amphibole. The chemical control for the divergent amphibole formation suggested by the local occurrence of riebeckite is discussed further under Mineral Chemistry. The mineralogical control appears to be the presence of titanomagnetite and fayalite.

Feldspar phenocrysts in T115 have not been analysed by X-ray methods. Optically, however, they have been identified as orthoclase. Turbidity occurs prominently along phenocryst edges and cleavage traces and assumes the normal brown colour observed elsewhere.

The groundmass in T115 is so fine-grained that the average grain-size is about one-tenth of that in other quartz porphyries. There are occasional shards and pumice fragments; these show broad folding round the phenocrysts. Folding of this nature is a feature almost exclusively characteristic of the strongly welded tuffs.

The preservation of its original welded groundmass texture provides evidence for the genetic link between the quartz

2mm

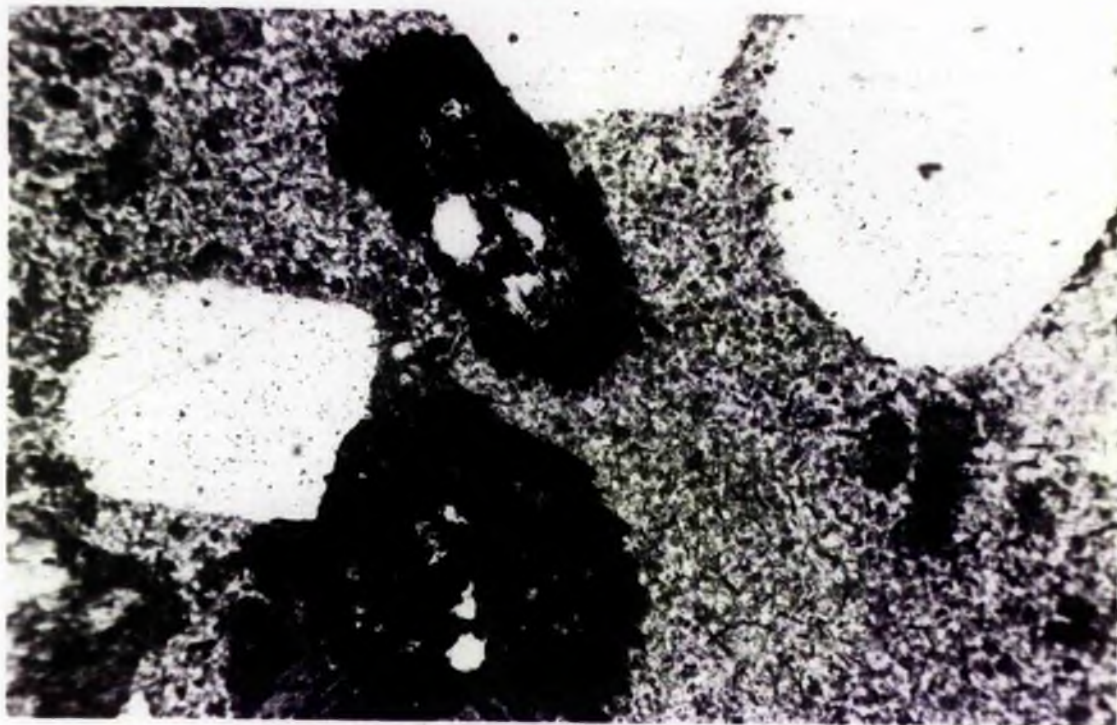


Plate 4.4J Pseudomorphs of spongy ferrichterite (dark) after ferrohedenbergite and fayalite. Acicular crystals of ferrichterite are abundant in the groundmass. Ferrichterite quartz porphyry (T133). Plane polarised light.

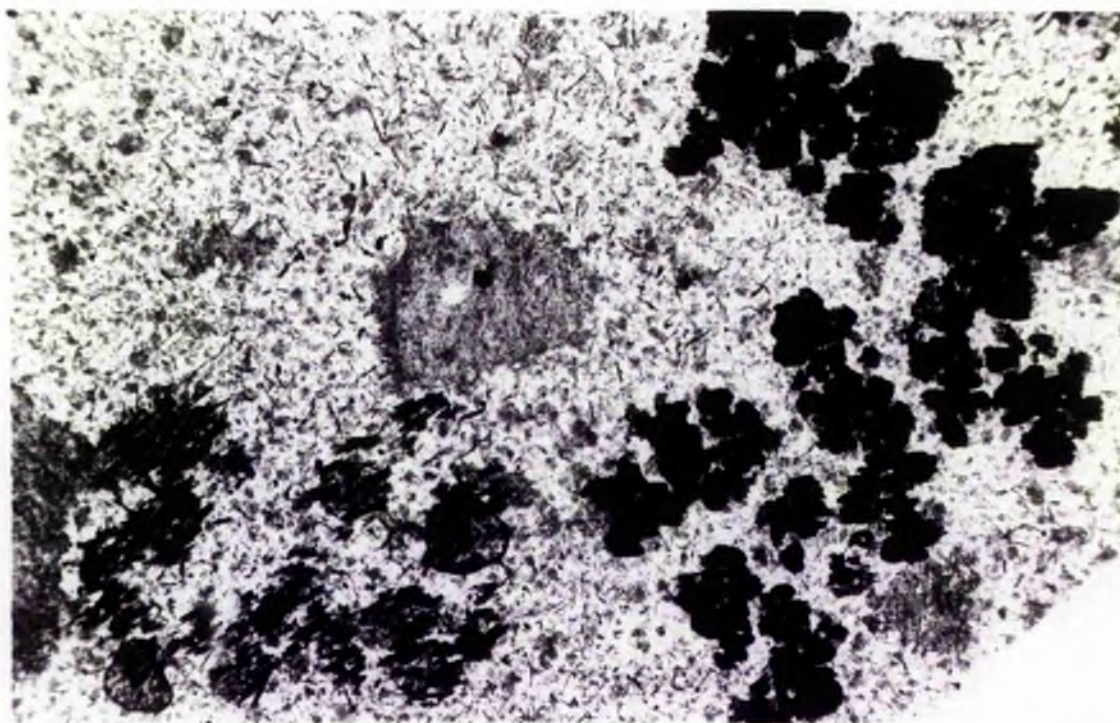


Plate 4.4K Spongy ferrichterite range in texture from those shown in Plate 4.4J to that seen here (right), and to 'bristles' and 'brushes' (left). Note the constant presence of the acicular crystals of same amphibole in the groundmass. Ferrichterite quartz porphyry (T133). Plane polarised light.

2mm

porphyries and the welded crystal tuffs.

T133 This locality represents the only facies of the quartz porphyry hydrothermal alteration in which a single amphibole species is the sole mafic phase.

In hand specimen it is blue in colour. Microscopically this distinctive blue colour can be seen to be due to the presence of numerous reticulate masses, 'sponges', 'bristles' and 'brushes' of blue ferrorichterite amphibole. Although no traces of pre-existing minerals are left, certain forms and shapes of the new amphibole are reminiscent of the fayalite and pyroxene phases encountered in the pristine and transitional rocks of the series (Plates 4.4J and K).

Feldspar phenocrysts are largely or entirely brown and turbid; microperthitic exsolution textures can be observed. By X-ray, these phenocrysts are found to have Al/Si ordering of the orthoclase range, more ordered than T169 though definitely less than T170.

Opaque oxides are restricted in occurrence in this rock and when present are found in the vicinity of the new amphiboles.

The general blue colour of the rock is also partly due to the pervasive crystallisation of acicular crystals and wisps of the same ferrorichterite in the groundmass. The amphibole is strongly pleochroic as follows: α = pale brownish-yellow, β = blue-black, γ = dark green-blue, $\beta > \gamma > \alpha$. The groundmass itself is thoroughly re-crystallised. In it turbid K-feldspar and twinned albite appear as discrete phases. The formation of the acicular groundmass phases of the amphibole is thought to be contemporaneous with the groundmass re-crystallisation.

4.4.4 The granite porphyry

Hand specimen description The rock is coarsely porphyritic and when fresh, greyish-green in colour. There is a general tendency for this colour to change within a short time, apparently on account of the rapid rate of surface oxidation. In the field therefore the granite porphyry is more familiar as a brownish, rather than greenish, rock.

The phenocrysts constitute about 40 percent by volume of the rock and consist of alkali feldspar, quartz, and mafic minerals. Phenocrysts of alkali feldspar are the most conspicuous in size and abundance, are generally euhedral to subhedral in form, and up to 18x11 millimetres in size. Quartz phenocrysts do not often exceed 7 millimetres in diameter and occur as bipyramidal prisms with round cross-sections. Mafic phenocrysts are found as dark specks interspersed among the larger felsic phenocrysts. The largest mafic crystal recorded was 5x2 millimetres in size but the average is generally less than 2mm long.

Microscopic features The alkali feldspar phenocrysts consist mainly of orthoclase cryptoperthites. These phenocrysts are commonly rimmed by greyish or brownish turbid zones which invariably penetrate the crystal along cleavages and fractures. Within these turbid areas slight unmixing to microperthite is apparent.

Some of the feldspar phenocrysts usually form a glomeroporphyritic texture which is evident even on smooth surfaces of hand specimens.

The principal mafic minerals are ferroaugite and ferrohedenbergite in continuous compositional variation which may be optically displayed in zoned crystals: generally a pale

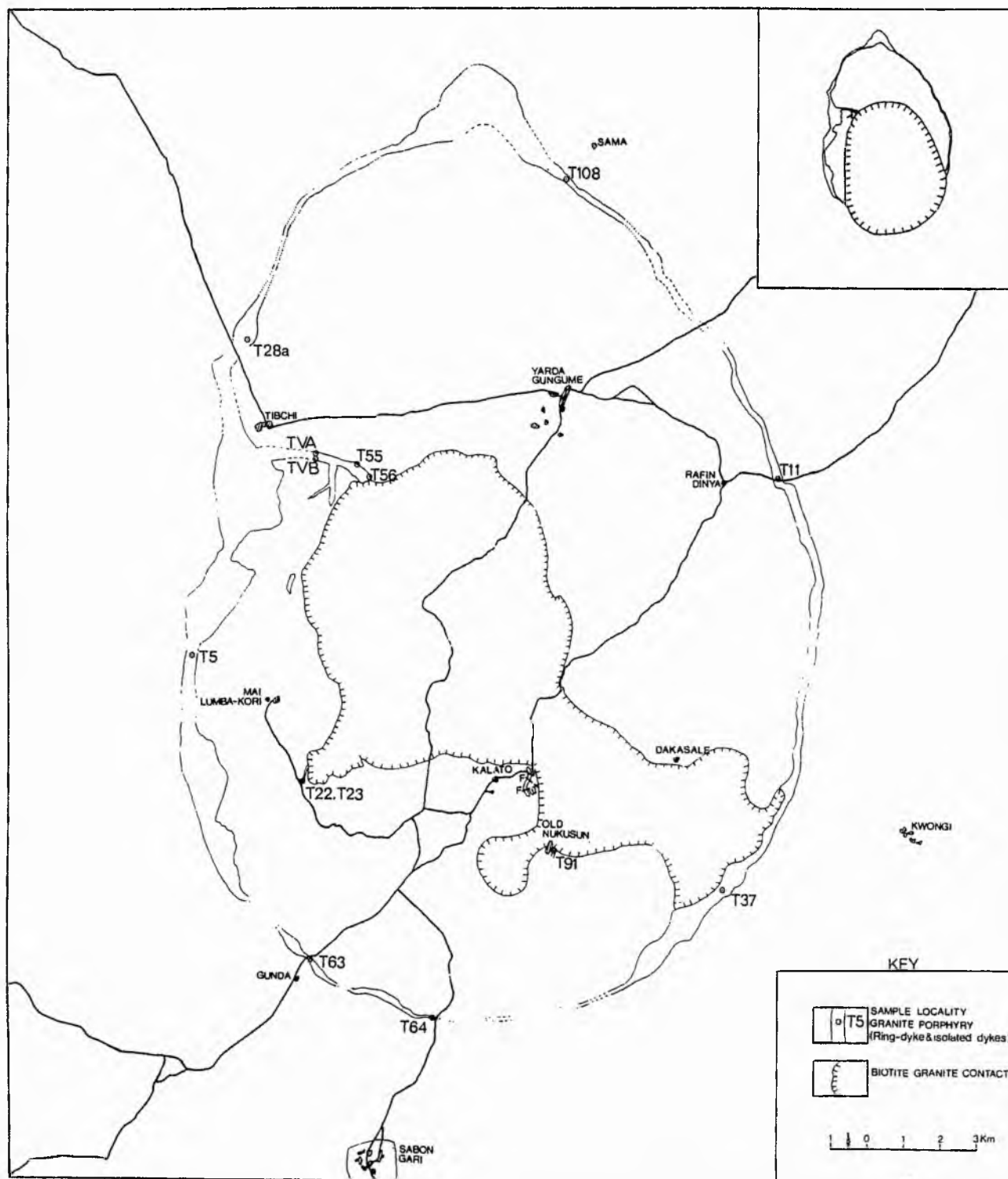


Figure 4.4.L Sample localities, granite porphyry (ring-dyke and isolated minor dykes). Inset illustrates concept of the subsurface eccentricity of the biotite granite relative to the earlier granite porphyry ring-dyke. This eccentricity is correlated with observed petrographical variation in the southern sector of the ring-dyke (see text).

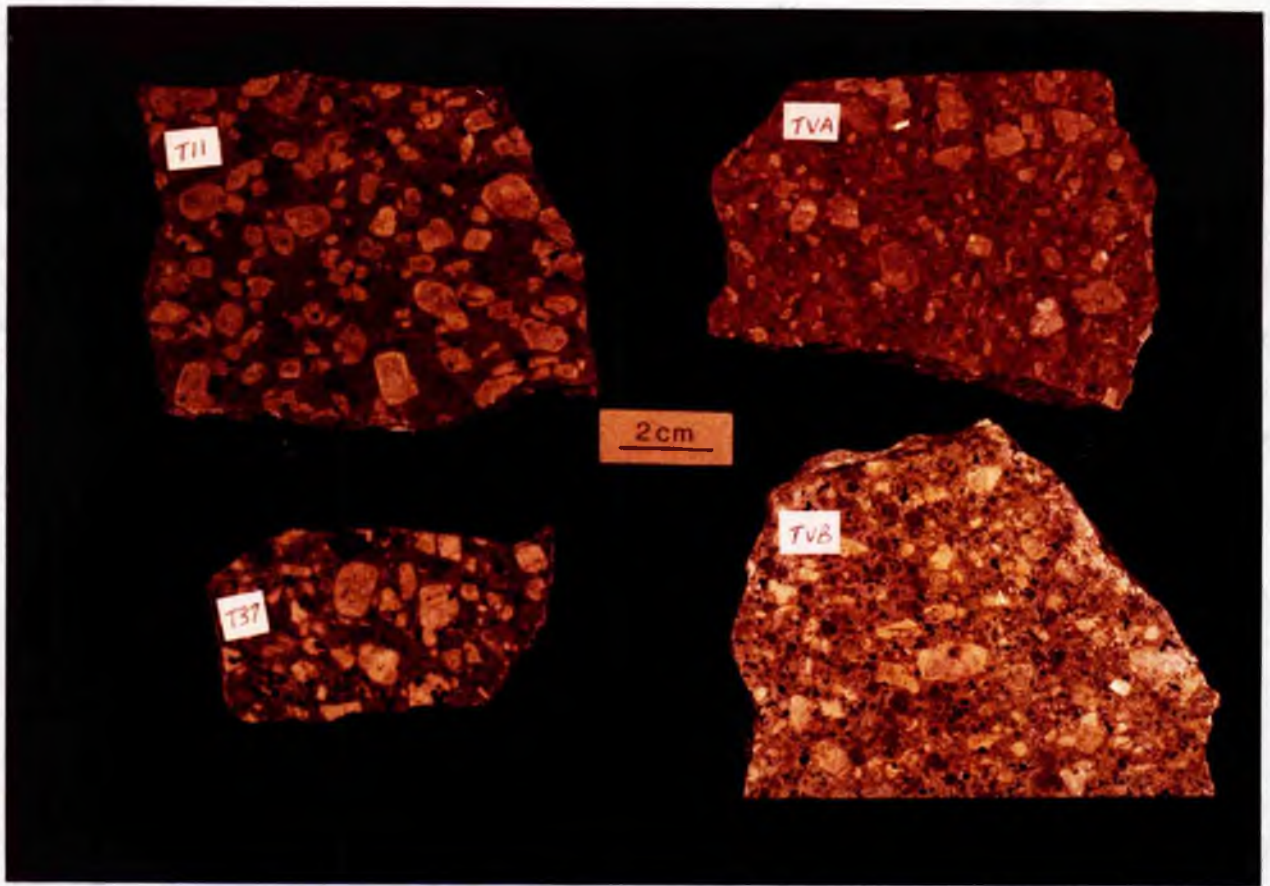


Plate 4.4NX Colour variation in samples from the granite porphyry ring-dyke. T11 is an unaltered specimen. Others are hydrothermally altered and referred to in the text.

brown ferroaugite transitional to a pale greenish-brown ferrohedenbergite. In other cases the latter may be found as the core to bright-green sodian ferrohedenbergite rim.

The groundmass is relatively coarse (ref. the quartz porphyries). Individual grains are up to 0.5x0.2mm in size and consist mainly of alkali feldspar and quartz. The texture of the groundmass varies, from equigranular crystals in some samples, to graphic intergrowth between feldspar and quartz, in others.

Accessory minerals include ilmenite, monazite, zircon, fluorite and apatite. Some of these minerals may be found as inclusions in the pyroxene, and feldspar, phenocrysts and may thus represent some of the earliest crystalline phases in the acid magma.

Localised variations in the petrography of the granite porphyry ring-dyke attributable to a restricted hydrothermal alteration zone

The western, northern and eastern sectors of the granite porphyry ring-dyke (Figure 4.4L) conform with the general petrographic description outlined above. In contrast, the southern sector has been observed to depart significantly from the general textural and mineralogical character. Apophyses of the ring-dyke, which branch into and cut the quartz porphyries on the north-western margin of the biotite granite, are hydrothermally altered along with the quartz porphyries. These changes are similar to those reported earlier for the quartz porphyries, involving essentially the degradation of the mafic minerals, Al/Si ordering of alkali feldspars, and recrystallisation of the groundmass. Consequently only the most essential

5mm

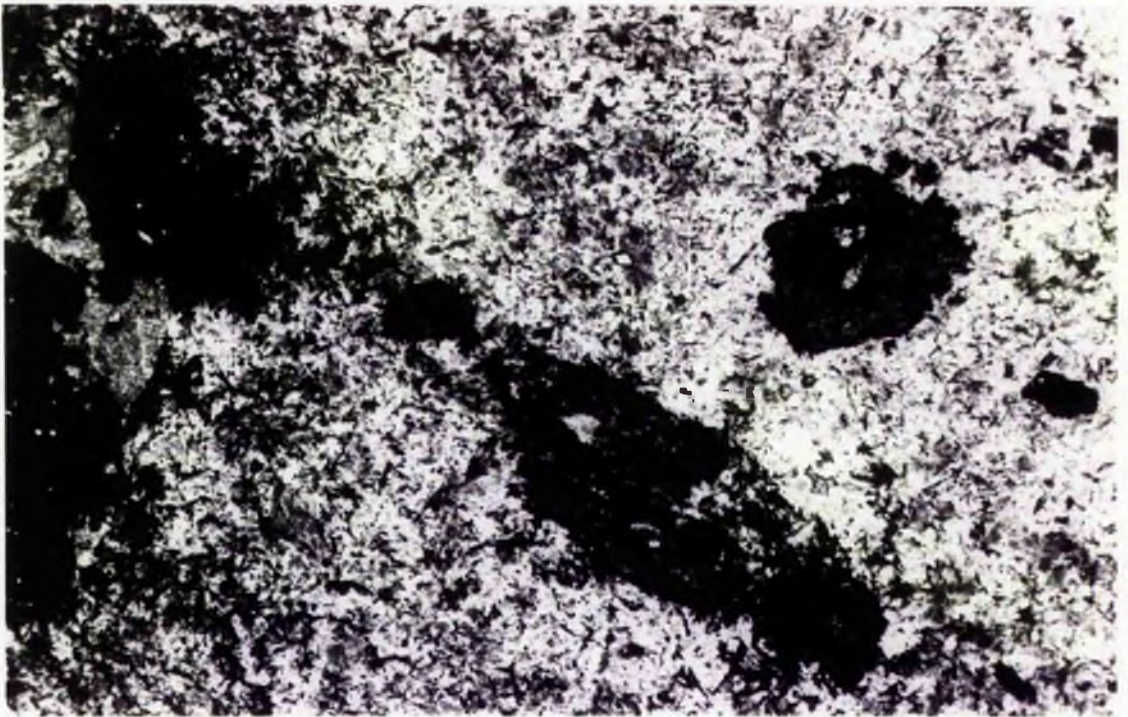


Plate 4.4.M Pseudomorphs of sodic pyroxene presumably after ferrohedenbergite. Note concentration of acicular crystals in the groundmass. Each pseudomorph consists of a multicrystalline aggregate of small individual grains of the sodic pyroxene. Hydrothermally altered locality (T64) of the granite porphyry ring-dyke.

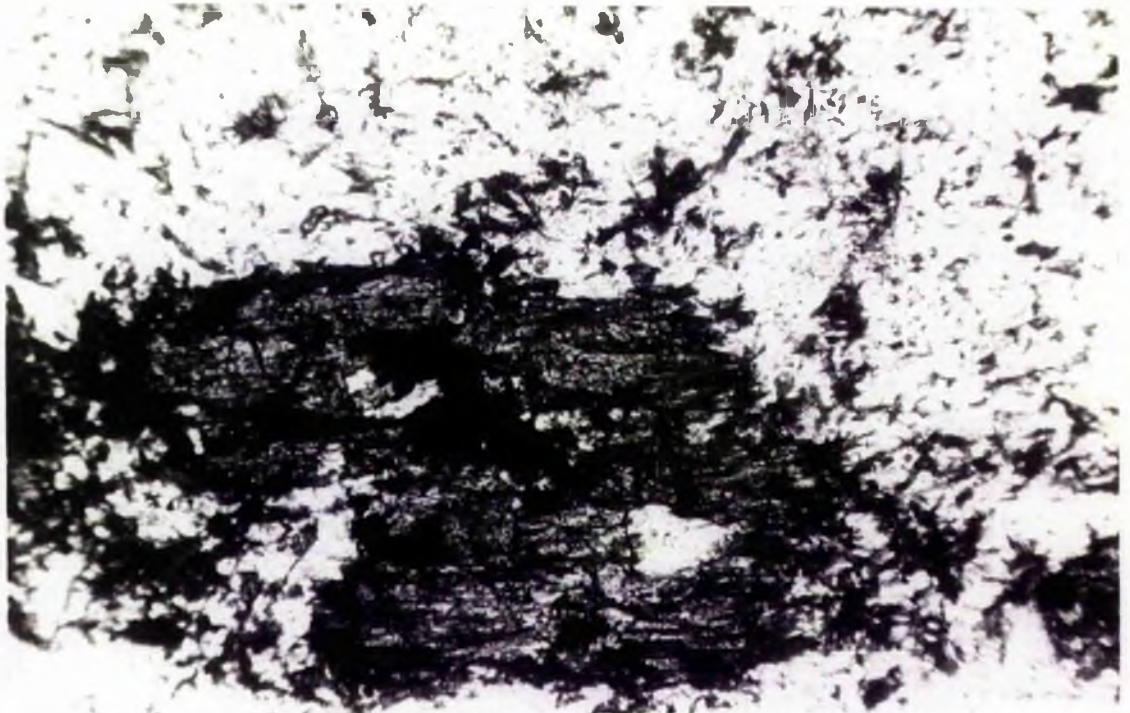


Plate 4.4.N Part of the lower central pseudomorph in Plate 4.4M magnified to show textural relationship between the sodic pyroxene and fringing blue amphibole. Most of the pseudomorph (with high relief) is sodic pyroxene, tuft-like fringe (low relief) is blue amphibole. Plane polarised light.

2mm

details will be necessary in the following descriptions of the alterations.

The Southern Sector of the Ring-dyke The 'southern sector' of the ring-dyke implied here may be defined as extending from a point near Gunda village in the south-west to another point near Kwongi village in the south-east.

Near Gunda, the pyroxene phenocrysts break down to an orange-yellow alteration product on which fresh-looking laths and plates of a dark bluish-green amphibole grow in multicrystalline aggregates. The amphibole is strongly pleochroic from violet-blue to pale yellow and dark bluish-green. The strong absorption impairs its low birefringence and masks its interference colours, as a result of which optical identification is difficult. Feldspar phenocrysts are usually brown and turbid. In the groundmass, granophyric intergrowth of quartz and alkali feldspar is prominently developed and may be conspicuously nucleated along the margins of the quartz and alkali feldspar phenocrysts. Discrete grains of albite may also be found.

At a second locality (T64) near the intersection of the Sabon Gari road with the ring-dyke, the granite porphyry is chilled and the ring-dyke is very thin. Multicrystalline aggregates of optically identified sodic pyroxene occur as pseudomorphs, most probably after original Ca-rich clinopyroxene phenocrysts (Plates 4.4M and 4.4N). These new sodic pyroxene crystals are in turn replaced along their margins by tufts and wisps of a blue amphibole. In the groundmass, both acicular amphiboles and stellate aggregates of the sodic pyroxenes and amphiboles, have been observed, the latter group nucleating along the rays of spherulites. The following

optical properties of the sodic pyroxene have been observed: strongly pleochroic: α = green, β = yellowish-green, γ = yellow; $\alpha > \beta > \gamma$; length-fast; strongly birefringent, maximum interference colour, 3rd Order red; $\alpha \wedge c = 17^\circ$. Optically this appears to be aegirine-augite.

A third locality (T37) located in the south-east near Kwongi is distinctive by virtue of having ferroedenite amphibole as the only mafic mineral in the rock. This amphibole crystallises in multicrystalline aggregates on sites of initial Ca-rich clinopyroxenes, and as large anhedral crystals. Evidence for the clinopyroxene precursor comes not only from the unaltered granite porphyry petrography given earlier, but also from the small granite porphyry dyke (T91) near Nukusun. Here ferroedenite amphibole partially replacing the pyroxene is preserved. Anhedral amphiboles in T37 are observed to have extensions penetrating into fractures in the quartz and feldspar phenocrysts.

Apophysis of the ring-dyke The apophysis of the ring-dyke south of Tibchi village is partially altered along a linear zone (TVB, Figure 4.4L)* adjacent to the hydrothermally altered quartz porphyries. Its exterior margin (TVA) is less altered. TVB has identical petrographic features with the ferrorichterite quartz porphyry (T133) including the characteristic occurrence of ferrorichterite as the only mafic phase.

Discussion: Petrographical changes in the hydrothermal alteration of the porphyries are inseparable from other criteria used in characterising the alteration. The petrographical data obtained in this chapter will be used,

* See also Plate 4.4NX

together with data from amphibole chemistry (Chapter 5) and rare-earth element chemistry (Chapter 6), in establishing the role of the hydrothermal alteration process in the petrogenetic scheme (Chapter 7).

The restriction of the hydrothermal modification of the granite porphyry ring-dyke to the southern sector of the dyke, is explicable by the concept of the subsurface displaced position of the biotite granite intrusion relative to the centre of the ring-complex as defined by the ring-dyke (Figure 4.4L). This concept has been discussed in Chapter 3.

The biotite granite outcrops south-easterly and may at depth extend southwards, possibly beyond the present confines of the ring-dyke. The observed increase in the hydrothermal alteration of the quartz porphyries as the biotite granite is approached, provides additional evidence for the structural control of the hydrothermal alteration process, and may perhaps be a pointer to the biotite granite as the petrological agent.

The petrological concept of the alteration is that fluid phase(s) associated with the cooling of the biotite intrusion, may be sufficient to cause the localised textural and mineralogical variations in the altered rocks. The nature of the fluid phase(s) is considered in Chapter 6.

Thus both the structural and petrological concepts individually, and together, focus on the biotite granite intrusion.

10 mm

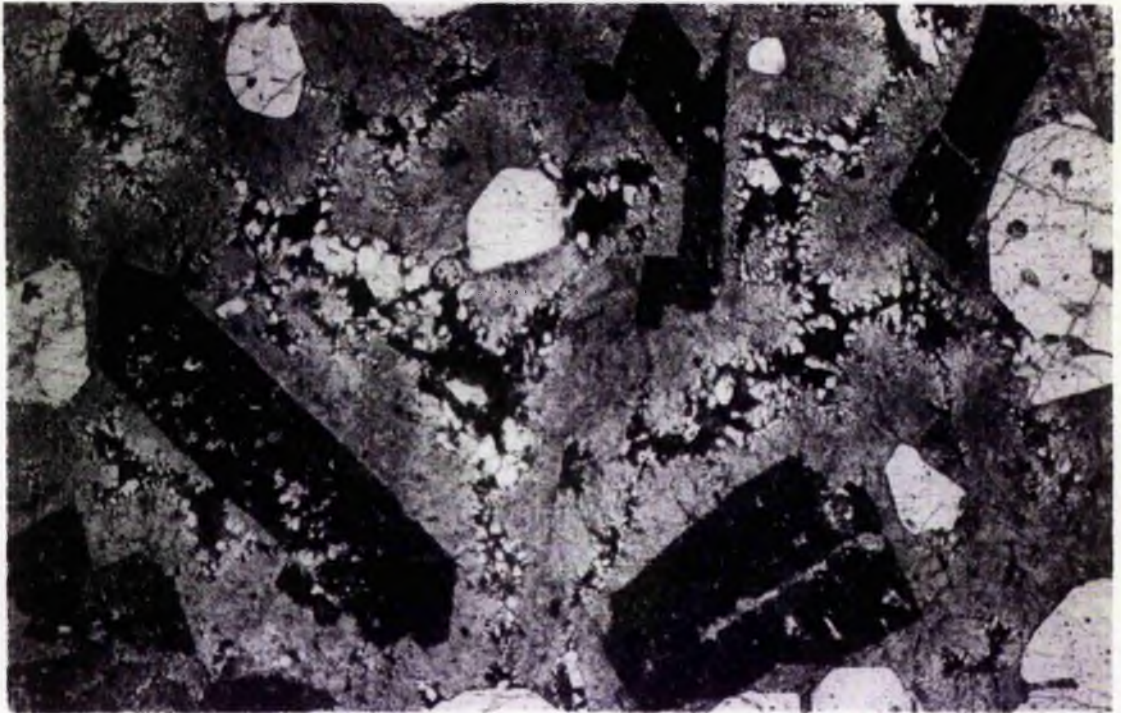


Plate 4.4P Perthite phenocrysts pseudomorphed by siderophyllite (dark). In the groundmass, dark, branching areas consist of siderophyllite selectively replacing alkali feldspar. (White = quartz) Granite porphyry (T23). Plane polarised light.



Plate 4.4R A portion of a siderophyllite pseudomorph magnified. Note isolated pockets with genthelvite (high relief), quartz (white, low relief) and opaque iron oxide (black).

2 mm

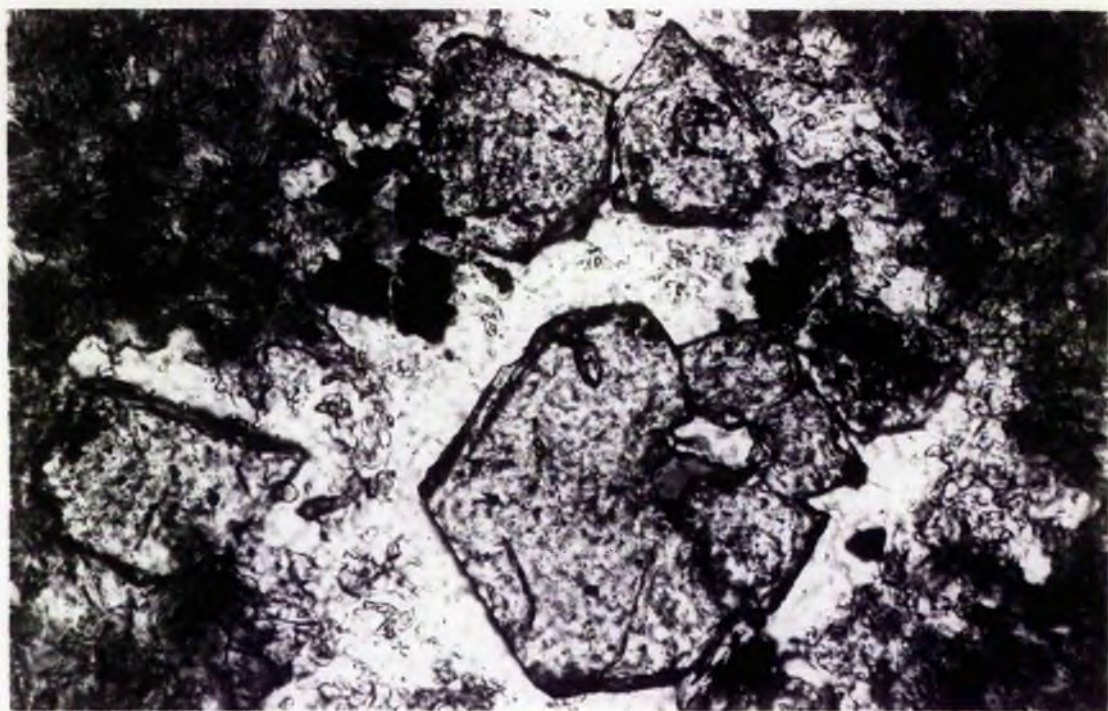


Plate 4.4T Genthelvite (high relief) in quartz pocket within siderophyllite pseudomorph of alkali feldspar phenocryst in Plate 4.4R. Dark grey = multicrystalline siderophyllite aggregate. White = massive quartz. Black = opaque iron oxide.

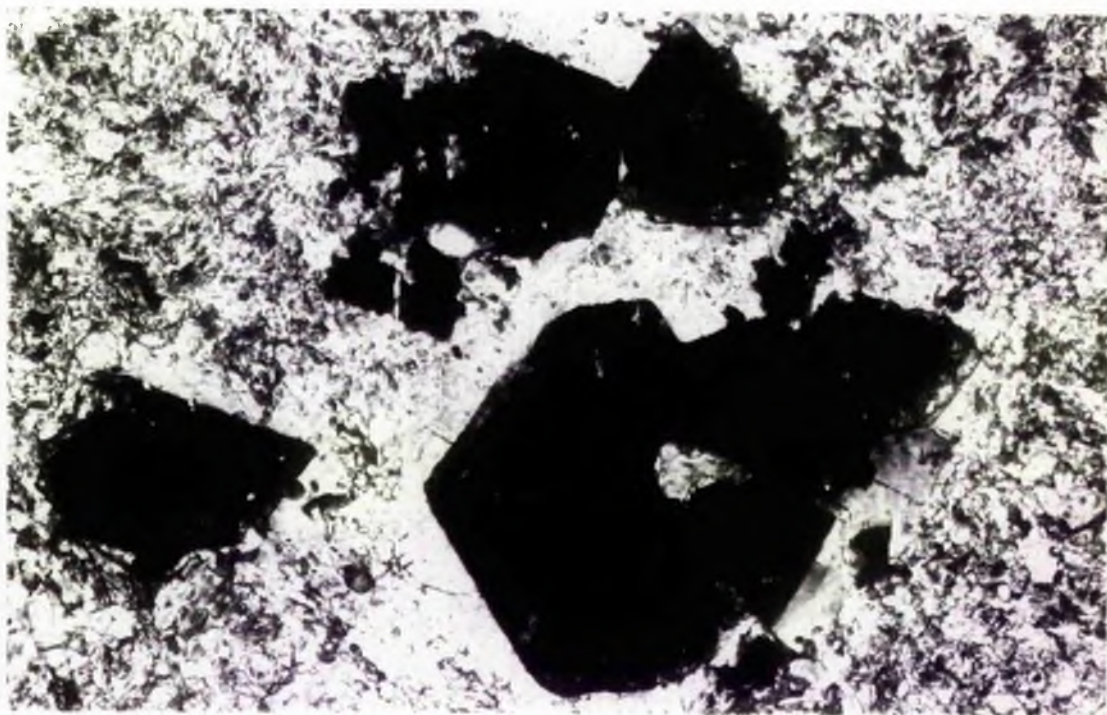


Plate 4.4W Same as Plate 4.4T, crossed polarised light.

Petrographical changes in the siderophyllitic metasomatic alteration of a granite porphyry dyke near Mai Lumba-Kori

A minor isolated granite porphyry dyke south-east of Mai Lumba-Kori (Figure 4.4L) is truncated at its northern extremity by the biotite granite, and is located for most of its remaining length on a flat-topped hilly outcrop. The southern extremity of the dyke is exposed on a slope, and on the cross-sectional view of the dyke thus displayed, can be seen, a prominent black replacement vein roughly bisecting the dyke and also associated with smaller parallel veins on both sides of it. The black central zone of each vein is transitional outward to a yellowish-grey peripheral zone, these being sampled as the more altered zone (T23) and less altered zone (T22) respectively.

The normal textural characteristics of the granite porphyry are still largely preserved in T22 while only the characteristic bi-pyramidal quartz phenocrysts can be seen macroscopically in T23.

Microscopically it is observed in the less altered zone (T22) that chlorite has replaced groundmass feldspars and has permeated cleavages and fractures in the feldspar phenocrysts. In the more altered zone (T23), siderophyllite has replaced both groundmass and phenocryst feldspars (Figure 4.4P and 4.4R). The metasomatic nature of the replacement can be seen from the preservation of the original euhedral forms of the feldspars. Each of these pseudomorphs consists of extremely minute individual siderophyllite crystals

(0.13x0.02 millimetres maximum size). Metamict zircon is common in the siderophyllite pseudomorphs and cloudy pleochroic haloes related to these zircons can be seen sometimes as protracted trails. Apart from remnant alkali feldspars, the rock consists of only siderophyllite and quartz, with zircon as the only accessory. Optical properties of the siderophyllite include: strong pleochroism, α = pale yellow, $\beta = \gamma$ = greenish-yellow, $\beta = \gamma > \alpha$; moderate birefringence, maximum interference colour, 2nd Order red.

In one thin section from elsewhere in the more altered zone, a dark green siderophyllite is also present (in addition to that described above) and in this green variety are found scattered pockets containing quartz, genthelvite and opaque iron oxide (Plates 4.4R, T, W).

In summary, the above metasomatic alteration is marked by the loss of almost all essential mineral constituents except quartz, and the pervasive presence of siderophyllite particularly replacing alkali feldspar. The reaction sequence appears to end with the formation of quartz, genthelvite, and iron ore.

4.4.5 Cognate enclaves in the quartz porphyries and the granite porphyry ring-dyke

Broadly the same group of inclusions of pre-existing rocks has been recorded in both the quartz porphyries and the granite porphyry. The similarity in the species of inclusions and the common structural control for emplacement through the ring-fracture and related fissures (Chapters 2 and 3) appear to be related aspects in the link between the quartz porphyries and

the present granite porphyry ring-dyke.

Xenoliths found in the quartz porphyries and the granite porphyry are mostly fragments of earlier basalts, rhyolites and pyroclastic rocks. These xenoliths are usually contact-metamorphosed. Chilling of the quartz porphyries and granite porphyry against these xenoliths is also apparent in some cases. At least the interphase between the xenoliths and the host rocks is well defined.

On the other hand, there is a group of inclusions found in the two porphyries which display different contact relationships with the porphyry host rocks. These inclusions show a very close and progressive petrographic relationship among themselves on the one hand, and with the porphyries on the other. Contacts between them and the porphyries are diffuse and irregular. These enclaves are thus considered to be cognate, and perhaps served as petrogenetic precursors to the porphyries. The following petrographic descriptions of these enclaves are divided according to the two types:-

(1) Fayalite ferroaugite microferrodiorite enclaves

In the hand specimen of a porphyry the fayalite ferroaugite microferrodiorite is seen as a fine-grained enclave, usually less than two centimetres across, and darker in colour than the host rock.

In thin section the enclaves (Plates 4.4X, Y, Z) show the following features. Constituent minerals are fayalite (Fa_{92}), ferroaugite, plagioclase (An_{32}), apatite and ilmenite.

Fayalite up to 1.5×0.5 mm has been found, but is generally less on average. Composition of the fayalite (Fa_{92}) has been obtained using the electron microprobe; the relatively more

2 mm

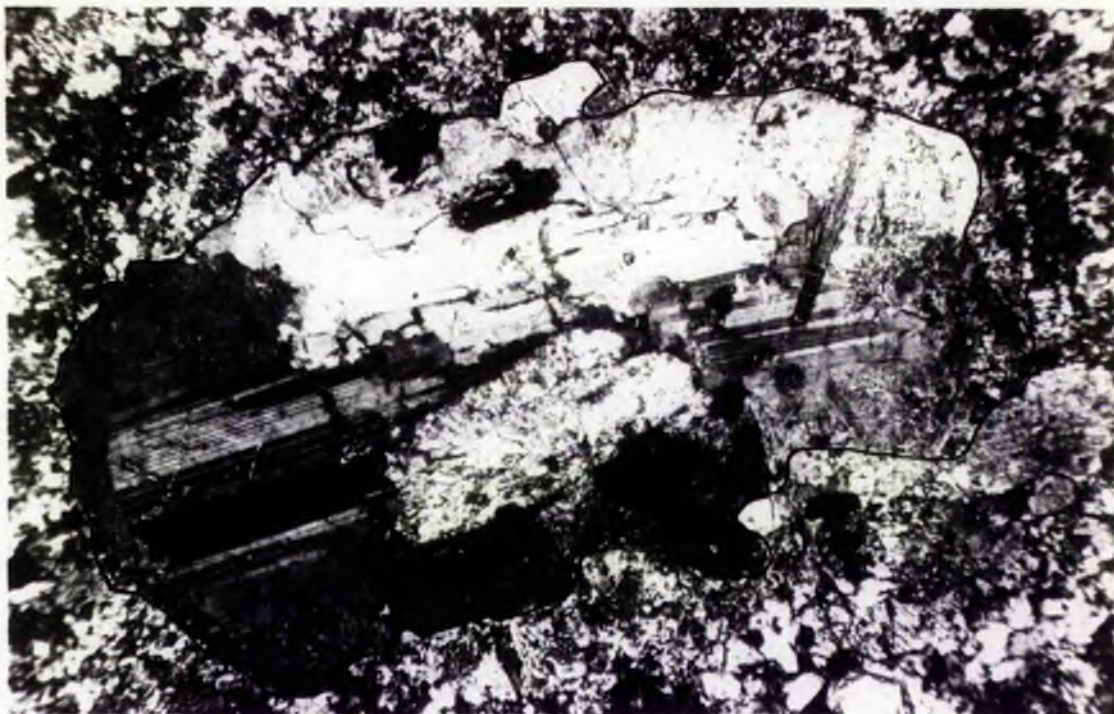


Plate 4.4X Fayalite ferroaugite microdiorite enclave (outline traced) in fayalite ferrohedenbergite quartz porphyry (T105). Fayalite = centre dark; anti-rapakivi plagioclase shows rim of homogeneous alkali feldspar; ilmenite = black. Crossed polarised light.

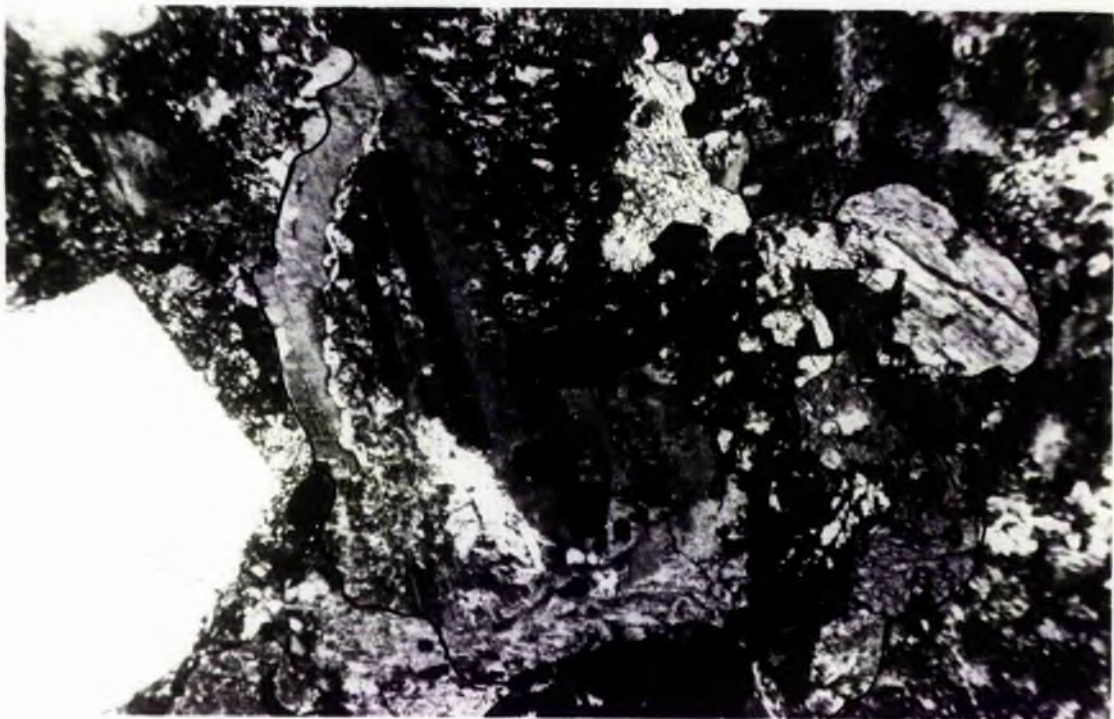


Plate 4.4Y Similar enclave as in Plate 4.4X. Fe = ferroaugite. Below F-f line, fayalite crystals. Crossed polarised light.

2 mm

5mm



Plate 4.4Z Microferrodiorite enclave in fayalite pyroxene quartz porphyry (T60) with ferroaugite (G) interstitial to plagioclase (P). Crossed polarised light.

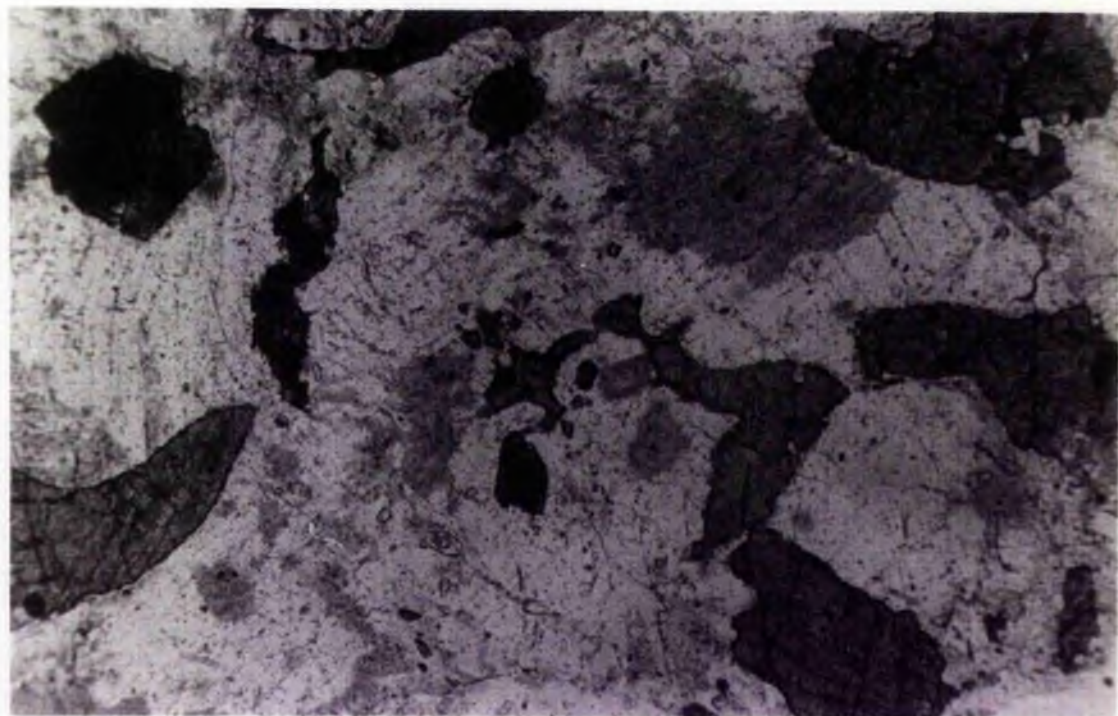


Plate 4.4Z(i) Part of the enclave in Plate 4.4Z magnified and shown in plane light. Note zig-zag habit of central ferroaugite (dark-grey) resulting from interstitial crystallisation.

2mm

1 mm



Plate 4.4Z(ii) Fayalite crystals in a protracted interstitial crystallisation relative to earlier plagioclase (white). Fayalite ferroaugite microferrodiorite enclave in fayalite ferrohedenbergite quartz porphyry (T105). Note abundance of apatite needles. Plane polarised light.



Plate 4.4Z(iii) Fayalite (eg. two crystals arrowed, top left quadrant) crystallised as discrete yet interstitial grains to earlier plagioclase crystals (white, and black right). Ferroaugite (E) is also interstitial. Same type of enclave as in Plate 4.4(i) and located in the same quartz porphyry (T105). Plane polarised light.

2 mm

magnesium rich composition compared with the range (Fa₉₇ to Fa₉₉) in the quartz porphyries, is noteworthy. Fayalite occurs as discrete grains and as interstitial crystals between plagioclase crystals (Plates 4.4Z(ii), (iii)).

Ferroaugite crystals are pale brown in plane light and are irregularly shaped, with extensions to interstice between plagioclase grains (Plates 4.4Z, 4.4Z(i)). Although colour zoning in the ferroaugite is doubtful, extinction zoning in crossed polars is conspicuous. The core consistently has the smaller extinction angle ($\gamma \wedge c$) than the rim, in all measured crystals:

Average $\gamma \wedge c$ in the rim	= 50.1°
Average $\gamma \wedge c$ in the core	= 44.5°
Mean difference	= 5.6°

Birefringence in the ferroaugite is moderate, maximum interference colour is 1st Order yellow. The ferroaugite has been identified from microprobe analyses, but only the cores of individual grains were analysed.

The plagioclase is anhedral, up to 2.3 millimetres across and very finely twinned. The most remarkable character of the plagioclase is the constant rim in nearly all crystals, of homogeneous (untwinned) and turbid K-feldspar (Plates 4.4X, Y), this being a typical anti-rapakivi texture (cf. Vorma, 1971). The plagioclase is often partially altered in its core to minute aggregates of sericitic mica. The composition of the plagioclase (An₃₂) was obtained by the Michel-Levy symmetrical extinction method (Heinrich, 1965) but in one suitable grain only. The K-feldspar rim is important to the extent of forming less than one-third of the modal proportion (visual

2 mm

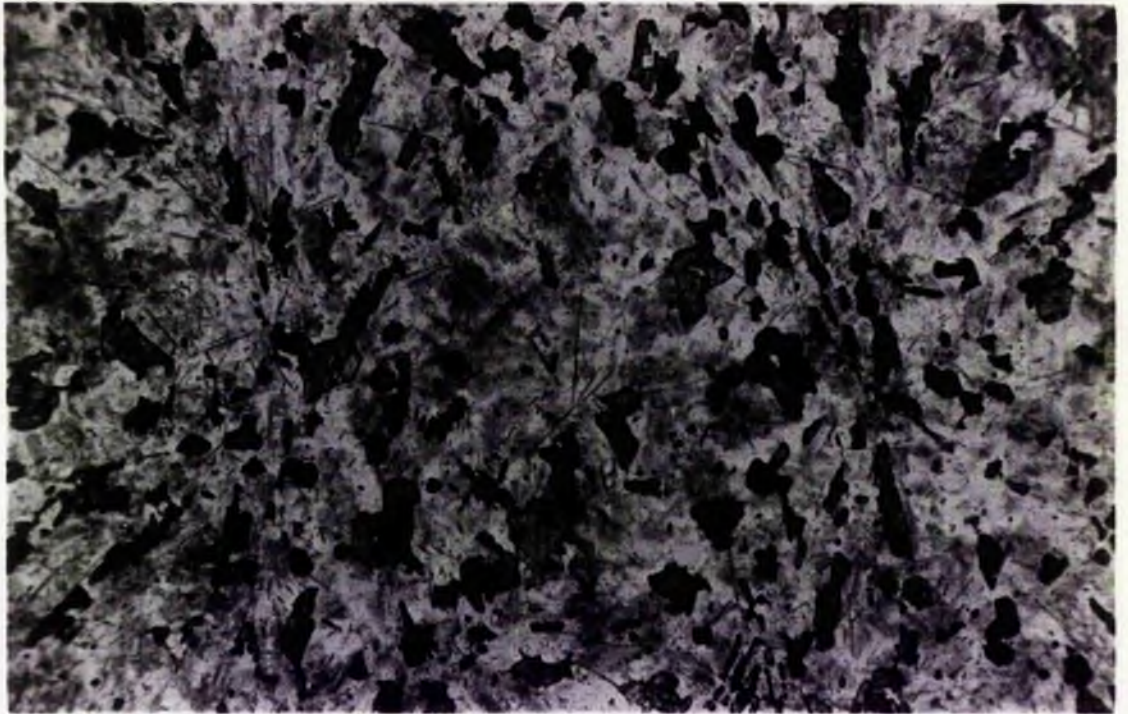


Plate 4.4.2A Skeletal ferrohedenbergite crystals nucleated along rays of spherulitic intergrowths in pyroxene microsyenite enclave. Granite porphyry ring-dyke (T11). Needles of apatite are abundant. Plane polarised light.

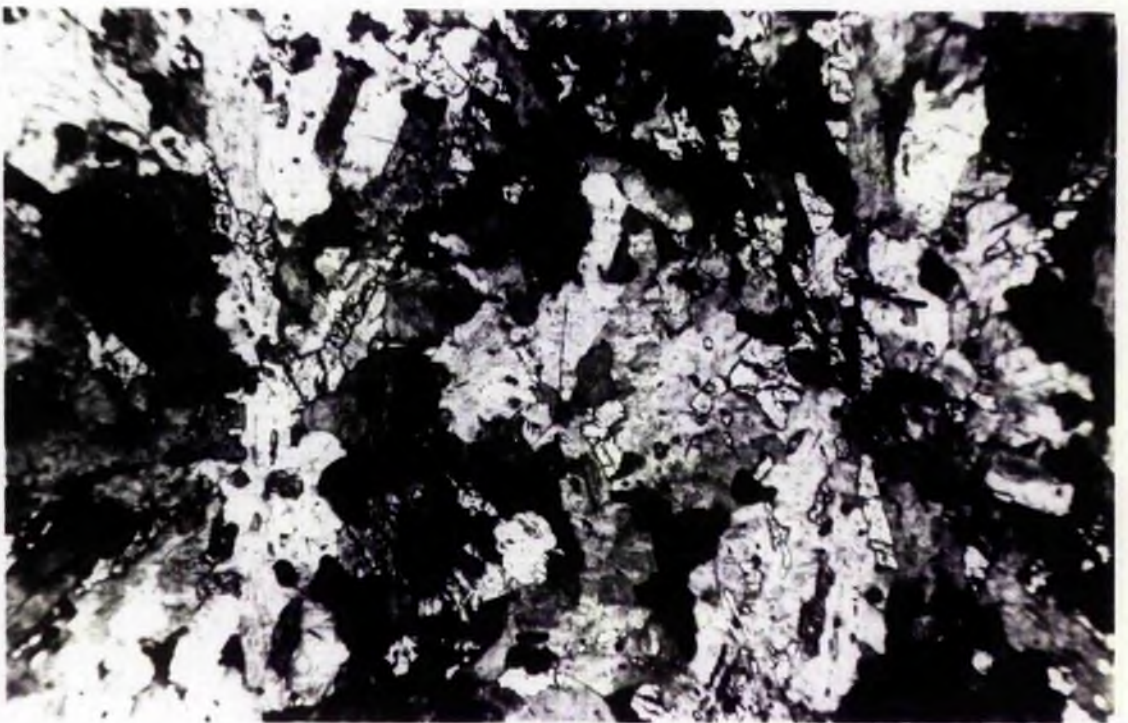


Plate 4.4.2B Same as Plate 4.4.2A, crossed polarised light. Spherulites consist of anti-rapakivi plagioclase.

2 mm

0.5 mm

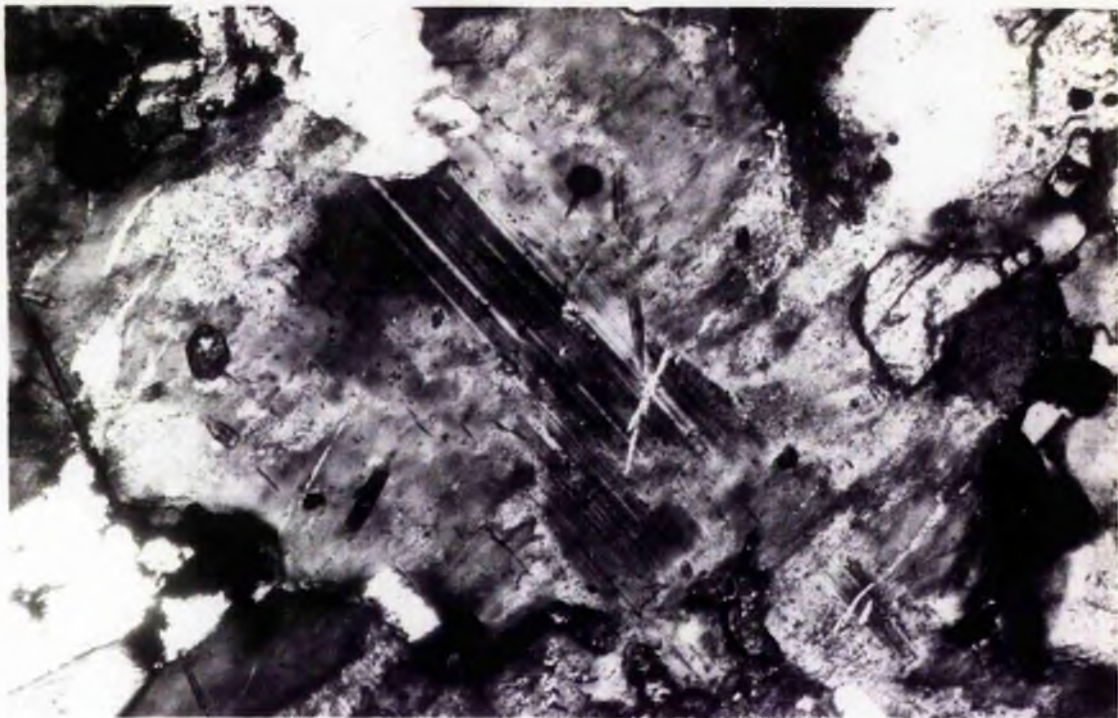


Plate 4.4.2D Anti-rapakivi plagioclase in Plate 4.4.2C, magnified. Crossed polarised light. (Plagioclase = twinned, dark grey; alkali feldspar untwinned, light grey.)

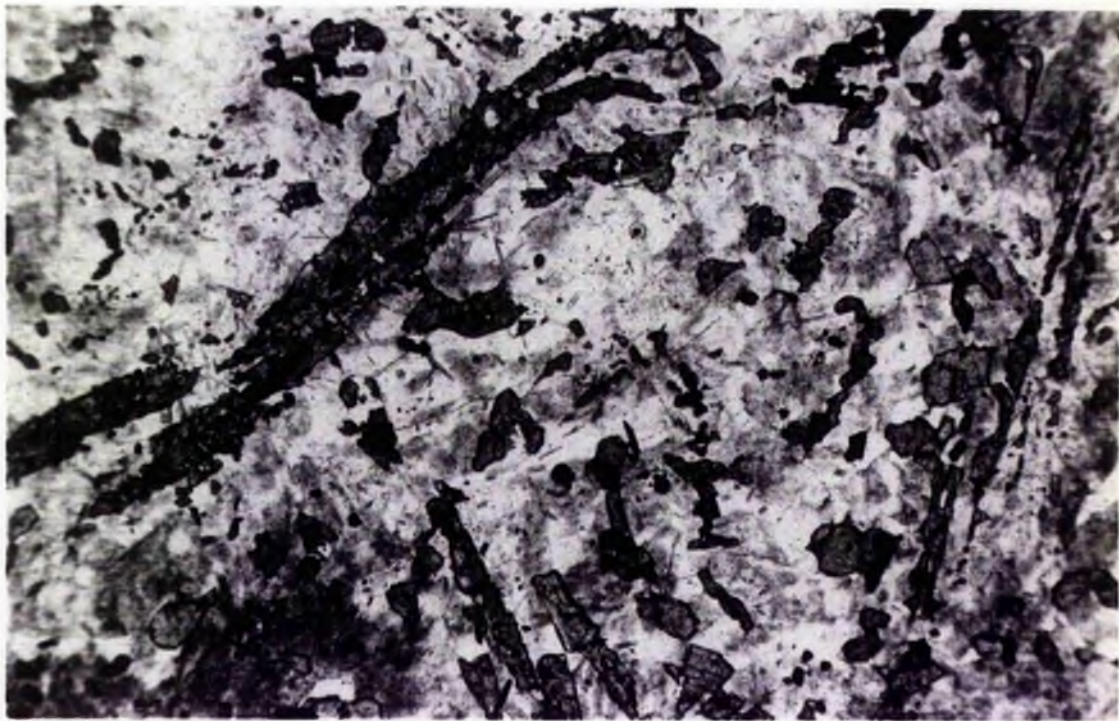


Plate 4.4.2C Skeletal pyroxene in ferrohedenbergite microsyenite enclave located in granite porphyry ring-dyke (T11). Plane polarised light.

2 mm

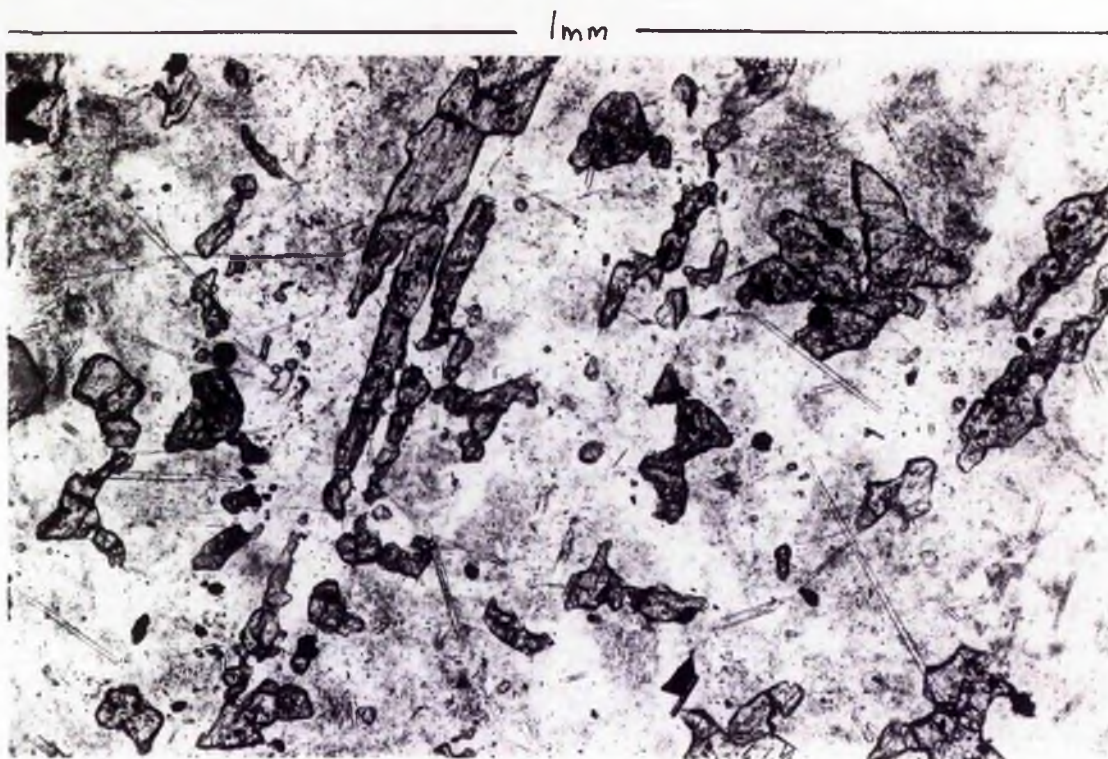


Plate 4.4.2E Ferrohedenbergite microsyenite enclave in granite porphyry ring-dyke (T11). Note abundance of apatite needles. Also granular titanomagnetite (black). Plane polarised light.

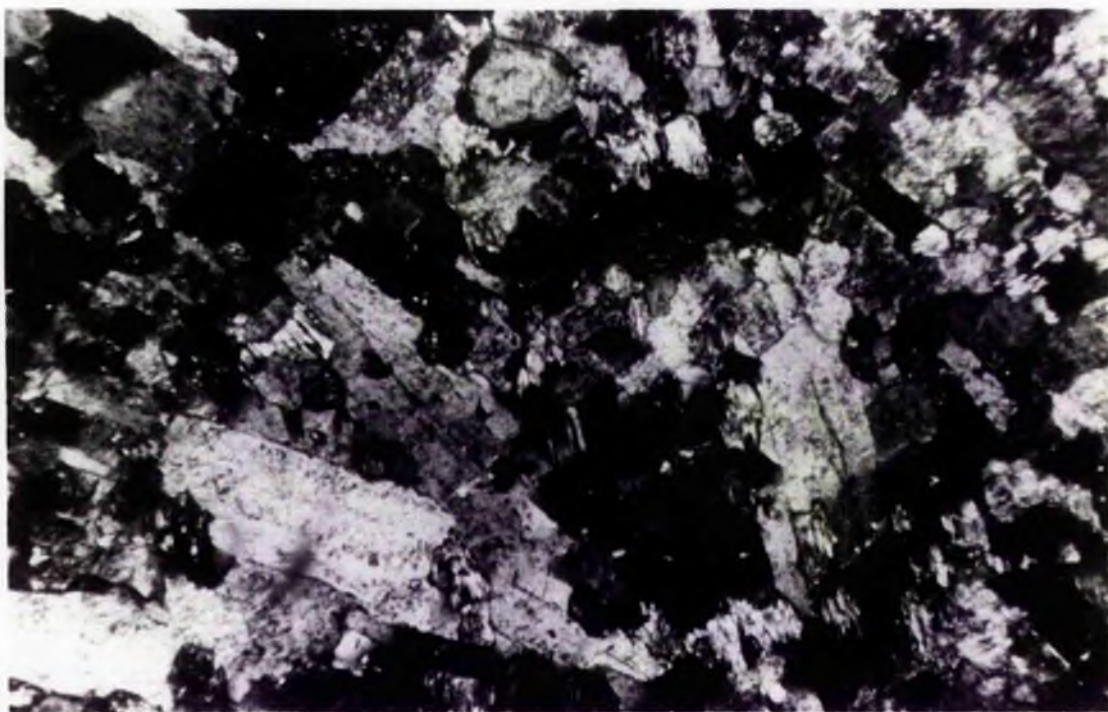


Plate 4.4.2F Texture of ferrohedenbergite microsyenite enclave in granite porphyry ring-dyke (T5). Note tabular to prismatic crystals of feldspar (white) and granular pyroxene (dark). Crossed polarised light.

estimation) of the total feldspar. However, no discrete grains of K-feldspar have been observed.

Apatite is abundant as needles often in criss-cross arrangement (Plate 4.4Z(ii)). Ilmenite is sparse and usually enclosed in the fayalite and ferroaugite.

With regard to crystallisation history, apatite needles are enclosed by nearly all other minerals (except perhaps ilmenite) and appear to be first formed. Both fayalite and ferroaugite are interstitial to plagioclase but the relationship between the two mafic phases is not clear; they are presumed to have been contemporaneous.

(2) Ferrohedenbergite microsyenite enclaves

These are extremely fine-grained and greyish-green in colour. Constituent minerals are plagioclase, alkali feldspar, clinopyroxene, iron oxide, apatite and quartz.

Texturally there is a gradation from a species with lath-shaped feldspars, and clinopyroxene having irregular margins and often in spherulitic intergrowth (Plates 4.4.2A, B); to those with subparallel arrangement of these minerals (Plate 4.4.2F); and to those with almost equigranular texture .

in which clinopyroxene is interstitial to feldspar. Those tending towards a porphyritic habit have also been observed (see later).

The plagioclase and alkali feldspar are characteristically intergrown but are also found as discrete phases. In the former case, plagioclase is always the core while the homogeneous alkali feldspar forms the rim, producing an anti-rapakivi texture (Plate 4.4.2D). The proportion between plagioclase and alkali feldspar is extremely variable, so that although the

group is for convenience called a microsyenite, this term is perhaps more appropriate for the most evolved members of the series. Thus there is a transition from the microferrodiorite enclaves.

The clinopyroxene analysed (by microprobe) was from the more evolved members of the series also, and gave ferrohedenbergite composition, but there is hardly any doubt (from optical examination) that the more plagioclase-rich enclaves would have pyroxene compositions extending backwards to ferroaugite. A 'skeletal' form of the pyroxene may be conspicuously well developed (Plate 4.4.2C).

Apatite is abundant as needles (Plate 4.4.2E) while opaque iron oxide is granular and mostly restricted to the pyroxenes.

The ferrohedenbergite quartz microsyenite enclaves grade from those with equigranular feldspar, no groundmass and rare quartz to those that tend towards a porphyritic texture with significant groundmass quartz. These quartz-bearing variants are thought to represent the link between the cognate group of enclaves and the porphyries.

Discussion Of great significance in these enclaves is the relationship between plagioclase and the two mafic phases - fayalite and clinopyroxene. The abundance of apatite is equally significant. Apatite and plagioclase are shown to be early while fayalite and clinopyroxene are late and often interstitial. Yet fayalite and clinopyroxene are found to represent some of the earliest phases in the granitoid rocks of the Nigerian Younger Granite province.

The cognate enclaves have no equivalents among the exposed rocks of the Tibchi Complex. Thus the early crystal-

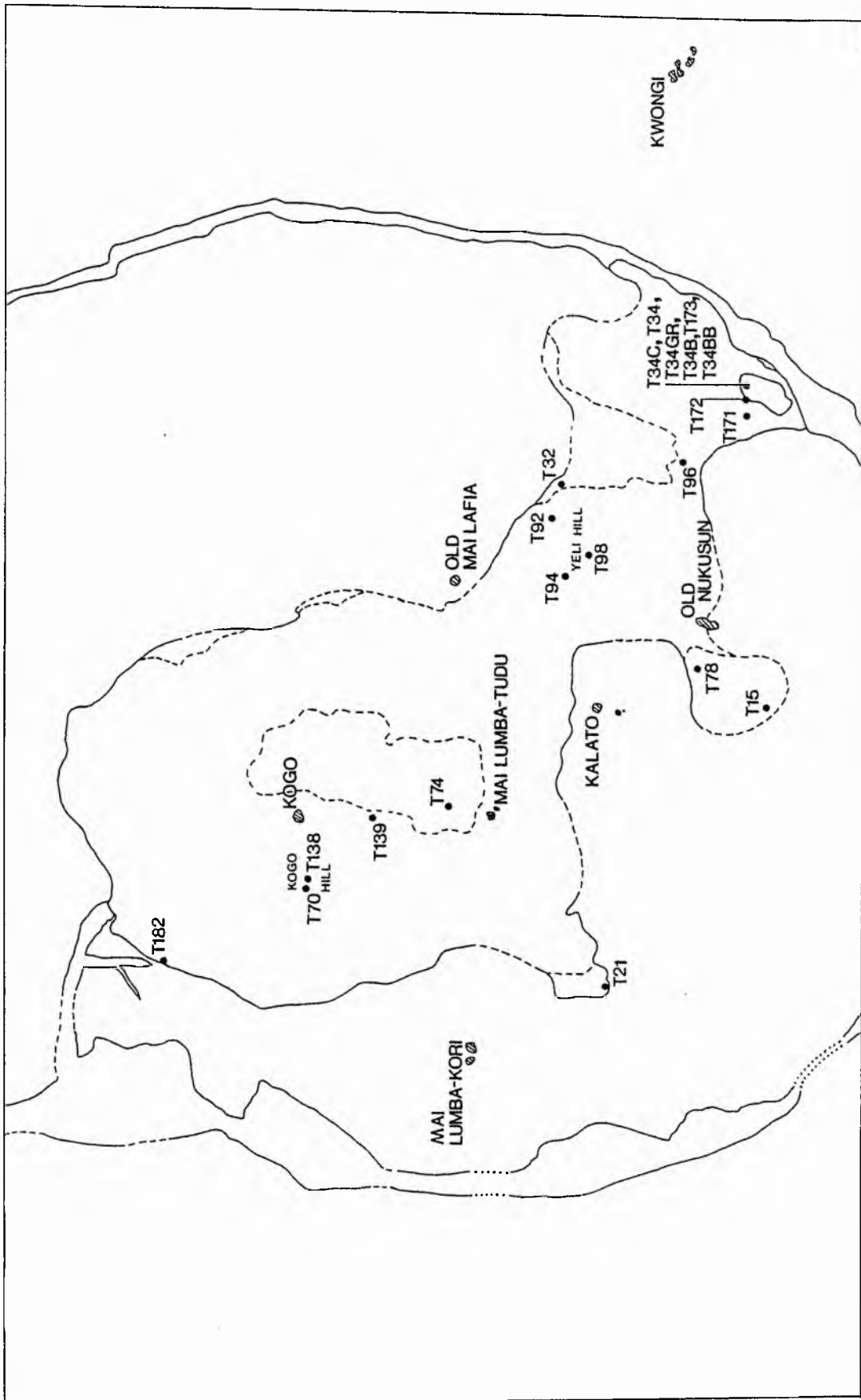


Figure 4.5 Sample localities of the biotite granite and microgranite referred to in the text. For key to geological units see 1:50,000 geological map.

lisation and removal of significant amounts of apatite and plagioclase at a stage corresponding to these enclaves is here evident and would be expected to reflect on the nature of the later differentiates (see Petrogenesis). The generally accepted low profile of plagioclase and lime in the Nigerian Younger Granite rocks can therefore be explained, if these early crystalline cognate enclaves represent part of the evolutionary sequence of the parental liquids from which the Younger Granites evolved.

4.5 Biotite granite and microgranite

4.5.1 Biotite granite

General The biotite granite consists of two variants:

a) alkali feldspar biotite granite in which plagioclase is scarcely found as a discrete phase; and b) plagioclase-bearing biotite granite. The former constitutes the greater part of the biotite granite intrusion while the latter appears to be restricted to two areas within the intrusion namely, the Yeli hill, and Kogo hill, areas (Figure 4.5).

The actual extent of occurrence of the plagioclase-bearing variant in these two areas has not been delineated in the field, nor has any intrusive contact been observed between the alkali feldspar and plagioclase-bearing variants. The nature of any possible transition between them has not, therefore, been investigated in this study.

The proportion of plagioclase in the relevant variant is up to 13 percent by volume of the rock and is maximum in the Kogo hill area. Representative modal analyses are shown in Table 4.5.

The Alkali feldspar biotite granite *

Hand specimen description The rock varies from pink to pale yellow in colour. It is medium-grained, with average grain size of about 3 millimetres.

Microscopic features Essential minerals are orthoclase microperthite, quartz and biotite. Accessory minerals include fluorite, iron oxide and zircon.

The microperthite consists mostly of irregular vein-type textures. Patchy perthitic textures with well-twinned albite also occur and this albite can be seen to be in optical continuity with feebly-twinned albite at the margins of the perthite grain.

Quartz occurs as isolated anhedral crystals, clustered aggregates and in chains, and often shows conspicuous strain shadows. These strain shadows are less prominent in the south-eastern area of the biotite granite intrusion where micrographic intergrowth between quartz and alkali feldspar is observed in the groundmass.

Biotite is predominantly brownish-green in plane light but along the contact of the intrusion with the volcanic rocks and quartz porphyries, the biotite is observed to be dark grey-green instead and often encloses some metamict zircons. In general the biotite crystals occasionally lose their colour, especially in the cores, to a colourless mica.

Fluorite and opaque iron oxides are frequently associated with the biotite crystals. The fluorite may be enclosed by, or surround, the biotite, while haematite is usually concentrated along the cleavages of the latter. Magnetite enclosed by the biotite can be seen in reflected light to show

* For modal analyses of selected biotite granites see Table 4.5 (Appendix).

5mm



Plate 4.5A Plagioclase mantled by perthite. Biotite granite (T92), Yeli hill. Crossed polarised light.



Plate 4.5B Inclusions of discrete plagioclase in perthite (centre). Plagioclase crystals were apparently in synnesis prior to growth of enveloping perthite. Note micaceous alteration characteristic of enclosed plagioclase. Biotite granite (T92), Yeli hill.

5mm

5mm



Plate 4.5E Coalescence of vein texture in perthite into patches, through coarsening of exsolved phase (grey = Na-phase, black = K-phase). Dusty patches (D) in quartz (Q) are caused by submicroscopic inclusions. Mineralised biotite granite (T138), Kogo hill. Crossed polarised light.

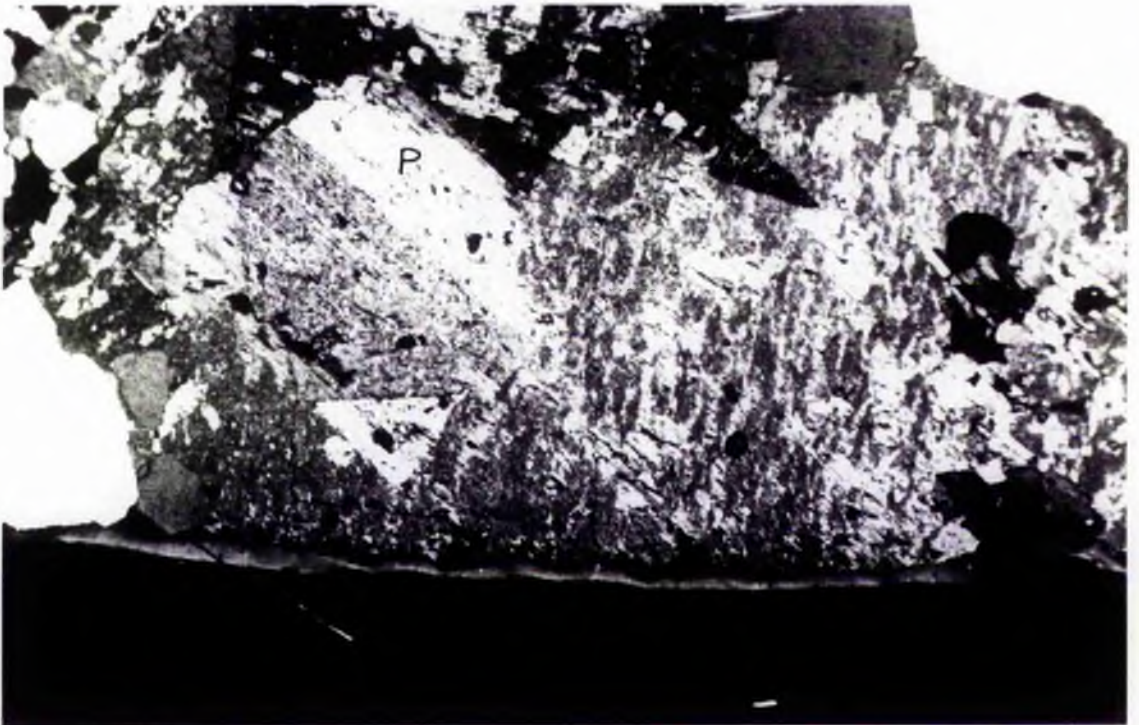


Plate 4.5F Textural evidence (?) for the replacement origin of 'mantling' of plagioclase by alkali feldspar. Remnants of initial plagioclase (twinned) can be seen within invading K-feldspar perthite, and can also be related to a major plagioclase remnant (P). Mineralised biotite granite (T138), Kogo hill. Crossed polarised light.

5mm

crystallographically controlled oxidation exsolution lamellae (Lindsley, 1975). In some samples, only haematite has been found but in crystal shapes more characteristic of magnetite grains. Such grains may suggest completion of the oxidation of magnetite to haematite.

The Plagioclase-bearing biotite granite The following description is based on the relatively unmineralised granites of Yeli hill area which are considered typical of the plagioclase-bearing variant.

Hand specimen description The rock varies from pale pink to whitish in colour, and is similar to the alkali feldspar biotite granite variant in grain size.

Microscopic features The following are the main points of difference from the descriptions for the alkali feldspar variant.

The presence of plagioclase ($\sim \text{An}_{26}$) as discrete crystals, or as cores to alkali feldspar perthites, is characteristic of the rock (Plate 4.5A). The cores of the plagioclase are usually altered to very fine crystals of light green mica and fluorite.

The development of vein perthitic textures in the alkali feldspar crystals is characteristically extensive. Albite veins in the perthite coalesce, through irregularly oriented stringers (Plate 4.5E), into broad and sometimes nodular lamellae. Replacement marginal albite is prominent also.

Irregular masses of secondary (?) quartz on perthites and plagioclase, can be easily distinguished from the normally well set quartz crystals in the rock.

Biotite varies from brown to brownish-green and green, even within the same rock sample. Magnetite rimmed by haematite (?) has been observed in reflected light.

Small xenoliths, usually not exceeding one centimetre long, and consisting of plagioclase ($\sim \text{An}_{26}$) mainly, and minor quartz and biotite, have been found in one locality (T94). In a typical example of these xenoliths, the margin of the xenolith is marked by a discontinuous film of secondary quartz. While the plagioclase crystals within the xenolith are usually unmantled by alkali feldspar, those in the marginal parts are observed to be. It is noteworthy that in the xenoliths, the plagioclase, is, both in appearance and composition, similar to that found in the main rock fabric as discrete, mantled or unmantled, plagioclase.

The mineralised plagioclase-bearing biotite granites of the Kogo hill area

The biotite granite which covers the area surrounding the Kogo village, especially in the vicinity of the Kogo hill (Figure 4.5), is plagioclase-bearing and is also dissected by numerous mineralised veins and lodes. While the petrography of mineralisation is beyond the scope of the present work, the petrography of the host granites in which mineralised veins and lodes are concentrated, is pertinent to the present account of the variation within the biotite granite pluton.

Any one of the following three host granites may be found in the Kogo hill area:

- (a) A coarse-porphyrific granite (T138) with a variegated pink-cream-black colour. Its megacrysts of plagioclase and

alkali feldspar make up over 50 percent by volume of the rock and are up to 10 millimetres across, though generally less. Owing to the coarse-grained texture of the rock and the colour contrast between the plagioclase and the alkali feldspar, the occurrence of alkali feldspar (pink) 'mantling' the plagioclase (cream) is conspicuous even in hand specimen.

The following microscopic features are distinctive from the general description (given earlier) of the plagioclase-bearing granites:

The quartz crystals commonly contain dusty inclusions (Plate 4.5E). The biotite is a strongly pleochroic dark brown variety, crowded with zircon or monazite, and often partially replaced by a green chlorite at the margins and along the cleavage. At an advanced stage of chloritisation, the chlorite is intergrown with a pale yellow mica.

The groundmass consists of an equigranular assemblage of alkali feldspar, quartz, albite ($\sim \text{An}_{6-9}$) and biotite.

(b) A cream coloured granite (T70) similar to (a) above in grain size and texture, and found to be associated with copper mineralisation. Mineralogically, there is a greater proportion of secondary albite ($\sim \text{An}_{6-10}$), and less alkali feldspar-mantled plagioclase here, than in (a).

Of special interest is the observed alteration of biotite phenocrysts leading to replacement by calcite. This alteration varies in extent throughout the rock but from a number of thin sections the sequence has been established as follows:

(1) The reddish-brown biotite is altered round its margins but more rapidly so along its cleavage, to a green chlorite. The Na-phase of adjoining perthites may also penetrate the same



Plate 4.5G Transitional stage in the replacement of reddish-brown biotite by calcite and muscovite. At this stage changes are: Reddish-brown biotite (B) — Green chlorite (G) — Calcite (C). Muscovite is not yet formed. A = Albite, Q = Quartz. Mineralised biotite granite (T70), Kogo hill. Crossed polarised light.

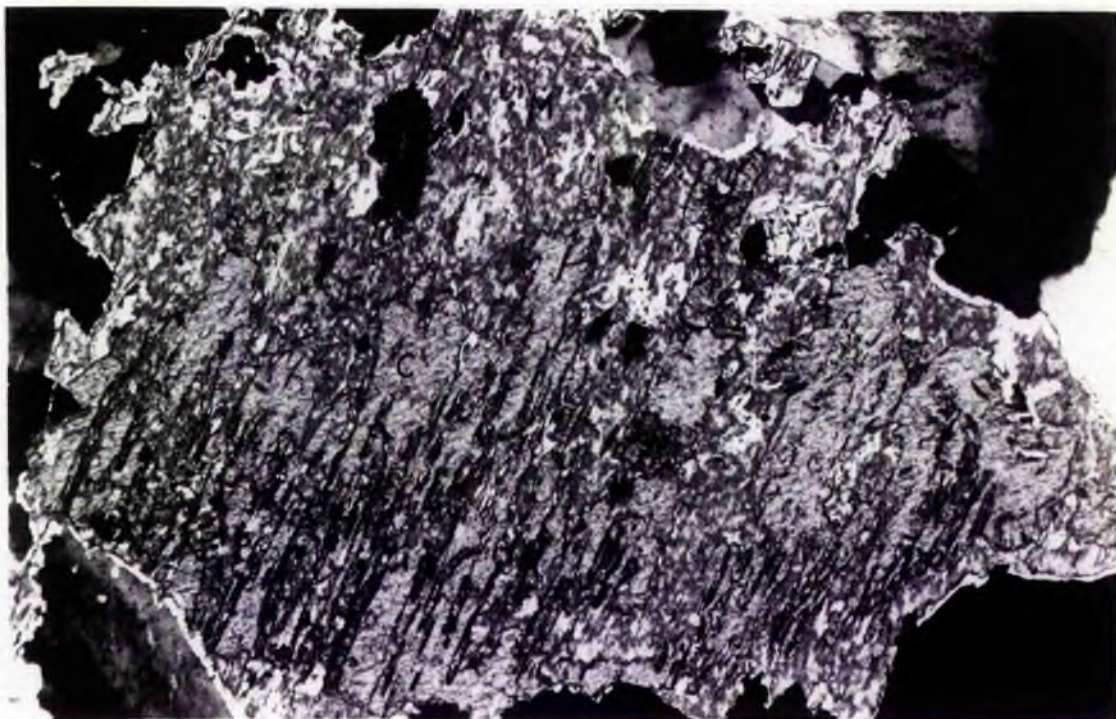


Plate 4.5H Consumption of replacement of reddish-brown biotite by calcite (C) and muscovite (M). Mineralised biotite granite (T70), Kogo hill. Crossed polarised light.

1mm



Plate 4.5J Calcite (C) accompanied by a minimal amount of muscovite (P) completely pseudomorphs a congregation of biotite flakes (left hand side of figure). On the right much more muscovite is formed, with calcite as an 'island'. Black = fluorite mostly; Q = quartz with inclusions. Mineralised biotite granite (T70), Kogo hill. Crossed polarised light.



Plate 4.5K Rod-like crystals (dark) of calcite nucleated round the margins of a fluorite inclusion (F) in biotite undergoing progressive replacement by calcite. Elsewhere massive calcite crystals (C) occur. Mineralised biotite granite (T70), Kogo hill. Plane polarised light.

1mm

cleavage planes thus intergrowing there with the chlorite (Plate 4.5G). It can, by this intergrowth, be inferred that the chloritisation was broadly contemporaneous with the replacement albite vein development in the alkali feldspar perthite.

(2) As the invading green (chlorite) areas increase and dominate the original reddish-brown (biotite), calcite appears within the green areas in lamellar pattern interconnected by small stringers. Calcite growth subsequently enlarges while chloritisation of the biotite proceeds to completion.

(3) Muscovite replaces the chlorite in turn beginning from the margins of the crystal and advancing towards the calcite already in the central areas. Both the calcite and muscovite appear to be stable relative to each other, as none is observed to transgress the other at their contact; thus both together pseudomorph the original biotite phenocryst (Plates 4.5H and J).

If fluorite is present in the biotite being replaced, calcite nucleates as stellate aggregates round the margin of the fluorite crystal (Plate 4.5K).

The calcite is light- to dark-grey in plane light and gives a negative uniaxial optic figure which distinguishes it from anhydrite (the latter is known in porphyry copper mineralisation).

The muscovite is pale yellow in plane light, and this distinguishes it from zinnwaldite which usually shows a bluish tint when found in the Younger Granites (Abernethy, pers. comm.).

(c) A medium-grained granite (T139) is the third plagioclase bearing mineralised granite in the Kogo hill area and is the host granite to the Kogo Lode.

Of particular interest here is the presence of plagioclase (An_{26-28}), unmantled by alkali feldspar, which contrasts with the two previous mineralised granites.

Biotite is a green variety, usually chloritised to various extents in individual crystals, and characterised by the concentration of haematite along its cleavages. Fluorite is almost always associated with the biotite and may be either enclosed by, or else surround, the biotite.

4.5.2 Biotite microgranite of the marginal and roof zone facies

Hand specimen description The rock is white to pink in colour, fine-grained and porphyritic. Phenocryst content is generally less than 10 percent (visual estimation) by volume of the rock. The phenocrysts, usually about 3 millimetres average size, consist of alkali feldspar, quartz and biotite; these minerals are also the essential components of the groundmass. The rock is often spotted with reddish stains arising from the partial breakdown of biotite to haematite.

Microscopic features The alkali feldspar phenocrysts exhibit vein-type perthite textures and are associated with marginal albite plates at perthite grain boundaries. Generally the K-phase of the perthites is dominant over the Na-phase. An important exception is the mineralised microgranite of the Kogo area (T74) where the Na-phase is the major component. Strictly, the alkali feldspars here are anti-perthites.

Biotite varies from brownish-green to dark green.

In the groundmass, albite and K-feldspar occur as discrete crystals. Graphic intergrowth between quartz and K-feldspar is common in some localities. Mirolitic cavities,

especially in the south-eastern part of the Complex, are sometimes developed, although these hardly exceed a few millimetres across. Accessory minerals include fluorite, opaque iron oxide, zircon and topaz. Topaz is particularly important in the mineralised Kogo microgranite.

Discussion The high-lights of the petrography of the biotite granite are four-fold namely,

- (i) The localised occurrence, within the pluton, of the plagioclase-bearing variant;
- (ii) The characteristic 'mantling' of the plagioclase by alkali feldspar microperthite;
- (iii) The association of mineralisation with the plagioclase-bearing variant;
- (iv) The occurrence of calcite and muscovite, in the mineralised granites.

If the localised occurrence of the plagioclase-bearing variant is to be explained on a magmatic evolutionary model, then the position of the biotite granite, in a magmatic sequence for the Complex however tentative, must first be ascertained. For this purpose, it is suggested that the biotite granite followed the cognate enclaves and porphyries, in that order, in the general evolutionary scheme. While plagioclase was a dominant mineralogical feature of the cognate enclaves, the porphyries are characteristically devoid of discrete plagioclase. This leads to an assumption that plagioclase fractionation, as a phase of the magmatic evolutionary trend, had been completed. If biotite granite is the final derivative of the same trend, it would be difficult to contemplate a reappearance of plagioclase-

clase, unless through extraneous contamination of the magma.

Contamination of the magma has support from two lines of evidence. First, the appearance and composition of the plagioclase in the (basement ?) xenoliths found in the (T94) biotite granite of the Yeli hill area, are shown to be similar to those of the plagioclase seen as discrete crystals elsewhere in the rock. Second, the rock sample (T24A) from the zone of hybridisation along the (alkali feldspar) biotite granite contact with the basement, and attributed to mechanical mixing of the two rock types (Chapter 2), is similar in appearance to the plagioclase-bearing rock (T138) of the Kogo hill area.

The origin of the characteristic 'mantling' of plagioclase by alkali feldspar, in the biotite granite, is suggested by textural relationships, especially evident in Plate 4.5F. It is conceived that in this plate, a large crystal initially of plagioclase, has reached advanced stages of 'mantling' by the microperthite. Small remnants of plagioclase within the perthite are observed to be in the same optical orientation with one another, and with a large remnant of plagioclase preserved at one extremity of the relict crystal. Albite lamellae in the perthite are also in the same optical orientation as above. It is suggested that the perthite has been formed through replacement of the initial plagioclase crystal.

Plate 4.5F is analogous to 'Fig. 14' of Vormaa (1971). Vormaa used the said figure to demonstrate the replacement origin, of microperthites, from existing automorphic plagioclase crystals found in the 'even-grained biotite granite No. 247/MT/56', of the Finnish rapakivi granites of the Wiborg

massif. "Evidently, a replacement phenomenon is involved (autometasomatism, K-feldspar replacing oligoclase). If the K-metasomatism took place at temperatures below the solvus temperature in the join $\text{KAlSi}_3\text{O}_8 - \text{NaAlSi}_3\text{O}_8$, as it is here presumed, then the perthite texture cannot, as a whole, be the result of exsolution but at least part of it must be a replacement perthite". Vorms (op.cit.) raised the question of how complete the reorganisation of the plagioclase component in the perthite may have been during perthite formation. During the replacement, according to Vorms (op.cit.), the Na-phase of the perthite "was left as a plagioclase relict where practically no reorganisation of the material has taken place. After its partial replacement of the plagioclase, the potash feldspar continued to grow xenomorphically" relative to the original shape of the plagioclase crystal. Vorms (op.cit.) concluded that the potassium autometasomatic processes took place in the crystallisation of the rapakivi granites. In the present writer's opinion, that conclusion is most probably applicable to the biotite granites of the Tibchi Complex.

The association of mineralisation with the plagioclase-bearing variant of the biotite granite, cannot be emphasised on the basis of evidence from the Tibchi Complex alone. However, it is hoped that information from other complexes of the Nigerian Younger Granite province would be forthcoming in support of this observation (Abernethy, Kinnaird, pers. comm.).

The replacement of biotite by calcite and muscovite, in the mineralised granite of Kogo hill, is texturally evident as a subsolidus process. The solubility of calcite in water is found to increase with increasing carbon dioxide pressure

and decreasing temperature while muscovite is associated with 'fluorine metasomatism (greisenisation) at granite/slate contacts' (Deer et al., 1975). It is suggested that the fluid phase associated with the copper mineralisation of the biotite granite may have been rich in carbon dioxide and fluorine. Calcium would be available from the (plagioclase-bearing) granite during recrystallisation. If, for example, the pressure of carbon dioxide decreased, or other suitable conditions prevailed, components of calcite held in solution in the fluid phase would reach a critical saturation point, ready to be discharged from the fluid phase. The preferred crystallisation of calcite on biotite (obviously through metasomatic exchange process) is not readily explicable, but it is thought to be probably due to the availability of a wider range of cations (than in the feldspars and quartz, or the groundmass) likely to have been conducive for the necessary chemical exchange between the crystalline phases and the fluid phase. The presence of fluorine in the biotite lattice may have had a catalytic role to play for the crystallisation of calcite. Evidence for this suggestion may be found in Plate 4.5K where rod-like crystals of calcite nucleate in a radial pattern round the margins of a fluorite 'inclusion' in the replaced biotite. If 'fluorine metasomatism' is favourable to the formation of muscovite, as referred to earlier, and the fluid phase was rich in fluorine, it would only be necessary for the transfer of mafic components in the biotite, into the fluid phase, for muscovite to form in the remaining part of the biotite unreplaced by calcite.



Plate 4.6.1A General texture of the chlorite microcline porphyry (T41) with cross-hatch twinned microcline phenocryst in centre. Crossed polarised light.

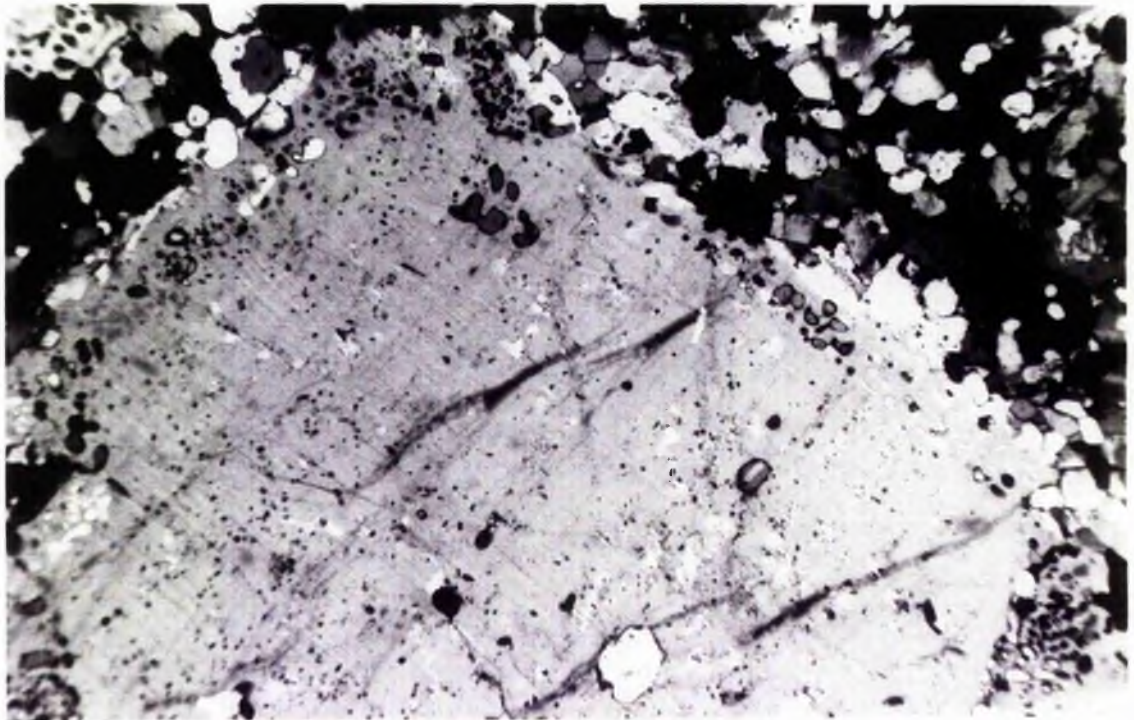


Plate 4.6.1B Part of the microcline phenocryst in Plate 4.6.1A magnified. Note overgrowth from original crystal boundary into the groundmass (see text), and the abundance of minute inclusions.

4.6 Miscellaneous rock types

4.6.1 The chlorite microcline porphyry T41

Hand specimen description The rock is grey in colour and porphyritic intexture. Phenocrysts constitute about 20 per cent by volume of the rock and consist essentially of microcline, quartz, and chlorite, set in a microcrystalline groundmass. The groundmass consists of quartz, microcline, albite and chlorite. Average size of the microcline phenocrysts is about 2 to 3 millimetres while that of quartz is about 0.5 to 2 millimetres.

Microscopic features Microcline phenocrysts occur as cross-hatch or pericline twinned crystals (Plate 4.6.1A). They may also be present as microperthites sometimes Carlsbad-twinned, with coarse vein perthitic textures. In plane light the microcline is observed to be consistently clear, that is, devoid of any turbidity. Granophyric overgrowth characteristically mantles the microcline phenocrysts (Plate 4.6.1B) and it is thought that this growth was contemporaneous with groundmass recrystallisation. X-ray data show that the microcline phenocrysts are fully ordered, structurally and compositionally, reaching the theoretical maximum triclinicity ($\Delta = 1.00$) and T_1O occupancy ($t_1O = 1.00$).

Plagioclase ($\sim An_6$) mantled by microcline is occasionally found, and in the core of the plagioclase, minute crystals of chlorite and fluorite are common.

Chlorite is brownish-green and strongly pleochroic, $\alpha =$ yellow, $\beta = \gamma =$ dark brownish-green. Microprobe analyses give chlorite composition as the iron-rich variety, daphnite (Chapter 5). Specimens of the chlorite hand-picked from the

crushed rock showed two habits: a platy (micaceous) habit and a prismatic habit. X-ray powder patterns obtained separately from each group were similar to each other, signifying that the prismatic habits merely represented relics and that no amphibole or pyroxene structures existed in their lattices. Microprobe analyses confirmed this also.

Accessory minerals include epidote and fluorite which may be found enclosed in chlorite. Fluorite is however dispersed throughout the groundmass and frequently contains fluid inclusions.

Discussion According to Ribbe (1975), Al/Si ordering in alkali feldspars involves the breaking and reforming of strong tetrahedral bonds, enabling preferential migration of aluminium into the T_1 sites, from the T_2 sites, of the tectosilicate framework.

The search for the controls of Al/Si ordering has preoccupied several workers, as recently reviewed by Badejoko (1977) and Parsons (1978). Especially relevant is the contribution of Martin (1974).

According to the above reviews, the controls of Al/Si ordering may be physical or chemical, but usually involving both to varying degrees. In the absence of water, however, "ordering is probably precluded" (Martin, 1974).

The physical controls are principally temperature, time and rate of cooling. Above 350–400°C, the rate of ordering is relatively rapid, and in experimental conditions the degree of order realised may be positively correlated with the temperature of annealing, the lower the temperature the more the ordering. Below the above temperature interval, pure volume diffusion of framework cations is extremely slow, thus caus-

ing a reversal of the trend.

Ordering generally increases with increase in time, given other necessary conditions. For example, through geological time maximum microcline should be expected from K-feldspars, through complete ordering. But this is not true in nature so that the question of time is most probably always constrained by other controls of Al/Si ordering.

Rate of cooling is assessed from the size and structural setting of the cooling mass of rock, and is also evident texturally. In general, for alkali feldspars of high temperature origin, temperature and time immediately become subordinate in importance to rate of cooling. Rapidly cooled hypabyssal rocks are normally associated with disordered alkali feldspars, while the ordered species are typical of slowly cooled intrusions. Disordered alkali feldspar may persist in the slowly cooled rocks if 'dry' conditions prevailed, but very well ordered alkali feldspar in rapidly cooled rocks is unusual.

Chemical controls are principally the presence, and composition, of a fluid phase in the rock. There is a general consensus that the presence of aqueous fluids is pre-eminently the controlling factor in Al/Si ordering in alkali feldspars. In the presence of water, a series of solution and redeposition reactions readily take place, with the rapid migration of H^+ ions which break the Al-O and Si-O bonds through reaction with bridging oxygens, enabling release and redistribution of tetrahedral cations. While peraluminous

conditions in the fluid phase retard ordering, peralkaline solutions increase ordering rates. Optimum conditions, according to the above review, necessarily involve the presence of an aqueous fluid phase, preferably with a peralkaline composition.

An important and currently raging question, is the source of the fluid phase. Parsons (1978) postulates that build-up of water in the course of igneous fractionation is naturally inherent in the general evolution scheme of plutons. The water so generated would be sufficient to account for the unmixing and ordering in alkali feldspars without the intervention of an extraneous aqueous fluid phase. Especially pertinent is Parsons' (op. cit.) recognition that peralkalinity increased with fractionation of the syenitic liquids on which he based his arguments.

On the other hand, the stable isotope studies of Taylor (1974) for example demonstrate large scale interactions between plutons and groundwaters, a view strongly favoured by Martin and Bonin (1976).

From a magmatic point of view, the presence of a fully ordered maximum microcline, not merely as groundmass phase but also as phenocrysts, in the clearly hypabyssal rock (T41), cannot be explained by action of an aqueous fluid phase internally derived from the rock, unless the magma was clearly water-saturated. In the latter case, a pegmatite or aplite would be expected. The fluid phase therefore must have been introduced. The dyke is older than the quartz, and granite, porphyries and the biotite granite pluton and may have passed through several cycles of thermal and hydrothermal reworkings

perhaps involving heated groundwater. Wright (1967) placed the thermal stability limit of maximum microcline at $375 \pm 50^{\circ}\text{C}$, on the basis of its conversion to orthoclase in a contact metamorphic aureole of the Eldora stock, Colorado. Working at 5 kilobars pressure Martin (1974) obtained a first-order transition between ordered orthoclase and maximum microcline, at approximately 575°C . If corrections due to differences in pressure are made, temperature similar to that of Wright (1967) should be expected. Chlorite, associated with the microcline in T41, is known to be a common product of hydrothermal alteration of primary mafic minerals in igneous rocks (Deer et al., 1975), and this is evident from the relict prismatic habits (after pyroxenes ?) observed in some of the chlorite crystals.

It is concluded that the present structural state of the microcline phenocrysts in the hypabyssal rock (T41), is not of direct magmatic origin. The texture of the rock is undoubtedly that of a rapidly cooled magma, but the complete Al/Si ordering of the feldspar and the occurrence of chlorite after initial mafic phases are modifications reflecting a hydrothermal overprint caused by an extraneous aqueous fluid phase.

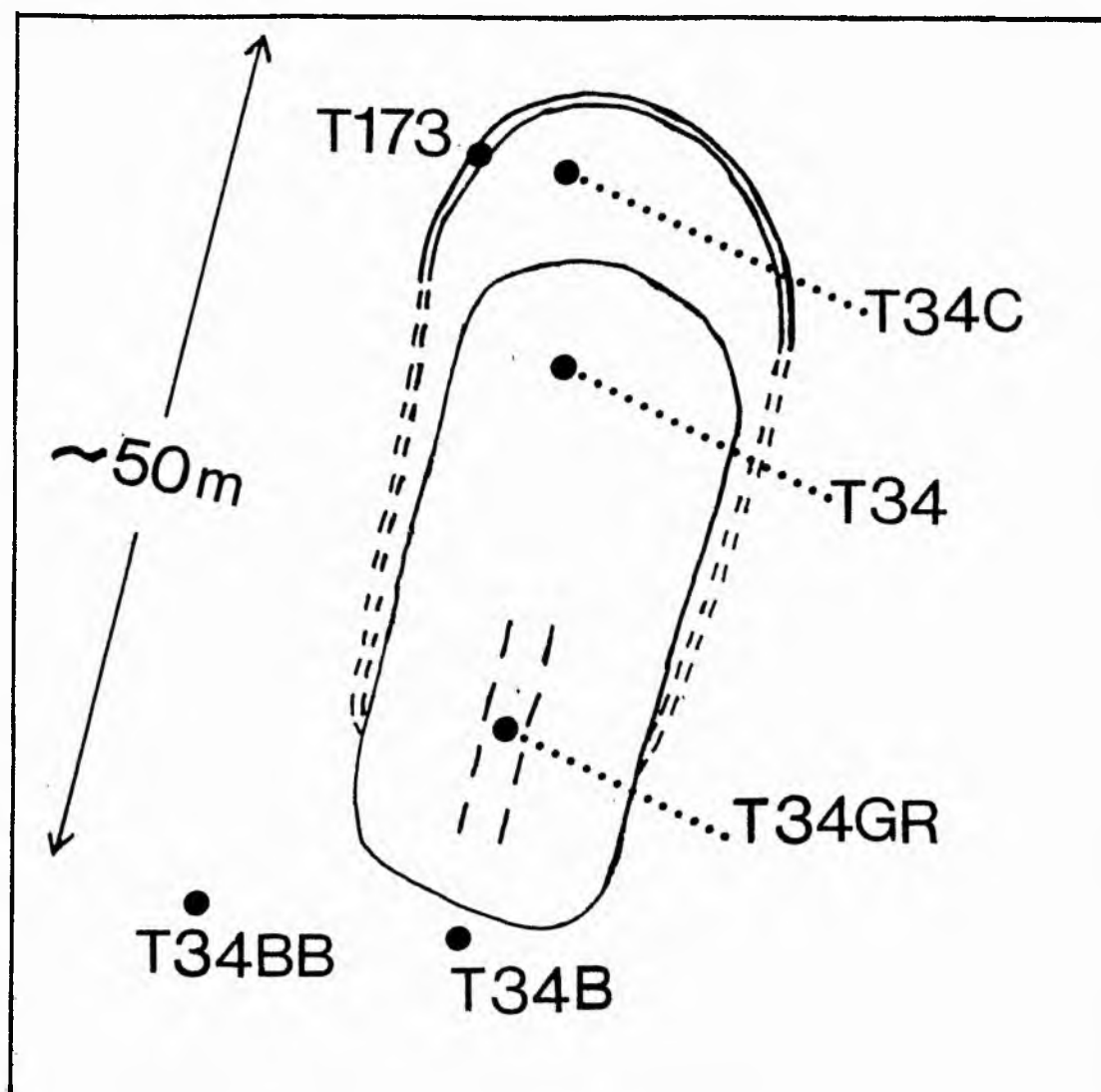


Figure 4.6.2 Sketch of the field relations and sample localities in the south-eastern oversaturated peralkaline suite. See also Figure 4.5 for location of suite on main geological map.

1mm

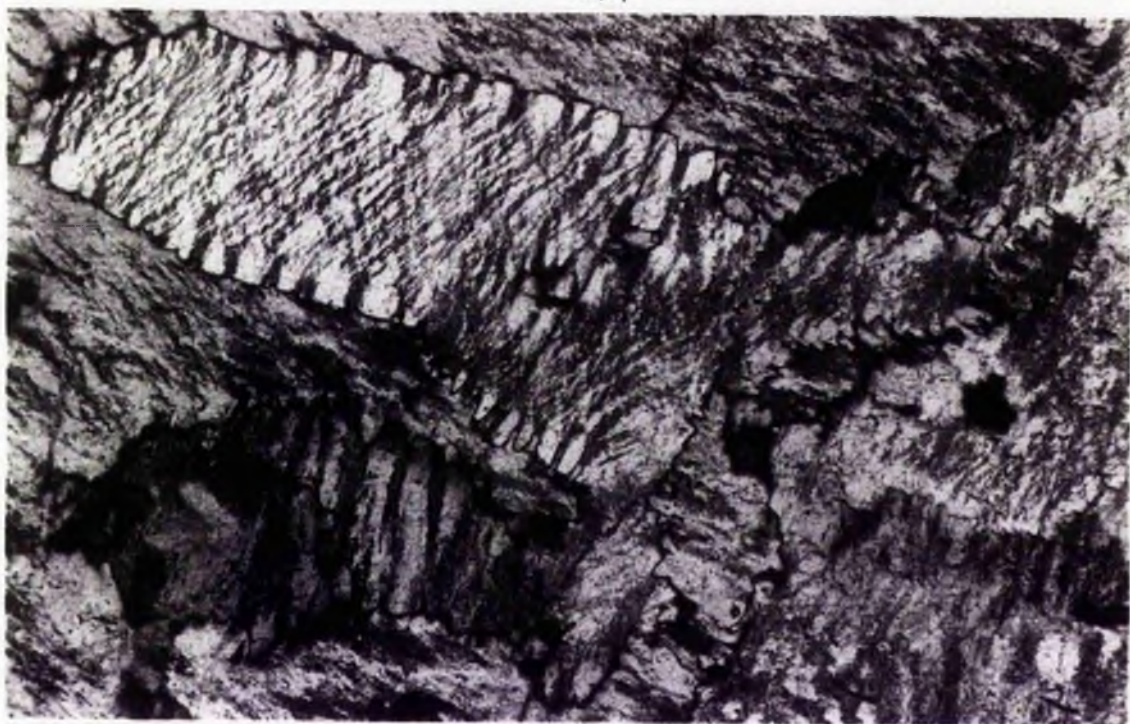


Plate 4.6A Lobate and serrated grain boundaries between adjacent perthites in Aegirine-augite ferrorichterite syenite (T34C). Braided perthitic texture (top left) is common. Feldspar is strictly antiperthitic (K-phase = dark grey; Na-phase = white). Crossed polarised light.

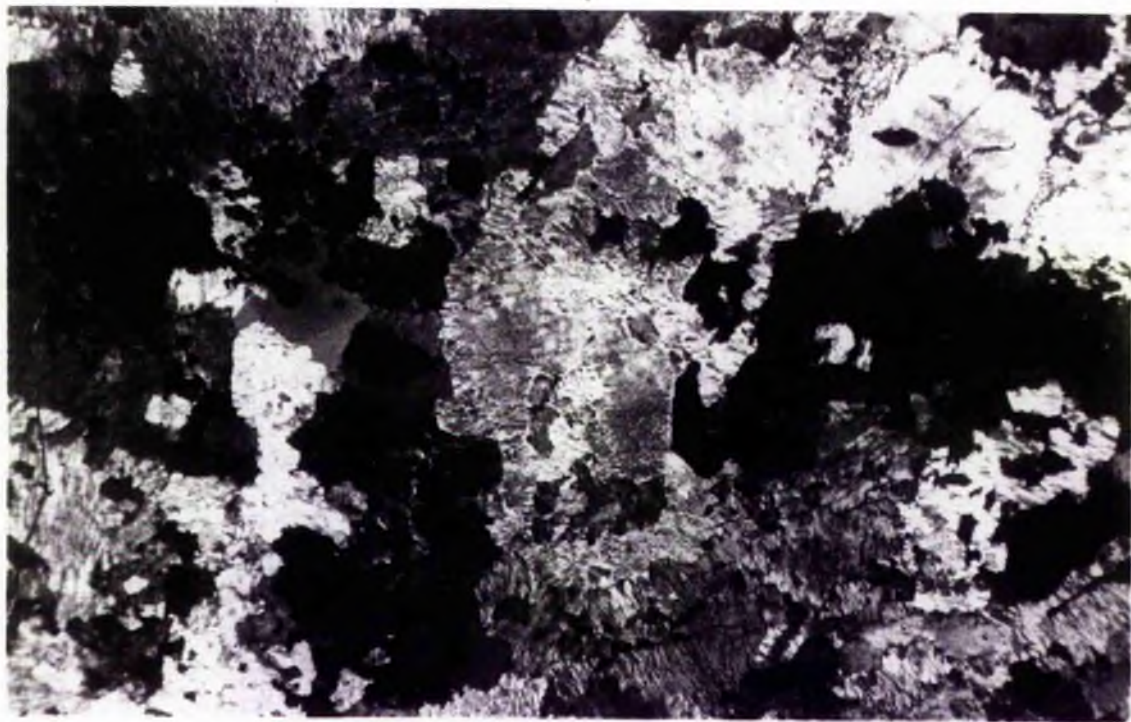


Plate 4.6B General texture of Aegirine-augite ferrorichterite syenite T34C (see text). Crossed polarised light.

2mm

2mm

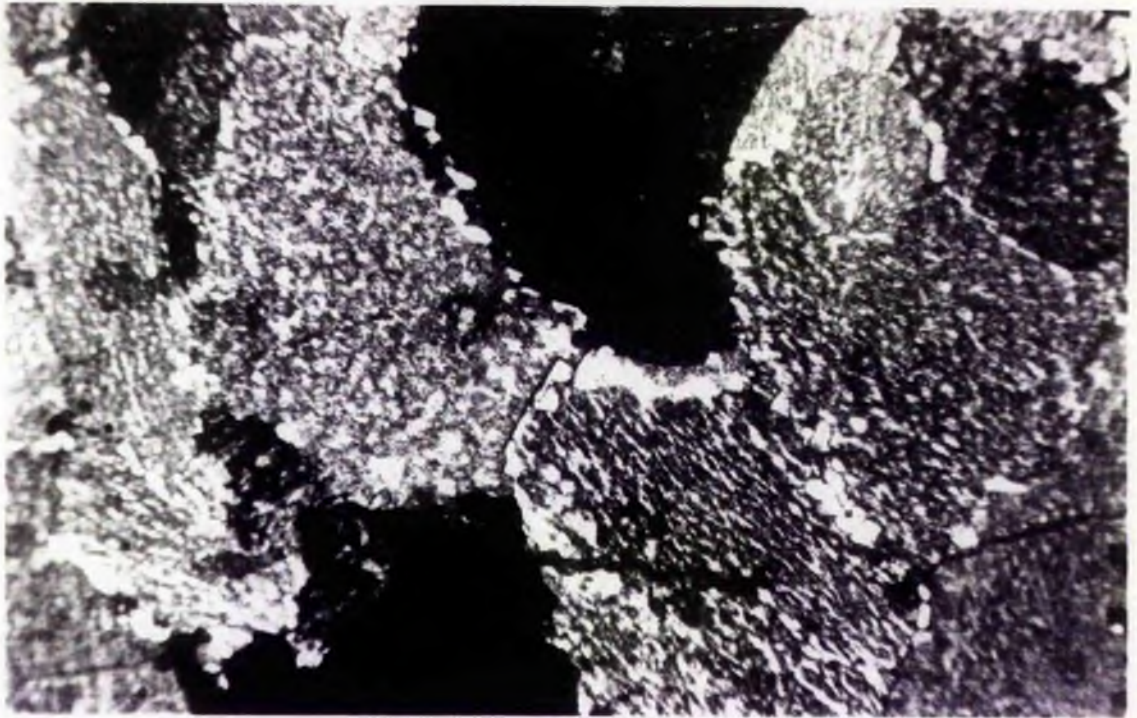


Plate 4.6C Granoblastic polygonal texture in Amphibole potash syenite (T34). Marginal albite (white) can be seen in optical continuity with perthitic albite phase, the latter being subordinate to the potassic phase (cf. T34C). Crossed polarised light.

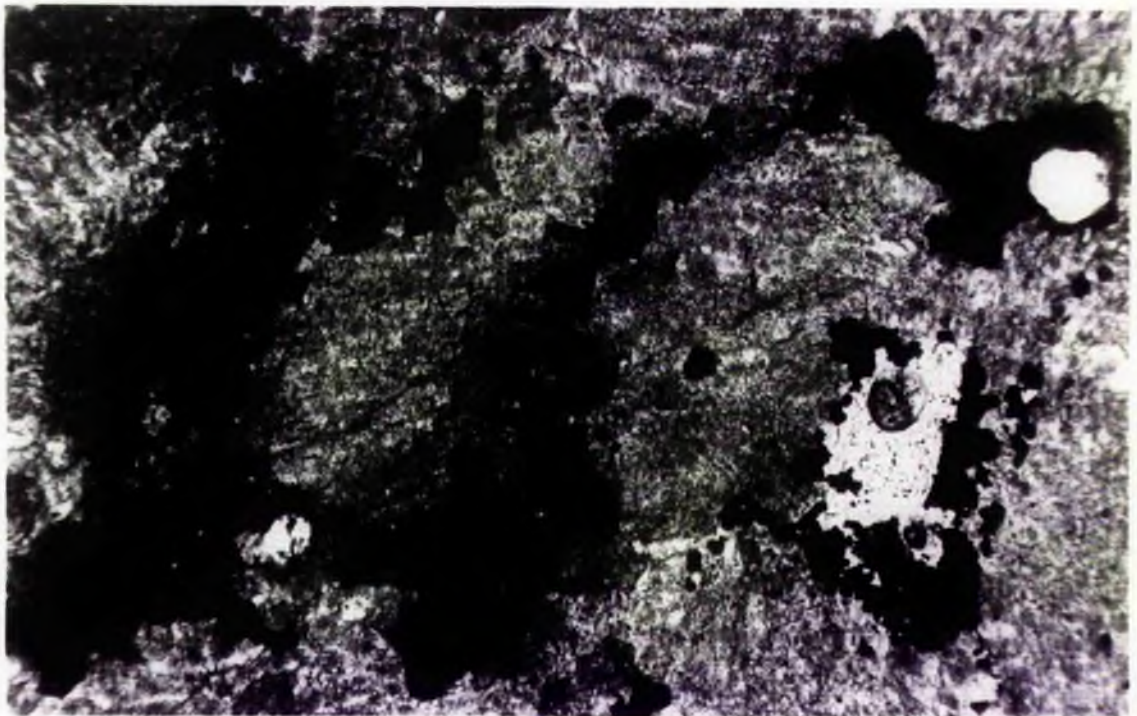


Plate 4.6D Interstitial role of amphibole (dark) in Amphibole potash syenite (T34) displayed. Amphibole traces the granoblastic polygonal texture of the rock, thus showing its late stage crystallisation during the metasomatic textural re-equilibration. On the right (upper & lower masses) amphibole is pseudomorphed by intergrown magnetite-haematite. Plane polarised light.

2mm

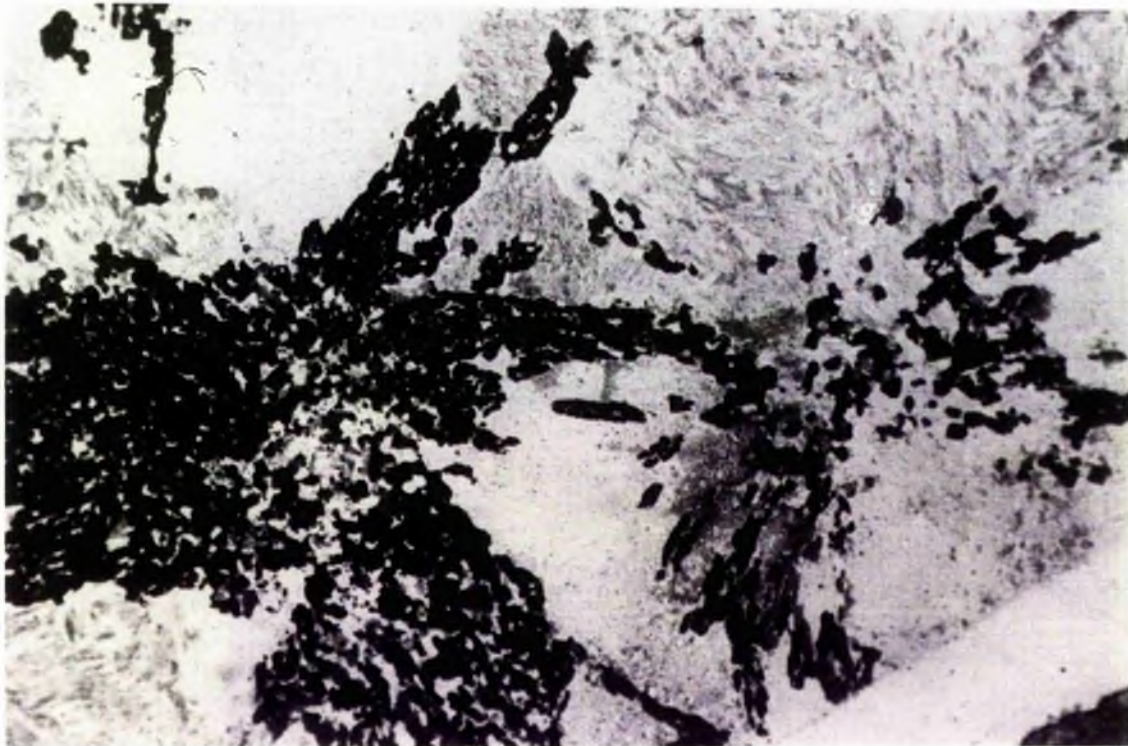


Plate 4.6E Arfvedsonite in peculiar stellate habit consisting of small elongate crystals that form discontinuous rays. Sodic granite (T173). Plane polarised light.

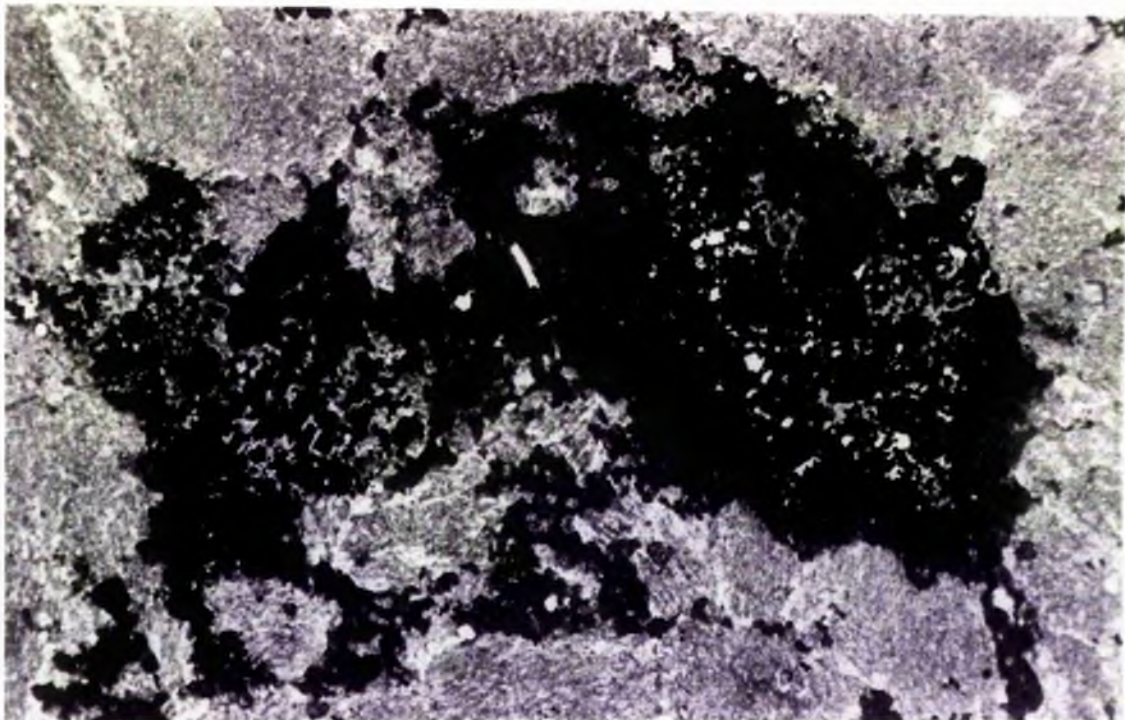


Plate 4.6F In Amphibole potash syenite (T34) intergrown magnetite-haematite replaces amphibole (A) to varying degrees during the potassic phase of metasomatism. F = Alkali feldspar microperthite.

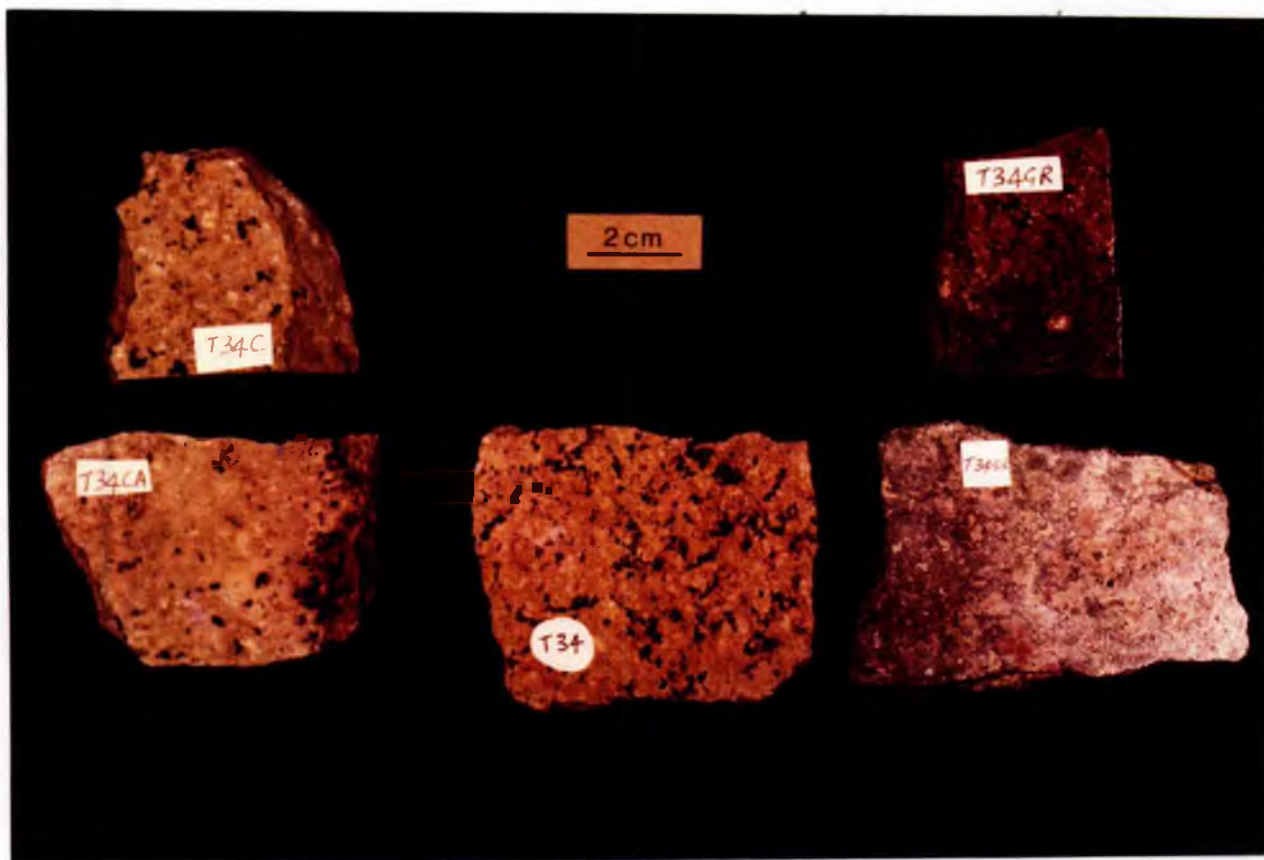


Plate 4.6AT The metasomatic transition in the oversaturated syenites of the south-eastern peralkaline rocks: T34C T34 T34GR through intermediate stages T34CA and T34G (see text).

4.6.2 The south-eastern suite of oversaturated and under-saturated peralkaline and peraluminous rocks

1. Oversaturated peralkaline rocks

The following order which roughly represents the spatial relationships in the field, of the various members of the oversaturated peralkaline group (Chapter 2), is adopted in presenting the petrographic descriptions (the reader is also referred to Figure 4.6.2 and to Plate 4.6AT):

- (a) Aegirine-augite ferrorichterite sodic syenite (T34C)
- (b) Arfvedsonite potassic syenite (T34)
- (c) Arfvedsonite haematite syenite (T34GR)
- (d) Contact facies between the syenites and the anti-perthite biotite granite
- (e) Anti-perthite biotite granite (T34B) and associated fine-grained biotite granite (T34BB).

(a) Aegirine-augite ferrorichterite sodic syenite (T34C)

Hand specimen description The rock is white in colour and medium-grained, average grain size being about 3 millimetres.

Microscopic features The rock is feldspathic, consisting mostly of alkali feldspar microperthite, with minor amounts of mafic minerals and traces of quartz. Accessory minerals include fluorite, and intergrown magnetite-haematite. Texturally the rock is granular but the average grain size may vary abruptly even within the same thin section (Plate 4.6B). The lobate, serrated and often convolute perthite grain boundaries is perhaps the most conspicuous microscopic feature of the rock.

The perthite has mostly regular striped lamellar textures and also occasionally braided textures (Plate 4.6A). The

K-phase is the minor component in the perthite so that strictly the alkali feldspar is antiperthite. From X-ray data, the structural state of the feldspar corresponds to that of orthoclase. Despite the suturing of the perthite grain boundaries, these boundaries appear stable, without marginal replacement albite or orthoclase. This situation contrasts with that observed in the potash syenite described later.

Although isolated grains of quartz comparable in size to the average feldspar grain may be found virtually anywhere in the rock, most of the quartz present is segregated. In these segregations the quartz may be poikilitically enclosed by, or may be interstitial to, the aegirine-augite. It is here also that most of the aegirine-augite is located.

Mafic minerals consist mainly of aegirine-augite, with subordinate amounts of ferrichterite. The aegirine-augite is prismatic in habit and strongly pleochroic, α = bright green, β = yellowish-green, γ = yellow; $\alpha > \beta > \gamma$; length-fast; $\alpha \wedge c = 16^\circ$. Wherever the ferrichterite occurs, it can be observed to have partially replaced the aegirine-augite. Usually the replacement begins at the margins of the pyroxene, penetrating eventually through its cleavage. At an advanced stage isolated remnants of pyroxene may be embedded in large plates of fresh ferrichterite. The ferrichterite is dark blue in colour and pleochroic, α = pale brown, β = blue-black, γ = dark blue; $\beta > \gamma > \alpha$; length-slow. The ferrichterite is compositionally transitional to arfvedsonite (Chapter 5).

The iron oxide consists of an intergrown magnetite-haematite as seen in reflected light (details in Chapter 5).

This oxide mineral is normally associated with the ferrorichterite, and is therefore found, together with the amphibole, at the periphery of the aegirine-augite. The iron oxide thus appears to be precipitated during the replacement of the pyroxene by the amphibole.

Fluorite is ubiquitous in the rock but is mostly associated with the mafic minerals in the quartz segregations.

(b) Amphibole potassic syenite (T34)

Hand specimen description This rock is brownish-pink in colour but is identical to the sodic syenite in grain size and general appearance. The presence of vugs, generally not exceeding one millimetre across, can be seen in the potassic syenite on a smooth surface. Sometimes black cross-cutting vein-lets of amphibole can be seen in some samples; the rock tends to split along such veins, exposing large amphibole crystals on the fracture surface. The pink colour, the presence of vugs, and black vein-lets, distinguish the potassic syenite (T34) from the sodic syenite (T34C).

Microscopic features Essential minerals are microcline microperthite and a dark blue amphibole transitional in composition from ferrorichterite to arfvedsonite, for convenience called arfvedsonite. Intergrown magnetite-haematite, fluorite, and traces of quartz, are also present.

The morphology of the feldspars give the rock a granoblastic polygonal texture (Plate 4.6C). In the microcline microperthite twinned albite appears in both patchy and vein perthitic textures. The potassic phase in the perthite is turbid and optically predominant as host to the sodic phase,

although X-ray data suggest a prevalence of the Na-phase. Marginal albite, as irregular bodies and discrete crystals, occur at perthite grain boundaries. The X-ray data give the potassic phase as intermediate microcline (with triclinicity (Δ) = 0.80 and $t_10 = 0.89$).

The amphibole is optically similar to the ferrorichterite of T34C described earlier but chemically transitional to arfvedsonite. The amphibole is pleochroic, α = golden yellow, β = blue-black, γ = dark blue, $\beta > \gamma > \alpha$; length-slow. Relict aegirine-augite and aegirine, completely or partially altered to haematite are found as globular remnants in the fresh and massive amphibole. Elsewhere the amphibole is interstitial to perthite grains and may show protracted bifurcations (Plate 4.6D).

Intergrown magnetite-haematite replaces the amphibole pervasively. The replacement appears to begin as dusty aggregates on amphibole, these aggregates coalescing eventually to reticulate or spongy masses (Plate 4.6F). Iron oxide occupying interstitial positions to the perthite grains, can be shown to have simply been mimetic on pre-existing interstitial amphibole (Plate 4.6D).

In this rock, as well as in T34C, magnetite component is dominant over haematite in the intergrown crystals.

(c) Arfvedsonite haematite syenite (T34GR)

In summary, this is a red and black rock. In it there is almost a complete replacement of amphibole by intergrown magnetite-haematite in which haematite is dominant. With intermediate stages established both in the field and in thin

section, it has become obvious that T34GR is apparently an extreme case of amphibole degradation and haematisation that started from T34 above.

Amphibole is optically and chemically close to end-member arfvedsonite. It is blue and strongly pleochroic, $\alpha = \beta = \text{blue}$, $\gamma = \text{yellow to greenish-yellow}$; $\alpha = \beta > \gamma$; length-fast. Alkali feldspar is a maximum microcline (with triclinicity (Δ) = 0.82 and $t_10 = 0.92$), thus showing increased Al/Si ordering relative to T34.

(d) Contact facies between the syenites and the anti-perthite biotite granite

At the contact zone between the sodic syenite (T34C) and the anti-perthite biotite granite (T34B) is a transitional rock (T173) which is similar in appearance to T34C but granitic rather than syenitic in composition.

The feldspar in the transitional rock (T173) is orthoclase microperthite with regular string and vein perthitic textures and frequent Carlsbad twinning. Braided perthite textures are also quite common. Twin planes are often wavy or serrated. Perthite grain boundaries are lobate, serrated and often quite convolute, but without marginal albite.

The transitional rock (T173) is characterised by the presence of arfvedsonite which is not associated with any other mafic mineral nor with replacement iron oxide. The arfvedsonite has a peculiar stellate habit (Plate 4.6E) consisting of small elongate crystals that form discontinuous rays.

At the contact between the potassic syenite (T34) and the anti-perthite biotite granite is a transitional biotite arfvedsonite granite (T174).

5mm

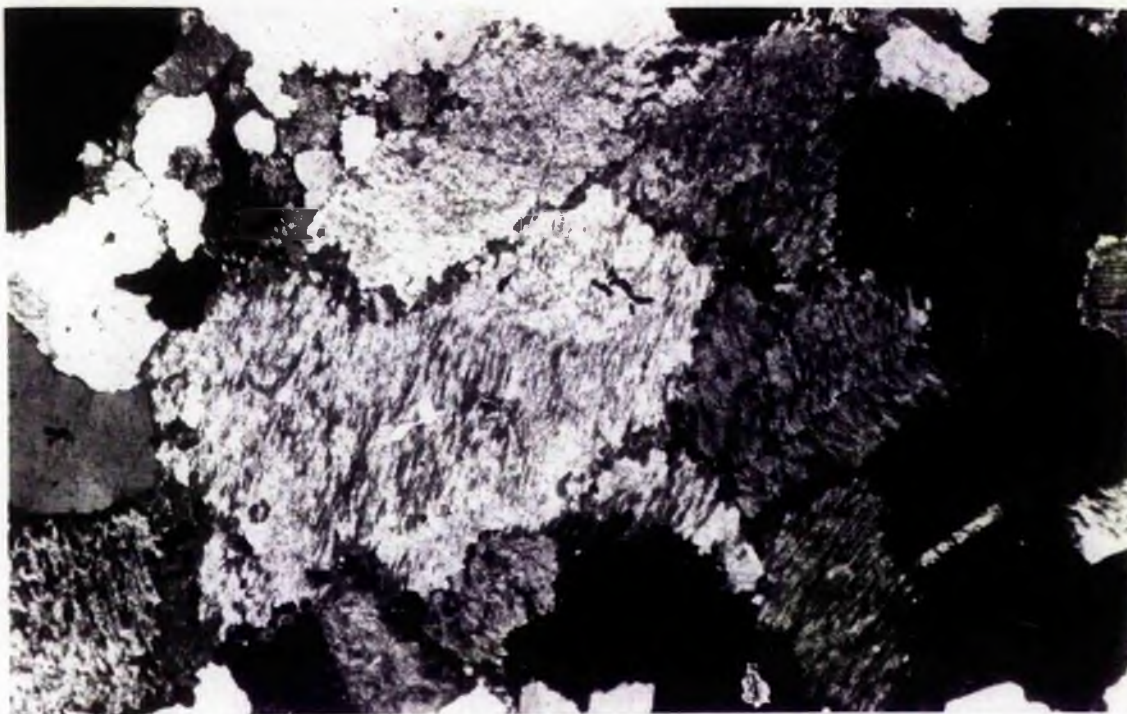


Plate 4.6G Antiperthite texture. Marginal K-phase (dark grey) occurs as a thin but definite lining round the edges of the large perthite (centre) and is optically continuous with perthitic K-phase lamellae (also dark grey) within the perthite itself. The K-phase is subordinate to Na-phase (white) in the perthite. Anti-perthite biotite granite (T34B). Plane polarised light.

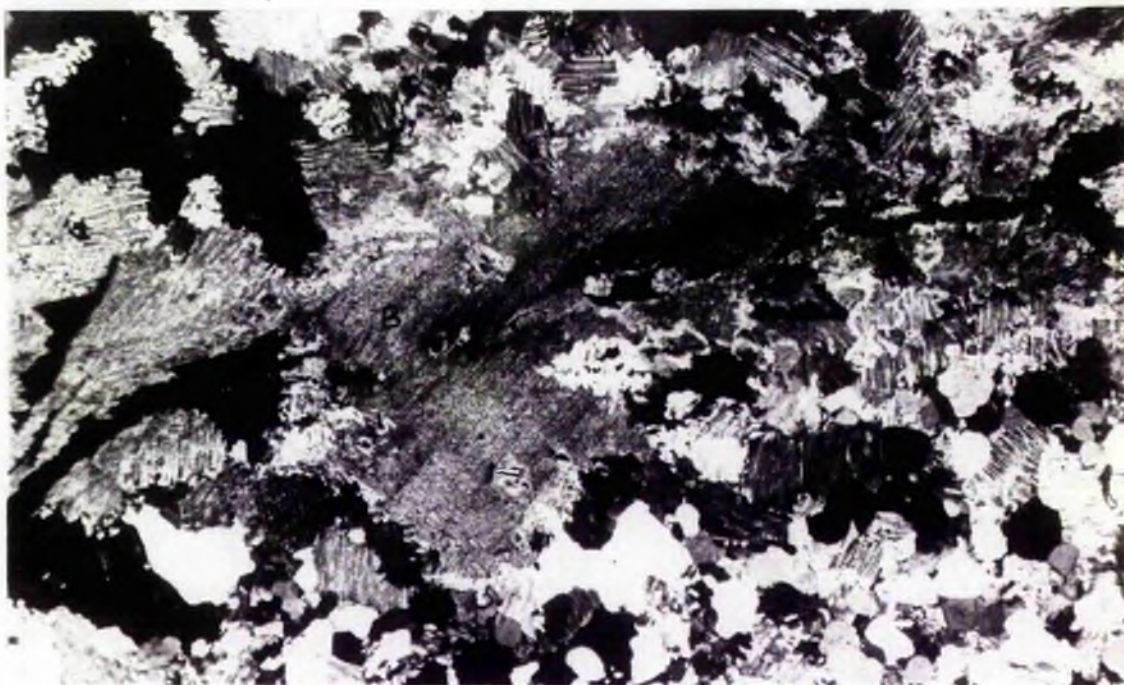


Plate 4.6H Textural evidence for the subsolidus origin of the biotite in the fine-grained biotite granite (T34BB). EF is an open fracture. Biotite crystal (B) can be seen clearly to transgress the fracture, thus postdating the fracture. (See also Plate 4.6J). Crossed polarised light.

0.5mm

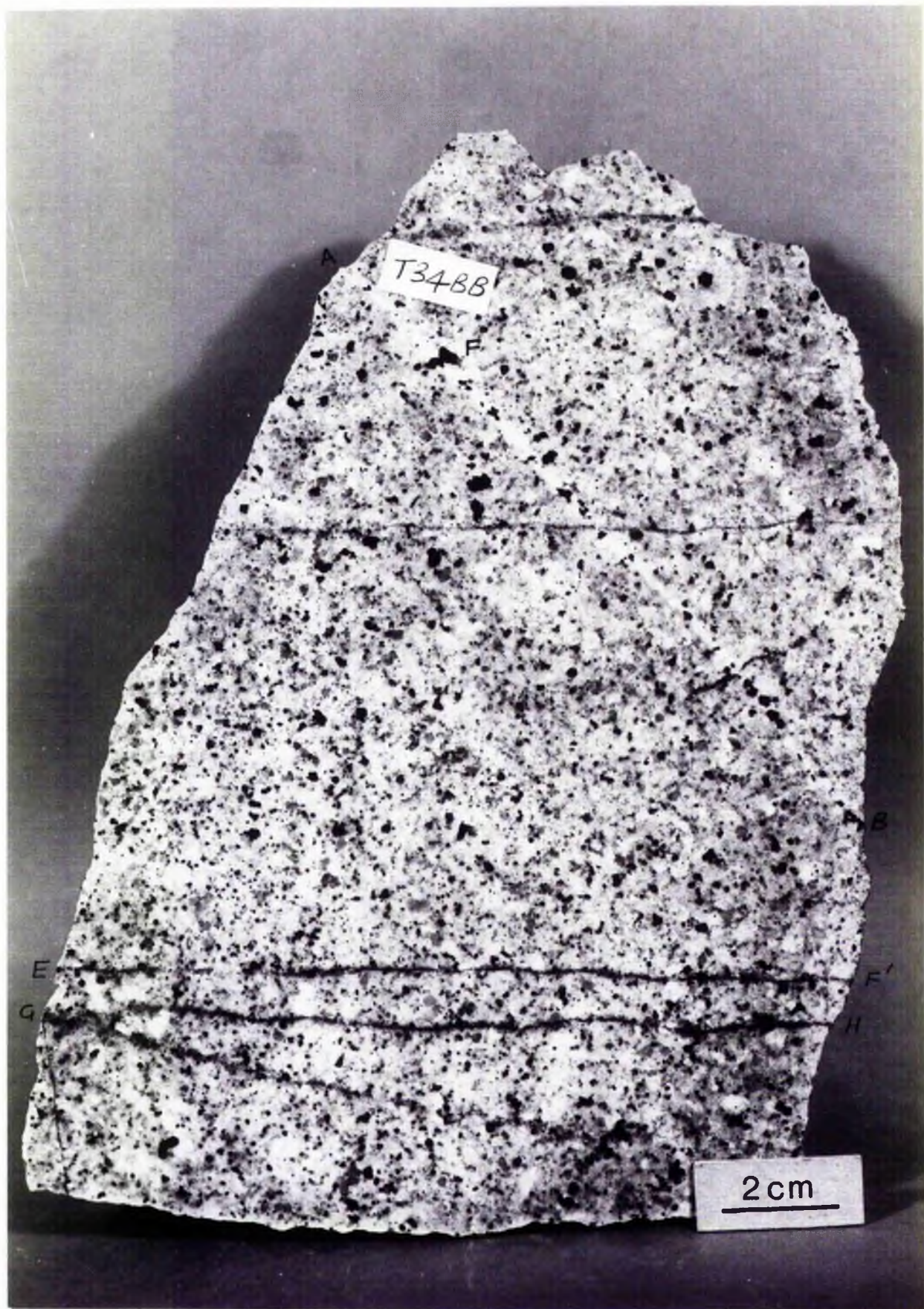


Plate 4.6J ^{grained} Fine biotite granite (T34BB). Biotite preferentially crystallises along the fracture AFB but the same biotite also grows across the width of the fracture plane (eg. at F) and throughout the rock. The healing of the fracture and the biotite crystallisation are probably contemporaneous and together attest the subsolidus recrystallisation of the rock (for CD, EF', GH see text).

(e) The anti-perthite biotite granite (T34B)

Hand specimen description The anti-perthite biotite granite is white in colour and medium-grained, with most mineral grains between 2 to 3mm across. Essential minerals are alkali feldspar, quartz and biotite.

Microscopic features The rock appears fairly equigranular with triple junctions quite common among essential mineral constituents.

The alkali feldspar is anti-perthitic, with the sodic phase dominant and the minor potassic phase forming the vein lamellae (Plate 4.6G). Occasionally both phases appear to be equal, corresponding perhaps to the 'mesoperthite' of Michot (Smith, 1974). The potassic phase is turbid; in all perthite grains observed it is this phase that always crystallises along the grain margins, sometimes completely encircling the grain. This marginal potassic phase is found to be in optical continuity with the potassic lamellae within the perthite. X-ray data give microcline with triclinicity (Δ) of 0.86, for the K-phase of the anti-perthite.

Quartz forms clusters and chains and displays conspicuous undulose extinction.

Biotite is yellowish-brown and pleochroic, α = pale yellow, $\beta = \gamma$ = yellowish-brown and compositionally corresponds to a siderophyllite (Chapter 5). It appears unstable at the edges and along cleavage, losing its colour to greenish tints, the green being in turn replaced by a pale yellow to colourless mica.

Accessory minerals include fluorite, opaque iron oxide, metamict zircon and monazite.

A fine-grained biotite granite T34BB is spatially related to the anti-perthite biotite granite. In hand specimen T34BB

is characterised by haematite staining, cross-cutting veins and healed fractures (Plate 4.6J). In thin section the biotite appears greenish, with cleavage planes often filled by haematite and compositionally corresponds to siderophyllite. Plate 4.6J shows a slab of T34BB displaying one of the healed fractures and some of the cross-cutting veins. Biotite may be seen to have preferentially crystallised along the fracture AB. The biotite is not, however, confined to the fracture plane, instead it cuts across the fracture plane into the main rock fabric in many cases. Microprobe analyses of several biotite grains located along the fracture and of biotite growing across the fracture into the rock fabric, as well as biotite in different locations in the main rock fabric itself, have all been carried out. The compositions show no significant difference. The crystallisation of the biotite in T34BB postdates the healed fracture AB (see also Plate 4.6H) but is earlier than the cross-cutting veins CD, EF, GH and KL.

There are in T34BB several ghostly trails of healed fractures and previous veins, which were perhaps passive and active pathways (respectively) of subsolidus fluid interaction and reconstitution of the rock (see Discussion).

Discussion The terms 'sodic' and 'potassic' syenites as used here, are based partly on whole-rock chemistry (Chapter 6) and partly on petrographical distinctions between the two rocks T34C and T34 respectively. The sodic/potassic distinction in the south-eastern suite of peralkaline rocks as a whole, becomes clear when Plates 4.6A, 4.6C and 4.6G are compared. In Plate 4.6A (sodic syenite, T34C) and 4.6G (antiperthite biotite granite, T34B), the perthites are strictly antiperthitic while

in Plate 4.6C (potassic syenite, T34), the reverse is the case. Some of the petrographical variations observed in members of the suite as a whole, depend strongly on whether the given rock belongs to the sodic or potassic group. However there are many more features that link the two groups than separate them, and the available range of transitional rock types testifies to the transition that exists. Regardless of the petrographical parameter used, a progression exists leading from the sodic to the potassic group.

In the sodic group are the syenite T34C and its associated granitic facies (T173). In the potassic group are the syenites T34 and T34GR. The anti-perthite granite T34B and associated gine-grained facies T34BB, belong to the sodic group but have been texturally modified by the subsequent potassic phase of activity, as their close spatial relationship with the potassic group implies.

The intricacy of perthite-perthite crystal boundaries has been found to be an effective petrographical tool in feldspathic rocks and is used here as the first test for the postulated progression from the sodic to the potassic peralkaline rocks. In the sodic group, grain boundaries are extremely complex (eg. Plate 4.6A) in both the syenite and granite. In the potassic group, the irregularity in grain boundaries is almost completely obliterated. Diffuse and irregular boundaries in the sodic group are the result of major subsolidus recrystallisation (Tuttle 1952), and represent textures frozen during the process of mutual grain adjustments (Spry, 1976). The granoblastic polygonal texture in the potassic group is an advanced stage towards textural re-equilibration, such as is found in metamorphic rocks.

Related to the question of the intricate grain boundaries is that of the integrity of the interface itself, and the nature of the exsolution textures within the perthite. Despite the complex morphology shown by the grain boundaries of the sodic group, the perthite-perthite interface remains essentially undisturbed by crystallisation of interfacial albite, and the exsolution textures are often regular. In the potassic group, on the other hand, albite crystallises as discontinuous beads along the perthite interface, and exsolution lamellae can be seen to be interconnected. Martin and Bonin (1976) and Parsons (1978) agree that such interfacial albite as seen in the potassic group here is evidence for the passage of an aqueous fluid phase along the perthite grain boundaries. The interconnecting perthite lamellae texture is an advanced stage in exsolution over the regular lamellae stage, and also implies the presence of an aqueous fluid phase.

Another tool for testing the postulated sodic-potassic transition is the Al/Si ordering in the feldspars. Reference to the preceding descriptions shows the progressive increase in Al/Si ordering, from the sodic to the potassic group, as depicted by T_1 occupancy and triclinicity (Δ) values. Thermometry arising from these data (Smith, 1974), shows an analogous progressive drop in temperature, the lowest temperature implied being less than $375 \pm 50^\circ\text{C}$ (Wright, 1967) in the potassic group (T34GR). Other mineralo-chemical tools are considered in Chapter 5. In each case the trend has been found to be the same, sodic to potassic.

It is therefore proposed that petrographically a sodic-potassic trend exists, the sodic phase occupying the higher

0.5mm

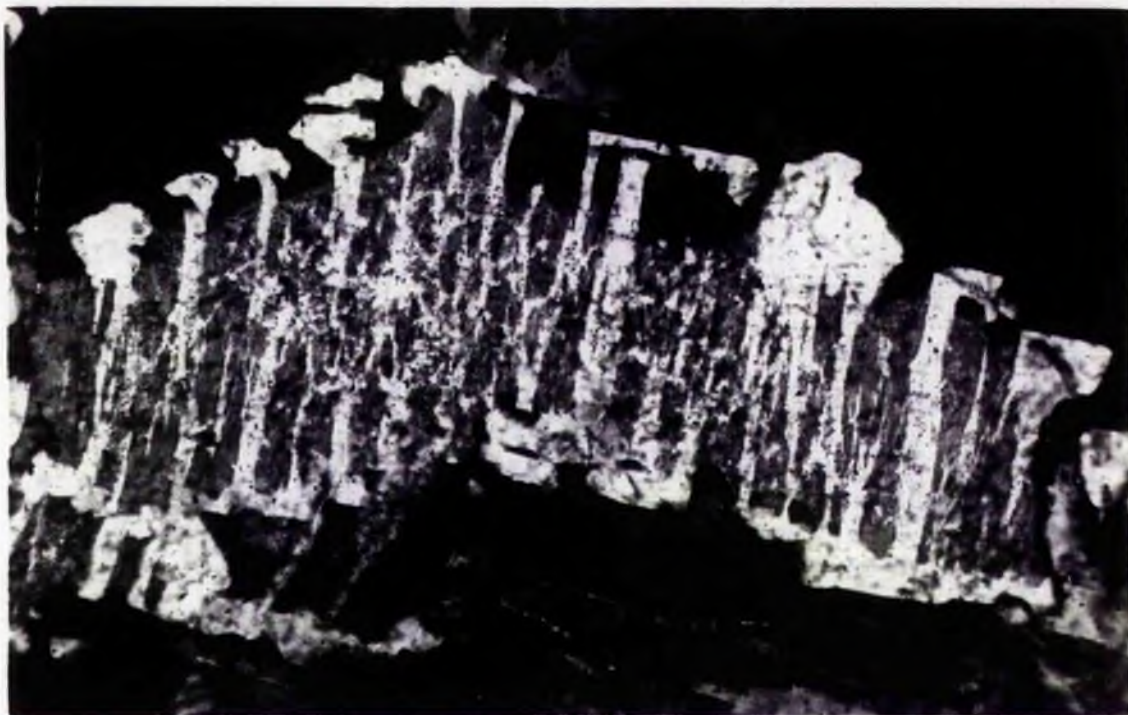


Plate 4.6K Replacement perthitic texture in fine-grained biotite granite (T34BB). Crossed polarised light.

0.5mm

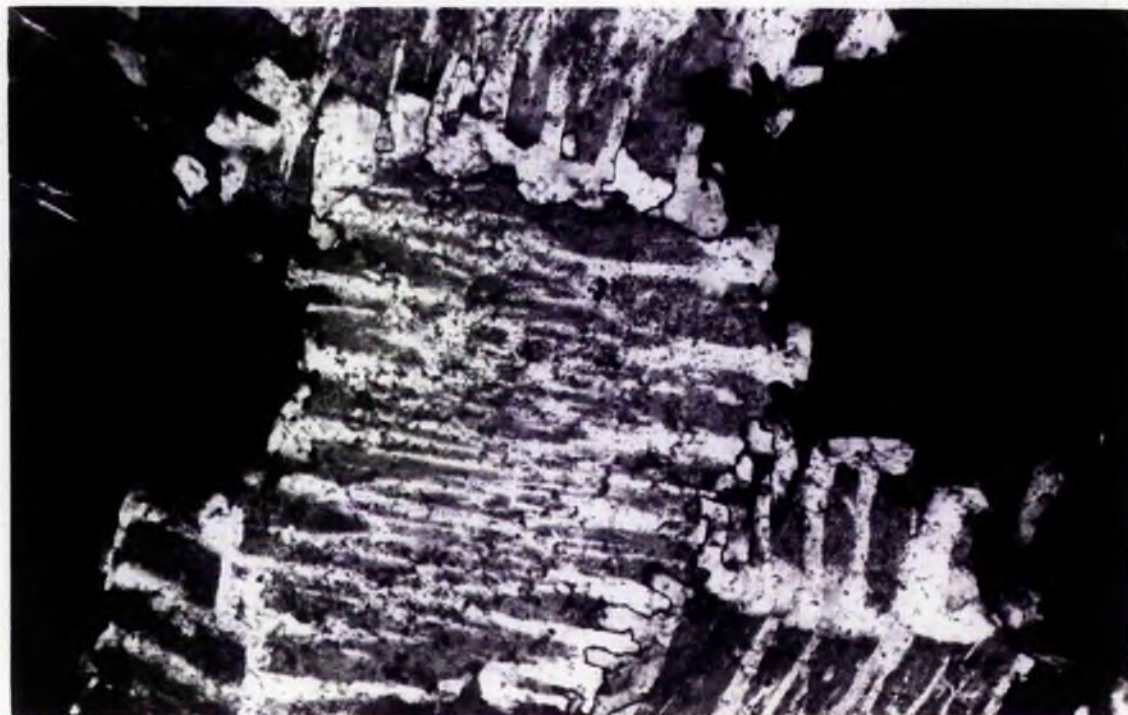


Plate 4.6L Textural relationship between adjoining perthites of the fine-grained biotite granite T34BB. Crossed polarised light.

2mm

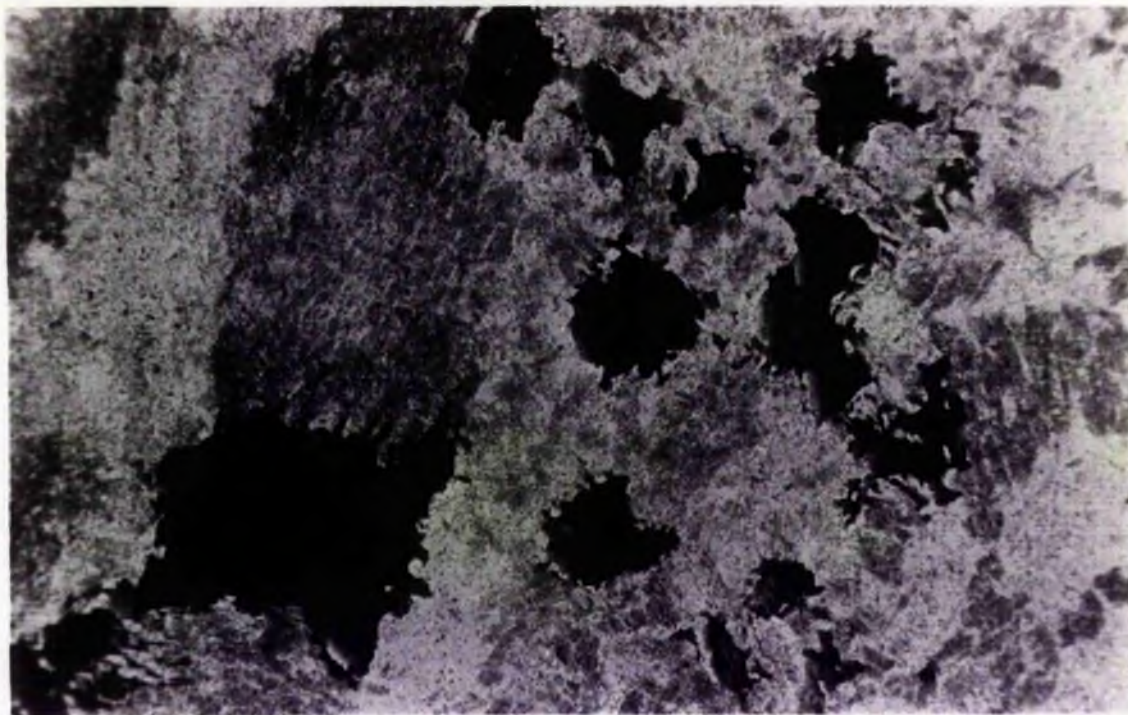


Plate 4.6M Green biotite (dark) with dactylitic outgrowths which selectively replace the K-phase (grey) of surrounding perthites. Biotite is post-exsolution. Fine-grained biotite granite (T34BB). Plane polarised light.

0.5mm

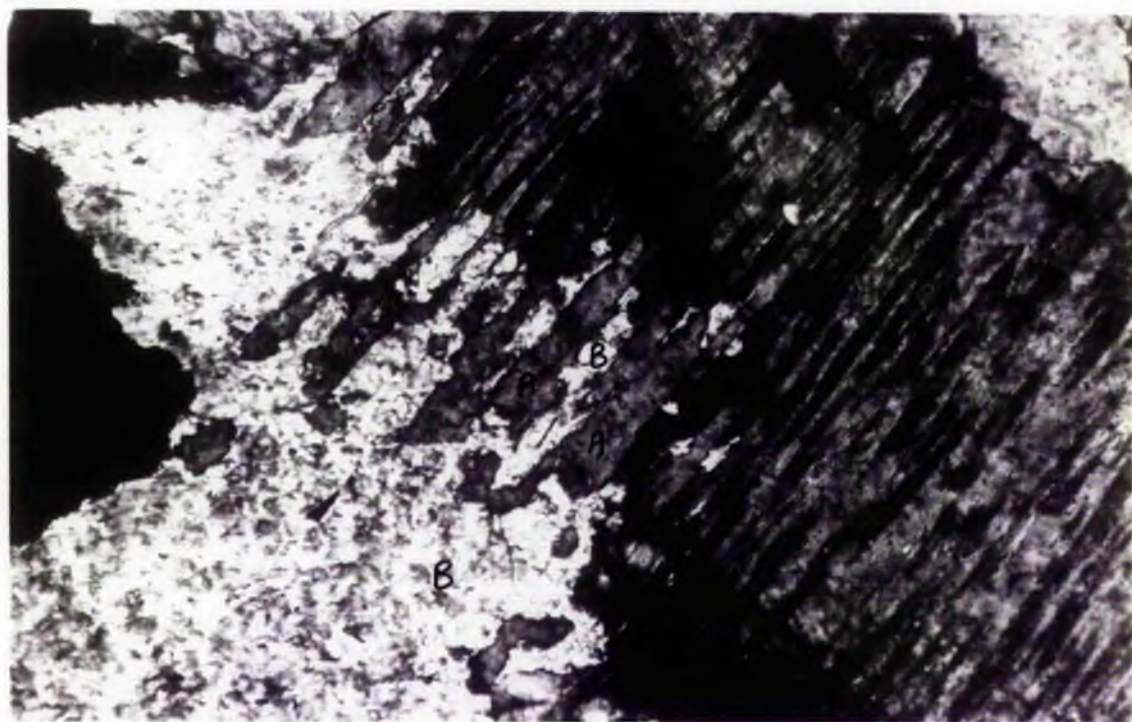


Plate 4.6N Magnification of part of a biotite crystal in Plate 4.6M, showing detailed textural relationship between the biotite (B) and perthite (right) at an advanced stage of selective replacement of the K-phase (black) in the perthite by the biotite. A "lamellar" interdigitation between the biotite and the Na-phase (A) is produced as the K-phase is used up. Crossed polarised light.

temperature region while the potassic phase occupies the lower temperature region.

The actual nature of the sodic and potassic phases of activity in the suite as a whole cannot be discussed until the chemical aspects of the rocks have been examined in detail (Chapters 5 & 6).

The anti-perthite biotite granite T34B and its associated fine-grained facies (T34BB) illustrate the petrographical effect of superimposition of the potassic phase on a 'wall-rock' already affected by an earlier sodic phase of activity. The crystallisation of turbid K-feldspar along the perthite interphase in T34B is analogous to that of interfacial albite, described earlier as related to the presence of an aqueous fluid phase. However, it is the potassic character of the new fluid phase that has left its imprint, in the crystallisation of the K-feldspar instead of albite. The extensive subsolidus modifications of the biotite granite 'wall-rock' are clearly evident in Plates 4.6J, K, L, M and N. Of special interest is the crystallisation of dactylitic outgrowths from biotite (Plates M & N), which selectively replace the K-phase of perthites. Clearly the biotite is post-exsolution and could not have been magmatic. Parsons (pers. comm.) considers that the relevant temperatures for the biotite crystallisation must have been in the region of 450°C or less. With maximum microcline in the anti-perthite granite T34B, prevailing temperatures must have been below 375[±] 50°C, (Wright, 1967).

2. Undersaturated peraluminous 'basement screen'

Hand specimen description The rock is dark green in colour

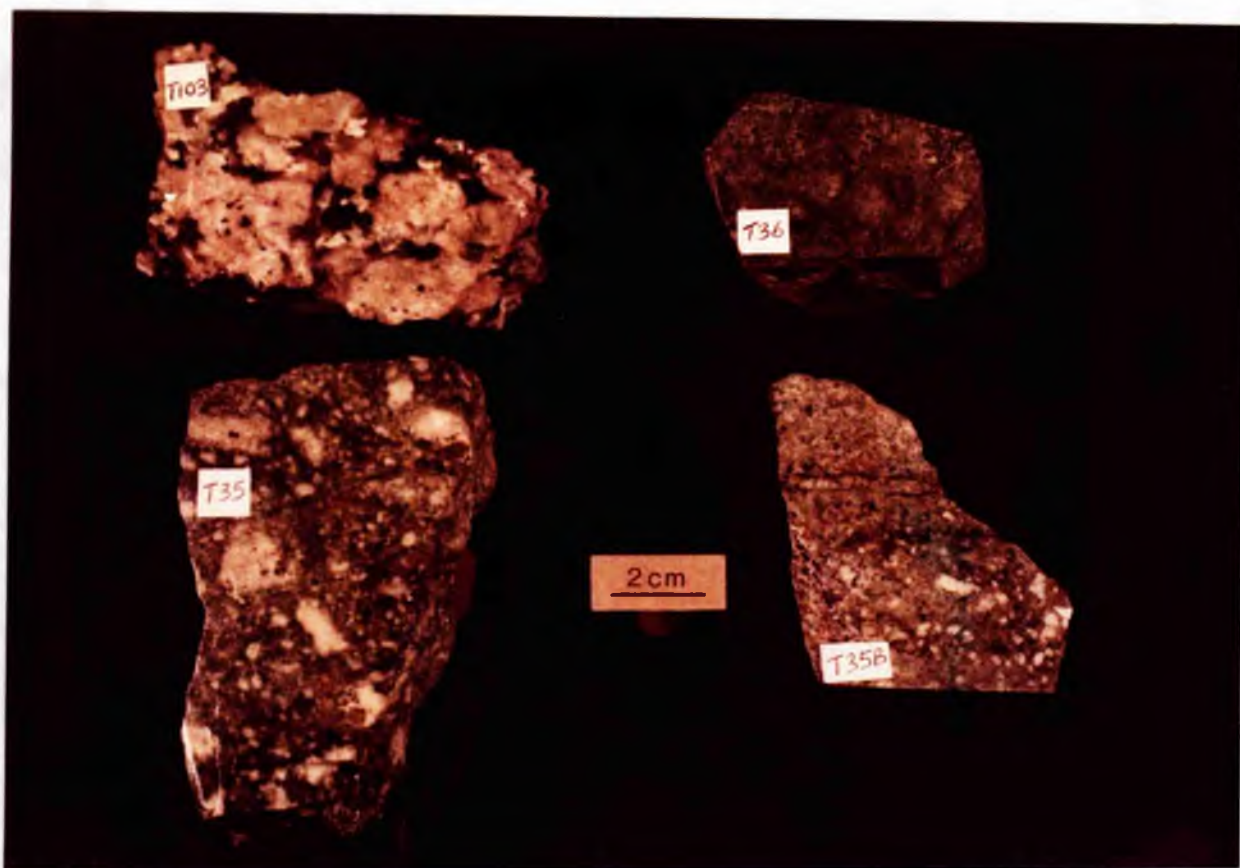


Plate 4.6PA Metasomatically altered 'basement screen' hand specimens showing gradational textural changes from the porphyritic, least altered rock (T35) through an intermediate stage (T35B) to an aphyric, most altered rock (T36). A normal Older Granite basement specimen (T103) is included for comparison.

and may be porphyritic to aphyric in texture. The change in texture is frequent, gradational, and irregular in distribution, and can be observed within the same hand specimen or over a distance of several centimetres in the field. (Plate 4.6PA).

The porphyritic part of the rock (T35) is characterised by megacrysts of sodic plagioclase up to 25x12 millimetres; these constitute up to 25 percent by volume of the rock and are set in a microcrystalline groundmass. The aphyric part (T36) is microcrystalline, while the transitional part is medium-porphyritic with granular plagioclase of up to 5 millimetres across.

A late stage swarm of minute dark veins of hastingsitic amphibole cross-cutting all mineral phases, is prominent and is found in all textural stages of the rock. Where the amphibole vein cuts the plagioclase megacrysts, a zone of whiter feldspar corresponding to a more sodic plagioclase, is developed. There are also irregular and diffuse brown veins and masses of calcite visible macroscopically.

Microscopic features The essential minerals are sodic plagioclase and hastingsitic amphibole, but only the former occurs as megacrysts in the porphyritic parts of the rock.

The plagioclase megacrysts are characteristically zoned such that the core is sharply twinned and relatively free of inclusions, while the rim is feebly twinned, has diffuse boundary with the groundmass and more importantly, is charged with numerous inclusions (Plate 4.6P). Extinction is greater in the rim by up to 5° , giving optically an average core of An_{16} and rim of An_{13} (by symmetrical extinction method). However X-ray data (Martin, perscomm.) give an average composition of An_4 for all megacrysts. This discrepancy between



Plate 4.6P Zoned plagioclase showing 'preferred' orientation of inclusions parallel to the albite twinning in the outer zone. Metasomatically altered "basement screen" (T35). Crossed polarised light.

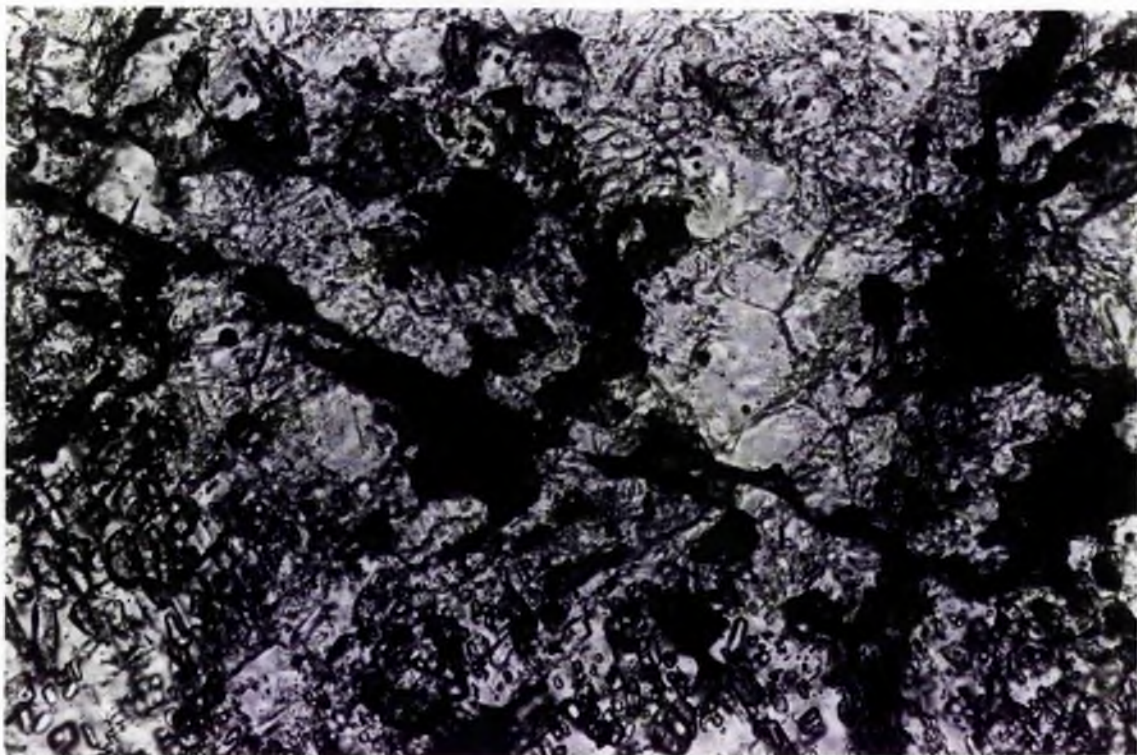


Plate 4.6Q Cross-cutting veins of hastingsite (dark). Metasomatically altered "basement screen". Plane polarised light.

optical and X-ray data is an expression of the anomalous state of the plagioclase and is discussed briefly later.

The amphibole consists essentially of hastingsite (I.M.A. classification, Leake, 1978) but in larger zoned crystals the core consists of hastingsitic hornblende (Table 6D, Chapter 5). Plate 4.6Q shows the form of the hastingsite veins in the general rock fabric.

Among the inclusions in the outer zone of the plagioclase megacrysts are prismatic crystals of hastingsite, epidote, zircon, calcite and others that are extremely difficult to identify optically. All these are characteristically oriented parallel to the albite twin lamellae of the plagioclase (Plate 4.6P). The same species of inclusions above are found in the groundmass as accessory minerals.

The groundmass is inhomogeneous both in grain size and appearance as a result of variable recrystallisation. A mosaic of albite is common.

Special relict features Two relict features found in the megacrystic portion of the rock (T35) are noteworthy. First is the occurrence of a rare (pale yellow) pyroxene with shreds of (green) hastingsite alteration. The pyroxene is non-pleochroic, contrasting with the strongly pleochroic amphibole alteration. The pyroxene has a moderate birefringence, with lower second order interference colours and an extinction angle $\gamma \wedge c$ of 46° . The second relict feature is the occurrence of plagioclase synneusis which is believed to be an original magmatic feature. Within the restricted inter-granular junctions of the plagioclase in the synneusis are small crystals of the above clinopyroxenes.

Discussion The most outstanding petrographic features of this rock are: (a) the anomalous character of the sodic plagioclase megacrysts; (b) the oriented inclusions in the plagioclase and general abundance of accessory minerals in the rock; (c) the cross-cutting amphibole veins, and the abrupt loss of the porphyritic texture; and (d) relict magmatic features.

Discrepancy between optical and X-ray data in feldspars have been found on many occasions (Martin, pers. comm.), although no adequate descriptions have been given of the reasons for such anomalies. These anomalies are believed to be due to "memory effects" or relict features evident in feldspars subjected to intense metasomatism of short duration; the metasomatic effects were not thorough enough to erase the observed inherited features. The discrepancy is perhaps not exclusively optic. In the Tibchi case, it is found that although certain unit cell parameters (β^* versus γ^* , and the calculated separation of the $2\theta_{131}$ and $2\theta_{1\bar{3}1}$ reflections) are in agreement with a plagioclase composition of An_4 , the t_{10} is found to be somewhat lower than expected. It appears therefore that these anomalies have resulted from the reconstitution of oligoclase or andesine under intense but short-lived metasomatism (Martin, pers. comm.).

The oriented inclusions in the outer zone of the plagioclase megacrysts may be briefly explained as resulting from continued growth of the megacryst during the recrystallisation of the groundmass. The crystallisation of these inclusions which are also found in the groundmass as accessory minerals, must have been controlled by the composition planes of the albite twin lamellae in the megacrysts. The abundance of

accessory minerals in general must be related to the bulk composition of the rock (Table 6D, Chapter 5), and the composition of the fluid phase. The conspicuous presence of a carbonate mineral may be due to a CO₂-rich fluid phase.

The eventual loss of the porphyritic texture is inferred to have been caused by several generations of minute (amphibole) veins cross-cutting the plagioclase megacrysts during each episode of groundmass recrystallisation. As these veins cannot be expected to be evenly distributed over the rock, abrupt changes in texture are bound to occur.

The relict magmatic features suggest that the pristine rock was probably an oligoclase or andesine clinopyroxene rock. It is uncertain how much quartz was originally present, but the ensuing metasomatic alteration involved progressive desilication (Table 6D, Chapter 5), if normative nepheline can be used as index. The composition of the hastingsitic amphibole (Chapter 5) would suggest a whole-rock bulk composition that can only be as calcic and aluminous as the basement rocks, but this is by no means certain.

CHAPTER 5
MINERAL CHEMISTRY

5.1 Introduction

The varied mineralogical assemblages described petrographically in Chapter 4 are here further defined in terms of chemical compositions and chemically determined crystallisation histories. It is apparent that, whatever may have been the initial mineralogical character of some of the Tibchi rocks, much of that has now been lost through post-magmatic processes.

In this chapter analytical data are presented for fayalites, pyroxenes, amphiboles, iron-titanium oxide minerals, and a selection of biotites and chlorites.

An attempt is made to establish the crystallisation histories of the Ca-rich pyroxenes and amphiboles. The trends obtained from the pyroxenes apparently portray the magmatic history of the early granitoid rocks. On the other hand, the trends obtained from the amphiboles appear to display the course of postmagmatic events.

The iron-titanium oxides have yielded some useful temperatures and of particular interest is the one related to the crystallisation of the peralkaline syenites.

5.2 Fayalite

5.2.1 General

Published chemical data on fayalites from the Nigerian Younger Granite province are non-existent. Yet fayalite has been optically identified as one of the most important mafic mineral species in the province. It is hoped that the new

TABLE 5.2 FAYALITE ANALYSES

	1	2	3	4	5	6
SiO ₂	30.39	29.85	29.41	29.59	30.56	30.15
TiO ₂	0.03	0.05	0.00	0.03	0.72	0.20
Al ₂ O ₃	0.03	0.04	0.06	0.03	0.09	0.07
Fe ₂ O ₃	0.00	0.00	0.34	0.00	0.10	0.40
FeO	64.26	66.71	66.33	67.38	60.81	65.02
MnO	1.74	1.99	1.77	1.81	3.43	1.01
MgO	3.23	1.05	1.07	0.28	3.47	1.05
CaO	0.36	0.38	0.39	0.32	1.13	2.18
TOTAL	100.04	100.07	99.37	99.44	100.31	100.11
FeO(T)	64.26	66.71	66.63	67.38		

Numbers of ions on the basis of 3 cations

Si	1.003	1.002	0.994	1.005	0.996	1.002
Al ^{IV}	-	-	0.002	-	0.004	-
Al ^{VI}	0.001	0.002	-	0.001	-	0.003
Ti	0.001	0.001	-	0.001	0.018	0.005
Fe ³⁺	-	-	0.009	-	0.004	0.011
Fe ²⁺	1.774	1.872	1.876	1.915	1.659	1.808
Mn	0.049	0.057	0.051	0.052	0.094	0.028
Mg	0.159	0.052	0.054	0.014	0.169	0.052
Ca	0.013	0.014	0.014	0.012	0.039	0.078

Mole percent fayalite component based on $Fa = \frac{100(Fe+Mn)}{(Fe+Mn+Mg)}$

Fa	91.99	97.34	97.45	99.28	91.20	97.26
----	-------	-------	-------	-------	-------	-------

FeO(T) = Total iron as FeO.

All values are expressed in weight percent.

1...Fayalite, Microferrodiorite enclave in quartz porphyry.

2...Fayalite, Quartz porphyry (T60). 3...Fayalite, Quartz porphyry (T105). 4...Fayalite, Quartz porphyry (T115).

5...Fayalite, Obsidian, Pantelleria (Carmichael, 1962).

6...Fayalite, Ferrodiorite, Kangerdlugssuaq, East Greenland (Deer and Wager, 1939).

1-4 = Electron microprobe analyses.

Analyst E.C.Ike

fayalite analyses presented here will provide a chemical definition of the range occurring in the granitoid rocks of the province, until further data from other complexes is forthcoming

Occurrence of fayalite in the Tibchi Complex is restricted to the quartz porphyries and the microferrodiorite enclaves. In the former rock fayalite is present only in the phenocryst phase.

5.2.2 Analytical data

Analyses have been carried out using the electron microprobe. The results are presented in Table 5.2. The original microprobe output of total iron as FeO (supplied in the table as FeO(T) has been recalculated to give Fe₂O₃ and FeO using the method of Finger (1972).

Individual grains of fayalite do not show any significant compositional zonation, nor variation from grain to grain. Therefore compositions for each rock given in the table, represent the average of single grain analyses within the same rock.

Analyses quoted from the literature are intended firstly for general comparison at the appropriate points within the range found in the Tibchi Complex. Secondly, the Fe₂O₃ content in the quoted analyses are of particular interest as discussed below.

5.2.3 Discussion

Fayalite compositions from the Tibchi Complex spread through the conventional range (Fa₉₀-Fa₁₀₀) for the iron-rich

olivines. If the calculated fayalite end-member component (Fa) can be used as an index of fractionation, then it is possible to arrange the new fayalites and their respective host rocks in a progressive order of evolution as follows:
 Fayalite ferroaugite microferrodiorite enclaves (Fa₉₂) →
 Fayalite ferroaugite ferrohedenbergite quartz porphyry (T60; Fa_{97.3}) → Fayalite ferrohedenbergite quartz porphyry (T105; Fa_{97.5}) → Fayalite ferrohedenbergite quartz porphyry (T115; Fa_{99.3}).

The above trend is marked by the progressive enrichment in (Fe + Mn) relative to Mg, this being the basis for the Fa calculation. Despite the above variation, the Mn values remain approximately constant. Genetically related fayalites are thought to exhibit approximately constant Mn content regardless of subsequent fractionation, since the partition coefficient between crystal and liquid is close to unity (Jensen, 1973). This relationship is reported by Neuman (1976) to successfully give an "olivine/liquid Mn geothermometer" for establishing source rocks. Unfortunately use of the above geothermometer was not possible for the present study owing to difficult access to the relevant unpublished thesis.

The Fe₂O₃ recalculation indicates that in the Tibchi fayalites Fe³⁺ was, for most of the evolutionary span of the fayalite-bearing rocks, insignificant.

5.2.4 Summary

The Tibchi fayalites vary in composition from Fa₉₂ to Fa₉₉. The variation enables the host rocks to be arranged in an increasing order of fractionation, with the micro-

ferrodiorite enclaves earliest and the quartz porphyry (T115) latest. It is believed on the grounds of approximately constant Mn content that the rocks arranged in the above sequence were comagmatic. It is also believed that the sequence represents a fractionation trend.

5.3 Pyroxenes

5.3.1 General

Although several analyses of Na-rich pyroxenes have been published for the Nigerian Younger Granite province, only one ferraugite analysis (Borley, 1963a) has so far been presented with regard to the Ca-rich pyroxenes. Both of these groups of pyroxenes are equally important with respect to occurrence and distribution in the Younger Granites. The reason for only one analysis of the Ca-rich pyroxenes may be due to difficulty found in separation. It would be easier to separate the usually coarser-grained Na-rich pyroxenes from their host rocks than it would for the usually finer-grained Ca-rich pyroxenes. The latter pyroxenes are also commonly intergrown with iron-oxide minerals; this situation would naturally make the separation process even more difficult and unsatisfactory. The analytical technique adopted in the present study overcomes the problems above associated with mineral separation.

Pyroxenes of the Tibchi Complex are dominantly the Ca-rich species namely the ferroaugite-ferrohedenbergite series. These have only been found in the quartz porphyries, the granite porphyries and the various fine-grained cognate enclaves located in these porphyries. In both types of porphyries ferrohedenbergite occurs as phenocrysts as well as groundmass constituents, while ferroaugite is apparently confined to the

phenocryst phase.

Aegirine-augite occurs in one locality (T64) within the hydrothermally altered segment of the granite porphyry ring-dyke. No sample from this locality was analysed. The only other occurrence of aegirine-augite observed, is in the sodic syenite (T34C). Analyses from this are presented.

The nomenclature adopted for the Ca-rich pyroxenes is based on Poldervaart and Hess (1951) and that of the Na-rich group on the suggested restrictions of Deer et al. (1978).

5.3.2 Analytical data

Sixty microprobe analyses of Ca-rich pyroxenes have been obtained, from eight polished thin sections belonging to seven rocks. Analyses from the porphyries refer only to the phenocryst phase. Additionally, five analyses of Na-rich pyroxenes, from one polished thin section, were also obtained.

Owing to the lack of variation in the Na-rich (aegirine-augite) compositions (probably partly because only one rock sample was involved), no discussion of the results has been initiated. In addition uncertainty exists about the true connection between the sodic syenite (T34C), host rock of the aegirine-augite, and the porphyries in which the Ca-rich pyroxenes occur. This uncertainty has necessitated extreme caution in attempting to correlate the aegirine-augite with the Ca-rich pyroxenes. Consequently the descriptions, diagrams and discussions presented hereafter pertain almost exclusively to the Ca-rich pyroxenes.

In two rocks (quartz porphyry (T60) and granite porphyry ring-dyke (T11)) the intimate relationship between ferroaugite

TABLE 5.3A REPRESENTATIVE FERROAUGITE ANALYSES

	1	2	3	4A*	5	6A	6B	6C	7	8	9	10	11
SiO ₂	49.12	49.18	48.68	49.30	49.06	49.34	49.05	48.41	47.82	48.76	49.10	49.44	48.18
TiO ₂	0.62	0.60	0.70	0.08	0.03	0.34	0.31	0.34	0.75	0.47	0.63	0.83	0.70
Al ₂ O ₃	1.22	1.21	1.57	1.32	0.52	0.51	0.45	0.45	2.59	0.99	1.07	1.31	1.06
Fe ₂ O ₃	1.30	1.77	3.22	0.72	0.68	1.48	2.51	1.78	3.37	3.36	3.17	0.88	1.46
FeO	21.75	21.64	20.12	22.24	25.64	23.55	24.05	25.46	20.55	19.42	21.97	21.64	26.08
MnO	0.59	0.56	0.67	0.66	0.68	0.65	0.76	0.77	0.89	0.73	0.98	0.42	0.53
MgO	6.36	5.99	5.91	6.62	3.71	4.79	4.28	3.31	4.76	5.93	3.70	6.92	3.52
CaO	18.66	18.99	18.38	17.86	18.73	19.12	19.10	18.76	18.52	19.47	18.86	18.23	18.90
Na ₂ O	0.38	0.47	0.84	0.46	0.39	0.44	0.44	0.45	0.90	0.66	0.92	0.29	0.23
K ₂ O	x	x	x	x	x	0.01	x	x	0.26	0.11	0.11	0.03	0.04
TOTAL	100.00	100.41	106.09	99.26	99.44	100.23	101.01	99.73	100.41	99.90	100.51	99.99	100.70
FeO(T)	22.92	23.24	23.02	22.88	26.26	24.89	26.31	27.06					
Numbers of ions on the basis of 4 cations													
Si	1.948	1.946	1.928	1.963	1.991	1.973	1.958	1.969	1.894	1.937	1.958	1.949	1.941
Al ^{IV}	0.052	0.054	0.072	0.037	0.009	0.024	0.024	0.022	0.106	0.048	0.042	0.051	0.051
Al ^{VI}	0.005	0.002	0.001	0.025	0.016	-	-	-	0.015	-	0.011	0.008	-
Ti	0.019	0.018	0.021	0.003	0.001	0.010	0.009	0.010	0.022	0.012	0.014	0.024	0.021
Fe ³⁺	0.039	0.053	0.096	0.022	0.021	0.045	0.075	0.054	0.100	0.100	0.096	0.026	0.044
Fe ²⁺	0.721	0.716	0.666	0.740	0.870	0.787	0.803	0.866	0.681	0.654	0.733	0.713	0.879
Mn	0.020	0.019	0.022	0.022	0.023	0.022	0.026	0.026	0.030	0.024	0.034	0.012	0.019
Mg	0.376	0.353	0.349	0.392	0.224	0.285	0.254	0.201	0.281	0.351	0.221	0.405	0.211
Ca	0.792	0.805	0.780	0.761	0.814	0.819	0.816	0.817	0.786	0.829	0.805	0.771	0.816
Na	0.029	0.036	0.065	0.036	0.031	0.034	0.034	0.035	0.069	0.052	0.072	0.024	0.017
K	-	-	-	-	-	-	-	-	0.013	0.005	0.005	0.002	0.002
Atomic percent													
Ca	40.66	41.37	40.89	39.29	41.70	41.83	41.34	41.60	41.85	42.5	42.6	40.0	41.5
Fe	40.04	40.49	42.43	40.47	46.82	43.61	45.79	48.17	43.19	39.5	45.7	39.0	47.8
Mg	19.30	18.14	16.68	20.24	11.48	14.56	12.87	10.23	14.96	18.0	11.7	21.0	10.7
FeO(T) Total iron as FeO. Fe = (Fe ²⁺ + Fe ³⁺ + Mn). x Less than 0.004% or absent. All values expressed in weight percent.													

1,2,3... Single grains of ferroaugite, fayalite ferroaugite microferrochlorite enclave in quartz porphyry. 4A, 5... Single grains of ferroaugite phenocrysts, Pyroxene granite porphyry ring-dyke (T11). 4A* = Core of an extensively zoned phenocryst with rim of ferroaugite phenocryst (for analysis of rim see no. 17B* Table 5.3B). 6A, 6B, 6C... Zoned skeletal (quenched) ferroaugite phenocryst, Fayalite pyroxene quartz porphyry (T60). 7... Ferroaugite from the Pankshin syenite, Sara-Fier Complex, Nigeria (Borley, 1963). 8, 9... Ferroaugites from pitchstones, East Iceland (Carmichael, 1960). 10, 11... Ferroaugites from ferrodiorites, Upper zone, Skaergaard Intrusion, East Greenland (Brown and Vinesent, 1963).

Nos. 1-7 refer to the Tibchi Complex, analyses by electron microprobe.

Analyst E.C. Ike

TABLE 5.3B REPRESENTATIVE FERROHEDENBERGITE ANALYSES, TIBCHI COMPLEX

	1	2	3	4	5A	5B	7	8	9
SiO ₂	48.14	49.69	48.51	47.52	47.74	48.40	46.81	47.95	48.37
TiO ₂	0.69	x	0.33	0.74	0.70	0.32	0.79	0.40	0.17
Al ₂ O ₃	1.57	0.11	0.43	0.93	0.90	0.45	0.68	0.29	0.27
Fe ₂ O ₃	3.02	0.58	1.20	1.90	0.84	1.07	2.23	1.10	2.16
FeO	24.72	27.01	28.69	25.69	28.23	28.73	28.86	28.92	26.02
MnO	0.76	0.71	0.74	0.89	0.82	0.76	0.89	0.78	0.80
MgO	3.12	2.68	1.70	2.64	1.78	1.37	0.62	1.27	2.34
CaO	18.02	19.06	18.77	19.39	18.63	18.62	18.60	18.59	19.68
Na ₂ O	0.88	0.55	0.39	0.29	0.36	0.51	0.43	0.42	0.38
K ₂ O	x	x	x	0.01	x	0.01	x	x	x
TOTAL	100.92	100.39	100.76	100.00	100.00	100.24	99.91	99.72	100.19
FeO(T)	27.44	27.53	29.77	27.39	28.99	29.68	30.86	29.91	27.97
Numbers of ions on the basis of 4 cations									
Si	1.931	2.010	1.977	1.938	1.958	1.984	1.941	1.980	1.971
Al ^{IV}	0.069	-	0.021	0.045	0.043	0.016	0.033	0.014	0.013
Al ^{VI}	0.005	0.005	-	-	-	0.006	-	-	-
Ti	0.021	-	0.010	0.023	0.022	0.010	0.025	0.012	0.005
Fe ³⁺	0.091	0.018	0.037	0.058	0.026	0.033	0.069	0.034	0.066
Fe ²⁺	0.829	0.913	0.977	0.876	0.968	0.984	1.001	0.999	0.886
Mn	0.026	0.024	0.025	0.031	0.028	0.026	0.031	0.027	0.027
Mg	0.187	0.161	0.103	0.161	0.109	0.083	0.039	0.078	0.142
Ca	0.774	0.826	0.819	0.847	0.818	0.817	0.826	0.822	0.859
Na	0.068	0.043	0.031	0.023	0.028	0.041	0.035	0.034	0.030
K	-	-	-	-	-	0.001	-	-	-
Atomic percent									
Ca	40.59	42.53	41.76	42.93	41.97	42.04	42.02	41.94	43.38
Fe	49.61	49.18	52.98	49.91	52.44	53.68	56.00	54.08	49.45
Mg	9.80	8.29	5.26	8.16	5.59	4.28	1.98	3.98	7.17

FeO(T) Total iron as FeO.

Fe = (Fe²⁺ + Fe³⁺ + Mn).

x Less than 0.004%.

1..Ferrohedenbergite, Microferrodiorite enclave in quartz porphyry. 2,3..Ferrohedenbergite, Microsyenite enclave in quartz porphyry. 4,5A,5B,7..Ferrohedenbergite phenocrysts, Quartz porphyry (T60). 8..Ferrohedenbergite phenocryst, Quartz porphyry (T169). 9..Ferrohedenbergite phenocryst, Quartz porphyry (T168). 10A,10B..Zoned ferrohedenbergite phenocrysts, Quartz porphyry (T105). 14A,14B..Zoned phenocryst, Sodian ferrohedenbergite phenocryst with rim of ferrohedenbergite, Quartz porphyry (T135).

10A	10B	14A	14B	15A	15B	16A	16B	17B*	18A	18B
47.36	47.80	48.68	47.67	47.82	48.49	47.95	48.78	48.72	47.46	48.64
0.05	0.02	0.25	0.39	0.30	0.29	0.23	0.26	x	0.08	x
0.93	0.40	0.20	0.49	0.30	0.23	0.23	0.54	0.22	0.90	0.19
2.96	2.57	5.34	0.92	1.77	2.87	0.95	2.66	4.71	1.93	2.43
26.92	27.61	24.60	29.77	29.34	27.95	30.08	27.52	23.91	28.32	26.51
0.91	0.82	0.79	0.76	0.76	0.76	0.65	0.80	0.74	0.78	0.79
1.45	1.43	0.96	1.12	0.32	0.40	0.13	0.18	1.74	0.92	1.34
19.09	18.71	17.09	17.36	18.87	17.66	18.82	15.44	18.64	18.97	19.36
0.39	0.39	2.04	0.43	0.57	1.34	0.54	2.19	1.43	0.39	0.79
x	x	x	0.19	x	x	x	x	x	x	x
100.06	99.75	99.95	99.10	100.05	99.99	99.58	98.37	100.11	99.75	100.05
29.59	30.01	29.41	30.59	30.94	30.53	30.94	29.91	28.15	30.06	28.70
1.946	1.970	1.986	1.984	1.979	1.994	1.994	2.025	1.979	1.961	1.990
0.045	0.019	0.010	0.016	0.015	0.006	0.006	-	0.011	0.039	0.009
-	-	-	0.008	-	0.006	0.005	0.026	-	0.005	-
0.002	0.001	0.008	0.012	0.010	0.009	0.007	0.008	-	0.003	-
0.092	0.080	0.164	0.029	0.055	0.089	0.030	0.083	0.144	0.060	0.075
0.925	0.957	0.839	1.036	1.015	0.961	1.046	0.955	0.812	0.978	0.907
0.032	0.028	0.027	0.027	0.027	0.026	0.023	0.028	0.025	0.027	0.027
0.089	0.088	0.058	0.070	0.020	0.025	0.008	0.011	0.105	0.056	0.081
0.840	0.826	0.747	0.774	0.836	0.778	0.838	0.687	0.811	0.839	0.848
0.031	0.032	0.162	0.035	0.045	0.107	0.044	0.176	0.113	0.031	0.063
-	-	-	0.010	-	-	-	-	-	-	-
42.47	41.74	40.71	39.98	42.81	41.41	43.08	38.92	42.75	42.81	43.76
53.03	53.81	56.13	56.40	56.17	57.26	56.51	60.43	51.71	54.33	52.06
4.50	4.45	3.16	3.62	1.02	1.33	0.41	0.65	5.54	2.86	4.18

A, B = Core, Rim respectively.

All values are expressed in weight per cent.

15A, 15B..Zoned ferrohedenbergite phenocryst, Quartz porphyry (T115). 16A, 16B..Zoned ferrohedenbergite phenocryst with sodian ferrohedenbergite rim, Quartz porphyry (T115).

17B*..Rim of zoned ferroaugite, for analysis of core see ferroaugite, Table 5.3A no.4A*.

Granite porphyry ring-dyke (T11). 18A, 18B..Zoned ferrohedenbergite phenocryst, Granite

porphyry ring-dyke (T11).

Electron microprobe analyses. Analyst E.C.Ike

and ferrohedenbergite is found to be inextricable since: firstly, both pyroxenes occur as discrete phases within the same rock, and secondly as co-existing phases within the same phenocryst. In the other five rocks, the pyroxene compositional variations within each rock is found to be confined to either the ferroaugite field or that of ferrohedenbergite. Despite the transitional link in (T60) and (T11), analyses for the ferroaugites and ferrohedenbergites are presented separately, in Tables 5.3A and 5.3B respectively. Information is supplied in the tables for locating the relevant transitional grains between the two groups. Fe_2O_3 recalculation is based on Finger (1972).

5.3.3 Discussion

(i) Zoning in individual grains of Ca-rich pyroxenes

Zoning appears to be most extensive in the pyroxenes of the granite porphyry ring-dyke in comparison to those of the quartz porphyries and the primitive fine-grained enclaves.

For example, a single zoned phenocryst in the granite porphyry ring-dyke (T11) has the following compositions in mole percent:

Core: $\text{Ca}_{39.29}\text{Fe}_{40.47}\text{Mg}_{20.24}$ (analysis no. 4A*, Table 5.3A)

Rim: $\text{Ca}_{42.75}\text{Fe}_{51.71}\text{Mg}_{5.54}$ (analysis no. 17B*, Table 5.3B)

The above zonation represents a decrease from core to rim of 14.70 mole percent of Mg and a commensurate enrichment in total Fe plus Ca. Conventionally this may be regarded as a typical normal zoning. This zoning is accompanied by a decrease towards the rim of Al and Ti, and an increase in Na and Fe^{3+} .

Reverse zoning has only occasionally been encountered in the series but its occurrence in the sodian ferrohedenbergite

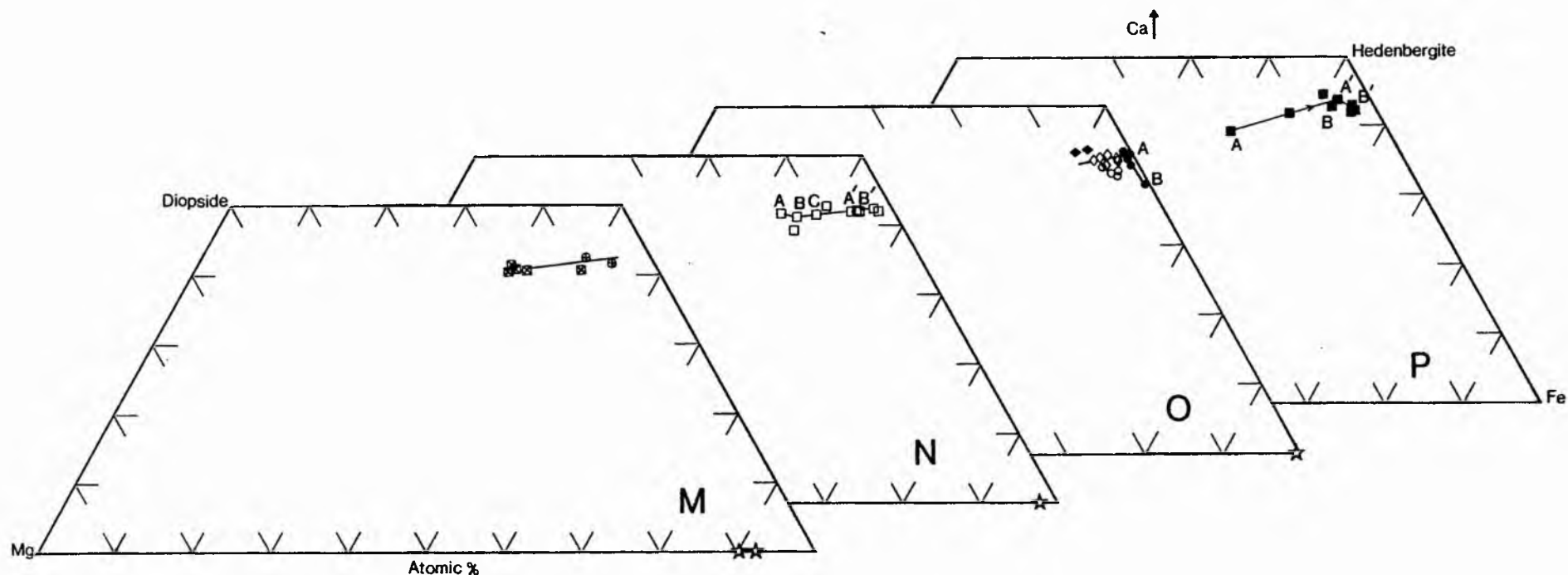


Figure 5.3.3.A Crystallisation trends of the Ca-rich pyroxenes, Tibchi Complex, plotted separately for the following rocks/groups: M = Cognate enclaves in the porphyries; N = Quartz porphyry T60; O = other quartz porphyries; P = Granite porphyry ring-dyke (T11). Symbols are as follows. Enclaves: squares with crosses = microferrodiorite; circles with crosses = microsyenite; Quartz porphyries: open squares = T60; filled diamonds = T169; open diamonds = T105; open circles = T135; filled circles = T115. A(A') = Cores, B(B') C(C') = rims, of same grains of pyroxene. Solid lines = approximate trends. Stars = compositions of co-existing fayalites.

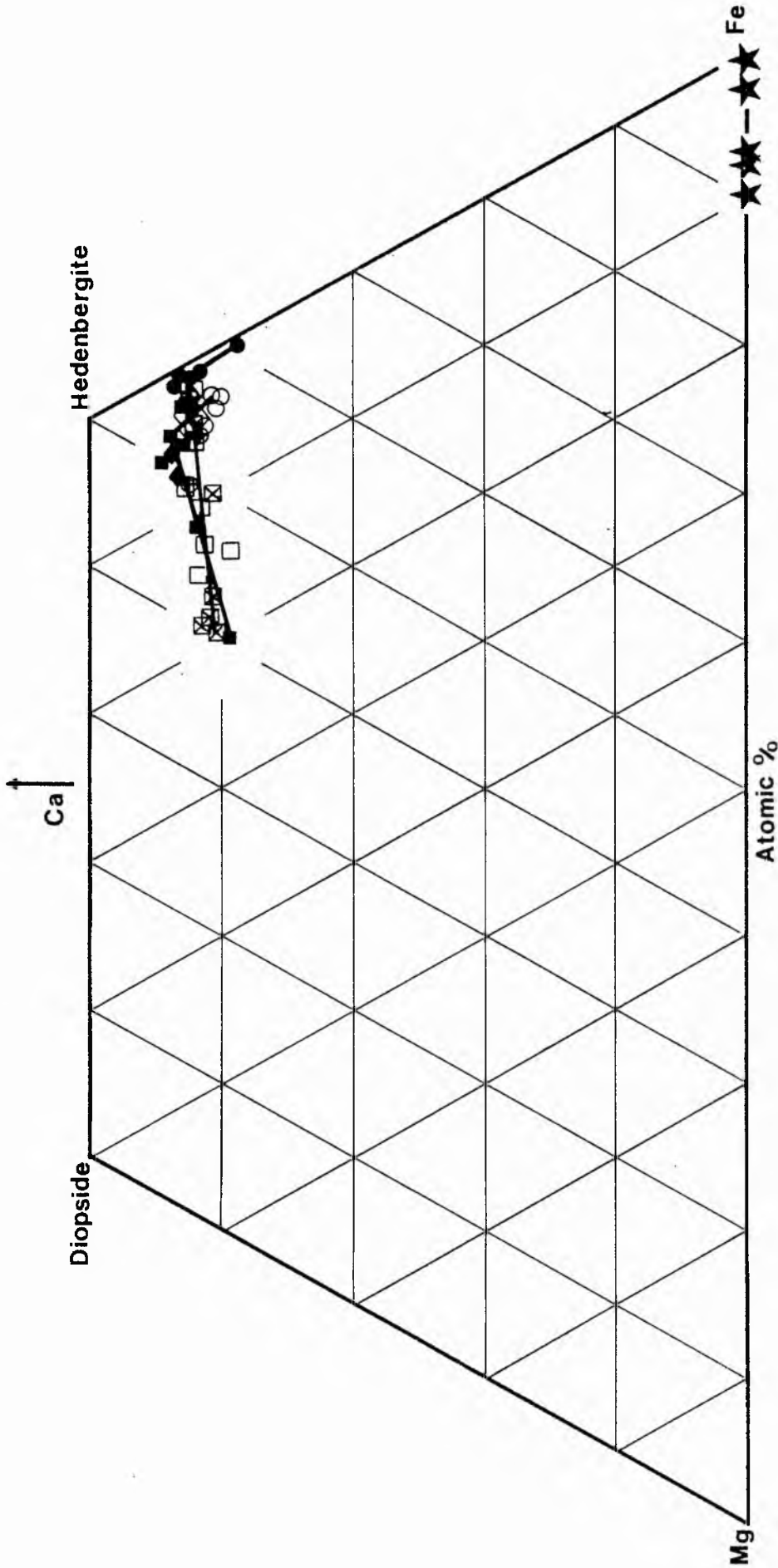


Figure 5.3.3B Crystallisation trends of the Ca-rich pyroxenes, Tibchi Complex, showing the two-fold pattern obtained when all the individual quadrilaterals of Figure 5.3.3A are combined. The two trends are similar in shape. The shorter trend, also with the greater slope, is the "granite porphyry pyroxene trend". The longer trend reaching the Hd-Fe sideline is the "quartz porphyry pyroxene trend". Stars = Co-existing fayalites.

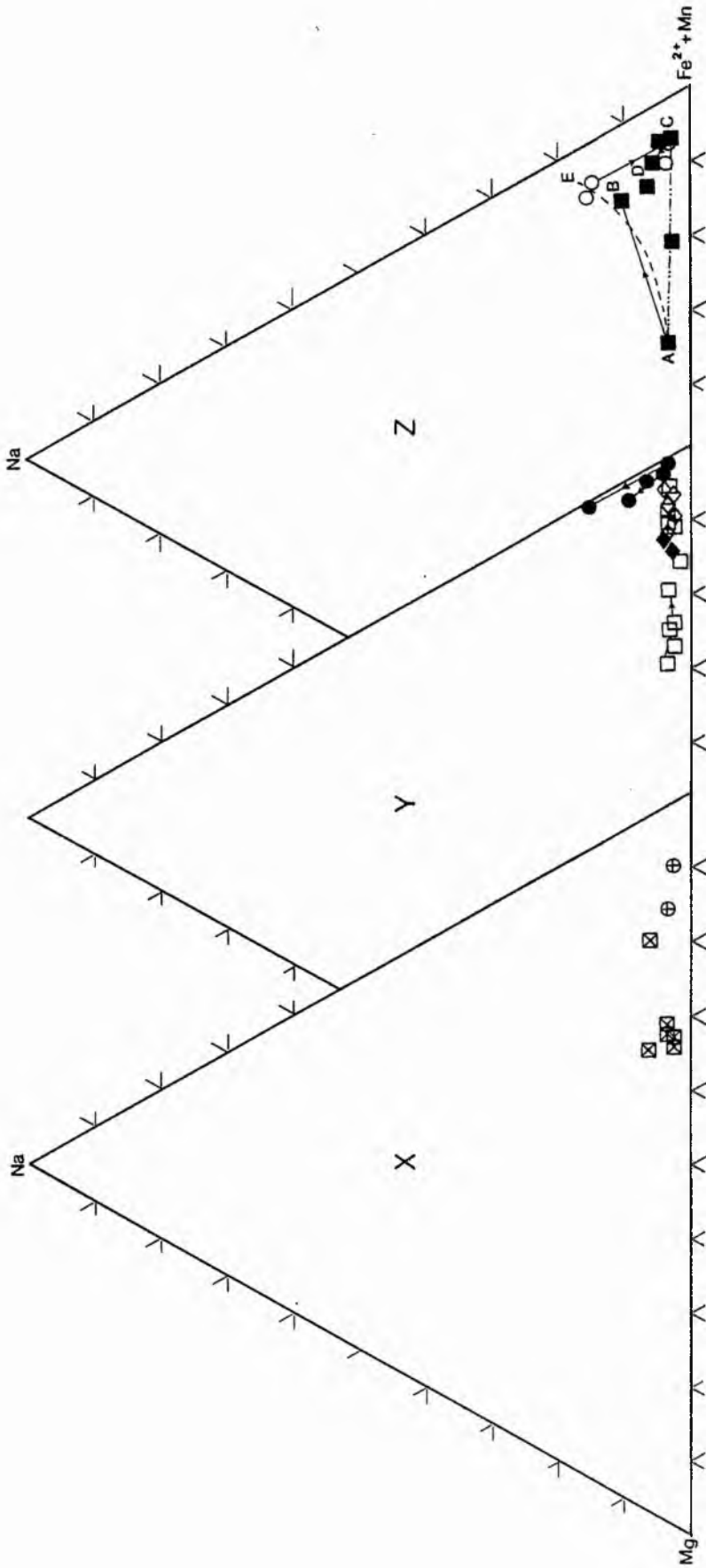


Figure 5.3.3C Plots of the Ca-rich pyroxenes, Tibchi Complex, in mole percent Mg (Diopside), Fe²⁺ + Mn (Hedenbergite) and Na (Acmite). Pyroxenes are grouped according to host rocks: X = Enclaves in porphyries; Y = Quartz porphyries; Z = Granite porphyry and quartz porphyry T135. Tie lines join zoned crystals with arrows pointing to the rims. Symbols are as in Figure 5.3.3A.

of the quartz porphyry (T135) probably deserves further comment (see representative analyses nos. 14A, 14B, Table 5.3B, A = Core, B = Rim). There is a consistent increase, from core to rim, of Fe^{2+} and Al, while Na and Fe^{3+} decrease conspicuously. It may be noted that total Fe remains almost constant in the cores and rims, depicting therefore, simply a change in $\text{Fe}^{3+}/\text{Fe}^{2+}$ ratio. The ferrohedenbergite rim formed during the reversed zoning contains a significant amount of K which is virtually absent elsewhere. It is tempting to conclude that the observed significant enrichment in K and Fe^{2+} in the rim may be indicating that the conditions that caused the reversed zoning may have been potassic rather than sodic in character as well as ferrous rather than ferric in relative oxidation state.

(ii) Crystallisation trends of the Ca-rich pyroxenes

The compositions of analysed Ca-rich pyroxenes have been recalculated to mole percent of the three principal cation components (besides Si) namely Ca, Fe and Mg (where $\text{Fe} = \text{Fe}^{2+} + \text{Mn} + \text{Fe}^{3+}$). These are then plotted in separate pyroxene quadrilaterals (Figure 5.3.3A) for purposes of comparison.

In Figure 5.3.3A it may be observed that the microferrodiorite and microsyenite enclaves together define a continuous linear trend. The quartz porphyry (T60) alone, (Figure 5.3.3A), defines a trend identical to that of the primitive enclaves above. The trend of the enclaves, however, begins and terminates earlier than that of the quartz porphyry (T60). The overlap between the above two trends and the progression of the (T60) trend towards the Hedenbergite-

Ferrosilite sideline, in apparent furtherance of the trend begun by the enclaves, is considered to be an evolutionary sequence. Such a scheme would be consistent with the observed field relationship where the quartz porphyry (T60) is later than, and encloses, the enclaves. Similarly the crystallisation trend of the other quartz porphyries can be seen to overlap the trend already defined. More importantly the crystallisation trend is observed to be extended to the Hedenbergite-Ferrosilite sideline, with an apparent deflection of the trend towards the Ferrosilite corner. Zoned crystals enable the crystallisation trends to be inferred with confidence.

The course of crystallisation of the granite porphyry pyroxenes (Figure 5.3.3A) is, on its own, continuous and well defined. Nearer the Hedenbergite-Ferrosilite sideline, its linear trend is deflected towards the Ferrosilite corner, as in the case of the final stages of the quartz porphyry trend. The slope of the granite porphyry pyroxene trend can be seen to be steeper and directed towards Hedenbergite when compared with the trends of the enclaves and quartz porphyries.

Hence when all the individual quadrilaterals of Figure 5.3.3A are put together, the two trends emerge (Figure 5.3.3B). One trend thus represents the crystallisation history of the pyroxenes of the cognate enclaves and the quartz porphyries. This trend is hereafter called "the quartz porphyry pyroxene trend". The other trend represents the crystallisation history of the pyroxenes of the granite porphyry, hereafter called "the granite porphyry pyroxene trend". Both trends are summarised below:-

The quartz porphyry pyroxene trend. This trend begins in the ferroaugite field at a composition close to $\text{Ca}_{40}\text{Fe}_{40}\text{Mg}_{20}$, the composition of the microferrodiorite enclaves. The entire trend is almost a straight line connection between the observed origin above, and a point almost on the Hedenbergite-Ferrosilite sideline at $\text{Ca}_{43.1}\text{Mg}_{0.4}\text{Fe}_{56.5}$ composition. This composition is observed to mark the end of crystallisation of Ca-rich pyroxenes in the Skaergaard and the Bushveld Intrusions (Brown and Vincent, 1963; Atkins, 1969). No natural composition with less than $\text{Mg}_{0.4}$ has yet been recorded, to the writer's knowledge. It is interesting to note therefore that at $\text{Mg}_{0.4}$ mole percent the Tibchi quartz porphyry trend is deflected sharply, apparently towards the ferrosilite apex. The maximum pseudo-enrichment in Fe in the new direction gives a composition of $\text{Ca}_{38.9}\text{Fe}_{60.4}\text{Mg}_{0.7}$. It will be shown later that the new direction has indeed departed from the pre-existing CaFeMg compositional plane, moving towards Acmite in the Acmite-Wollastonite-Enstatite-Ferrosilite tetrahedron.

The sodian ferrohedenbergites of quartz porphyry (T135), which appear to deviate from the main trend towards Fe enrichment, can be explained similarly as not lying within the CaFeMg plane, but also moving towards the acmite apex.

The Granite porphyry pyroxene trend. Crystallisation apparently began in the ferroaugite field at a point close to the beginning of the quartz porphyry pyroxene trend. Within the context of available data, this common point of origin shown by the two trends may provisionally be interpreted as indicating identical magmatic parental liquid(s).

Crystallisation at the middle stages of the trend shows an apparent preferential enrichment in Ca relative to Fe as Mg was depleted. A peak in Ca enrichment is reached at Ca_{44.5} mole percent, whereupon a dramatic deflection towards Fe is observed. Compositionally no real difference in Ca content can be seen to exist between the pyroxenes of the granite porphyry and the quartz porphyry at that point of apparent Ca enrichment in the granite porphyry trend. The reason for the relative displacement of the trends is not believed to be due to absolute Ca enrichment but, as will be shown later, due to upward rise of the granite porphyry trend, from the onset, towards Acmite.

The deflection near the end of the granite porphyry pyroxene trend will be shown later (when the acmite component is included in the discussion), to have followed a course that coincides with the apparent deviation, from the quartz porphyry trend, of sodian ferrohedenbergites from T135.

(iii) The role of Na and Fe³⁺ in the crystallisation history of the Ca-rich pyroxenes, Tibchi Complex

Nolan's (1969) experimentally determined data was perhaps the first firm confirmation of earlier postulates that a complete solid solution series could exist in the 'ternary' system Diopside-Hedenbergite-Acmite. The solid-solution between acmite and diopside-hedenbergite series is postulated by Nolan (op. cit.) to be dependent on the chemical substitution of NaFe³⁺ for Ca(Mg, Fe²⁺). Evidence for the above solid solution is now abundant (Larsen, 1976; Barker and Hodges, 1977; Ferguson, 1978). Therefore, consideration of the crystallisation history of the Ca-rich pyroxenes requires some

account of the role of the Na, Fe³⁺ components during crystallisation.

It is now common practice to represent the above 'ternary' system by plotting the mole percent Mg (Diopside), Fe²⁺ + Mn (Hedenbergite) and Na (Acmite). Figure 5.3.3C shows plots of the Tibchi Ca-rich pyroxenes on that basis.

From the above plots it may be observed that the pyroxenes of the enclaves show a consistent low level of the acmite component throughout their crystallisation history. The quartz porphyries show the same except for the last member of the series (T115) which shows significant enrichment of the acmite component in the rims of zoned phenocrysts.

Barker and Hodges (1977) have observed the change in alkali rocks of "sodian augite toward hedenbergite, and then toward acmite. The more sodic pyroxenes crystallised later than feldspars and nepheline from residual liquids after emplacement at the now-exposed level". Ferguson (1978) noted that "the presence of late crystallising Na-rich pyroxenes is related to the development of peralkalinity in the late-stage melts". Clearly the sodian ferrohedenbergite rims in quartz porphyry T115 were late in occurrence, and had developed only in the last member (T115) of the quartz porphyry series in Figure 5.3.3C no.Y. Therefore if the late Na-pyroxene rims are regarded as evidence for development of peralkalinity (as quoted above) then the residual fraction of the quartz porphyry trend must have been peralkaline in contrast to the preceding main trend liquid.

The case of the granite porphyry pyroxene trend (Figure 5.3.3C no.Z) is notably different. The join AC in the above figure indicates that the pyroxenes here may have fractionated

initially in the same (low acmite) condition as did those of the quartz porphyries. Especially significant is that the zoned crystal CD (C = core, D = rim) probably indicates that deflection towards Acmite apex took place as expected (ref. the quartz porphyry trend) at the natural end of the granite porphyry trend. If the above completion of trend was the case, then, all points of composition above AC may be regarded as only a distortion of an already established trend.

There are at least two possible ways to account for the above distortion:

Either (a) It occurred after the trend had terminated unperturbed as AC. In this case the zoning CD would be contemporaneously developed on the last crystal, as AB would on the first. The most probable explanation for such a situation would be that the residual peralkaline fraction was kept in contact with the initial crystalline phases for an appreciably long time.

Or (b) The distortion occurred soon after crystallisation had begun, and as the latter continued, the distortion had the effect of broadening the axis of the fractionation trend as a result of progressive enrichment in the acmite component. In that case the first formed crystals need not necessarily be in contact with the successive liquid fractions. This mechanism would, however, not be able to explain why the zoning AB was so extensive, as a reasonable length of time between the early phenocrysts and the successive fractions must have been essential.

Compositions of the sodic ferrohedenbergite in the enigmatic quartz porphyry (T135), which show reversed zoning are plotted in the granite porphyry diagram also (Figure 5.3.3C no.Z). Note

the reversed zoning E (core) \rightarrow C (rim). If the rim at C is plotted in the quartz porphyry trend instead (diagram no.Y, same figure), it would take up position among the low acmite composition range. It is therefore suggested that the sodic ferrohedenbergite cores at E (in diagram no.Z) were initially formed by completion of a 'distorted' trend (now completely obliterated) of the granite porphyry pyroxene type, either through the path ACE or along (the dashed path) AE. By some remote process, the rock as a body was subsequently affected by rocks of the new low-acmite quartz porphyry pyroxene trend, causing the reversed zoning as demonstrated by E \rightarrow C.

(iv) The possible role of oxygen fugacity and volatiles

From experimental and petrological data, Yagi (1966) proposed a model showing the relationship between the prevailing oxygen fugacity and the composition of the crystallising pyroxene in the Acmite-Hedenbergite series. He concluded that low oxygen fugacity in volcanic rocks favours the crystallisation of Ca-rich pyroxenes while high oxygen fugacity would promote the crystallisation of pyroxenes high in the acmite component. That is, low oxygen fugacity could be taken to imply a high activity of Fe^{2+} relative to Fe^{3+} , and a high activity of Fe^{2+} is conducive to the continued crystallisation of the hedenbergite species in which the acmite component is low (Larsen, 1976). On the basis of low oxygen fugacity therefore, the observed quartz porphyry trend would be consistent with the above. But the disturbed trend in the granite porphyry pyroxenes would imply a fluctuation in oxygen fugacity or at best a gradual build up.

The quartz porphyries are ignimbritic in character;

this is especially evident in the textures. In Chapter 3 it was suggested that the quartz porphyries were emplaced by a fluidisation mechanism which would, by its postulated nature (Reynolds, 1956), involve a predominant role of the gas phase. The textural evidence for explosive action in the Tibchi quartz porphyries may imply enrichment in volatiles in the gas phase. On the other hand the granite porphyry ring-dyke was proposed to have been emplaced by quiescent intrusion after the almost complete loss of volatile constituents.

There appears to be a correlation between the presence of volatiles and low activity of Fe^{3+} in the magma (Kogarko, 1974). Even if Fe^{3+} activity was equal in the magmas of both the quartz porphyry and granite porphyry trends, an apparently low Fe^{3+} activity would be observed in the quartz porphyry trend as a result of its high volatile content. In that case the formation of hedenbergite low in acmite component would be promoted by the mere presence of sufficient volatiles.

(v) Estimates of temperatures associated with the pyroxene crystallisation

The natural occurrence of inverted ferriferous β -Wollastonite reported in the Skaergaard ferrohedenbergites by Wager and Deer (1939) and Brown and Vincent (1963) was based on certain textural features, notably the characteristic mosaic texture. Similar textures have not been observed in the Tibchi pyroxenes, even in those close in composition to the type ascribed to inversion in the Skaergaard. The temperature of inversion of the relevant Skaergaard

pyroxene has since been experimentally determined and fixed as $990^{\circ} - 950^{\circ}\text{C}$ (Yoder et al., 1963; Lindsley et al., 1969). According to the data, ferriferous β -Wollastonite would be suppressed at lower temperatures and/or higher pressures. That the Tibchi Complex could have formed under conditions of higher pressures than the Skaergaard, is unlikely. Therefore, the only reasonable explanation for the absence of this inversion in the Tibchi Complex must be a lower temperature. It is therefore suggested that the ferrohedenbergites of the Tibchi Complex have been directly precipitated from the magma at temperatures below 950°C .

The ferrohedenbergite of the quartz porphyry (T115) with a composition of $\text{Ca}_{43.1}\text{Fe}_{56.5}\text{Mg}_{0.4}$ had been proposed earlier as marking the completion of the quartz porphyry trend in the plane of the Diopside-Hedenbergite-Ferrosilite-Enstatite quadrilateral (see Figures 5.3.3A no.0, 5.3.3B and 5.3.3C no.Y). On the assumption that the departure of the rim composition of this Tibchi pyroxene towards acmite apex involved lower temperatures, estimation of the temperature at $\text{Ca}_{43.1}\text{Mg}_{0.4}\text{Fe}_{56.5}$ is considered essential.

From the phase relations of Lindsley and Munoz (1969), determined for the $\text{Ca}_{0.5}\text{Fe}_{0.5} \rightarrow \text{FeSiO}_3$ join, at and below 2 Kb pressure, the above Tibchi ferrohedenbergite becomes $\text{Ca}_{0.43}\text{Fe}_{0.57}$ (if Mg is assumed negligible) and gives a temperature of 800°C approximately. At this temperature the quartz porphyry crystallisation trend departed from the plane of the (Di-Hd-Fs-En) quadrilateral towards the Acmite apex. This is thus taken to represent the maximum temperature of the residual peralkaline fraction discussed earlier. It is however realised that the conditions in experimental models can be too

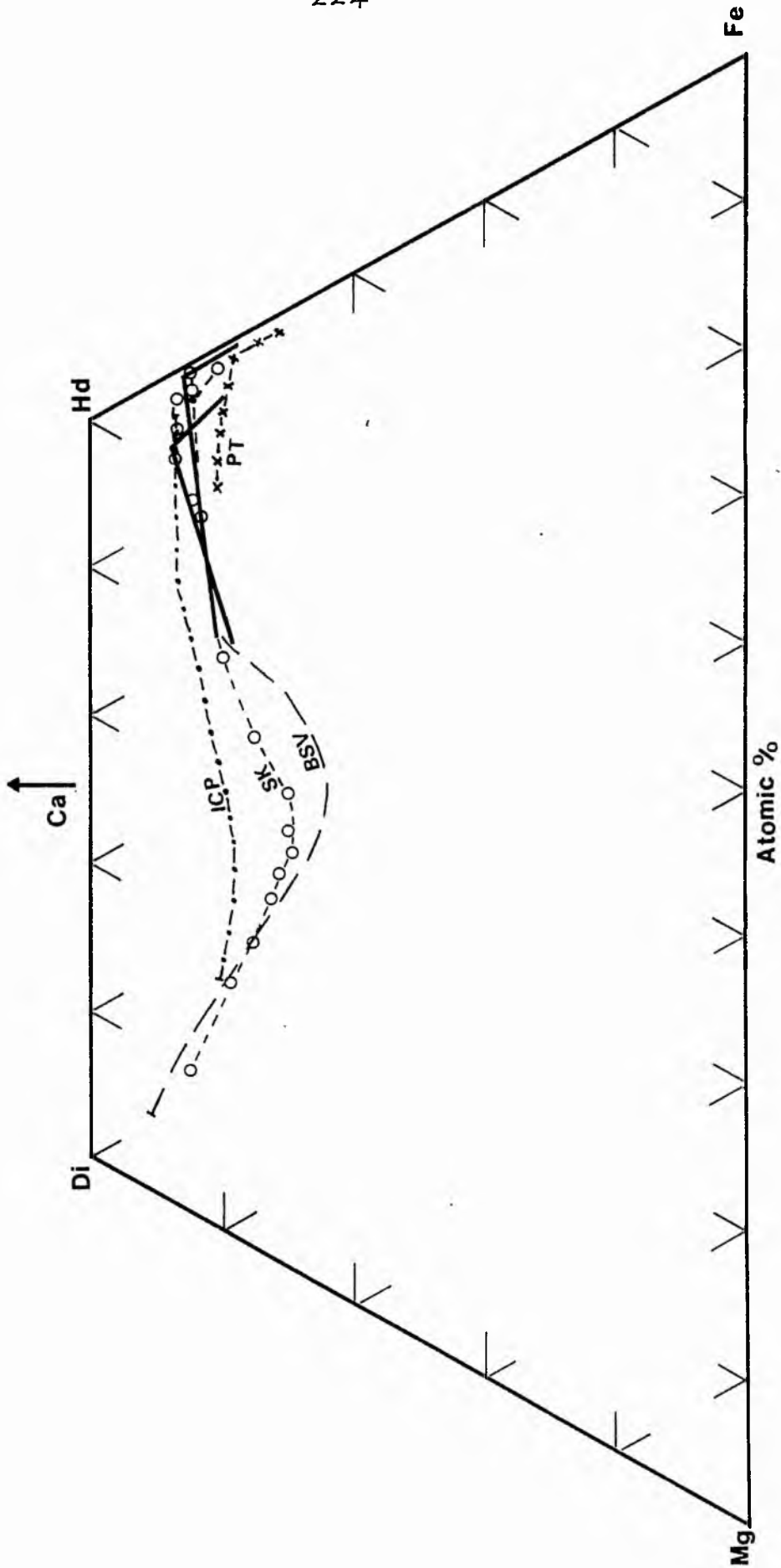


Figure 5.3.3D Comparison of the pyroxene trends of the Tibchi Complex (solid lines) with those of the Bushveld (BSV) and Skaergaard (SK) intrusions, Thingmuli Central Volcano (ICP) and Pantellerites (PT). Sources of data in text.

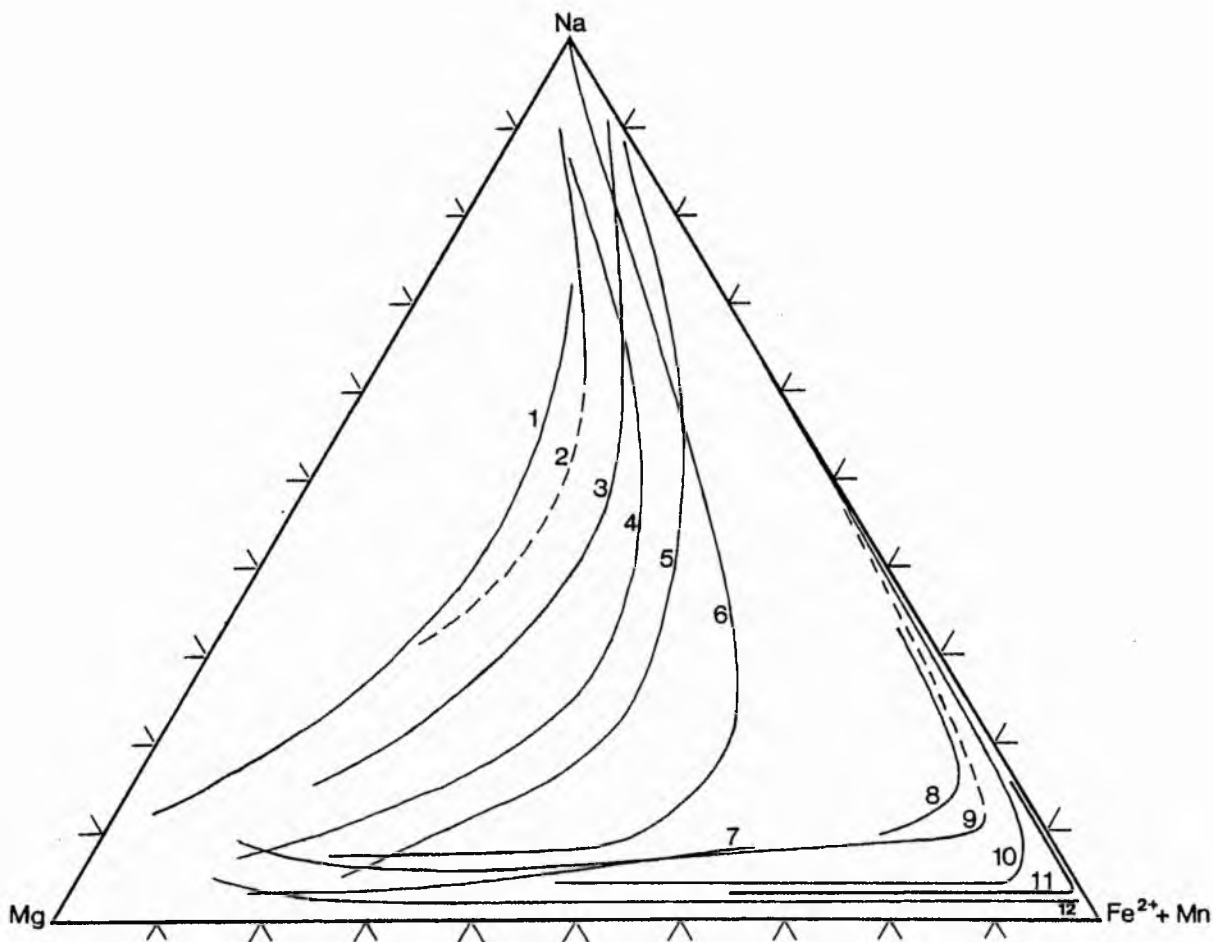


Figure 5.3.3E A comparison of published alkali pyroxene trends (atomic percent) with those of the Tibchi Complex and the Skaergaard Intrusion, East Greenland.

Undersaturated (1) Auvergne, France (Varet, 1969); (2) Lovozero, U.S.S.R. (Bussen & Sakharov, 1972); (3) Itapirapua (Gomes et al., 1970); (4) Uganda (Tyler & King, 1967); (5) Morotu, Sakhalin (Yagi, 1966); (6) South Qoroq Centre, South Greenland (Stephenson, 1972); (10) Ilimaussaq intrusion (Larsen, 1976).

Oversaturated (7) Japanese alkali basalts (Aoki, 1964); (8) Pantellerites (Nicholls & Carmichael, 1969); (9) Nandewar volcano, Australia (Abbot, 1969); (11) Tibchi Complex (this study); (12) Skaergaard (Brown and Vincent, 1963).

simplistic to take into account the role of several variables operating in natural conditions. The above temperature is at best an approximation.

(vi) Comparison of the Tibchi pyroxene trends with related trends elsewhere

Ca-rich pyroxene trends involving the ferroaugite-ferrohedenbergite series have been documented for several intrusions. Of relevance are those of the Skaergaard Intrusion (Brown and Vincent, 1963), the Bushveld Intrusion (Atkins, 1969), the Tertiary pitchstones from East Iceland (Carmichael, 1960, 1963, and 1967) and Pantellerites (Nicholls and Carmichael, 1969) are shown and compared with the Tibchi trends in Figure 5.3.3D.

The Skaergaard and the Bushveld are known to consist of parental magma and differentiates of tholeiitic affinity. Both are slowly cooled plutonic bodies characterised by strong igneous layering. Carmichael's (1960, 1963) work was an attempt to analyse pyroxenes from the possible acid volcanic differentiates of tholeiitic magmas. It is possible to criticise Carmichael's (1967) selection of samples from several lavas and dykes apparently unrelated in some cases. It would be unsatisfactory, when comparing pyroxene trends from genetically related intrusions, to use data from such widespread sources. In recognition of this shortfall, the trend plotted in Figure 5.3.3D for the Icelandic Pitchstones have been selected from Carmichael's several publications and ensured to relate only to the pitchstones from the Thingmuli Central Volcano, Iceland.

The Pantellerite trend (Nicholls and Carmichael, 1969)

consists of two limbs. The limb parallel to the Diopside-Hedenbergite joint belongs to phenocrysts in pantellerite, Pantelleria, while the limb parallel to the Hedenbergite-Ferrosilite sideline consists of pyroxene phenocrysts in Comendites from New Zealand.

Of published Ca-rich pyroxene trends accessible to the writer, the most comparable to those of the Tibchi Complex are those of the late stages of the Skaergaard and Bushveld Intrusions and that of the Thingmuli Central Volcano. All are tholeiitic in origin.

Comparison between the Tibchi quartz porphyry trend and that of the Skaergaard is of particular interest. In the Mg - (Fe²⁺Mn) - Na plot (Figure 5.3.3E), in which the acmite molecule is involved, the Tibchi and Skaergaard trends are superimposed on published alkali pyroxene trends (Larsen, 1976), for comparison:-

It can be observed from Figure 5.3.3E that the Skaergaard main trend was consistently low in acmite through to the end. On the other hand, while Tibchi quartz porphyry pyroxene trend simulates the Skaergaard's low profile, the influence of a new acmite component is strong on the last pyroxenes of the series. Compared with the rest of the alkali pyroxene trends, the Tibchi quartz porphyry trend can only be described as showing a belated alkali pyroxene affinity. This is shown by the observation in Figure 5.3.3D that the two Tibchi pyroxene trends end on the peralkaline trend of pantellerites.

5.3.4 Summary and conclusions

The Ca-rich pyroxenes of the microferrodiorite and microsyenite enclaves, and those of the quartz porphyries, define a common continuous trend. It is inferred by this that the quartz porphyries evolved directly from a liquid whose composition is, in all probability, represented by those crystalline primitive enclaves.

The granite porphyry pyroxenes on the other hand define a slightly different trend from the above. This second trend is better understood on the Diopside-Hedenbergite-Acmite triangle rather than the Diopside-Enstatite-Ferrosilite-Hedenbergite quadrilateral and can be considered a modification of the quartz porphyry trend.

Both the "granite porphyry trend" and the "quartz porphyry trend" originate from about the same initial ferro-augite composition. It is inferred that the rocks of the above two trends were therefore consanguinous.

The quartz porphyry trend was under consistently low Na and Fe^{3+} activities throughout nearly all its span. The role of oxygen fugacity was apparently important but the presence of volatiles may account for much of the difference between the two established trends.

If the general pattern of published pyroxene trends can be a guide, the Tibchi pyroxenes (and their host rocks) would be placed among those of tholeiitic affinity, but distinguished as one with a mildly alkaline character.

Ferrohedenbergites of the quartz porphyries were precipitated from the magma below $950^{\circ}C$. The reaction between the most evolved ferrohedenbergites in the terminal rock fraction with the residual liquid is estimated to have occurred

at below 800°C (< 2 Kb pressure).

The question of initial peralkaline liquid parent is thus put in doubt as peralkalinity is here observed to have been developed at a late stage in already evolved differentiates.

5.4 Amphiboles

5.4.1 General

The most extensive work yet carried out on amphiboles from the Nigerian Younger Granites was by Borley (1963b). On the basis of analytical data obtained, she divided the amphiboles into two contrasting groups namely, ferrohastingsites and alkali amphiboles. Re-examination, in the present study, of the "ferrohastingsite" group in the light of recent I.M.A. classification (Leake, 1978), shows that four groups of calcic amphiboles were represented. Of the nine analyses reported, six now belong to the hastingsitic hornblende group, and one each to hastingsite, ferroedenite and ferrorichterite.

Two of the problems concerning the Nigerian amphiboles, which may be found to apply elsewhere, are embodied in the work of Borley (op. cit.). Firstly, the relationship between the calcic and alkali amphiboles was found to be obscure. Secondly, the observed variation in the composition of the alkali amphiboles was a type that made precise classification difficult. New information presented in the present study focuses on the above problems, and exposes in particular, new compositions in the calcic and sodic-calcic range.

5.4.2 Analytical data

A total of sixty-two microprobe analyses were carried out, from twelve polished thin sections belonging to eleven

TABLE 5.4A REPRESENTATIVE ANALYSES OF CALICIC AND SODIC-CALICIC AMPHIBOLES, TIBCHI COMPLEX

	← Calcic														→ Sodic-calcic						
	1	2	3A	3B	4	5	6	7	8A	8B	9	10A	10B	10D	11	12	13A	13B	14	15	16
SiO ₂	37.64	37.99	39.03	37.57	46.82	44.23	43.25	41.10	42.04	44.04	46.60	48.73	47.68	46.59	47.89	49.23	47.41	47.84	46.30	46.19	47.89
TiO ₂	0.34	0.49	0.20	0.23	0.15	0.11	0.27	1.30	1.32	1.03	0.51	0.14	0.81	1.23	1.26	0.93	1.49	1.40	1.26	0.46	0.60
Al ₂ O ₃	8.03	12.13	9.79	11.12	2.46	3.47	6.07	6.06	6.22	5.39	1.18	0.75	1.56	1.91	1.20	1.13	1.52	1.42	3.80	1.47	1.28
Fe ₂ O ₃	4.58	5.27	3.92	5.15	0.57	1.98	1.19	0.00	0.00	0.00	0.00	0.00	0.00	0.00	0.00	0.00	0.00	0.00	0.00	0.00	0.00
FeO	25.00	24.26	26.63	26.29	31.44	31.13	31.64	33.94	32.91	32.98	34.35	34.56	34.32	34.22	34.80	36.03	34.24	33.80	33.23	32.48	32.20
MnO	0.49	0.50	0.59	0.59	1.23	1.99	1.05	0.50	0.78	0.89	0.00	1.50	0.96	0.87	0.68	0.38	0.75	0.54	0.20	1.63	2.30
MgO	2.78	2.79	2.66	2.04	2.37	1.36	1.49	1.17	1.80	2.16	0.40	0.36	0.44	0.31	0.34	0.61	0.14	0.15	0.13	1.15	0.57
CaO	11.05	10.90	11.26	10.52	10.92	10.42	10.65	9.84	10.08	9.88	6.76	7.79	6.61	5.84	4.85	2.78	4.45	3.69	3.35	4.18	2.38
Na ₂ O	1.67	1.17	2.01	1.49	0.67	0.96	1.34	2.06	2.06	1.64	3.00	2.15	3.47	4.10	5.01	5.14	5.12	5.44	4.88	5.47	6.41
K ₂ O	1.61	1.68	1.48	1.78	0.41	0.46	0.87	1.00	1.20	1.04	0.83	0.36	0.80	1.06	1.11	0.82	1.20	1.22	2.55	1.06	-
TOTAL	93.19	97.18	97.57	96.78	97.04	96.11	97.82	96.97	98.41	99.05	93.63	96.34	96.65	96.13	97.14	97.05	96.32	95.50	95.70	94.09	-
FeO(T)	29.12	29.00	30.16	30.92	31.95	32.91	32.71	33.94	32.91	32.98	34.35	34.56	34.32	34.22	34.80	36.03	34.24	33.80	33.23	32.48	32.20
Numbers of ions on the basis of 23 oxygens																					
Si	6.407	6.116	6.331	6.157	7.567	7.312	7.014	6.820	6.833	7.057	7.877	7.986	7.808	7.702	7.826	7.990	7.803	7.902	7.644	7.789	7.981
Al ^{IV}	1.593	1.884	1.669	1.843	0.433	0.676	0.986	1.180	1.167	0.943	0.123	0.011	0.192	0.298	0.174	0.010	0.197	0.098	0.356	0.211	0.019
T	8.000	8.000	8.000	8.000	7.988	8.000	8.000	8.000	8.000	8.000	8.000	8.000	8.000	8.000	8.000	8.000	8.000	8.000	8.000	8.000	8.000
Al ^{VI}	0.019	0.418	0.203	0.306	0.035	-	0.175	0.005	0.026	0.075	0.113	0.129	0.109	0.075	0.057	0.206	0.099	0.178	0.383	0.081	0.232
Fe ³⁺	0.587	0.638	0.479	0.635	0.070	0.246	0.145	-	-	-	-	-	-	-	-	-	-	-	-	-	-
Ti	0.044	0.059	0.025	0.029	0.018	0.033	0.163	0.161	0.124	0.065	0.017	0.100	0.153	0.155	0.114	0.185	0.174	0.156	0.058	0.075	-
Mg	0.705	0.669	0.643	0.499	0.570	0.336	0.361	0.290	0.436	0.516	0.101	0.088	0.107	0.076	0.084	0.149	0.035	0.037	0.033	0.290	0.142
Fe ²⁺	3.559	3.266	3.613	3.604	4.249	4.304	4.292	4.711	4.474	4.419	4.856	4.737	4.699	4.730	4.756	4.891	4.714	4.668	4.588	4.581	4.489
Mn	0.070	0.069	0.081	0.081	0.168	0.279	0.144	0.071	0.107	0.121	-	0.208	0.133	0.122	0.094	0.052	0.105	0.076	0.027	0.233	0.325
C	4.984	5.119	5.044	5.154	5.110	5.178	5.150	5.240	5.204	5.255	5.135	5.179	5.148	5.156	5.146	5.412	5.138	5.133	5.187	5.243	5.263
XC	-	0.119	0.044	0.154	0.110	0.178	0.150	0.240	0.204	0.255	0.135	0.179	0.148	0.156	0.146	0.412	0.138	0.133	0.187	0.243	0.263
Ca	2.016	1.881	1.957	1.847	1.891	1.845	1.851	1.748	1.755	1.696	1.225	1.367	1.159	1.034	0.848	0.483	0.785	0.653	0.592	0.755	0.425
Na _B	-	-	-	-	-	-	-	0.012	0.041	0.049	0.640	0.454	0.693	0.810	1.006	1.105	1.077	1.214	1.221	1.002	1.312
B	2.016	2.000	2.001	2.001	2.001	2.023	2.001	2.000	2.000	2.000	2.000	2.000	2.000	2.000	2.000	2.000	2.000	2.000	2.000	2.000	2.000
Na _A	0.550	0.365	0.632	0.472	0.210	0.307	0.421	0.651	0.608	0.460	0.343	0.228	0.409	0.503	0.582	0.514	0.556	0.528	0.342	0.787	0.759
K	0.349	0.345	0.306	0.373	0.084	0.096	0.179	0.211	0.248	0.212	0.179	0.075	0.168	0.224	0.232	0.169	0.252	0.257	0.537	0.228	0.191
A	0.900	0.709	0.938	0.845	0.294	0.403	0.600	0.862	0.856	0.672	0.522	0.303	0.577	0.727	0.814	0.683	0.808	0.785	0.879	1.015	0.950

FeO(T) = Total iron as FeO. T = Tetrahedral site. C = Octahedral site. XC = Excess from C over a total of 5.00 cations. B = XC + Total Ca + Na_B = M₄ site. A = (Total Na - Na_B) + K.

All values are expressed in weight percent.

1...Hastingsitic hornblende, Older Granite basement (T103). 2...Hastingsite, Older Granite basement (T103). 3A,3B...Zoned hastingsitic hornblende (A) with rim of hastingsite (B), Basement "screen" (T36). 4...Ferroactinolite, Quartz porphyry (T169). 5...Ferroactinolitic hornblende, Quartz porphyry (T169). 6...Ferroedenite, Quartz porphyry (T169). 7...Ferroedenite, Quartz porphyry (T168). 8A,8B...Zoned ferroedenite, Granite porphyry ring dyke (T37). 9...Silicic ferroedenite, Quartz porphyry (T170). 10A,10B,10D...Zoned ferroactinolite with rim of ferrichterite (for C see appendix), Quartz porphyry (T170). 11...Ferrichterite crystallised along fracture in

alkali feldspar phenocryst, Quartz porphyry (T115). 12...Ferrichterite associated with riebeckite in fayalite phenocryst (see text), Quartz porphyry (T115). 13A,13B...Zoned spongy "porphyroblast" of ferrichterite, Quartz porphyry (T133). 14...Ferrichterite nucleated on and growing into pre-existing alkali feldspar phenocryst, Quartz porphyry (T133). 15,16...Ferrichterites showing range in composition, Sodic syenite (T34C).

Electron microprobe analyses

Analyst E.C.Ike

230

TABLE 5.4B ANALYSES OF SODIC PYROXENES AND ALKALI AMPHIBOLES, TIBCHI COMPLEX

	Sodic pyroxenes			Alkali amphiboles			
	1	2		3	4	5	6
SiO ₂	50.27	50.53	SiO ₂	48.68	49.88	48.85	50.21
TiO ₂	0.15	0.13	TiO ₂	0.51	0.73	0.05	0.05
Al ₂ O ₃	0.29	0.26	Al ₂ O ₃	1.28	1.22	1.32	0.09
Fe ₂ O ₃	17.24	16.68	Fe ₂ O ₃	2.28	5.47	4.48	10.15
FeO	12.69	13.55	FeO	28.85	27.48	28.68	28.71
MnO	1.64	1.68	MnO	2.08	1.11	1.70	0.42
MgO	0.31	0.29	MgO	0.91	0.22	0.17	0.24
CaO	9.91	9.82	CaO	2.60	1.10	0.68	1.24
Na ₂ O	7.05	6.95	Na ₂ O	6.55	7.58	8.25	6.38
K ₂ O	x	x	K ₂ O	0.97	0.84	1.38	0.00
TOTAL	99.55	99.89	TOTAL	94.69	95.62	95.55	97.48
FeO(T)	28.20	28.56	FeO(T)	30.90	32.40	32.70	37.84

Numbers of ions
on the basis of
4 cations

Numbers of ions
on the basis of
23 oxygens

Si	2.002	2.008	Si	8.000	8.051	8.000	8.000
Al ^{IV}	-	-	Al ^{IV}	-	-	-	-
Al ^{VI}	0.014	0.012	T	8.000	8.051	8.000	8.000
Ti	0.005	0.004	Al ^{VI}	0.248	0.232	0.255	0.018
Fe ³⁺	0.516	0.499	Fe ³⁺	0.282	0.665	0.552	1.218
Fe ²⁺	0.423	0.450	Ti	0.062	0.088	0.006	0.006
Mn	0.055	0.057	Mg	0.223	0.052	0.042	0.058
Mg	0.019	0.017	Fe ²⁺	3.965	3.709	3.927	3.826
Ca	0.423	0.418	Mn	0.289	0.152	0.236	0.056
Na	0.544	0.535	C	5.070	4.899	5.018	5.180
K	-	-	Xc	0.070	-	0.018	0.180
			Ca	0.457	0.190	0.119	0.212
			Na _B	1.473	1.810	1.863	1.608
			B	2.000	2.000	2.000	2.000
			Na _A	0.615	0.562	0.755	0.362
			K	0.203	0.174	0.289	-
			A	0.818	0.736	1.044	0.362

FeO(T) = Total iron as FeO. x Less than 0.004%.

All values are expressed in weight percent.

1...Granular aegirine-augite, Sodic syenite (T34C). 2...Ragged aegirine-augite, Sodic syenite (T34C). 3...Arfvedsonite, Sodic syenite (T34C). 4...Arfvedsonite, Sodic granite (T173). 5...Arfvedsonite, Haematite syenite (T34GR). 6...Riebeckite surrounding ilmenite inclusion in partially altered fayalite (see Plate 4.4I), Quartz porphyry (T115).
Electron microprobe analyses. Analyst E.C.Ike

rocks. The halogens, lithium, zinc, lead, phosphorus, and water were not determined. Altogether the above minor constituents may add up to an amount varying from less than 3% up to 7% depending on the group of amphibole, using Borley's (1963b) analyses as a guide.

A computerised recalculation procedure (Papike et al., 1974) calculates the amphibole structural formula on a water-free (and halogen-free) basis to 23 oxygens, and 2(OH, F, Cl) assumed. On the principle of charge balance for the total cations present Fe_2O_3 is obtained from the microprobe output of total iron as FeO. The Papike programme has been updated by Dr. W.E. Stephens to perform a simultaneous classification of the amphibole on the current I.M.A. scheme (Leake, 1978). Amphibole microprobe data obtained and presented in this study have been processed as above.

The amphiboles of the Tibchi Complex fall into the three main groups: Calcic, Sodic-calcic and Alkali. Representative analyses of the Calcic and Sodic-calcic groups are presented in Table 5.4A while those of the Alkali group may be found together with alkali pyroxene analyses, in Table 5.4B. Usually the purpose for those displayed in the above tables is to show the available range in composition within each group of amphibole; additionally, those formed under certain peculiar circumstances are included in the tables for comparison with the main trends. The rest of the analyses may be found in the appendix.

According to the I.M.A. classification (Leake, 1978) the three main groups of amphiboles may be chemically defined as follows:

TABLE 5.4

IRON END-MEMBERS OF AMPHIBOLES OF THE TIBCHI
 COMPLEX ACCORDING TO THE NOMENCLATURE OF
 LEAKE (1978).

CALCIC

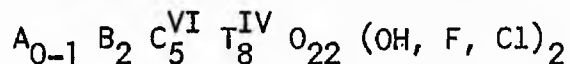
Ferroactinolite	$\text{Ca}_2\text{Fe}_5^{2+}\text{Si}_8\text{O}_{22}(\text{OH})_2$
Ferroedenite	$\text{NaCa}_2\text{Fe}_5^{2+}\text{Si}_7\text{Al}_2\text{O}_{22}(\text{OH})_2$
Hastingsite	$\text{NaCa}_2\text{Fe}_4^{2+}\text{Fe}^{3+}\text{Si}_6\text{Al}_2\text{O}_{22}(\text{OH})_2$

SODIC-CALCIC

Ferrorichterite	$\text{NaCaNaFe}_5^{2+}\text{Si}_8\text{O}_{22}(\text{OH})_2$
-----------------	---

ALKALI

Arfvedsonite	$\text{NaNa}_2\text{Fe}_4^{2+}\text{Fe}^{3+}\text{Si}_8\text{O}_{22}(\text{OH})_2$
Riebeckite	$\text{Na}_2\text{Fe}_3^{2+}\text{Fe}_2^{3+}\text{Si}_8\text{O}_{22}(\text{OH})_2$

Standard Amphibole Formula

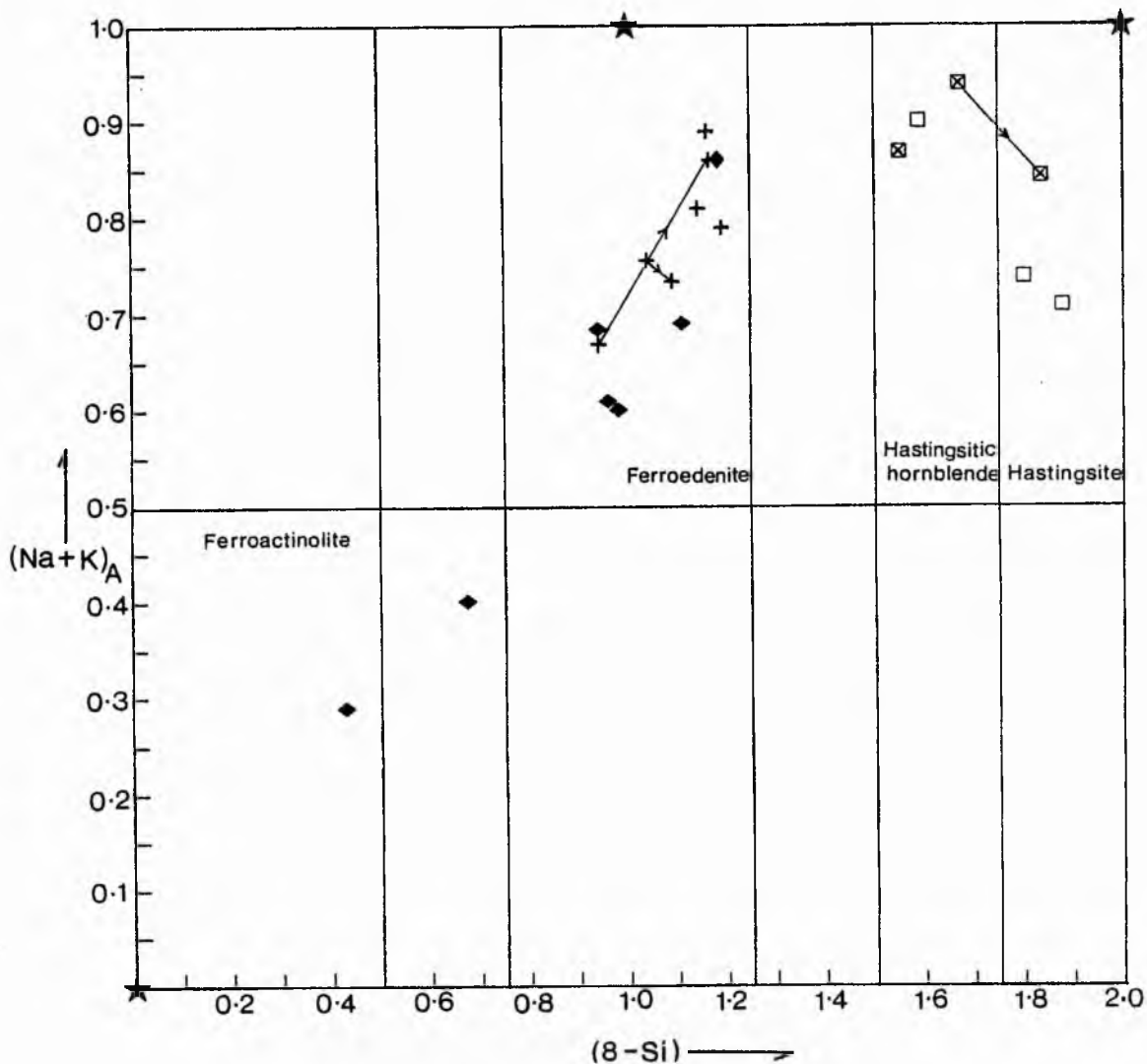


Figure 5.4.2A Plot of $(\text{Na}+\text{K})_A$ against $(8-\text{Si})$ subdividing the calcic amphiboles analysed. Calcic amphiboles with $(8-\text{Si})$ less than 0.1 are considered Al-poor and are plotted together with Al-poor amphiboles in Figure 5.4.2B. All the calcic amphiboles plotted above have $\text{Na}_B = 0.05$, and occur in the following rocks: filled flat diamond = quartz porphyry (T169); filled upright diamond = quartz porphyry (T168); crosses = granite porphyry ring-dyke (T37); squares with crosses = basement 'screen' (T36); open squares = Older Granite basement (T103). Each tie-line joins one zoned crystal. Black stars represent end-member compositions of respective amphibole groups. Note the linear distribution between ferroactinolite and ferroedenite compositions.

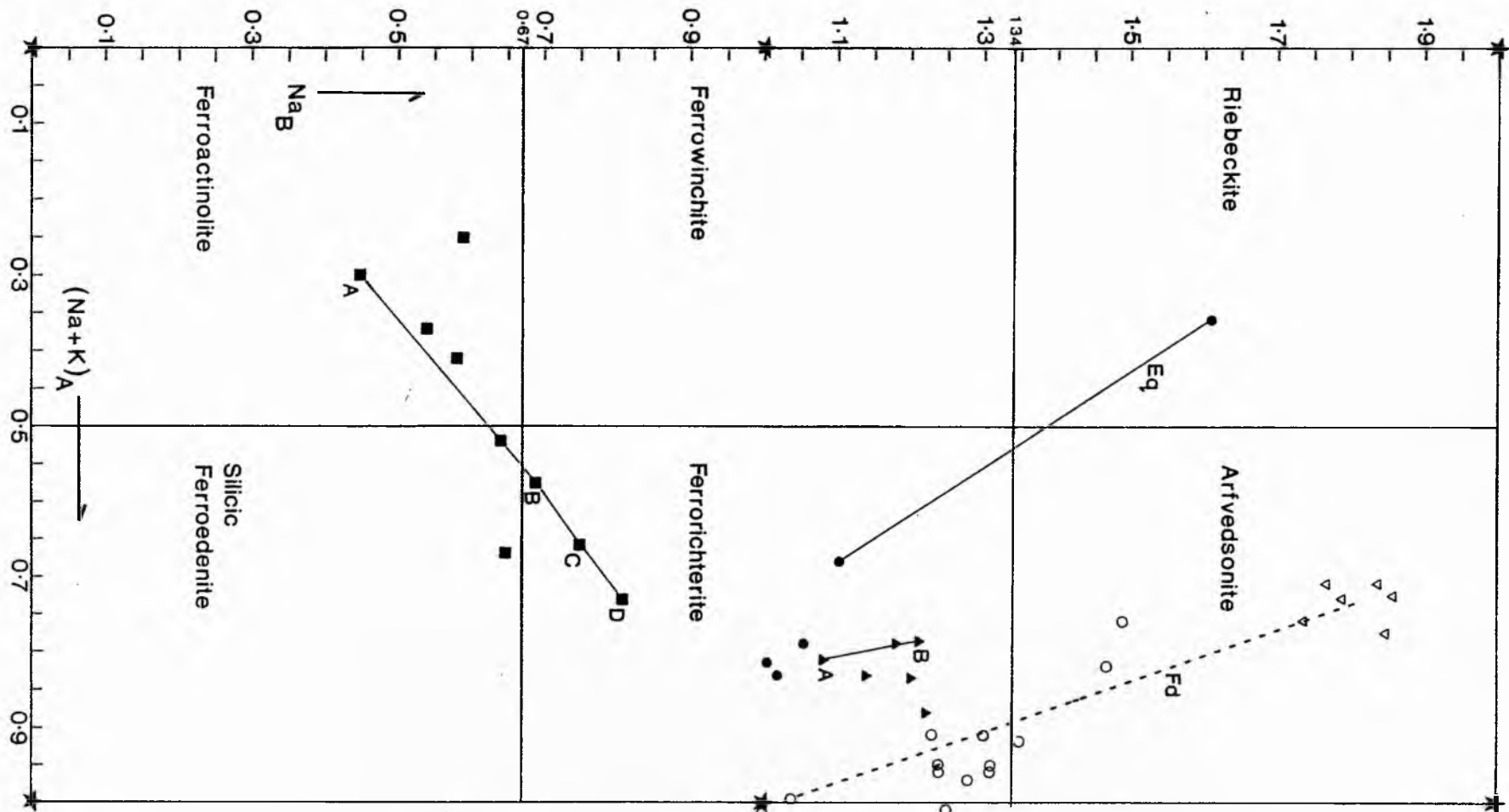


Figure 5.4.2B Plot of Na_B against $(Na+K)_A$ subdividing the sodic-calcic and Alkali amphiboles analysed. Al-poor calcic amphiboles (8-Si) 0.1) are also plotted. Amphiboles analysed belong to the following rocks: Filled squares = Quartz porphyry (T170); filled circles = quartz porphyry (T115); filled triangles = quartz porphyry (T133); open circles = sodic syenite (T34C); open triangles = sodic granite (T173). Each tie-line joins one zoned crystal. A = core, B = rim; ABCD = A(core) D(rim). Tie-lines marked Eq and Fd are explained in text. Black stars = End-member compositions of respective groups.

Calcic: Monoclinic amphiboles in which $(Ca+Na)_B \geq 1.34$ and $Na_B < 0.67$. Generally $Ca_B > 1.34$.

Sodic-calcic: Monoclinic amphiboles in which $(Ca+Na)_B \geq 1.34$ and $0.67 \leq Na_B < 1.34$. Generally $0.67 < Ca_B < 1.34$.

Alkali: Monoclinic amphiboles in which $Na_B \geq 1.34$.

Diagrammatic subdivision of the above main groups is based on Figure 1 of Leake (op. cit.). A plot of $(Na+K)_A$ against $(8-Si)$ subdivides the calcic main group into the respective groups as shown in Figure 5.4.2A. Calcic amphiboles with $(8-Si) < 0.1$ are considered Al-poor and are therefore plotted with the Al-poor amphiboles. Sodic-calcic and alkali amphiboles analysed are typically Al-poor, especially with respect to Al^{IV} , so that $(8-Si)$ is found to be always less than 0.25. Figure 5.4.2B shows a plot of Na_B against $(Na+K)_A$ subdividing the sodic-calcic and alkali amphiboles analysed.

The iron end-members of the amphiboles of the Tibchi Complex are given in Table 5.4.

For convenience further information on the analysed amphiboles will be given separately below.

5.4.3 Calcic amphiboles

Calcic amphiboles of the Tibchi Complex consist of six groups namely, hastingsite, hastingsitic hornblende, ferroedenite, silicic ferroedenite, ferroactinolitic hornblende and ferroactinolite (Figure 5.4.2A). All represent the iron-rich members of their respective solid solution series.

Hastingsitic hornblende and hastingsite analysed co-exist in each of the two basement rocks studied namely, the Older Granite (adamellite) basement (T103) and the nepheline-

normative altered basement 'screen' (T36). In T103 while the stable (fresh-looking) phase is found to be hastingsitic hornblende in composition, the unstable phase apparently forming a substrate for co-existing biotite gives hastingsite composition. In T36, one relatively large, zoned, grain (nos.3A, 3B Table 5.4A and Figure 5.4.2A), had a yellowish hastingsitic hornblende rimmed by a bluish hastingsite. Hastingsite is however the dominant phase in the whole rock.

The ferroedenites occur in the hydrothermally altered southern segment of the granite porphyry ring-dyke (Figure 4.4L, Chapter 4) and in the similarly altered quartz porphyries (T168 and T169, Figure 4.4A). The directional distribution pattern for analysed ferroedenites in Figure 5.4.2A is depicted clearly by the extensively zoned crystal from T37. In the quartz porphyry (T169) freshly formed ferroedenite laths are found as well as apparently transitional (indistinct-looking) ferroactinolite. It may be recalled (Chapter 4) that all ferroedenites and associated ferroactinolites were shown petrographically to have formed directly from the breakdown of pre-existing Ca-rich pyroxenes. Therefore the complementary linear distribution between ferroactinolites and ferroedenites in Figure 5.4.2A could be inferred to confirm the petrographical observation of possible transition from ferroactinolite to ferroedenite during their crystallisation history.

Ferroactinolite optically distinguishable from the species above, and also described as "unstable-looking", occurs in the hydrothermally altered quartz porphyry (T170, ref. Figure 4.4A). This second species is found in same rock with freshly formed multicrystalline aggregates of ferrichterite (rather than

ferroedenite). The link between the calcic and sodic-calcic amphiboles is demonstrated below.

5.4.4 Sodic-calcic amphiboles

A large pseudomorph of ferroactinolite (after Ca-rich pyroxene) in the above-mentioned quartz porphyry (T170) was analysed. Its linear compositional transition into the ferrorichterite field (Figure 5.4.2B) is noteworthy.

The sodic-calcic amphiboles of the Tibchi Complex consist almost exclusively of ferrorichterite. As can be seen from Figure 5.4.2B, the compositional variation cuts across the entire ferrorichterite field. The ferrorichterites of the quartz porphyries (T115 and T133) define a linear trend towards the field of arfvedsonite, as can be clearly inferred from the zoned crystal. One ferrorichterite is distinctive; it is associated with riebeckite in a fayalite phenocryst of T115 and will be discussed later.

Ferrorichterite found in the sodic syenite (T34C) is seen to be transitional in composition from end-member ferrorichterite to calcian arfvedsonite (Figure 5.4.2B). The ferrorichterite is a blue variety. It was not possible to optically distinguish the arfvedsonites and ferrorichterites in thin section.

5.4.5 Alkali amphiboles

Alkali amphiboles of the Tibchi Complex consist mostly of arfvedsonite and are found in the syenites (T34C, T34 and T34GR) and the sodic granite (T173). Arfvedsonites of the sodic syenite (T34C) have already been mentioned earlier as

compositionally originating from a transitional ferrorichterite series as shown in Figure 5.4.2B. Arfvedsonite, less calcic than those of T34C, is found in the sodic granite (T173), this granite is transitional in the field from T34C. The dashed tie-line (Fd) in Figure 5.4.2B is a hypothetical trend for obtaining the arfvedsonites of T173 through the ferrorichterite-arfvedsonite series of T34C on the basis of observed field relation.

Riebeckite is found in the Tibchi Complex only as a trace and in a rather special environment of formation. The tie-line (Eq) in Figure 5.4.2B joins analysed riebeckite, found in a fayalite phenocryst of quartz porphyry (T115), with ferrorichterite in the same fayalite grain. While the (green) ferrorichterite forms alteration rims on the fayalite, the (indigo-blue) riebeckite crystallises only around titanomagnetite inclusions. This relationship of riebeckite to titanomagnetite inclusions in fayalite has been optically observed in other thin sections of the above rock and in other quartz porphyries, and appears to be fairly well established.

5.4.6 Discussion

Evidence from the pyroxene crystallisation trends in the Tibchi porphyries clearly indicate a significant range in composition. The amphiboles described here had been shown petrographically (Chapter 4) to have formed on pre-existing pyroxene and fayalite crystals in these porphyries. Therefore it is foreseeable that whatever might be the reactions involved in the late formation of these amphiboles, a key role had to be played by the compositional variation observed in the pyroxenes.

Figure 5.4.5A Plot of Ca against (Na+K) for amphiboles of the Tibchi Complex. Symbols are as in previous figures. Dashed line arrows depict subsolidus transitional trends, each arrow being directed by a distinct chemical control (see text) as follows: 1. Al-rich Ca-rich ferroactinolite-ferroedenite series. 2. Al-poor Ca-poor ferroactinolite-ferrichterite-arfvedsonite series. 3. Titanomagnetite-controlled riebeckite formation. Trend no.4 belongs to the basement rocks and has not been properly investigated. Tie-lines join zoned crystals A = core B = rim; A(core) D(rim). Stars mark positions of end member compositions.

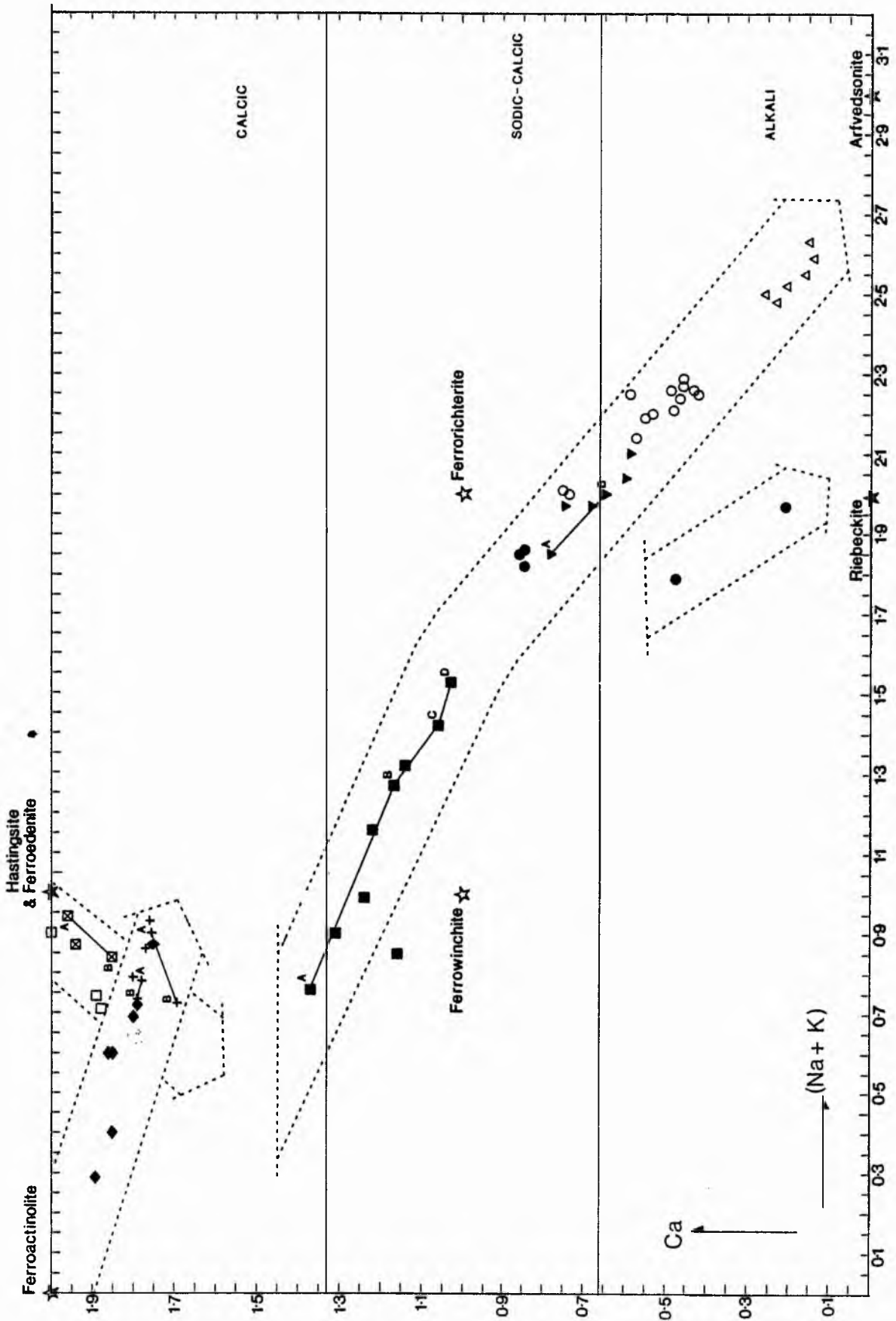


Figure 5.4.5A

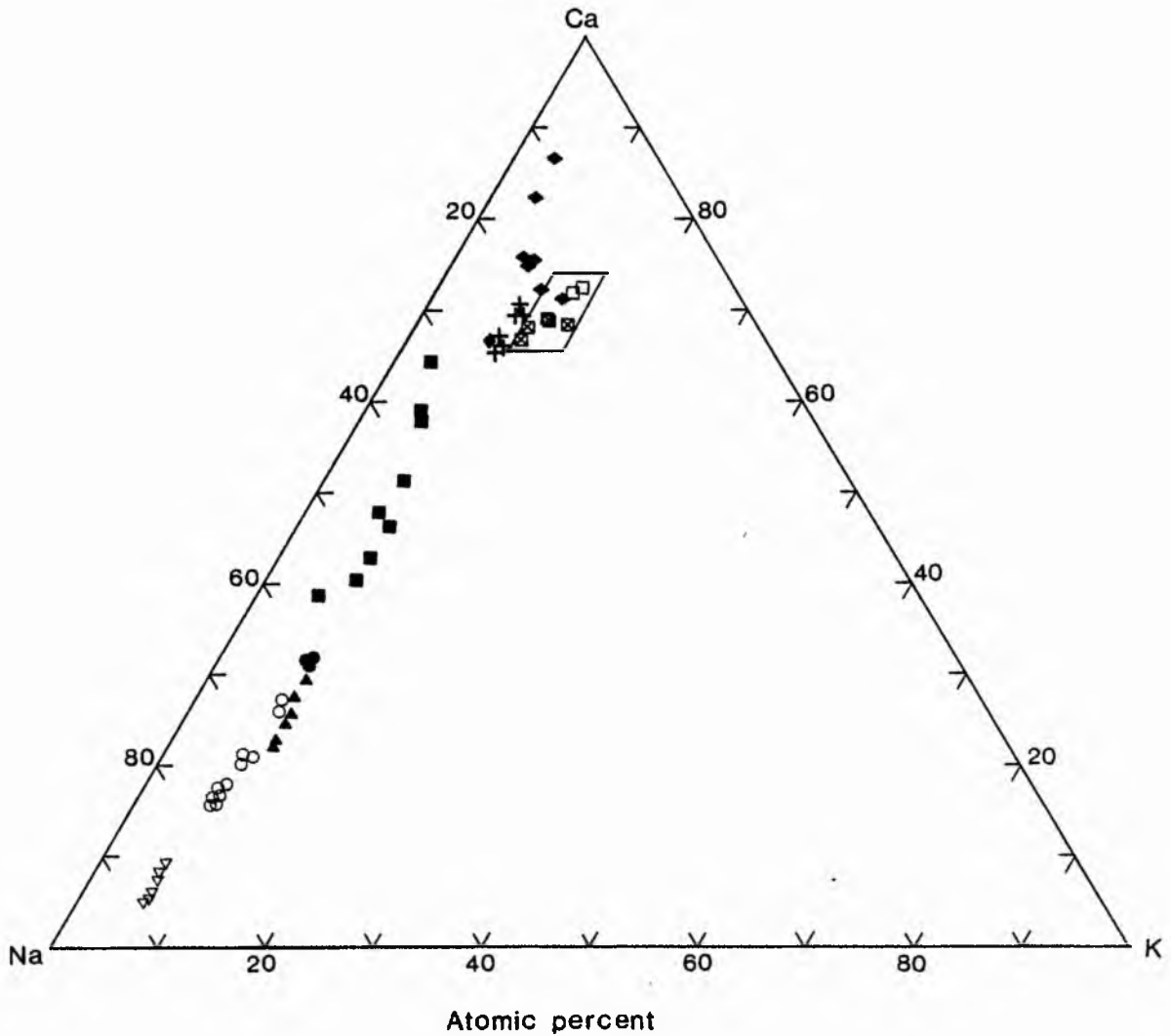


Figure 5.4.5B Amphiboles of the Tibchi Complex plotted on the basis of alkali components and calcium. On gross outlook miscibility from calcic to alkali members is apparently complete. Compositions in the parallelogram belong to the basement rocks. Symbols are as in Figures 5.4.2A and 5.4.2B.

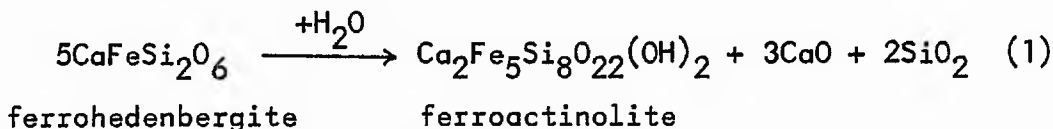
Amphibole reactions have been shown to be excessively slow at low fluid pressure (Akella and Winkler, 1966; Liou *et al.*, 1974). Temperature and oxygen fugacity are important factors also involved in amphibole stability.

From Figure 5.4.5B, the basement group can be seen to be more potassic in character. Owing to its isolation this group will not be discussed further.

The Younger Granite calcic amphiboles of the Tibchi Complex follow a two-fold divergent trend with starting compositions in the ferroactinolite field (ref. Figures 5.4.2A, 5.4.2B and 5.4.5A). One trend is the ferroactinolite-ferroedenite series; the other is the ferroactinolite-ferrorichterite series.

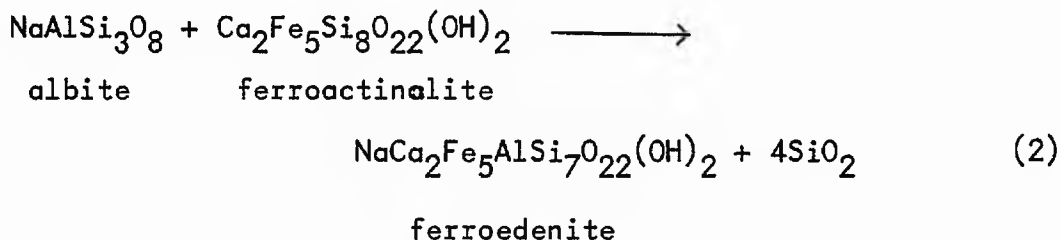
It had been observed petrographically that in either trend the ferroactinolite is the unstable (or metastable) phase while ferroedenite and ferrorichterite respectively are the freshly formed phases. Thus the directions of the reactions involved can be seen to point in divergent directions away from the ferroactinolite field when Figures 5.4.2A and 5.4.2B are put together. In Figure 5.4.5A the directions are at best parallel and cannot therefore meet.

Relative to the amphiboles, the composition of the ferroactinolite end-member appears to be most representative of the Tibchi Ca-rich pyroxenes. If hydrothermal alteration was indeed responsible for the late appearance in the porphyries of those amphiboles, then initial hydration of the pyroxene can be assumed to convert Ca-rich pyroxenes into a metastable phase within the ferroactinolite field according the equation:



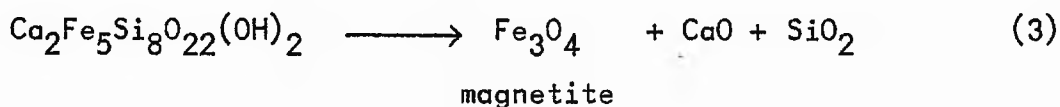
A 'whitish substance' occupying the fibrous cleavage of individual ferroactinolite crystals has been petrographically observed (Chapter 4) and may be a compound of the $3\text{CaO} + 2\text{SiO}_2$ above.

The reaction leading to the observed transition from ferroactinolite to ferroedenite appears to be consistent with the "edenite substitution" suggested by Grapes and Graham (1978), where $(\text{Na}+\text{K})_{\text{A}}\text{Al}^{\text{IV}}$ substitutes for $_{\text{A}}\text{Si}^{\text{IV}}$ in the ferroactinolite formula as follows:



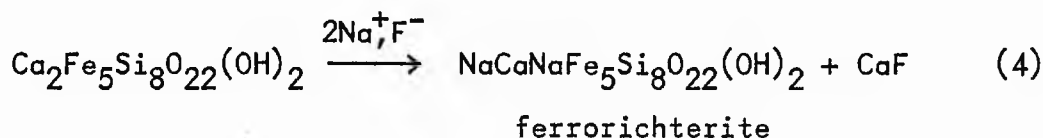
Evidence for possible 'consumption' of albite component during the hydrothermal process is shown in Figure 6.3.3B of Chapter 6 in which the relevant whole rock chemical data are plotted. The albite component could have been generated and made available, from the recrystallisation of the groundmass. Progressive enrichment in silica during the hydrothermal process is also evidence in the above-mentioned figure.

The following reaction probably accompanies equation (2):-



The CaO released would probably constitute fluorite, and/or monazite. Equation (3) is based on the petrographic observation that titanomagnetite accompanies ferroedenite laths when degradation of Ca-rich pyroxene to ferroedenite is completed (ref. Plates 4.4E to H, Chapter 4). Fluorite and monazite are also petrographically observed.

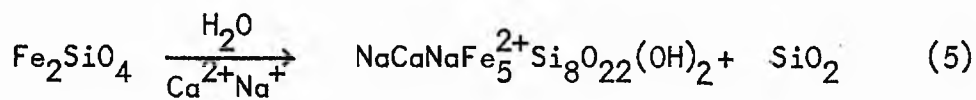
The ferroactinolite-ferrorichterite transition can be inferred from Figure 5.4.2B as possibly due to the substitution of $\text{Na}_B(\text{Na}_B\text{Na}_A)$ (in ferrorichterite) for Ca_B (in ferroactinolite) as follows:



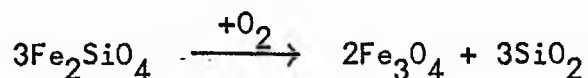
The recrystallisation of groundmass constituents is perhaps sufficient to furnish the requisite Na^+ and F^- above.

Co-existing ferrorichterite and riebeckite observed in the fayalite phenocrysts of the quartz porphyries is believed to constitute a paragenetic equilibrium assemblage under two simultaneously operating chemical controls as follows:-

1. At the periphery of the phenocryst, hydration of fayalite and recrystallisation of the groundmass were likely at the initial stages of the hydrothermal process. Thus, Ca^{2+} and Na^+ would be circulating cations generated from the groundmass phase Ca-rich pyroxenes and salic components. The following reaction is envisaged.



2. In the presence of titanomagnetite and with the availability of Na^+ by diffusion from the recrystallising groundmass, riebeckite could be produced by hydration of fayalite, as long as the temperature is appropriate. Locally, at least, the oxygen fugacity required would be that which is above the fayalite-magnetite-quartz buffer assemblage, enabling the reaction:



to take place in one direction. The fact that titanomagnetite is also present as an inclusion in the fayalite, probably means that around that inclusion Fe^{3+} activity could be very high. Those cations that could play a negative role in riebeckite formation under normal conditions, (i.e. if the titanomagnetite inclusion were not present), would be outstripped by the new Fe^{3+} activity. Thus riebeckite could form round the titanomagnetite inclusion as observed.

From the experimental phase relations of Ernst (1968) most amphiboles have been found to be stable between 400-600°C, at fluid pressures of 0-3 Kb, irrespective of composition. The thermal stability of iron-rich amphiboles is particularly susceptible to changes in oxygen fugacity; the lower the fugacity the greater the stability. Thus the breakdown of the iron-rich amphiboles of ferrichterite-arfvedsonite composition, to magnetite-hematite assemblage in the peralkaline syenites (T34 and T34GR), may have been a function of the increased oxygen fugacity. The oxygen fugacity had increased to the magnetite-hematite buffer level as evidence from iron-titanium oxide minerals shows (see later).

The maximum temperature of stability of the end-member ferrorichterite is $535 \pm 10^{\circ}\text{C}$ at $P_{\text{total}} = 1 \text{ Kb}$ and oxygen fugacity defined by the quartz-fayalite-magnetite buffer (Charles, 1977). This is particularly pertinent to the present study, as ferrorichterite has been found to be quite important among the amphiboles of the Tibchi Complex.

Ferrorichterite has been produced in the Tibchi Complex under two sets of conditions:

1. It forms, together with ferroedenite, the final stable amphibole assemblage in the hydrothermal alteration of the porphyries. Ferroedenite completes the transition in the Al-rich calcic amphibole transition series while ferrorichterite concludes that of the Al-poor calcic to sodic-calcic series. The thermal stability limit of ferrorichterite, $535 \pm 10^{\circ}\text{C}$, gives a strong indication that the hydrothermal alteration must have been concluded at less than that temperature if $P_{\text{total}} = 1 \text{ Kb}$ is assumed and oxygen fugacity is not less than that defined by the fayalite-magnetite-quartz buffer.
2. In the peralkaline syenite series T34C, T34 and T34GR ferrorichterite became eventually replaced by arfvedsonite. The transition may have depended, not only on temperature, but also on oxygen fugacity, the latter having made a vast, progressive, increase before the final stages of the postulated transition series. The beginning of the transition (T34C) must have occurred below the maximum stability limit of ferrorichterite.

5.4.7 Summary and conclusions

Amphiboles of the Tibchi Complex are classified and shown to represent as closely as possible the iron-rich members of their respective solid-solution series.

The compositional discontinuity in prograde metamorphic reactions between actinolitic and edenitic calcic amphiboles (Hallimond, 1943; Sundius, 1946) is not applicable to the subsolidus (hydrothermal) reactions in the quartz porphyries of the Tibchi Complex. On the contrary, the recent observations by Grapes and Graham (1978) during a detailed review of existing and new data on the supposed "miscibility gap", and their conclusions that a miscibility gap between the two end members does not exist, is supported here.

The present study shows that continuous miscibility between ferroedenite and ferrorichterite may not exist, at least under hydrothermal conditions. A compositional divide is found to exist within the ferroactinolite compositional field, directing two divergent reactions to ferroedenite and ferrorichterite respectively. That compositional divide between the two divergent reaction series is determined by their intrinsic requirement of Al^{IV} and Ca_B . Depending on what co-ordinates are chosen, certain plots may show apparently complete miscibility between the two trends.

Borley (1963b) suggested that Nigerian alkali amphiboles be called "riebeckitic arfvedsonites or arfvedsonites" since "none of the amphiboles analysed approaches the formula of the theoretical riebeckite". The recent I.M.A. classification leaves little doubt as to where a given alkali amphibole now belongs between riebeckite and arfvedsonite species, provided that analytical data are available. The term "riebeckite arfvedsonite" is thus probably no longer required.

TABLE 5-5 REPRESENTATIVE ANALYSES OF IRON-TITANIUM OXIDE MINERALS

	FERRIAN ILMENITES								TITANOMAGNETITES					MAGNETITES					HAEMATITES				
	1	2	3	4	5	6	7†	8†	9	10	11	12	13	14	15	16	17	18	19	20	21		
SiO ₂	0.00	0.02	0.15	0.00	0.34	0.73	0.57	0.51	n.d.	0.07	0.14	0.08	0.07	0.08	0.19	0.29	0.73	1.14	0.19	0.08			
TiO ₂	50.36	50.20	44.25	46.21	45.48	42.54	50.31	50.02	23.38	22.72	23.32	9.94	1.53	1.29	0.94	1.81	1.64	0.21	0.17	0.13			
Al ₂ O ₃	0.03	0.06	0.14	tr	0.20	0.37	tr	n.d.	0.70	0.29	0.32	0.05	0.10	0.08	0.08	0.09	0.23	0.05	0.05	0.07			
Fe ₂ O ₃	3.97	4.19	8.04	6.42	6.78	10.43	3.92	4.19	52.62	55.13	22.48	49.14	64.81	65.44	66.41	97.64	96.41	96.49	99.13	99.15			
FeO	42.86	44.15	37.86	43.47	43.54	39.40	43.30	42.18	20.58	19.26	51.40	39.75	31.22	30.97	31.07	0.98	1.39	0.37	0.13	0.00			
MnO	2.14	0.86	1.75	1.90	2.42	1.68	0.65	1.44	0.54	1.09	0.98	0.28	0.82	0.94	0.43	0.77	0.91	0.53	0.12	0.16			
MgO	0.03	0.08	x	n.d.	n.d.	1.76	0.62	0.46	0.02	0.04	0.00	0.02	0.05	0.03	0.04	0.04	0.01	0.00	0.00	0.00			
CaO	0.05	0.00	n.d.	n.d.	n.d.	2.78	0.46	0.71	0.06	n.d.	0.05	0.12	0.01	0.00	0.02	0.03	0.07	0.01	0.00	0.00			
TOTAL	99.44	99.56	92.19	98.00	98.76	99.69	99.83	99.51	98.22	98.53	98.62	99.44	98.63	98.82	99.04	101.54	98.91	98.89	99.79	99.59			
FeO(T)	46.43	47.91							67.92	68.87	71.63	83.97	89.53	89.85	90.83	88.84	86.37	87.19	89.33	89.00			
Molecular proportions																							
SiO ₂	-	-	0.002	-	0.006	0.012	0.009	0.008	0.005	-	0.001	0.002	0.001	0.001	0.001	0.003	0.012	0.023	0.003	0.001			
TiO ₂	0.630	0.628	0.554	0.529	0.569	0.532	0.630	0.626	0.293	0.284	0.292	0.124	0.019	0.016	0.012	0.023	0.016	0.021	0.003	0.002			
Al ₂ O ₃	-	0.001	0.001	-	0.002	0.004	-	-	0.007	0.003	0.003	-	0.001	0.001	0.001	0.001	0.001	0.001	-	0.001			
Fe ₂ O ₃	0.025	0.026	0.050	0.040	0.042	0.065	0.025	0.026	0.329	0.345	0.141	0.308	0.406	0.431	0.416	0.611	0.591	0.604	0.621	0.621			
FeO	0.597	0.614	0.527	0.605	0.606	0.548	0.603	0.597	0.286	0.268	0.715	0.553	0.435	0.431	0.432	0.014	0.005	0.019	0.005	-			
MnO	0.030	0.012	0.025	0.027	0.034	0.024	0.009	0.020	0.008	0.015	0.014	0.004	0.012	0.013	0.006	0.011	0.013	0.008	0.002	0.002			
MgO	0.001	0.002	-	-	-	0.044	0.015	0.011	-	0.001	-	-	0.001	0.001	0.001	0.001	-	-	-	-			
CaO	0.001	-	-	-	-	0.050	0.008	0.013	0.001	-	0.001	0.002	-	-	-	-	0.001	-	-	-			
TiO ₂ [*]	49.06	48.95	47.97	44.05	45.67	42.53	49.19	49.11	32.08	31.00	25.11	12.69	2.29	1.95	1.50	3.92	5.05	4.04	0.79	0.48			
Fe ₂ O ₃ [*]	1.95	2.11	4.40	3.33	3.50	5.40	1.93	2.01	36.17	37.99	12.34	31.02	46.51	47.08	47.98	92.16	90.66	93.94	98.57	99.20			
FeO [*]	48.99	48.94	47.63	52.62	50.83	52.07	48.88	48.88	31.75	31.01	62.55	56.29	51.20	50.97	50.52	3.92	3.09	2.02	0.64	0.32			

All values are expressed in weight percent.

FeO(T) = Total iron oxide as FeO. x = not determined. TiO₂^{*} = TiO₂ + SiO₂; Fe₂O₃^{*} = Fe₂O₃ + Al₂O₃; FeO^{*} = FeO + MnO + MgO + CaO.

† Excludes Cr₂O₃ and V₂O₅ reported originally.

1...Ilmenite; Microferrochlorite enclaves in quartz porphyry. 2...Ilmenite enclosed in ferroaugite phenocryst, Fayalite pyroxene quartz porphyry (T60). 3,4...Ilmenites; Porphyries, Birim (Ivriasi) Complex, Nigeria (Borley, 1963). 5,6...Ilmenites; Amphibole biotite granites, Sara-Fior and Joo-Bukuru Complex, Nigeria (Borley, 1963). 7,8...Ilmenites; Ferridiorites, Skarvsand Intrusion, East Greenland (Vincent and Phillips, 1954). 9...Ferrian ilmenite enclosed in alkali feldspar, Fayalite pyroxene quartz porphyry (T60). 10...Ferrian ilmenite; Groundmass, Fayalite pyroxene quartz porphyry (T60). 11...Titanomagnetite; Microsyenite onclave in quartz porphyry.

12...Titanomagnetite; Riproduct, ferrosedenbergitite → ferrocenite alteration, quartz porphyry (T169). 13...Relict magnetite in haematite, Sodic syenite (T34C). 14,15...Relict magnetites in haematites, Potassic syenite (T34). 16,17...Haematite Sodic syenite (T34C). 18. Haematite co-existing with magnetite, Potassic syenite (T34). 20,21...Haematites, Haematite syenite (T34GR).

Nos. 1,2 and 9-21 = Electron microprobe analyses.

ANALYST E.C.Ive

5.5 Iron-Titanium oxide minerals

5.5.1 General

Borley (1963a) reported some analyses of ilmenites from the porphyries of the Ririwai (Liruei) Complex, and the amphibole biotite granites of the Sara-Fier and Jos-Bukuru Complexes. Little else is known of the chemical composition of iron-titanium oxide minerals from the Younger Granites of Nigeria.

Iron-titanium oxide minerals analysed in the present study include ilmenites and ferrian ilmenites found in the microferrodiorite enclaves, the quartz porphyries and the granite porphyry ring-dyke; titanomagnetites in the micro-syenite enclaves and the hydrothermally altered quartz porphyries; intergrown magnetite and haematite in the peralkaline syenites; and intergrown magnetite and haematite from the vapour-phase crystalline assemblage within the lumen of a vesiculated fiamme in a welded tuff.

The nomenclature adopted for iron-titanium oxide minerals is that of Haggerty (1976) Fe_2O_3 calculations is based on Finger (1972).

5.5.2 Analytical data

The electron microprobe analyses presented in Table 5.5 are representative of the compositions obtained. The rest of the analyses may be found in the appendix. The analyses of Nigerian ilmenites by Borley (1963a) as well as ilmenites from the late-stage ferrodiorites of the Skaergaard Intrusion (Vincent and Phillips, 1954) are included in the table for comparison with the Tibchi ilmenites.

The analyses have been recast in molecular proportions

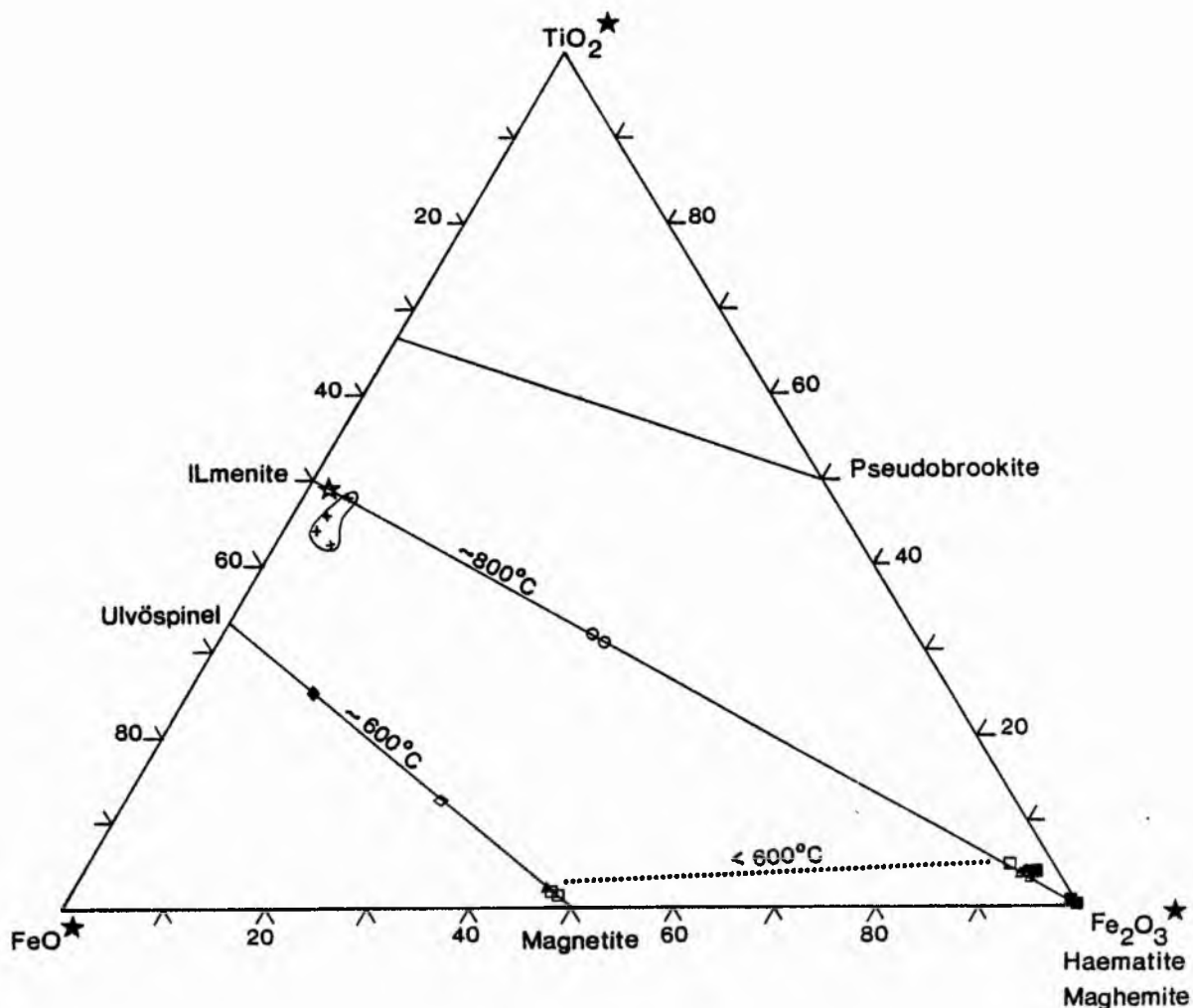


Figure 5.5.2 Molecular compositions of analysed iron-titanium oxide minerals. $\text{TiO}_2^* = (\text{TiO}_2 + \text{SiO}_2)$; $\text{FeO}^* = (\text{FeO} + \text{MnO} + \text{MgO} + \text{CaO})$; $\text{Fe}_2\text{O}_3^* = (\text{Fe}_2\text{O}_3 + \text{Al}_2\text{O}_3)$. Open star = Position of five Tibchi ilmenites (this study), & two Skaergaard ilmenites (Vincent and Phillips, 1954). Field of crosses = Some Nigerian ilmenites analysed by Borley (1963). Temperatures on solid lines = Critical points for each solvus; Temperature on dashed line = Equilibrium oxidation of magnetite to haematite (Haggerty, 1976). Circles = Ferrian ilmenites in quartz porphyry (see text; Filled upright diamond = Titanomagnetite in micro-syenite enclave; Open flat diamond = Titanomagnetite from hydrothermal breakdown of ferrohedenbergite to ferroedenite in quartz porphyry (T169); Magnetites and haematites belong to following rocks: Triangles = Sodic syenite (T34C); Open squares = Potassic syenite (T34); Filled squares = Haematite syenite (T34GR); Filled circle = Vapour phase crystallisation in lumen of fiamme, welded tuff (T114).

from which the molecular percentages of $TiO_2^* + Fe_2O_3^* + FeO^* = 100$, have been calculated such that: $TiO_2^* = (TiO_2 + SiO_2)$, $Fe_2O_3^* = (Fe_2O_3 + Al_2O_3)$ and $FeO^* = (FeO + MnO + MgO + CaO)$. The values obtained are plotted in a triangular diagram (Figure 5.5.2).

The recalculation procedure adopted above thus takes into account any possible role of the minor oxide constituents in the iron-titanium oxide minerals (Vincent and Phillips, 1954; Buddington and Lindsley, 1964; Haggerty, 1976), and contrasts with the procedure of some workers (Carmichael, 1963; Borley, 1963a).

5.5.3 Discussion

5.5.3A Review of analytical data in relation to reflected light microscopy

(a) Ilmenites and ferrian ilmenites

Reflected light microscopic examination showed that the ilmenites and ferrian ilmenites analysed occur as discrete homogeneous grains. The ilmenites deviate very little from a mean composition of $Ilm_{98}Hem_2$ and are commonly enclosed by fayalite and/or Ca-rich pyroxene crystals. On the other hand, ferrian ilmenite has been found as inclusion in feldspars enclosed by skeletal ferroaugite and gives a composition (one analysis) of $Ilm_{64}Hem_{36}$. Ferrian ilmenite also occurs in the groundmass and gives a composition (one analysis) of $Ilm_{62}Hem_{38}$.

(b) Titanomagnetites

The two titanomagnetites analysed are optically homogeneous discrete grains, in their respective rocks, and have been observed to have contrasting paragenetic histories. The

The titanomagnetite ($\text{Usp}_{75}\text{Mt}_{25}$) of the microsyenite enclave is of magmatic origin as no alteration or recrystallisation has been observed in this particular enclave. On the other hand the titanomagnetite ($\text{Usp}_{38}\text{Mt}_{62}$) of the quartz porphyry (T169) is an observed product of the hydrothermal breakdown of ferrohedenbergite to ferroedenite as shown in Plates 4.4G and H (Chapter 4). Despite their contrasting origins, both titanomagnetites analysed can be seen to lie on the $\text{Ulv}^{\text{spinel}}$ -Magnetite solid solution join (Figure 5.5.2).

(c) Magnetites and haematites

Throughout the series of the peralkaline syenitic rocks (T34C, T34 and T34GR), iron-titanium oxide minerals have, in reflected light, been found to consist of intergrown magnetite and haematite in the same grain. In the sodic syenite (T34C), continuous rims of haematite have been observed surrounding large cores of magnetite. In the same rock subhedral and euhedral cubic and octahedral sections of magnetite pseudomorphed by haematite can be seen. In the potassic syenite (T34) the iron-titanium oxide mineral is granular, sometimes massive, and can be seen to form from the breakdown of amphiboles (Plate 4.6F). Intergrowth of co-existing magnetite and haematite in the granular and massive grains of T34, is irregular in texture. The irregularity of such intergrown textures is more obvious in the haematite syenite (T34GR). In this latter rock haematite is dominant over magnetite, with irregular 'islands' of apparently relict magnetite in haematite. Sometimes complicated fern-like textures are observed, consisting mainly of haematite with remnant magnetite.

Intergrown magnetite-haematite in the vapour phase

crystalline assemblage located in the lumen of the vesiculated fiamme of the welded tuff (T114), consists of cubic sections of magnetite with rims of haematite. Haematite composition gives $\text{Ilm}_6\text{Hem}_{94}$. Magnetite analysis was unsuccessful.

5.5.2B Special comment on Ilmenites of the Tibchi Complex

Borley (1963a) compared the ilmenite analyses she obtained with those of the Skaergaard Intrusion and arrived at the conclusion that "the Nigerian ilmenites have an unusual composition; they are deficient in TiO_2 relative to FeO and other divalent oxides, and they contain a high percentage of ferric oxide. In contrast the Skaergaard ilmenites have ferrous oxide and titania contents that are very close to those of an ideal ilmenite" Examination of Table 5.5 and Figure 5.5.2 leaves little doubt that the Skaergaard and Tibchi ilmenites are identical with respect to the major oxide constituents. Borley's (op.cit.) ilmenites are, on the other hand, more variable in composition and plot in a field that departs appreciably from the Ilmenite-Haematite solid-solution join on which the Skaergaard and Tibchi ilmenites plot (Figure 5.5.2). Pending further work in other Nigerian Complexes, the Tibchi Complex could, meanwhile, be excluded from Borley's conclusions cited above.

5.5.3C Origin of the oxide minerals and estimates of temperatures

The optical homogeneity of analysed ilmenites does not rule out the possibility of cryptocrystalline exsolution

textures. For purposes of the present discussion crypto-crystalline exsolution will be regarded as broadly equivalent to a 'homogeneous' texture.

The homogeneous ilmenites of the Tibchi rocks may have originated from three possible sources: (a) by total unmixing of an initial single Ilm-Hem_{ss} phase; (b) by total oxidation of an initial single phase ulvöspinel rich Usp-Mt_{ss}; (c) by direct precipitation from the magma. The probability of (a) and (b) above occurring is almost negligible, given that fayalite and/or Ca-rich pyroxenes are found to be stable and co-existing in the same rock, with the above ilmenites. Buddington and Lindsley (1964) have studied the question of 'exsolution' of titaniferous magnetite to discrete grains of magnetite and ilmenite. They arrived at an unequivocal conclusion that ilmenites with more than 36% TiO₂ cannot be produced by oxidation of even pure ulvöspinel, let alone oxidation of a member of the ulvöspinel-magnetite solid-solution series. They believe that ilmenites with more than 36% TiO₂ undoubtedly reflect primary precipitation from the magma. The Tibchi ilmenites have not less than 49.9% TiO₂ and are therefore assumed to have been precipitated directly from the magma.

The ferrian ilmenites, of the quartz porphyry, enclosed in the feldspar and occurring in the groundmass, appear to be of primary origin (despite TiO₂ < 36%). Interesting to note is the slight, but progressive, enrichment in the haematite component (Figure 5.5.2) from the ferrian ilmenite in the enclosed feldspar to that in the groundmass. This observed trend is consistent with falling temperature during a magmatic process.

The Tibchi ilmenites and ferrian ilmenites lie on the Ilmenite-Haematite solid solution join (Figure 5.5.2). These may be considered to have crystallised above 800°C, this being the critical point (Haggerty, 1976) for the solvus of the above solid solution.

Evidence from the pyroxene fractionation trends shows that the microferrodiorite enclaves were more primitive than the microsyenite enclaves. Data from the iron-titanium oxide minerals show therefore that the primary crystallisation of ilmenite in the microferrodiorite enclaves was followed by precipitation of primary titanomagnetite in the microsyenite enclaves. Analyses presented are not sufficient to reveal the expected co-precipitation of ilmenite and magnetite in later differentiates (Vincent and Phillips, 1954).

The homogeneity of the titanomagnetite formed from the ferrohedenbergite -ferroedenite hydrothermal reaction in quartz porphyry (T169), and its position on the Ulvöspinel-Magnetite solid solution join, indicates that the hydrothermal process may have begun at some temperature above 600°C, the critical point for the Ulvöspinel-Magnetite solvus.

Magnetite-haematite intergrowth has been observed in all members of the peralkaline syenite series (T34C, T34, T34GR). One possible explanation is that the proposed metasomatic process, which is believed to be responsible for the observed transition in the peralkaline syenites listed above, may have been initiated above 1500°C, the magnetite-haematite solvus (Lindsley, 1976). The possibility of such a high temperature being involved is very unlikely, owing to the low temperature mineral paragenesis observed. The likely explanation is the oxidation of magnetite to haematite.

Experimental phase relation studies (Lindsley, 1976) reveal that "at temperatures below approximately 600°C, non-equilibrium oxidation of magnetite yields metastable cation-deficient magnetite-maghemite solid-solutions, whereas equilibrium oxidation produces hematite". The Fe_2O_3 mineral co-existing with magnetite in the peralkaline syenites of the Tibchi Complex is believed to be haematite ($\infty \text{Fe}_2\text{O}_3$) and not maghaemite ($\gamma \text{Fe}_2\text{O}_3$) as shown by:-

- a) its anisotropism (maghaemite is isotropic);
- b) reflection pleochroism (maghaemite is non-pleochroic);
- c) the relationship that oxidation of magnetite to haematite is produced from Ti-poor magnetites while maghaemites typify oxidation from more titaniferous magnetites (Haggerty, 1976).

Thus the haematite-magnetite relationship in the peralkaline syenites is consistent with equilibrium subsolidus oxidation of magnetite to haematite below 600°C (Lindsley, 1976). It is perhaps implied therefore that the primary iron-titanium oxide mineral produced at each stage of the series (T34C, T34 and T34GR) was magnetite, which underwent subsolidus oxidation to haematite. The conditions (eg. temperature, oxygen fugacity, etc.) necessary for the oxidation appear to have been available from the onset of the transition, at T34C. If that was so, then the petrographically observed feldspar grain boundary adjustments and other textural and mineralogical evidence of subsolidus re-equilibration, in the series of peralkaline syenites above, could be assumed to have occurred below 600°C.

Haggerty (1976) has investigated the partial decomposition of silicate phases (eg. biotite and amphibole) to magnetite and observed that "these magnetites are typically

very close to stoichiometric Fe_3O_4 " The magnetites of the peralkaline syenites, above, were formed mostly from pre-existing amphiboles and can be seen in Figure 5.5.2 to plot close to stoichiometric magnetite. The haematites produced from the magnetite by subsequent subsolidus oxidation are generally close to stoichiometric haematite, up to a value of $\text{Ilm}_1\text{Hem}_{99}$.

5.5.4 Summary and conclusion

Ilmenites of the Tibchi Complex are close to the ilmenite end-member composition of the Ilmenite-Haematite solid-solution series; in that respect they are identical to those of the late stages of the Skaergaard Intrusion.

In the petrogenetic scheme, ilmenite was precipitated as a primary phase from the magma followed by titanomagnetite and ferrian ilmenite as the magma evolved.

Hydrothermal breakdown of ferrohedenbergite to ferroedenite and titanomagnetite in the appropriate quartz porphyries may have begun above 600°C . The chemical and mineralogical transitions observed within the suite of peralkaline syenites were oxidative and most probably occurred below 600°C . The magnetites and haematites associated with the above syenites are found to be close to the stoichiometric compositions.

5.6 Biotites and chlorites

5.6.1 General

Chemical considerations of biotites and chlorites from the Tibchi Complex are limited by the inability of the

TABLE 5.6 ANALYSES OF SELECTED BIOTITES AND CHLORITES

	BIOTITES											CHLORITES				
	1	2	3	4	5	6	7	8	9	10	11	12	13	14	15	
SiO ₂	31.58	29.95	36.92	31.65	33.64	33.60	34.84	33.92	37.01	33.60	39.60	SiO ₂	22.81	22.54	22.18	22.27
TiO ₂	0.50	0.07	0.64	0.44	1.66	1.28	1.71	1.45	0.02	0.06	0.21	TiO ₂	0.01	0.06	0.04	0.08
Al ₂ O ₃	19.80	20.79	9.54	21.04	15.75	14.38	14.27	17.27	15.89	22.36	22.80	Al ₂ O ₃	18.24	19.19	20.04	21.40
Fe ₂ O ₃	x	x	x	x	x	x	x	x	tr	1.44	0.79	Fe ₂ O ₃	x	x	7.35	0.67
FeO ^t	32.30	31.25	35.07	28.66	33.13	34.03	34.27	29.86	30.16	28.54	20.98	FeO	44.41	44.68	35.23	43.01
MnO	0.12	0.12	0.42	0.65	0.41	0.38	0.40	0.41	1.01	0.33	0.29	MnO	0.54	0.48	0.02	0.05
MgO	0.47	2.25	1.55	0.08	0.20	0.16	0.15	0.97	0.22	0.10	0.46	MgO	1.11	0.14	3.79	2.35
CaO	0.03	0.06	0.27	0.00	0.02	0.01	0.05	0.02	0.10	0.14	1.52	CaO	0.04	0.05	0.40	0.15
Na ₂ O	0.28	0.05	0.00	0.26	0.13	0.17	0.18	0.20	0.58	0.46	tr	Na ₂ O	0.00	0.00	0.07	0.35
K ₂ O	8.76	8.85	7.72	8.92	8.92	8.83	8.97	8.97	9.02	8.90	8.95	K ₂ O	0.07	0.01	0.02	
TOTAL	93.84	93.39	92.13	91.70	93.86	92.84	94.84	93.07	94.01	95.93	95.60	TOTAL	87.23	87.15	89.14	90.33
	Numbers of ions on the basis of 22 oxygens											Numbers of ions based on 28 oxygens				
Si	5.240	4.988	6.303	5.286	5.615	5.714	6.779	5.601	6.032	5.317	5.945	Si	5.448	5.387	5.272	5.058
Al ^{IV}	2.760	3.012	1.697	2.714	2.385	2.286	2.221	2.399	1.968	2.683	2.055	Al ^{IV}	2.552	2.613	2.728	2.942
T	8.000	8.000	8.000	8.000	8.000	8.000	8.000	8.000	8.000	8.000	8.000	T	8.000	8.000	8.000	8.000
Al ^{VI}	1.111	1.069	0.222	1.427	0.714	0.595	0.567	0.963	1.085	1.488	1.980	Al ^{VI}	2.584	2.794	2.890	2.788
Ti	0.062	0.008	0.082	0.055	0.209	0.164	0.214	0.180	0.003	0.007	0.024	Ti	0.002	0.011	-	0.014
Fe ³⁺	-	-	-	-	-	-	-	-	0.000	0.172	0.089	Fe ³⁺	-	-	-	0.115
Fe ²⁺	4.481	4.351	5.005	4.002	4.623	4.838	4.752	4.123	4.111	3.777	2.634	Fe ²⁺	8.873	8.931	8.321 ^t	8.172
Mn	0.017	0.018	0.061	0.092	0.058	0.055	0.056	0.056	0.139	0.044	0.037	Mn	0.108	0.097	-	0.009
Mg	0.115	0.558	0.394	0.020	0.049	0.042	0.037	0.238	0.053	0.024	0.103	Mg	0.395	0.050	1.343	0.796
C	5.786	6.004	5.764	5.596	5.653	5.694	5.626	5.560	5.338	5.512	4.867					
Ca	0.004	0.011	0.050	-	0.004	0.002	0.008	0.003	0.018	0.024	0.245	Ca	0.011	0.013	0.101	0.037
Na	0.089	0.017	-	0.084	0.043	0.057	0.058	0.062	0.183	0.141	-	Na	-	-	0.031	0.152
K	1.855	1.881	1.682	1.900	1.900	1.916	1.898	1.890	1.876	1.797	1.714	K	0.022	0.003	0.004	-
AB	1.948	1.909	1.732	1.984	1.947	1.975	1.964	1.958	2.077	1.962	1.959	C	11.993	11.899	12.690	12.08

t = Total iron as FeO.

x = not determined separately.

tr = trace.

All values are expressed in weight percent.

1...Siderophyllitic biotite, Altered granite porphyry minor dyke (T22), ref. Plate 4.4P.
 2...Siderophyllitic biotite, Altered crystal tuff (T76),
 3...Iron-biotite co-existing with fluorite and magnetite-hematite pair in lumen of vesiculated fiamme, Lithic tuff (T114),
 4...Siderophyllitic biotite, Late vein in sodic syenite (T34C).
 5...Siderophyllitic biotite, Antiperthite biotite granite (T34B).
 6...Siderophyllitic biotite, nucleated along fracture in host rock, Biotite granite (T34BB).
 7...Siderophyllitic biotite in the main rock, co-existing with no.6 above, in biotite granite (T34BB).
 8...Siderophyllitic biotite, partially replaced by chlorite (no.13), Mineralised biotite granite (T138), Kogo hill.
 9,10,11...Representative siderophyllites of Foster

(1960, Table 11, nos.132, 135, 129 respectively). Excludes: no.9, LiO₂=1.01% (Li^{VI} 0.33), water, halogens, etc.=5.22%; no.10, LiO₂=0.32% (Li^{VI} 0.10), water, halogens = 2.98%; no.11, water, halogens = 5.2%.
 12...Brownish-green chlorite co-existing with microcline phenocrysts in dyke rock (T41), ref. section 4.6.1.
 13...Green chlorite partially replacing siderophyllitic biotite (no.8), Mineralised biotite granite (T138), Kogo hill.
 14...Oxidised daphnite (Thuringite), Fortuna mine, Lahn, Germany (Deer et al., 1971). Excludes: water, CO₂=10.7%.
 15...Unoxidised green daphnite, Bas Vallon, Foret de Lorges, Quintin, Cotes-du-Nord, France (Deer et al., 1971). Excludes water=10.2%.

Nos.1-8 and 12-13 = electron microprobe analyses.

Analyst E.C.Ike

electron microprobe to give separate values for Fe_2O_3 (total iron being expressed as FeO), and the absence of data for Li_2O , F, Cl and water. All or some of the above constituents must be known in order to correctly classify, and sufficiently discuss, the biotite and chlorite variations that are thought to exist.

Owing to the above constraints, the purpose here is primarily to present analyses of only those biotites and chlorites observed to have formed under special (usually localised) conditions and which have been spotlighted earlier petrographically. The analyses are presented in Table 5.6.

To the writer's knowledge, there is no published work on micas and chlorites from the Nigerian Younger Granite province comparable to that of Borley (1963a) on amphiboles, but Abernethy (in preparation) is currently engaged in this. It may be observed here, that, at present, a certain degree of confusion appears to have set in, in the Nigerian literature, concerning a variety of green micas encountered in the Younger Granites.

The nomenclature adopted here is that of Foster (1960) for biotites, and of Heys (1954) for chlorites.

5.2.2. Biotite

Of the eight biotite analyses from Tibchi Complex (Table 5.6), seven are thought to be siderophyllitic (hereafter called "siderophyllites"); one (no.3), is provisionally called "iron biotite".

The Tibchi siderophyllites are characterised by relatively low silica and lime while showing a generally high total iron and, in two cases, high magnesium. Abernethy

(per.comm.) has also observed abnormally high magnesium values in siderophyllites formed under hydrothermal conditions. The "iron-biotite" is extremely iron-rich, also high in magnesium, but comparatively poor in aluminium.

5.5.3 Chlorite

The analysed chlorites of the Tibchi Complex are particularly rich in iron and poor in magnesium (Table 5.6).

The three most important parameters for characterisation of chlorite chemically, are ferric iron, silicon and total iron (Deer et al., 1961). Inferences based on ferric iron are not possible here, owing to the method of analysis. On the basis of silicon values, however, the two chlorite analyses fall within the 'Thuringite' class of Heys (1954).

KEY TO TABLES 6A to 6D

Alkalic index = Molecular $\frac{\text{Na}_2\text{O} + \text{K}_2\text{O}}{\text{Al}_2\text{O}_3}$

Iron index = Weight percent $\frac{\text{FeO} + \text{Fe}_2\text{O}_3}{\text{FeO} + \text{Fe}_2\text{O}_3 + \text{MgO}}$

Diff. (Differentiation) Index = Normative Q + or + ab + ne

TABLE 6A WHOLE-ROCK MAJOR AND TRACE ELEMENT ANALYSES OF BASEMENT AND EXTRUSIVE VOLCANIC ROCKS

Field No.	Granitic basement			Basalts				Andesine basalt	Trachyta	Early rhyolites		Poorly welded tuff	Welded lithic tuff	Welded crystal tuff 1	Welded crystal tuff 2	Hydrothermally altered crystal tuff 2
	T 103	T 20	T 145	T 122	T 162	T 163	T 53	T 53A	T 153	T 154	T 51	T 126	T 117	T 158	T 112	T 44
Weight %																
SiO ₂	68.60	68.59	72.35	49.90	45.57	50.50	43.60	54.30	65.90	80.40	74.90	78.80	74.60	74.00	75.35	77.30
TiO ₂	0.46	0.39	0.27	0.20	3.72	2.73	2.90	2.50	0.90	0.56	0.50	0.12	0.22	0.40	0.33	0.22
Al ₂ O ₃	14.65	14.42	14.50	14.78	14.21	14.68	15.17	13.00	11.83	10.32	12.75	11.00	11.57	11.20	11.61	11.20
Fe ₂ O ₃	1.25	1.24	0.60	4.53	5.13	3.66	2.74	9.08	7.89	0.24	0.30	0.20	2.35	2.28	0.68	0.39
FeO	2.45	2.33	1.10	9.58	11.17	9.42	12.26	6.79	2.79	3.36	3.69	0.14	0.91	1.37	2.00	2.15
MnO	0.06	0.07	0.03	0.17	0.26	0.20	0.41	0.27	0.11	0.06	0.03	0.01	0.04	0.08	0.04	0.04
MgO	0.25	0.45	0.43	6.84	5.44	3.62	3.72	1.50	0.22	0.76	1.53	0.09	0.05	0.12	0.15	0.22
CaO	2.01	1.48	1.09	9.20	9.16	8.98	14.04	6.44	2.04	0.25	0.93	0.12	0.45	0.60	0.63	0.36
Na ₂ O	3.44	3.82	3.69	3.16	2.34	2.34	1.40	2.98	3.23	0.29	0.35	0.18	4.01	3.46	3.87	1.59
K ₂ O	5.22	5.58	4.65	0.73	0.27	0.63	0.82	0.36	2.96	2.24	3.31	8.48	4.38	4.60	4.72	6.77
P ₂ O ₅	0.09	0.02	0.01	0.22	0.63	0.20	0.14	0.45	0.22	0.00	0.02	0.00	0.01	0.00	0.05	0.04
H ₂ O ⁺	0.85	0.91	0.62	0.79	2.17	2.39	2.07	1.85	2.32	0.96	1.30	1.30	0.97	1.07	0.38	0.48
H ₂ O ⁻	0.08	0.07	0.10	0.17	0.14	0.12	0.07	0.22	0.09	0.11	0.18	0.15	0.11	0.25	0.08	0.10
TOTAL	99.41	99.37	99.44	100.27	100.21	99.47	99.34	99.74	100.50	99.55	99.79	100.59	99.67	99.43	99.89	100.86
Agpaitic																
Index	0.77	0.85	0.77	0.41	0.29	0.31	0.22	0.41	0.72	0.29	0.34	0.86	0.98	0.96	0.98	0.89
Iron																
Index	0.94	0.89	0.86	0.67	0.75	0.78	0.80	0.91	0.98	0.83	0.72	0.79	0.98	0.97	0.95	0.92
CIPW Norm																
Q	22.98	20.23	29.65	-	3.14	9.16	-	21.95	31.72	66.13	53.37	44.92	33.85	35.10	32.68	39.65
or	30.84	32.97	27.47	4.31	1.60	3.72	4.84	2.13	17.49	13.23	19.59	50.10	25.88	27.18	27.89	40.00
ab	29.09	32.31	31.21	26.73	19.79	19.79	11.84	25.20	27.32	2.45	2.96	1.52	33.92	29.26	32.73	13.45
an	0.12	5.73	5.34	23.99	27.47	27.69	32.69	21.04	8.68	1.24	4.48	0.60	0.64	1.45	0.38	1.52
ne	-	-	-	-	-	-	-	-	-	-	-	-	-	-	-	-
c	-	-	1.44	-	-	-	-	-	0.13	6.96	6.95	1.31	-	-	-	0.70
ac	-	-	-	-	-	-	-	-	-	-	-	-	-	-	-	-
wo	-	-	-	-	-	-	-	-	-	-	-	-	0.49	0.19	-	-
two	0.11	0.62	-	8.44	5.78	6.49	15.05	3.33	-	-	-	-	0.14	0.45	1.01	-
dien	0.02	0.19	-	4.51	3.13	3.02	5.57	2.26	-	-	-	-	0.12	0.30	0.14	-
fs	0.10	0.46	-	3.66	2.45	3.40	9.76	0.81	-	-	-	-	-	0.12	0.97	-
hyen	0.60	0.93	1.07	7.41	10.41	5.99	0.10	1.48	0.55	1.89	3.81	0.22	-	-	0.24	0.55
hfs	2.72	2.28	1.13	6.02	8.16	6.74	0.18	0.53	-	5.16	5.76	-	-	-	1.67	3.34
olfs	-	-	-	3.58	-	-	2.51	-	-	-	-	-	-	-	-	-
olfsa	-	-	-	3.21	-	-	4.85	-	-	-	-	-	-	-	-	-
nt	1.81	1.80	0.87	6.57	7.44	5.31	3.97	13.17	6.74	0.35	0.43	0.14	2.43	3.31	0.99	0.57
ha	-	-	-	-	-	-	-	-	3.24	-	-	0.11	0.68	-	-	-
ll	0.87	0.74	0.51	0.38	7.06	5.18	5.51	4.75	1.71	1.06	0.95	0.23	0.42	0.76	0.63	0.42
ns	-	-	-	-	-	-	-	-	-	-	-	-	-	-	-	-
ap	0.21	0.05	0.02	0.52	1.49	0.47	0.33	1.07	0.52	-	0.05	-	0.02	-	0.12	0.09
Diff.																
Index	82.91	85.51	88.33	31.04	24.53	32.67	16.68	49.28	76.53	81.81	75.92	96.54	93.65	91.54	93.30	93.10
Ppm																
Li	11	45	84	25	13	18	11	28	6	29	50	4	52	8	19	23
Be	3	5	5	-	1	4	6	3	3	2	11	5	14	25	7	8
Cu	14	12	10	-	17	7	21	17	11	-	9	-	-	-	18	11
Zn	109	273	77	140	590	282	1064	279	151	91	100	10	643	294	224	172
Hb	129	215	264	12	23	13	22	19	60	73	687	210	409	276	237	263
Sr	175	188	142	446	365	421	402	286	332	28	-	67	17	31	-	106
Zr	385	366	199	218	250	268	231	330	650	396	104	407	963	641	478	455
SnO ₂	10	40	40	40	30	40	30	30	30	10	10	40	30	30	10	20
Pb	28	78	-	-	33	-	64	27	29	-	-	-	34	-	-	32

± 1σ
± 1σ

Analysts: R.A. Batchelor and E.C. Ikes E. Cox (trace elements)

TABLE 6B WHOLE-ROCK MAJOR AND TRACE ELEMENT ANALYSES OF THE PORPHYRIES

Field No. →	Granite porphyry ring-dyke					Isolated granites porphyry minor dykes					Quartz porphyries						
	T 11	T 108	T 5	T 37	T VA	T VB	T 91	T 22	T 23	T 60	T 135	T 167	T 168	T 169	T 170	T 133	T 105
Weight %	72.75	72.98	72.99	71.99	76.01	75.40	72.20	76.50	72.20	73.50	76.28	75.88	73.37	74.08	77.28	76.49	73.03
SiO ₂	0.35	0.30	0.30	0.40	0.21	0.22	0.40	0.16	0.20	0.30	0.30	0.20	0.41	0.30	0.10	0.20	0.37
Al ₂ O ₃	12.54	11.36	11.42	12.74	11.75	11.44	12.28	11.17	10.93	11.38	10.61	11.04	11.93	11.70	10.41	10.85	12.68
Fe ₂ O ₃	2.22	2.82	2.07	1.75	2.45	2.02	1.85	2.66	0.34	1.45	1.33	1.80	2.22	2.35	1.66	1.30	1.43
FeO	1.46	0.98	1.78	2.26	0.23	1.08	1.81	2.84	7.29	2.35	1.48	1.30	1.65	1.20	0.78	1.41	1.98
MnO	0.06	0.08	0.11	0.10	0.03	0.09	0.07	0.04	0.05	0.08	0.04	0.06	0.08	0.08	0.04	0.05	0.08
MgO	0.09	0.12	0.08	0.14	0.03	0.03	0.08	0.04	0.11	0.08	0.03	0.09	0.10	0.14	0.03	0.02	0.08
CaO	0.81	0.83	0.83	1.04	0.23	0.35	0.91	0.85	1.03	1.04	0.46	0.54	0.73	0.80	0.26	0.33	0.93
Mg ₂ O	4.09	4.07	4.19	4.02	3.53	3.79	3.72	4.16	2.44	4.30	4.12	3.85	3.88	4.00	3.55	4.08	4.01
K ₂ O	5.21	5.10	5.08	5.17	5.26	4.94	4.96	4.95	2.67	5.06	4.91	4.83	5.02	4.89	4.77	4.85	5.10
P ₂ O ₅	0.04	0.03	0.04	0.06	0.02	0.02	0.01	0.00	0.00	0.03	0.02	0.01	0.01	0.01	0.01	0.00	0.00
H ₂ O ⁺	0.61	0.75	0.54	0.27	0.61	0.27	0.77	0.95	1.54	0.24	0.24	0.25	0.46	0.49	0.29	0.18	0.36
H ₂ O ⁻	0.11	0.23	0.04	0.05	0.15	0.10	0.13	0.09	0.11	0.12	0.11	0.10	0.14	0.15	0.09	0.04	0.11
TOTAL	100.34	99.67	99.45	99.95	100.56	99.83	99.18	98.91	98.91	99.94	99.74	100.20	99.90	100.19	99.27	99.62	100.13
Asphaltic																	
Index	0.98	1.07	1.09	0.95	0.98	1.01	0.75	0.63	0.63	1.10	1.14	1.05	1.00	1.01	1.06	1.11	0.96
Iron																	
Index	0.98	0.97	0.98	0.97	0.99	0.99	0.98	0.99	0.99	0.98	0.99	0.97	0.97	0.96	0.99	0.99	0.98
GFPM Norm																	
Q	27.82	29.67	28.21	26.27	35.72	34.10	29.46	42.85	39.57	27.94	35.07	34.32	30.38	31.21	38.45	34.77	27.82
or	30.78	30.13	30.01	30.55	31.08	29.19	29.30	8.57	15.77	29.90	29.01	28.54	29.66	28.89	28.18	28.77	30.13
ab	34.59	30.14	30.46	34.00	29.86	31.34	31.46	35.18	20.64	30.36	27.24	29.89	32.82	32.96	26.99	28.69	33.92
an	0.43	-	-	1.45	0.69	-	2.17	4.22	5.11	-	-	-	-	-	-	-	1.94
ne	-	-	-	-	-	-	-	-	-	-	-	-	-	-	-	-	-
c	-	3.77	4.39	-	-	0.63	-	1.21	2.16	4.22	3.27	2.35	-	0.77	2.67	3.18	-
ac	0.77	1.11	-	-	0.05	0.32	-	-	-	-	-	-	0.59	1.11	-	-	-
wo	0.59	0.52	1.64	1.38	0.09	0.35	0.98	-	-	2.07	0.90	1.09	0.88	0.52	0.51	0.68	1.28
di	0.22	0.30	0.13	0.20	0.07	0.07	0.15	-	-	0.11	0.03	0.17	0.25	0.35	0.05	0.02	0.13
fs	0.36	0.20	1.68	1.30	-	0.30	0.32	-	-	2.21	0.98	1.02	0.67	0.14	0.51	0.76	1.29
hy	-	-	0.07	0.14	-	-	0.05	0.10	0.27	0.09	0.04	0.06	-	-	0.02	0.03	0.07
by	-	-	0.84	0.93	-	-	0.34	4.48	12.87	1.76	1.32	0.33	-	-	0.22	1.60	0.71
ol	-	-	-	-	-	-	-	-	-	-	-	-	-	-	-	-	-
fo	-	-	-	-	-	-	-	-	-	-	-	-	-	-	-	-	-
fa	3.22	2.20	0.80	2.54	0.23	2.61	2.68	0.96	0.49	-	-	1.43	3.22	3.02	1.07	-	2.07
ht	-	-	-	-	-	2.29	-	-	-	-	-	-	-	-	-	-	-
ll	0.66	0.57	0.57	0.76	0.40	0.42	0.76	0.30	0.38	0.57	0.57	0.38	0.78	0.57	0.19	0.38	0.70
rs	-	-	-	-	-	-	-	-	-	0.28	0.91	-	-	-	-	0.51	-
sp	0.09	0.07	0.07	0.14	0.05	0.05	-	-	-	-	0.05	0.02	0.02	0.02	0.02	-	-
Diff.																	
Index	93.19	89.94	88.68	90.82	96.66	94.63	90.22	86.60	75.98	88.20	91.32	92.75	92.86	93.06	93.62	92.23	91.87
Ppm																	
Li	10	21	18	6	10	32	6	21	78	18	43	30	18	-	18	68	14
Be	5	4	5	5	5	15	5	5	26	4	6	5	5	7	6	11	7
Ba	14	12	13	15	9	15	7	14	15	12	11	10	13	10	10	11	13
Zn	186	157	266	230	151	392	182	691	900	187	227	218	177	153	307	247	175
Rb	123	100	112	120	103	201	156	183	374	120	160	134	110	144	174	230	127
Sr	33	33	33	47	9	7	38	47	53	34	22	22	41	45	13	-	37
Zr	476	460	504	567	411	524	558	425	412	542	620	462	529	534	477	439	557
Sm ₂	10	40	40	20	40	20	50	50	70	40	40	40	40	40	40	40	10
Pb	24	34	33	28	38	32	39	67	93	25	34	34	63	16	32	37	46

Analysts: R.A. Batchelor and E.C. Ike; E. Cox (trace elements)

16

TABLE 60 WHOLE-ROCK MAJOR AND TRACE ELEMENT ANALYSES OF SAMPLES FROM THE BIOTITE GRANITE PLUTON

Field No.	S.E. Sector, Biotite granite pluton				N.W. Sector				Yell Hill sector				Kogo Hill sector				Marginal and roof-zone microgranites			
	T 171	T 172	T 348	T 96	T 58	T 182	T 92	T 92V ¹	T 94	T 98	T 138	T 70	T 139	T 154	T 78	T 21	T 74			
SiO ₂	77.40	77.21	76.90	77.60	77.70	77.14	76.30	74.91	76.60	78.72	74.80	76.10	75.60	77.00	77.33	76.90	77.86			
TiO ₂	0.09	0.08	0.10	0.05	0.05	0.07	0.10	0.05	0.07	0.09	0.20	0.07	0.05	0.08	0.01	0.05	0.10			
Al ₂ O ₃	11.79	12.01	11.35	11.29	11.29	12.12	12.06	12.23	11.95	11.45	12.10	12.18	12.26	11.74	11.42	11.50	11.85			
Fe ₂ O ₃	0.59	0.76	0.17	0.17	0.24	0.48	0.30	0.81	1.00	1.17	0.73	0.14	0.21	0.33	1.12	0.37	0.08			
MnO	0.02	0.65	0.94	1.03	1.08	0.69	0.86	1.30	0.37	0.00	2.12	1.24	1.31	0.89	0.20	0.91	0.94			
MgO	0.03	0.03	0.02	0.04	0.02	0.02	0.02	0.03	0.02	0.02	0.04	0.03	0.02	0.02	0.02	0.03	0.03			
CaO	0.45	0.57	0.46	0.62	0.39	0.46	0.30	0.90	0.63	0.44	0.85	0.58	0.62	0.01	0.05	0.03	0.02			
Na ₂ O	3.68	3.86	4.16	3.78	3.56	3.83	3.52	4.60	3.43	3.20	3.23	3.61	3.15	3.88	4.15	4.06	4.45			
K ₂ O	4.69	4.58	4.58	4.63	4.36	4.55	4.74	4.48	4.44	4.81	4.41	4.45	4.55	4.59	4.32	4.53	4.26			
P ₂ O ₅	0.01	0.00	0.00	0.00	0.02	0.00	0.00	0.00	0.00	0.01	0.00	0.00	0.00	0.00	0.00	0.00	0.00			
H ₂ O ⁺	0.53	0.42	0.38	0.36	0.85	0.44	1.07	0.30	0.20	0.51	0.42	0.64	1.02	0.59	0.42	0.28	0.39			
H ₂ O ⁻	0.13	0.10	0.18	0.12	0.05	0.12	0.08	0.08	0.12	0.09	0.08	0.10	0.10	0.11	0.06	0.10	0.05			
TOTAL	100.08	100.30	99.36	99.71	100.13	99.95	99.57	99.74	99.08	100.60	99.06	99.17	98.91	99.50	99.49	99.27	100.50			
Asphatic Index	0.94	0.94	1.05	1.00	0.89	0.92	0.91	1.02	0.89	0.92	0.83	0.88	0.83	0.97	1.01	1.01	1.01			
Iron Index	0.98	0.98	0.98	0.97	0.99	0.98	0.98	0.98	0.96	0.93	0.97	0.98	0.99	0.99	0.96	0.98	0.98			
CIPM Norm	36.87	35.95	35.01	36.38	38.72	36.08	36.05	29.33	37.48	40.67	35.83	35.85	37.53	35.78	36.28	34.81	34.56			
or	27.71	27.06	27.65	27.35	25.76	26.88	28.00	26.47	27.41	28.42	26.05	26.29	26.88	27.12	25.52	26.76	25.17			
ab	31.12	32.65	32.32	31.97	30.11	32.39	29.77	37.96	29.01	27.06	27.32	30.53	26.64	32.82	34.04	33.93	37.23			
an	1.81	1.93	-	0.17	1.80	2.28	2.48	-	3.12	2.12	4.22	2.88	3.08	1.07	-	-	-			
ne	-	-	-	-	-	-	-	-	-	-	-	-	-	-	-	-	-			
c	-	-	0.49	-	0.56	0.06	0.23	-	0.14	0.21	0.47	0.37	1.03	-	-	-	-			
ac	-	-	-	-	-	-	-	0.83	-	-	-	-	-	-	0.41	0.36	0.23			
wo	-	0.15	0.38	1.21	-	-	-	0.02	-	-	-	-	-	-	0.68	-	-			
dien	0.02	0.05	0.03	0.07	-	-	-	1.84	-	-	-	-	-	0.09	0.14	1.06	0.97			
fs	0.15	0.36	1.04	1.28	-	-	-	1.93	-	-	-	-	-	0.12	0.06	0.03	0.03			
hy	0.06	0.02	0.02	0.02	0.05	0.07	0.05	-	0.12	0.22	0.20	0.07	0.05	0.10	1.12	1.06	0.02			
fs	0.48	0.13	0.56	0.43	1.74	0.79	1.20	-	-	-	3.03	2.10	2.19	1.16	-	0.32	0.55			
ol	-	-	-	-	-	-	-	-	-	-	-	-	-	-	-	-	-			
fa	-	-	-	-	-	-	-	-	-	-	-	-	-	-	-	-	-			
at	0.86	1.10	-	0.25	0.35	0.70	0.43	0.76	1.05	-	1.06	0.20	0.30	0.48	0.68	0.36	-			
ha	-	-	-	-	-	-	-	0.27	0.27	1.17	-	-	-	-	0.51	-	-			
ll	0.17	0.15	0.19	0.09	0.09	0.13	0.19	0.09	0.13	0.04	0.38	0.13	0.09	0.15	0.02	0.09	0.19			
ns	-	-	0.54	-	-	-	-	-	-	-	-	-	-	-	-	-	0.03			
ap	0.02	-	-	-	0.05	-	-	-	-	0.02	-	-	-	-	-	-	-			
Diff. Index	95.70	95.66	94.98	95.70	94.59	95.36	93.82	93.76	93.90	96.15	89.20	92.67	91.05	95.72	96.44	95.50	96.96			
Ppm	72	115	230	234	145	176	84	314	80	109	195	106	120	122	156	274	18			
Li	11	10	8	8	3	9	11	13	10	8	14	10	5	12	9	18	6			
Be	14	12	15	10	11	16	7	9	7	10	91	7	8	7	11	10	9			
Cu	73	181	129	44	90	93	38	58	29	40	380	513	274	61	40	52	31			
Zn	436	521	534	-	253	739	476	368	425	340	505	517	603	594	660	989	559			
Sr	7	-	39	-	68	51	2	2	2	2	444	-	1	-	-	20	-			
Zr	131	141	60	-	676	112	100	120	92	74	227	80	89	80	101	138	-			
SnO ₂	10	30	40	40	110	90	50	40	10	60	20	10	30	20	40	40	20			
Pb	50	46	37	-	32	48	3	57	46	33	63	51	-	59	-	44	56			

Analyses: R.A. Batchelor and E.C. Iker, E. Cox (trace elements)

TABLE 6D WHOLE-ROCK MAJOR AND TRACE ELEMENT ANALYSES OF MISCELLANEOUS ROCKS

Field No. →	Undersaturated 'basement screen'			Suite of peralkaline syenites and granites, S.E.Sector Biotite Granite, Pluton				Average compositions of Nockolds (1954)		
	T 35	T 36	T 41 ¹	T 173	T 34C	T 34	T 34B	ALKALI GRANITE	PERALK. GRANITE	PERALK. SYENITE
Weight %										
SiO ₂	58.40	56.14	76.82	71.95	67.26	62.78	76.90	75.01	71.08	61.65
TiO ₂	0.56	0.60	0.11	0.09	0.05	0.05	0.10	0.17	0.40	0.52
Al ₂ O ₃	20.55	20.47	12.11	14.63	17.16	15.76	11.35	13.16	11.26	14.73
Fe ₂ O ₃	1.09	1.75	0.75	1.34	1.07	5.02	0.17	0.94	4.28	4.56
FeO	2.04	1.67	0.85	0.67	0.25	1.84	0.94	0.88	2.19	3.68
MnO	0.10	0.11	0.02	0.03	0.02	0.15	0.02	0.07	0.11	0.20
MgO	0.44	0.48	0.05	0.03	0.01	0.03	0.02	0.24	0.25	0.70
CaO	6.42	7.50	0.80	0.55	0.46	0.34	0.46	0.56	0.84	1.87
Na ₂ O	7.76	7.54	3.74	7.72	7.32	5.58	4.16	3.48	4.92	6.69
K ₂ O	0.34	0.30	4.72	2.32	5.86	7.20	4.58	5.01	4.21	4.65
P ₂ O ₅	0.19	0.20	0.01	0.02	0.00	0.00	0.00	0.11	0.07	0.17
H ₂ O ⁺	0.80	0.57	0.78	0.23	0.02	0.42	0.38	0.37	0.39	0.58
H ₂ O ⁻	0.08	0.08	0.09	0.07	0.18	0.12	0.18			
TOTAL	98.77	97.40	100.85	99.65	99.66	99.29	99.36	100.00	100.00	100.00
Agpaitic										
Index	0.64	0.62	0.92	1.04	1.07	1.07	1.05	0.85	1.12	1.09
Iron										
Index	0.88	0.88	0.97	0.99	0.99	>0.99	0.98	0.88	0.96	0.92
GIPW Norm										
Q	-	-	35.24	17.92	3.98	3.36	35.01	34.1	26.2	1.6
or	2.01	1.77	27.89	13.71	34.62	42.54	27.65	29.5	25.0	27.8
ab	64.31	58.86	31.63	62.33	55.64	40.98	32.32	29.3	34.6	49.2
an	20.25	21.13	2.32	-	-	-	-	2.2	-	-
ne	0.72	2.66	-	-	-	-	-	-	-	-
C	-	-	-	-	-	-	-	1.3	-	-
ac	-	-	-	2.61	3.10	5.48	0.49	-	6.0	6.5
wo	1.20	4.04	-	0.31	0.56	-	-	-	-	-
di	3.12	2.12	0.66	0.77	0.39	0.70	0.95	-	-	-
en	1.10	1.19	0.10	0.07	0.02	0.05	0.03	1.3	3.7	9.6
fs	2.11	0.83	0.62	0.78	0.41	0.73	1.04	-	-	-
hy	-	-	0.03	-	-	0.02	0.02	-	-	-
en	-	-	0.18	-	-	0.26	0.56	-	-	-
fs	-	-	-	-	-	-	-	-	-	-
mt	1.58	2.54	1.09	0.63	-	4.53	-	1.4	3.2	3.5
hm	-	-	-	-	-	-	-	-	-	-
il	1.06	1.14	0.21	0.17	0.09	0.09	0.19	0.3	0.8	0.9
ns	-	-	-	-	0.64	-	0.54	-	-	-
ap	0.45	0.47	0.02	0.05	-	-	-	0.3	0.2	0.4
Diff.										
Index	67.04	63.29	94.76	93.96	94.24	86.88	94.98	92.9	85.8	78.6
Ppm										
Li	10	6	14	178	46	310	230			
Be	11	19	13	173	118	230	8			
Cu	21	19	9	19	15	18	15			
Zn	378	141	128	394	282	882	129			
Rb	7	17	489	233	597	1103	534			
Sr	2706	3476	-	35	39	69	39			
Zr	1094	1384	197	161	60	162	60			
SnO ₂	10	20	40	80	40	80	40			
Pb	34	23	58	37	50	93	37			

¹ see text

Analysts: R.A.Batchelor and E.G.Ike; E.Cox (trace elements)

CHAPTER 6

WHOLE-ROCK MAJOR AND TRACE ELEMENT GEOCHEMISTRY

6.1 General

Fifty-six samples belonging to various rock-types of the Tibchi Complex have been analysed for whole rock major and trace elements. Of the above number, three belong to the basement, thirteen to the extrusive volcanic rocks, nine to the granite porphyry ring-dyke and isolated granite porphyry minor dykes, eight to the quartz porphyries, seventeen to the biotite granite pluton and six to the 'miscellaneous rocks'.

Major element analyses have been carried out mainly by atomic absorption spectrometry. Analyses of samples chosen at random, and any particularly doubtful analyses, have been confirmed by X-ray fluorescence at the University of Edinburgh.

Trace element concentrations have been determined by X-ray fluorescence in St. Andrews. The technique is under continuing improvement so that although the results obtained are presented, they are not discussed. Instead, the results of a contemporaneous investigation on rare-earth element concentrations in pre-selected groups of rocks from the Tibchi Complex (Moyes, 1979) are summarised and discussed briefly in the light of major element chemistry in those rocks.

6.2 Analytical data

Analytical data are presented in four separate tables as follows: Basement and extrusive volcanic rocks in Table 6A, the granite porphyries and quartz porphyries in Table 6B, the

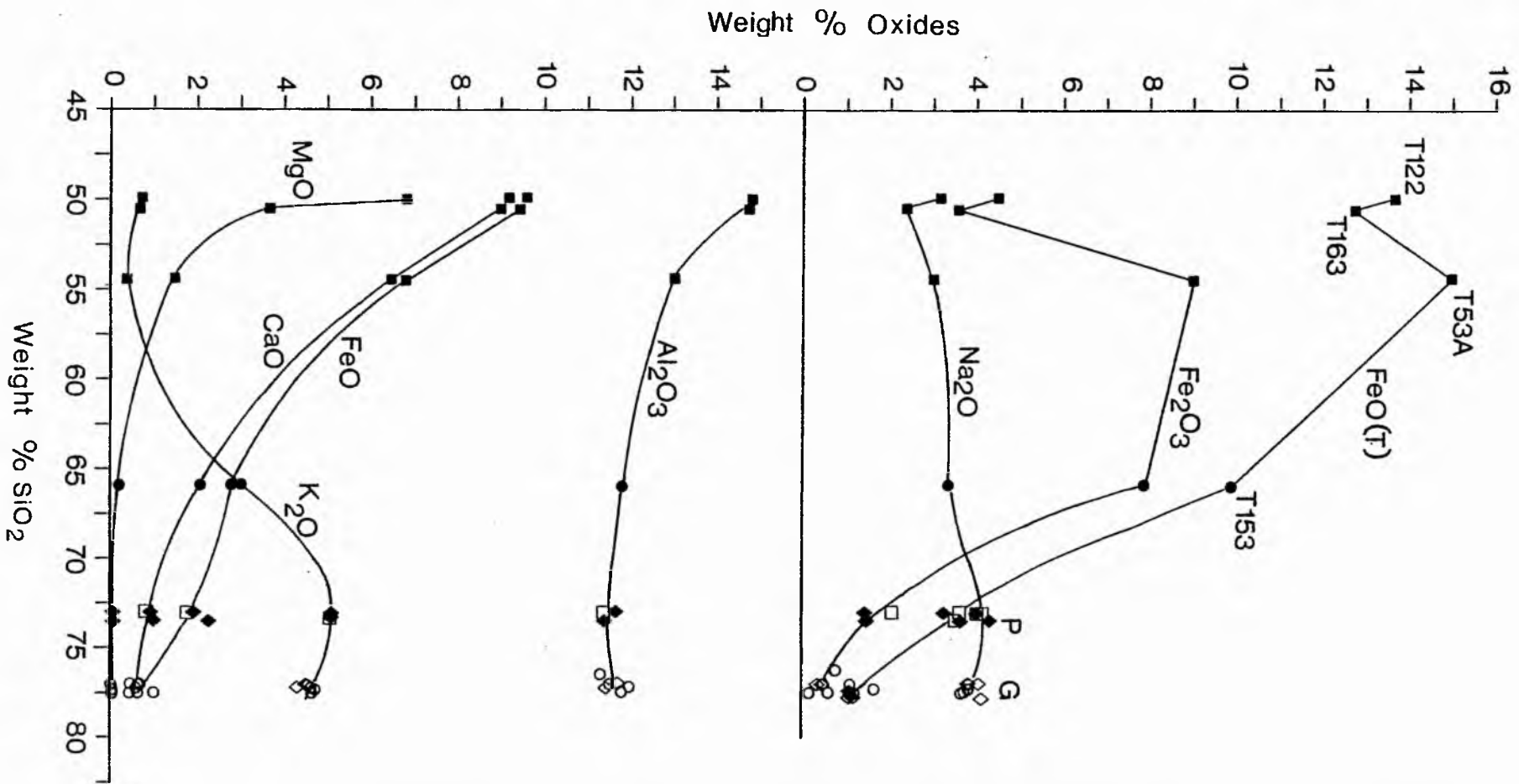


Figure 6.3.1A The Harker variation diagram for rocks of the Tibchi Complex. Filled squares represent basalts as follows: T122 = Olivine tholeiite; T163 = Tholeiite; T53A = Andesine basalt. Filled circle (T153) = trachyte. The pristine porphyries (P) are represented as follows: filled diamond = quartz porphyries, open squares = granite porphyry ring-dyke. Unmineralised biotite granites (G) comprise: open circles = granite, open diamond = microgranite.

biotite granite pluton in Table 6C, and the 'miscellaneous' rocks in Table 6D. CIPW normative compositions as well as certain useful ratios are included in the tables.

The analyses have been expressed in a number of chemical variation diagrams: two bivariant plots and three sets of triangular diagrams. The first of the series is the Harker diagram (Figure 6.3.1A), with the individual major oxides plotted against silica, in weight percent. The second bivariant plot is also a silica variation diagram (Figure 6.3.2A) but with iron-enrichment index, $\frac{\text{FeO} + \text{Fe}_2\text{O}_3}{\text{FeO} + \text{Fe}_2\text{O}_3 + \text{MgO}}$ against SiO_2 , in weight percent.

Of the triangular diagrams, the first is the AFM plot (Figure 6.3.2B), with total iron oxide expressed as FeO. The second shows the distribution of normative albite, orthoclase and quartz (Figure 6.3.3A), accompanied by secondary adaptations of the main plot for illustrative purposes. The third is the normative albite-anorthite-orthoclase diagram (Figure 6.3.4A).

6.3 Chemical Variation Diagrams

6.3.1 The Harker Diagram

General It is noted that in plotting the Harker diagram, the current practice (ref. Carmichael et al., 1974) is to select rocks such that the trends obtained may represent as closely as possible the true liquid lines of descent. Fortunately, the rocks of the Tibchi Complex which determine the trends obtained in the Harker diagram (Figure 6.3.1A) are mostly lavas and dyke rocks. Two of the basalts (T53 and T162) are contact-metamorphosed to such a degree that initial

anhydrous mafic minerals have been completely replaced by amphiboles. The above rocks are excluded from the diagram. The porphyries and coarse-grained granites cluster in the 72-80 percent SiO_2 range. Much of the cluster can be directly related to the hydrothermally or metasomatically altered rocks among them, or to those that are mineralised. These late stage modifications are better illustrated in the Ab-Or- SiO_2 - H_2O diagram (see later). The affected rocks are therefore excluded here for purposes of clarity.

Discussion The following succession of rocks (with increase in SiO_2) can be identified in the diagram:

(1)	(2)	(3)
T 122	T 163	T 53A
Olivine tholeiite	Tholeiite	Andesine basalt
(4)	(5)	(6)
T 153	Pristine	Unmineralised
Trachyte	porphyries	biotite granites & microgranites

Classification of tholeiites is based on CIPW norms (Hutchison, 1974).

The following observations have been made:

- (a) The initial marked decrease in MgO apparently represents the crystallisation of early Mg-rich clinopyroxene, optically identified in the olivine tholeiite (T122) as 'augite' (Chapter 4). Normatively, olivine disappears from subsequent basalts after (T122).

- (b) The almost parallel decrease in MgO, FeO, CaO and Al₂O₃ after tholeiite (T163), coincides with the observed crystallisation of (Ca, Mg, Fe)-rich clinopyroxene, optically identified as 'augite', in (T163); and plagioclase.
- (c) The culmination of iron-enrichment in the andesine basalt (T53A) in the Harker diagram is petrographically observed also. Iron-oxide is seen to be subordinate modally, only to plagioclase, in the rock above, even in the presence of mafic minerals.
- (d) The culmination of alkali oxide trends and a commensurate impoverishment in CaO and Al₂O₃, in the acid stages in the Harker diagram, coincides with the petrographical observation at these stages of the dominance of alkali feldspar over plagioclase.
- (e) The Harker diagram ends with maximum SiO₂ and alkali oxides in rocks petrographically rich in quartz and alkali feldspar and chronologically found to be the uppermost in the sequence.

Conclusion The Harker diagram gives a normal series of trends expected from the fractional crystallisation of a basaltic magma. The petrographically observed early crystallisation of Mg-rich clinopyroxene and plagioclase, the marked crystallisation of iron-oxide in the intermediate stages and the late crystallisation of alkali feldspar and quartz coincide with changes in the diagram of relevant major oxide constituents.

Figure 6.3.2A Iron-enrichment ratio, $\text{FeO} + \text{Fe}_2\text{O}_3 / \text{FeO} + \text{Fe}_2\text{O}_3 + \text{MgO}$, plotted against SiO_2 (weight percent) for the Tibchi Complex and superimposed on the plots of Osborn's synthetic liquid, the Skaergaard Intrusion, the Cascade Series and the Thingmuli Volcano in Iceland. An initial liquid, n , fractionally crystallised in the system $\text{MgO} - \text{FeO} - \text{Fe}_2\text{O}_3 - \text{SiO}_2$ (Osborn, 1959) at constant total composition, takes the course $n-132-40-24$; at a constant partial pressure of oxygen the successive liquids take the course $n-c-d$, and at an increasing partial pressure of oxygen the successive liquids of n take the course $n-a-b$ (after Carmichael, 1964). Symbols and numbers for the Tibchi trend are as in Figure 6.3.1A.

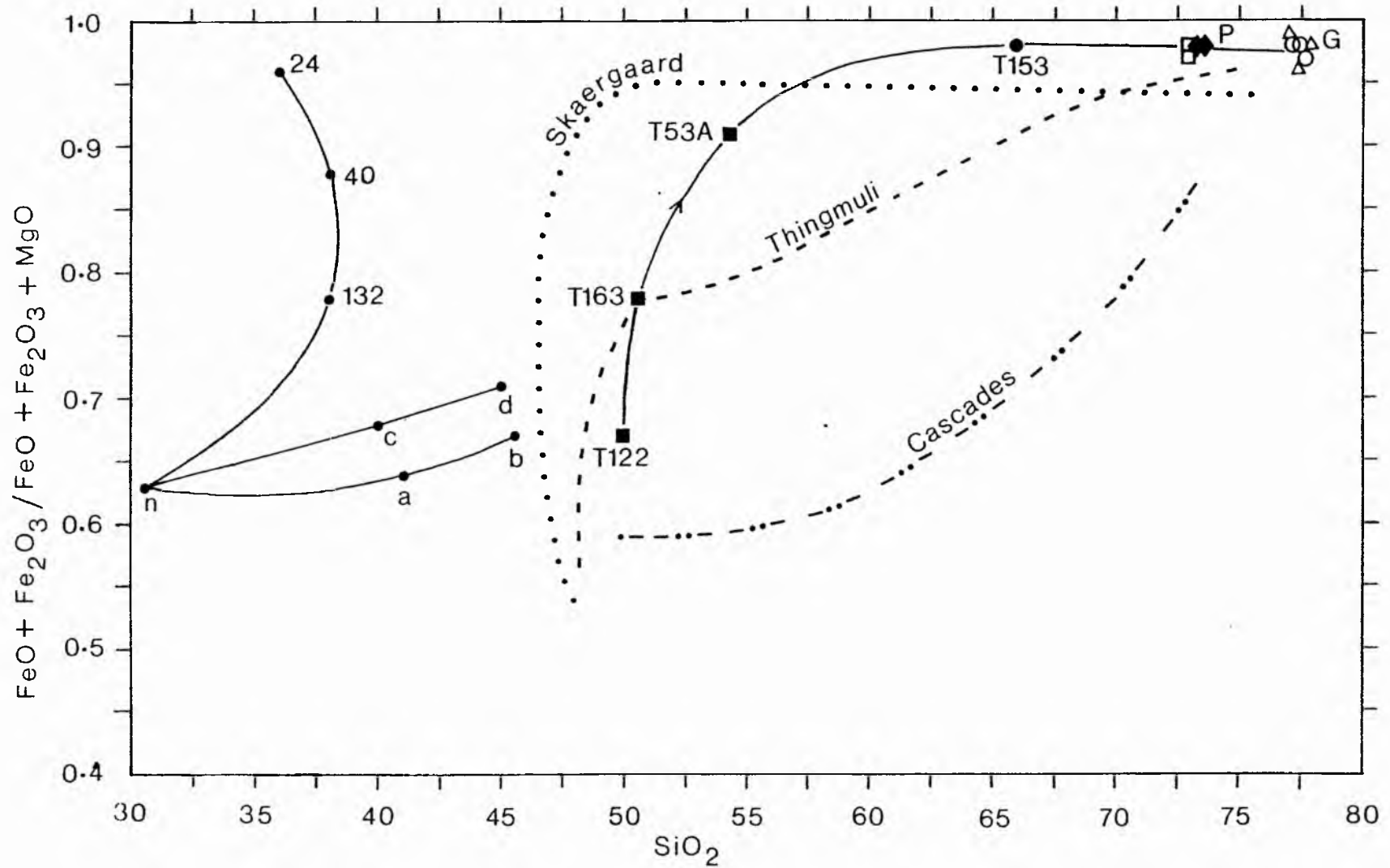


Figure 6.3.2A

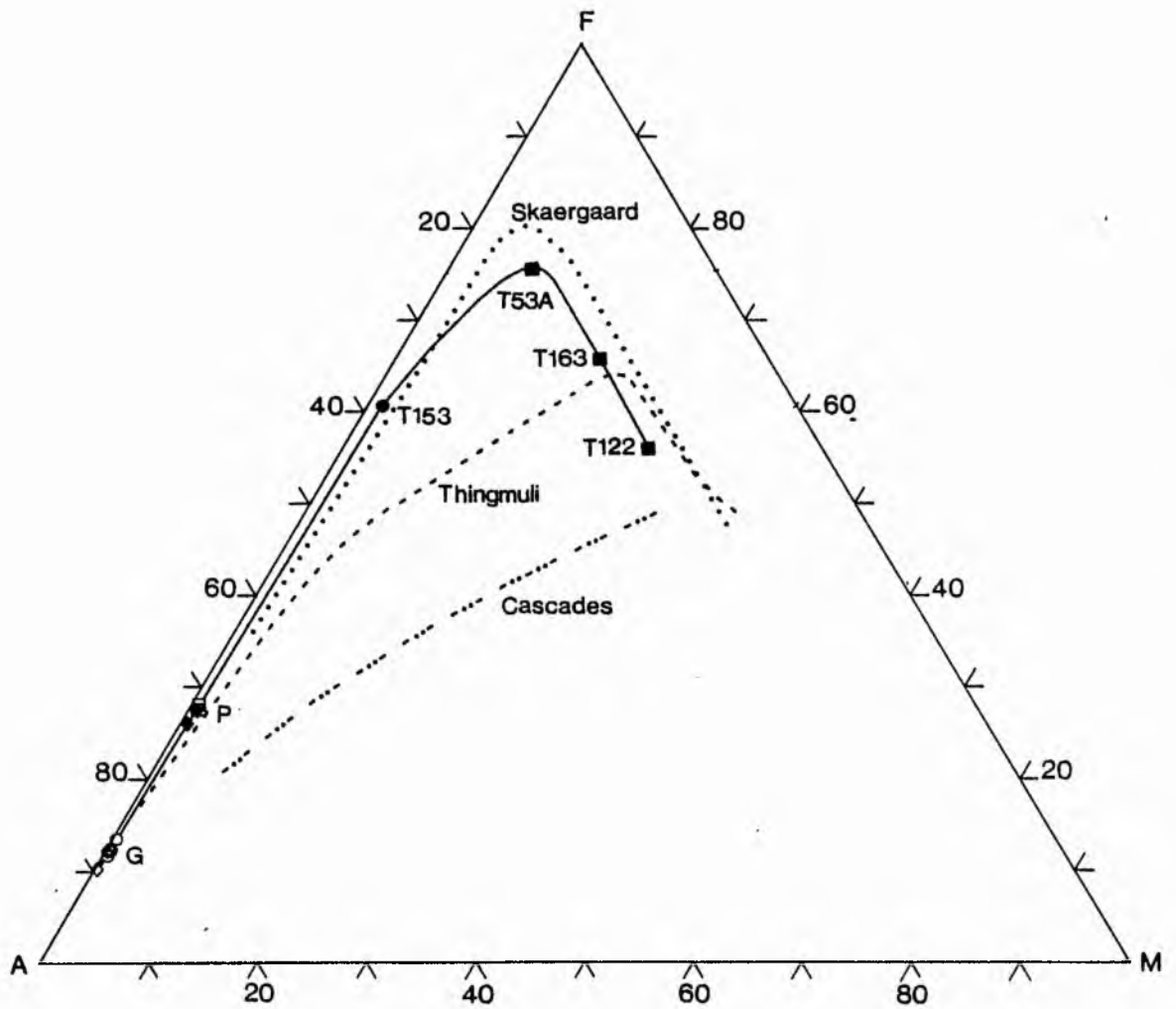


Figure 6.3.2B AFM diagram for rocks of the Tibchi Complex with $A = \text{Na}_2\text{O} + \text{K}_2\text{O}$, $F =$ total iron oxide as FeO and $M = \text{MgO}$ in weight percent. Symbols and numbers are as in Figure 6.3.1A.

6.3.2 The $\frac{\text{FeO} + \text{Fe}_2\text{O}_3}{\text{FeO} + \text{Fe}_2\text{O}_3 + \text{MgO}}$ vs SiO_2 plot and AFM diagram

General Osborn (1959) investigated the fractional crystallisation path of a synthetic liquid of basaltic composition in the quaternary system $\text{MgO-FeO-Fe}_2\text{O}_3\text{-SiO}_2$. Two principal trends, with respect to the direction of change in liquid composition, were observed, and were attributed to alternative roles of oxygen pressure (P_{O_2}). If total composition of the mixture remained constant in mass (therefore implying no gain or loss of oxygen in the system), the oxygen partial pressure was observed to decrease during fractional crystallisation. Alternatively, if through addition from outside the system, the oxygen partial pressure was made to remain constant or to increase during fractional crystallisation, the total composition of the system changed through certain components.

Osborn (op.cit.) illustrated the above trends by plotting the ratio (in weight percent of) $\frac{\text{FeO} + \text{Fe}_2\text{O}_3}{\text{FeO} + \text{Fe}_2\text{O}_3 + \text{MgO}}$ against SiO_2 , for successive fractions of his synthetic liquid obtained under each of the above conditions of oxygen partial pressure (Figure 6.3.2A). In the first case, with oxygen partial pressure decreasing during fractional crystallisation (constant composition), the ratio of iron oxide to iron oxide plus magnesia rose steeply with increasing silica content. On the other hand, it rose only gently if oxygen partial pressure remained constant, and showed almost negligible rise when the oxygen partial pressure was increased.

The similarity between the trend obtained at 'constant

composition' of the synthetic liquid and that of the initial liquids of the Skaergaard Intrusion was inferred by Osborn (op.cit.) to mean that the Skaergaard initially crystallised at a low, fixed oxygen content. The trend obtained from the Cascade Orogenic Series resembled that of the synthetic liquid crystallising under constant oxygen partial pressure, enabling Osborn to conclude that the Cascade series resulted from fractional crystallisation under a variable oxygen content (constant PO_2).

The rocks of the Tibchi Complex have been plotted on the basis of Osborn's iron-enrichment ratio against silica and superimposed on the original plots of Osborn's synthetic liquid, the Skaergaard Intrusion, the Cascade Series, and the Thingmuli Central Volcano in Iceland (Carmichael, 1964), for comparison (Figure 6.3.2A). The contact metamorphosed basalts are, however, excluded as are the hydrothermally altered porphyries.

Discussion The initial slope of the Tibchi trend coincides with the initial slope of the Thingmuli trend, which Carmichael (1964) had favourably compared to the initial slope of the Skaergaard. The deflection at approximately 50 percent silica in the Thingmuli trend was correlated (Carmichael, op.cit.) with the appearance of magnetite as a phenocryst phase in the sequence. Magnetite phenocrysts have not been observed in the Tibchi lavas, hence the continued rise of the Tibchi trend towards increased iron-enrichment.

The almost vertical slope between the olivine tholeiite (T122) and tholeiite (T163) coincides with the disappearance from the norm of Mg-olivine as described for the Harker diagram

earlier and also presumably with crystallisation of Mg-rich clinopyroxene. The change of slope at the andesine basalt (T53A) composition coincides with a petrographically conspicuous crystallisation of iron oxide (presumably magnetite) in the above rock. The change in (T53A) also coincides with the extensive build-up in (T53A) of Fe_2O_3 and FeO(T) in the Harker diagram which, from Osborn's (1959) hypothesis corresponds to a change from the initial crystallisation at constant composition (low, fixed oxygen content) to higher oxygen content approaching constant partial pressure. It may be concluded that in the intermediate and acid stages of the Tibchi trend, oxygen partial pressure approached constant value or may have increased. Osborn (1959) had concluded that a basaltic magma fractionally crystallising at constant composition initially, would be expected to eventually approach conditions where the decreasing oxygen partial pressure would remain constant or indeed increase. The Tibchi trend parallels this behaviour.

One reason for such an increase in oxygen partial pressure in the later stages of the Tibchi trend may be related to the high level of emplacement of the later differentiates in such a way that it was possible for atmospheric oxygen to have entered into the differentiating magma (Haslam, 1968).

Thus the extreme iron-enrichment, relative to magnesium, in the Tibchi Complex is clearly demonstrated and may be explained in brief as follows: Iron accumulated in the magma during the initial stages of fractionation owing to the prevailing oxygen conditions, while magnesium decreased, such

that, by the intermediate and acid stages, when conditions were favourable for the precipitation of iron oxide, the amount that could crystallise was insufficient to significantly change the already established $\frac{\text{FeO} + \text{Fe}_2\text{O}_3}{\text{FeO} + \text{Fe}_2\text{O}_3 + \text{MgO}}$ ratio.

The above extreme iron-enrichment in bulk composition is correlated with the observation that the compositions of the minerals (Chapter 5) are always close to the iron end-members of their respective solid-solution series. This may be explained with reference to fractional crystallisation of a basaltic liquid with low, fixed oxygen content, as follows:-

"With perfect fractional crystallisation all liquids after reaching a univariant line move continuously . . . toward the fayalite-magnetite-tridymite eutectic As this happens the composition of each solid solution crystal, olivine, pyroxene, and magnesioferrite, moves also to the right approaching the high iron oxide end-member of each series."

(Osborn, 1959)

Bulk chemical compositions of rocks, and analytical data on minerals, from the Nigerian Younger Granite province (Jacobson et al., 1958; Borley, 1963; Macleod et al., 1971; Turner and Bowden, 1979; Bennett (in preparation); and others), have proved the extreme iron-enrichment of the rocks and minerals, although no adequate explanation has yet been documented.

That the climax of iron-enrichment in the Tibchi Complex was reached at the andesine basalt (T53A) composition, is also clearly demonstrated in the AFM diagram (Figure 6.3.2B). From this diagram it can also be inferred that if the Skaergaard trend is accepted as an example of a fractionally crystallised basaltic liquid trend, then that of the Tibchi

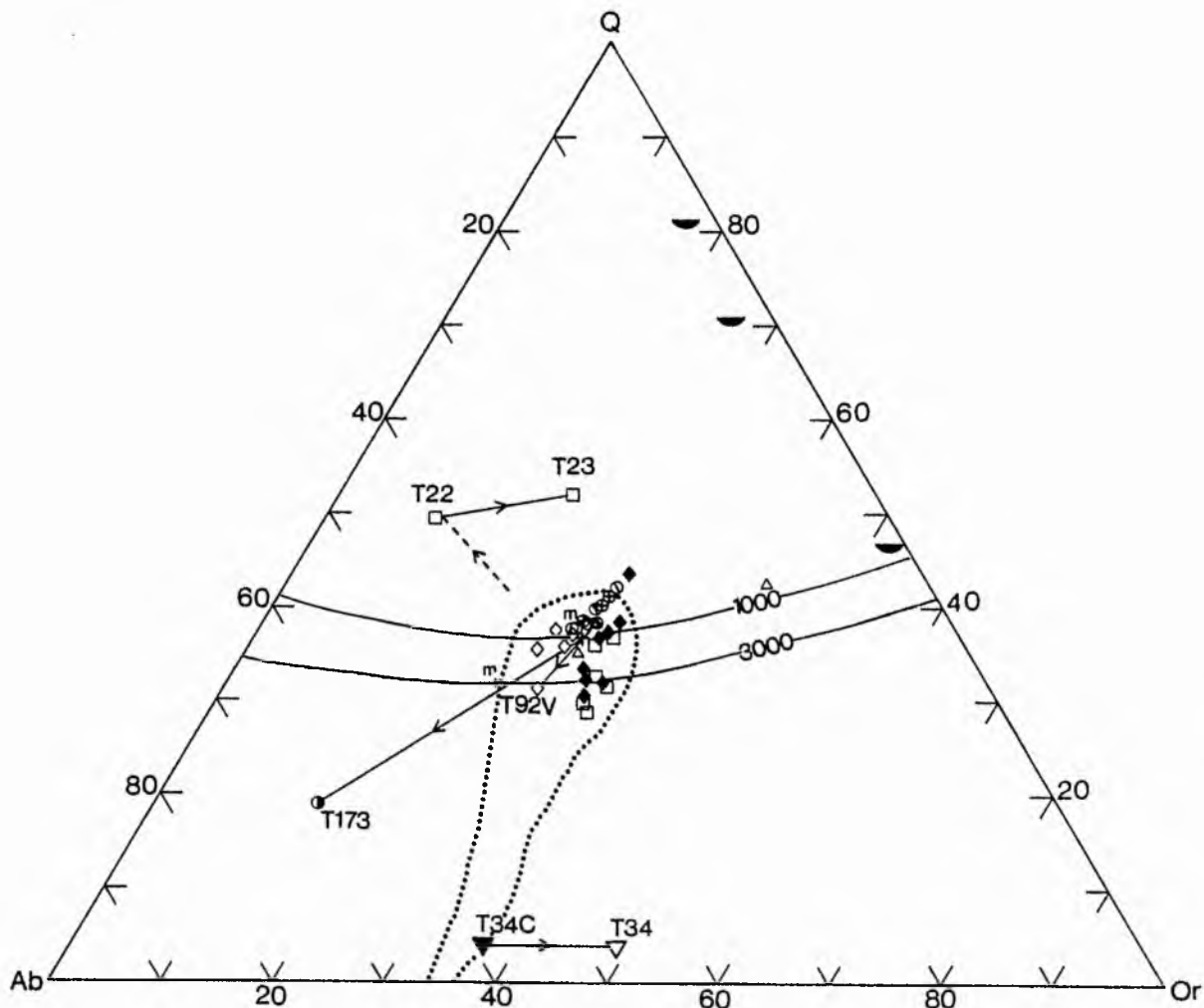


Figure 6.3.3A Plot of normative albite, orthoclase and quartz, for rocks of the Tibchi Complex. Phase boundary curves for water vapour pressures at 1000 and 3000kg/cm² and ternary minima (m) for the respective phase boundary curves are superimposed (Tuttle and Bowen, 1958). Dotted line shows composition field of the Nigerian Younger Granites (Macleod *et al.*, 1971). Filled triangle = Sodic syenite (T34C); open triangle = Potassic syenite (T34); half-filled circle = Sodic granite (T173); filled diamond = quartz porphyries; open squares = granite porphyry; open circles = biotite granite; circle with crosses = mineralised plagioclase-bearing biotite granites of Kogo hill; circle with diagonal = plagioclase-bearing biotite granite of Yeli hill; open diamond = biotite microgranite; open triangles = crystal tuffs; filled semi-circle = early rhyolite lavas (see text). Arrows indicate directions of subsolidus transition to more altered rocks (see text), solid arrows = definite trends, dashed = hypothetical.

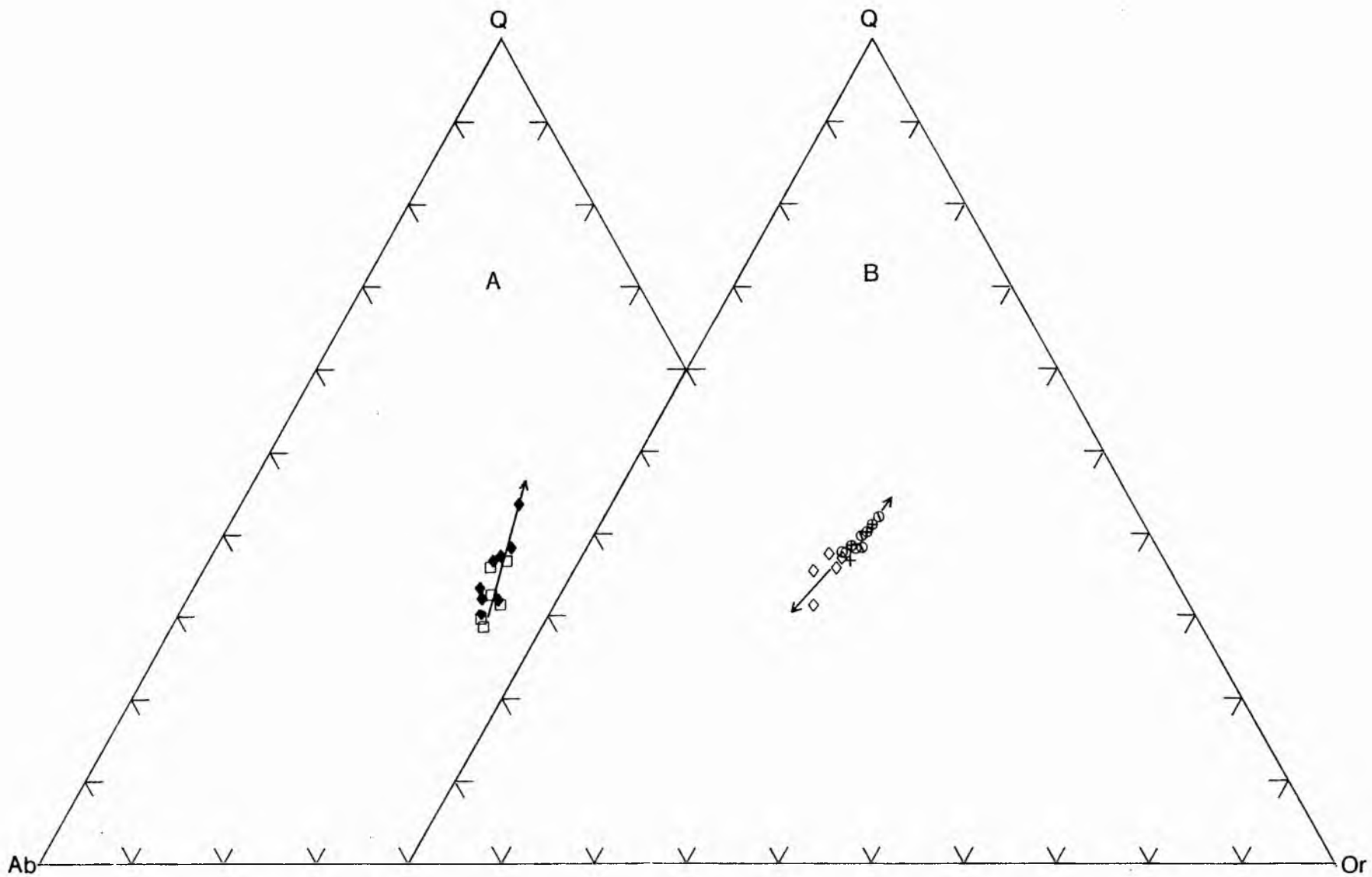


Figure 6.3.3B Linear trends in porphyries (A), and biotite granites and microgranites (B) - see text. Individual symbols are as in Figure 6.3.3A.

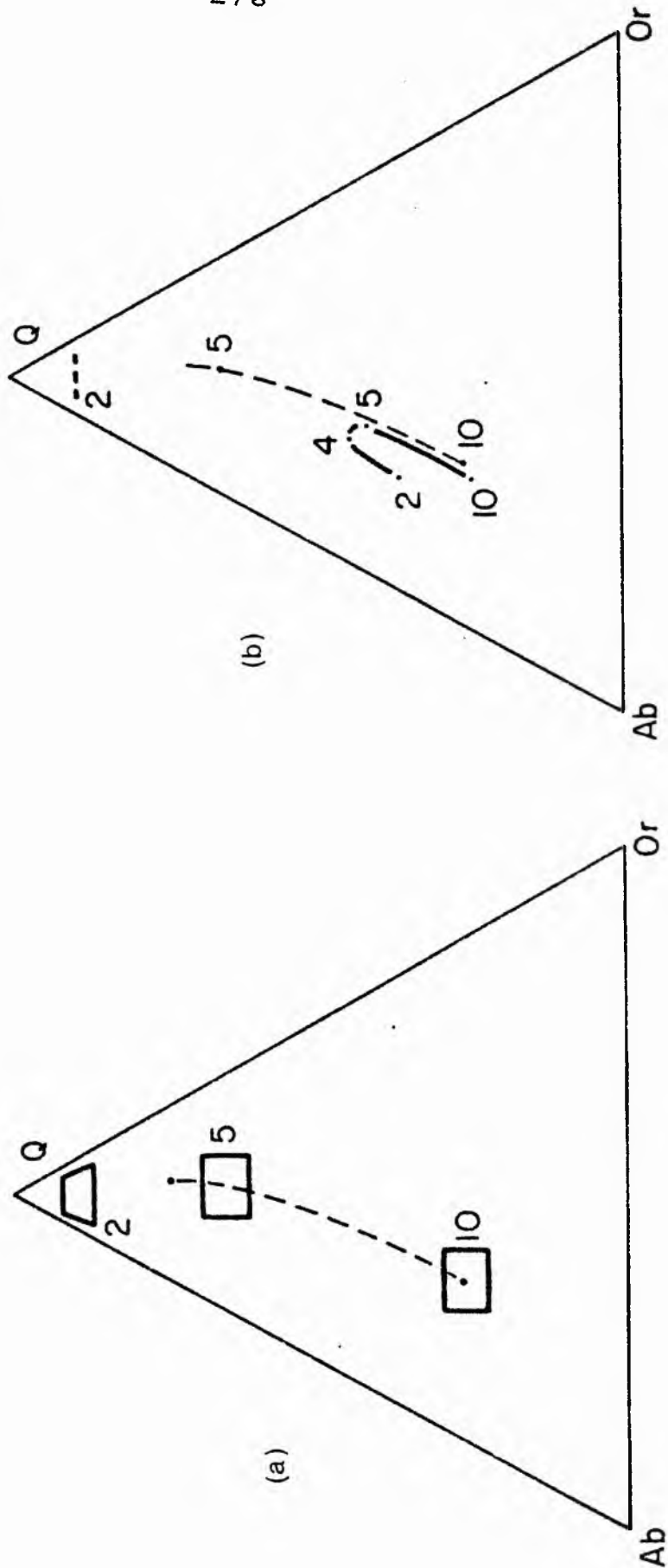


Figure 6.3.3C Projections unto the anhydrous base of the tetrahedron Ab-Qr-Q-H₂O illustrating vapour phase relations. (a) The composition of the vapour phase which coexists with quartz and albite-rich alkali feldspar at approximately 25° below the solidus temperature at 5 and 10 Kb. No such points exist at 2 Kb, but the vapour phase which coexists with quartz and an alkali feldspar is quite silica-rich as shown. (b) Relationship of subsolidus vapour phase composition (dashed curve) and the vapour phase compositions coexisting with melt (dash-dot curve) at respective pressures (Luth 1969).

Complex must be similarly regarded. The very close similarity between these two trends in iron-enrichment, the course of the liquid path and other considerations established elsewhere in this study such as mineral chemistry, is demonstrated in each case.

Conclusion Despite the limitations of experimental work, it is convincing that the results of Osborn (1959), on the fractional crystallisation of a basaltic liquid, can be favourably applied to the evolution of rocks of the Tibchi Complex. Thus in the Tibchi Complex, initial conditions were of low, fixed oxygen content which enabled iron-enrichment to take place while magnesium was continuously being removed from the system by crystallisation of magnesium-rich mafic phases.

Iron-enrichment reached its culmination in a liquid fraction of andesine basalt composition.

The observation that mafic minerals of the Tibchi Complex, and indeed the Nigerian Younger Granites, are always extremely close to the iron end-member of their respective solid solution series is explicable by initial fractional crystallisation of a basaltic magma under low, fixed oxygen content and the consequent decrease in oxygen partial pressure.

6.3.3 The Ab-Or-Q-H₂O diagram

General Rocks of the Tibchi Complex with the sum of normative albite, orthoclase and quartz over 80 percent (Tuttle and Bowen, 1958) have been plotted (Figure 6.3.3A). Phase boundary curves for selected water vapour pressures and ternary minima for the respective phase boundary curves are superimposed on the diagram. Also the composition field of

the Nigerian Younger Granite "rhyolites, granites and syenites" (Macleod et al., 1971) is superimposed on the diagram for comparison.

Discussion The following observations have been made from the above diagram (Figure 6.3.3A):

- (1) The majority of the Tibchi salic rocks plot in the quartz oversaturated, terminal portion, of the Nigerian Younger Granite field.
- (2) A few Tibchi rocks show 'anomalous' positions. These rocks include (a) early volcanic rocks which show extreme depreciation in normative albite relative to orthoclase and quartz; (b) metasomatically altered granite porphyry (T22, T23); (c) the peralkaline granites and syenites (T173, T34C and T34). Although the sum of the relevant normative salic components do not reach the prescribed 80 percent in (T23), this rock has been included in the diagram only for the purpose of illustrating the trend from its precursor (T22). For convenience, the rocks belonging to group (1) above will be discussed first, followed by those of group (2).

Group (1)

This is made up of the quartz porphyries, the granite porphyries, biotite granite and biotite microgranite. Generally the porphyries define a linear trend (Figure 6.3.3B) showing progressive enrichment in normative quartz component. This linear trend is petrographically correlated with hydrothermal alteration in the quartz porphyries; the greater the amount in the quartz component above, the more the petrographically observed hydrothermal alteration.

The biotite granites occupy a central position (Figure

6.3.3B) between the mineralised biotite granites (which are richer in the quartz component) and the biotite microgranites (which show a tendency towards enrichment in albite component). The hydrothermal alteration in the porphyries and the mineralisation in the biotite granites thus show, in the present system, a common affinity for enrichment in normative quartz relative to alkalis. The tendency towards albite enrichment in the microgranites stands in marked contrast to the above hydrothermal alteration and mineralisation trends.

Conscious that experimental data must be applied with caution in resolving natural problems, it seems only necessary to refer broadly to the conclusions of Luth and Tuttle (1969) concerning the composition of the aqueous vapour phase in the granitic system (Figure 6.3.3C); these conclusions seem relevant to the observed enrichment in normative quartz in the hydrothermal alteration and mineralisation above, and the albitic tendency in the biotite microgranites. Two of their conclusions are cited here. Firstly, the vapour phase that co-exists with crystalline quartz and alkali feldspar(s) at less than 5kb pressure and 25°C below the solidus temperature, is significantly enriched in normative quartz relative to the liquid participating in the solidus reaction. At 2kb the enrichment is even more, at the same temperature as above. Such a quartz enriched vapour phase escaping from the biotite granite could be accountable for the hydrothermal alteration in the porphyries (however, see later); if the vapour phase remained in the biotite granite it could locally concentrate as mineralising fluid.

On the other hand, under conditions as above but at temperatures of 25°C above the solidus, Luth and Tuttle (op.cit.)

found that the vapour phase would tend to be enriched in normative quartz as well as albite relative to the co-existing melt, if the co-existing alkali feldspar was potassic. If, however, the co-existing alkali feldspar was sodic, then the enrichment in the vapour phase would tend towards quartz and orthoclase instead. The fact that the biotite granites have potassic alkali feldspar would then mean that the vapour phase would tend to be sodic, as the chilled microgranites (inferred to contain the residual fractions of the biotite granite melt) show in the present diagram.

It is observed in the field that the biotite granite did not chill against the porphyries although it did so against basement rocks. This is here interpreted to mean that the porphyries were probably retaining some amount of residual heat, enabling the biotite granite intrusion to cool normally against them. The implication from the foregoing phase relations is that near the porphyries the albitic tendency in the vapour phase in the granite would disappear as the granite solidus temperature is approached, enabling a regime of aqueous vapour, enriched in normative quartz only, to operate on the quartz porphyries at sub-solidus temperatures. However, Moyes (1979) has come to the conclusion that the hydrothermal alteration observed in the quartz porphyries (this study), had to be due to interaction of acid groundwater generated by the biotite granite intrusion. His conclusion is based on the pattern of rare-earth mobility obtained with increase in hydrothermal alteration and the observation (this study) that the hydrothermal alteration increased towards the biotite granite contact. Moyes (op.cit.) suggests that the

rare-earth patterns obtained could be best produced under conditions of low pH, with acidity increasing towards the biotite contact and hence with increased alteration. The above conditions would be suitable for the acid complexing necessary for a progressive decrease in REE, and especially the light REE, as observed.

If a quartz enriched vapour phase escaping from the biotite granite into the adjacent quartz porphyries were to be fully accountable for the hydrothermal alteration observed, the amount of vapour required to be lost in order to produce the observed effect, would be large. Pegmatisation could be expected to occur. On the contrary, however, pegmatites are conspicuously absent from the granite/quartz porphyry contact suggesting that all available vapour phase passed into the porphyries.

The overall trend shown by the Nigerian Younger Granite rhyolites, granites and syenites (Macleod et al., 1971) lies within the 'Thermal Valley' (Figure 6.3.3A). Macleod and co-workers inferred that this alignment along the 'Thermal Valley' meant that those Nigerian rocks "could thus represent the initial liquid formed by partial fusion from a wide range of rock types". Such an alignment had been interpreted as representing fractionation paths from syenite to granite, with change in composition being controlled by the thermal valley (Tuttle and Bowen, 1958). The latter interpretation applied to the Tibchi porphyries and granites, as successors to syenitic liquids, in time, during the fractional crystallisation of the parent liquid would be strongly supported by evidence from mineral chemistry (Chapter 5) and earlier parts of the present chapter.

Group (2)

The following observations have been made in respect of rocks belonging to this group:

- (a) The early rhyolites and tuffs show varying degrees of loss of normative albite, perhaps due to post-depositional processes.
- (b) The metasomatic alteration in the granite porphyry minor dyke in which siderophyllite (with traces of genthelvite) pseudomorphs alkali feldspar phenocrysts (Plate 4.4P, Chapter 4), is shown in Figure 6.3.3A as T22 \longrightarrow T23, T23 being the more altered zone. It is unlikely that the position now occupied by (T22, T23) can be explained by fractional crystallisation. Petrographical evidence is in favour of some form of metasomatism. Thus (T22) was initially modified from a composition similar to the pristine porphyries in the centre of the diagram, along a trend represented by enrichment in quartz and albite relative to orthoclase. The T22 \longrightarrow T23 transition observed intact in the field clearly shows a potassic metasomatism in which normative quartz was stable. Hence it is suggested that an initial sodic phase of metasomatism was followed by a later potassic phase.
- (c) The peralkaline granite T173 can be seen to occupy a position completely estranged from the rest of the Tibchi granites. In the field it is seen as a kind of 'wall rock' alteration on the existing biotite granite by reactions connected with the formation of the peralkaline syenites (below). It is suggested that a sodic metasomatic reaction characterised by desilication and alkali enrichment was involved in the formation of (T173) from biotite granite.

(d) The peralkaline sodic syenite (T34C) is enigmatic. It lies close to the position of the 'Thermal Valley' in which the syenites of the Nigerian Younger Granites plot (ref. Figure 6.3.3A). Thus (T34C) may be regarded as occupying its initial magmatic bulk composition position despite overwhelming evidence elsewhere in this study, that it had undergone intensive postmagmatic re-equilibration (ref. Mineral Chemistry, Chapter 5 and Petrography, Chapter 4). While the true origin of (T34C) may be deliberately kept open, the transition T34C \rightarrow T34 (potash syenite) is suggested to represent a true metasomatic event. The direction of transition (ref. Figure 6.3.3A) is clearly opposed to established fractional crystallisation liquid trends. This conclusion is also supported by various arms of this study as cited above for (T34C).

Conclusion In the context of salic normative components involved in the present diagram, the Tibchi rocks most probably evolved from syenitic precursors by fractional crystallisation. This re-affirms earlier conclusions.

The final fraction of the biotite granite melt apparently co-existed with an aqueous vapour phase enriched in normative quartz and albite. That final fraction is represented by the (chilled) biotite microgranite.

Hydrothermal alteration of the porphyries and mineralisation in the biotite granites appear to have been due to the action of an aqueous vapour phase enriched in normative quartz. This vapour phase is shown to have originated from the biotite granite pluton and operated at subsolidus temperatures, thus following the microgranite-related vapour phase in time and

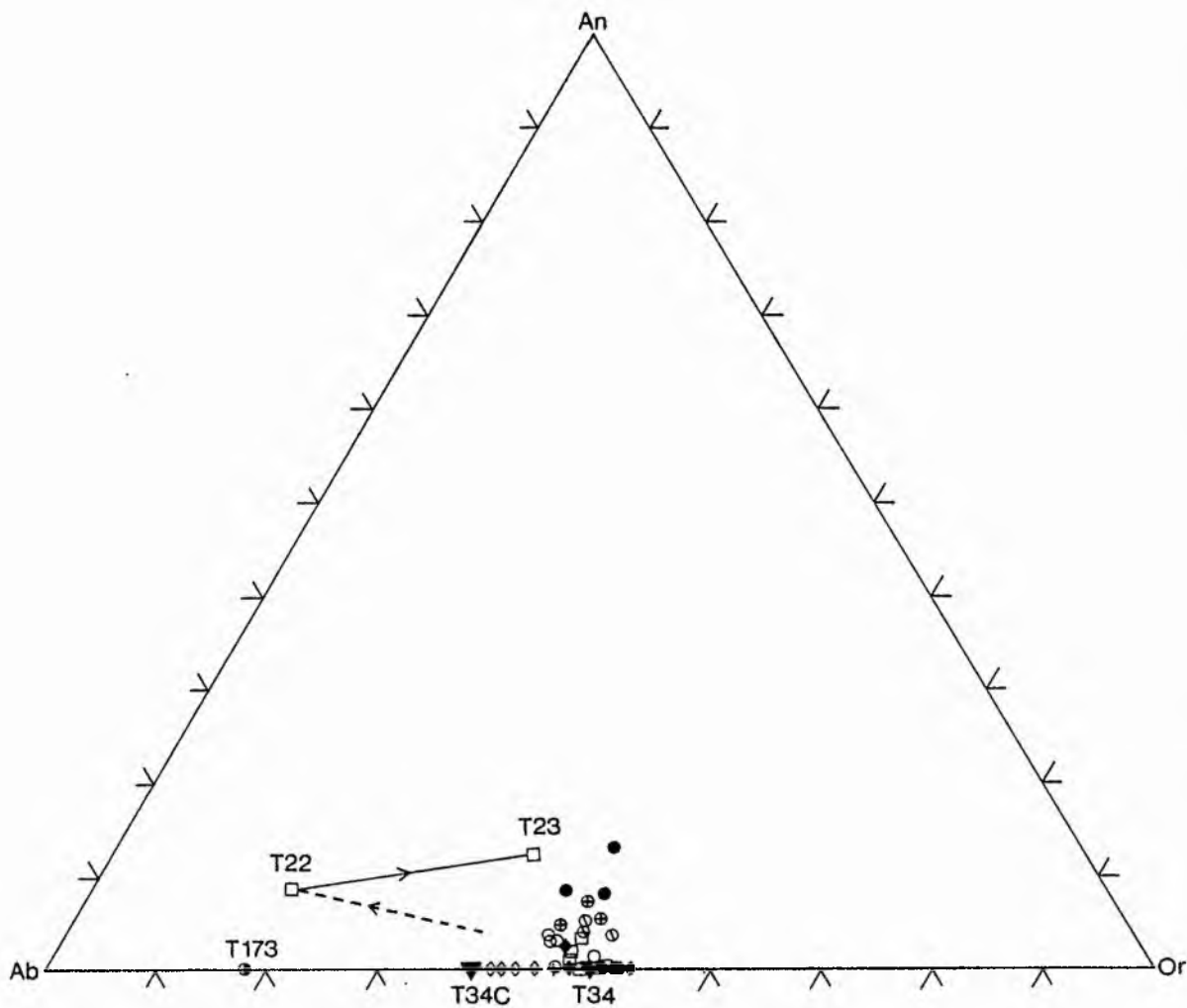


Figure 6.3.4 Plot of normative albite, anorthite and orthoclase for rocks of the Tibchi Complex. Symbols, numbers and arrows are as in Figure 6.3.3A.

temperature. Chilling of the biotite granite against the porphyries not being observed in the field is therefore explicable.

While the vapour phase from the biotite granite seems an adequate explanation for the mineralisation phenomenon, evidence from rare-earth element study apparently makes the above a less attractive explanation for the observed hydrothermal alteration (see 6.3.5).

Metasomatic alteration of pre-existing rocks occurred in the Tibchi Complex and consisted of two principal types. In one, quartz was a stable phase; in the other, desilication was a dominant process. However each involved an alternation of sodic and potassic phases of activity.

6.3.4 The Ab-An-Or diagram

General Rocks of the Tibchi Complex are finally plotted in terms of normative albite, anorthite and orthoclase (Figure 6.3.4A). It is considered pertinent to include in this diagram, compositions of rocks of the granitic basement.

Discussion Of particular interest is the spread of the biotite granite compositions from the albite-orthoclase join to the field of the basement rocks. This field involves a range in the anorthite component of about 7-14 mole percent.

In detail, the above spread of the biotite granite can be effectively correlated with the petrographical subdivision of the lithology of the biotite granite pluton:-

(a) The biotite granites of Yeli and Kogo hill areas (the latter showing extensive mineralisation), were shown to contain substantial plagioclase (An_{26}) with replacement 'mantles' of alkali feldspar perthites. The samples T92, T94, T98

(Yeli hill) and T139, T70 and T138 (Kogo hill) represent these plagioclase-bearing rocks, and can be seen in Figure 6.3.4A to plot towards, and actually encroach on, the basement granite field.

(b) The rest of the biotite granite pluton was found to be virtually devoid of discrete plagioclase and was designated "alkali feldspar biotite granite". In Figure 6.3.4A these plot nearer or on the albite-orthoclase join.

Conclusion It is concluded that the alkali feldspar variant of the biotite granite pluton may have been the logical end-product of the basaltic liquid fractional crystallisation postulated for the Tibchi Complex. It is compelling, however, to add that some form of basement contamination may have been involved in the formation of the localised variant in which oligoclase plagioclase 'mantled' by micropertthite, is found.

6.3.5 Rare-earth element geochemistry

(i) General

In a study that in part complements the present one, Moyes (1979) has used the neutron activation technique to analyse the following samples for whole-rock rare-earth element (REE) concentrations:-

(see following page)

<u>Rock type</u>	<u>Field No.</u>	<u>Remarks</u>
Granite porphyry	T5	Ring-dyke
	T108	
Quartz porphyries	T60	West-East traverse
	T135	across zone of
	T167	hydrothermal
	T168	alteration
	T169	
	T170	
Biotite granite	T96	Biotite granite pluton
Anti-perthite	T34B	South-eastern suite of oversaturated peralkaline rocks
biotite granite		
Sodic syenite	T34C	
Potassic syenite	T34	
Basalt	T122	Parental(?) liquid

(ii) Summary of REE Geochemistry

The following are the main points of the results and conclusions of Moyes (1979) based on the above REE analyses. REE abundances of individual elements in the respective rock samples are not reproduced here, the reader is therefore referred to the above writer for those and other details. However, the total rare-earth element abundance (ΣREE), the europium anomaly (Eu/Eu^*) and the light/heavy rare-earth element ratio ($\Sigma\text{Ce}/\Sigma\text{Y}$) for each rock sample, are given in Table 6.3.5 for purposes of the discussion. The above data and the diagrams

TABLE 6.3.5Granite porphyries

	T5	T108
Σ REE(ppm)	836.00	811.44
Eu/Eu*	0.33	0.20
Σ Ce/ Σ Y	11.96	10.08

Quartz porphyries

	T60	T135	T167	T168	T169	T170	T133
REE	886.05	436.07	794.20	584.77	645.01	280.47	397.63
Eu/Eu*	0.33	0.32	0.21	0.13	0.21	0.26	0.13
Σ Ce/ Σ Y	11.82	8.38	9.01	12.11	9.19	6.67	5.29

Granites Syenites and basalt

	T96	T34B	T34C	T34	T122
Σ REE	885.83	484.17	107.12	558.56	110.23
Eu/Eu*	0.12	0.07	0.08	0.08	0.49
Σ Ce/ Σ Y	9.12	6.51	4.56	11.68	7.21

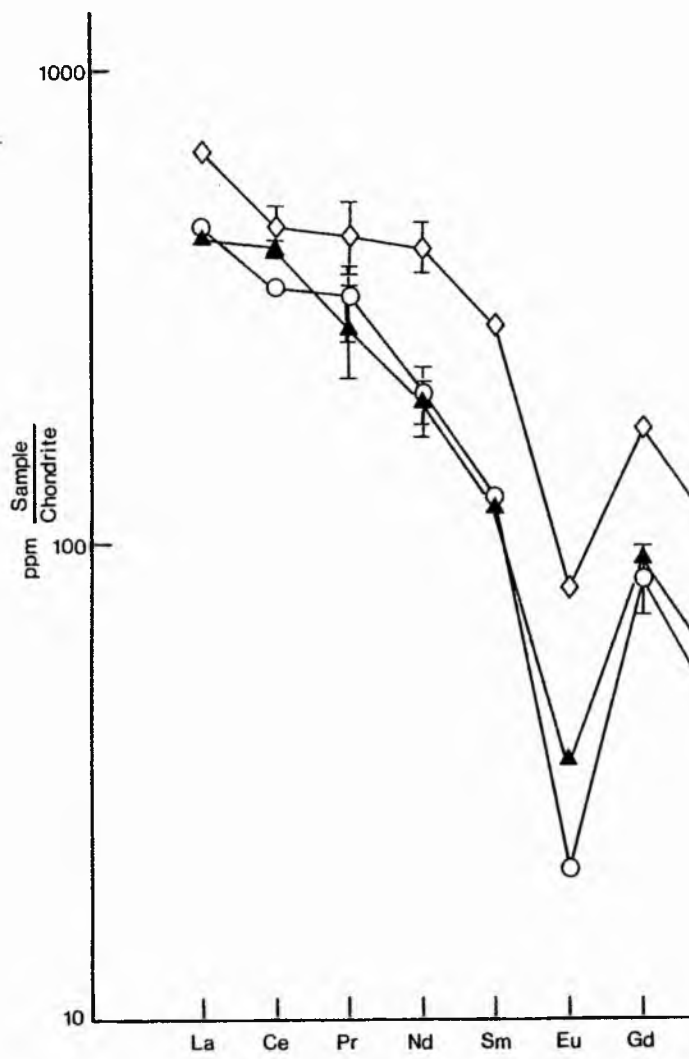
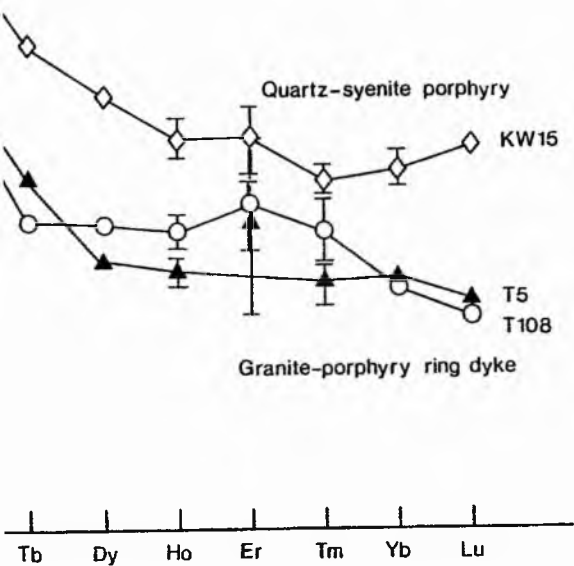


Figure 6.3.5A Comparison of the chondrite-normalised REE abundances of the Tibchi granite porphyry (T5, T108) with those of the quartz syenite (KW 15) Kila-Warji Complex.



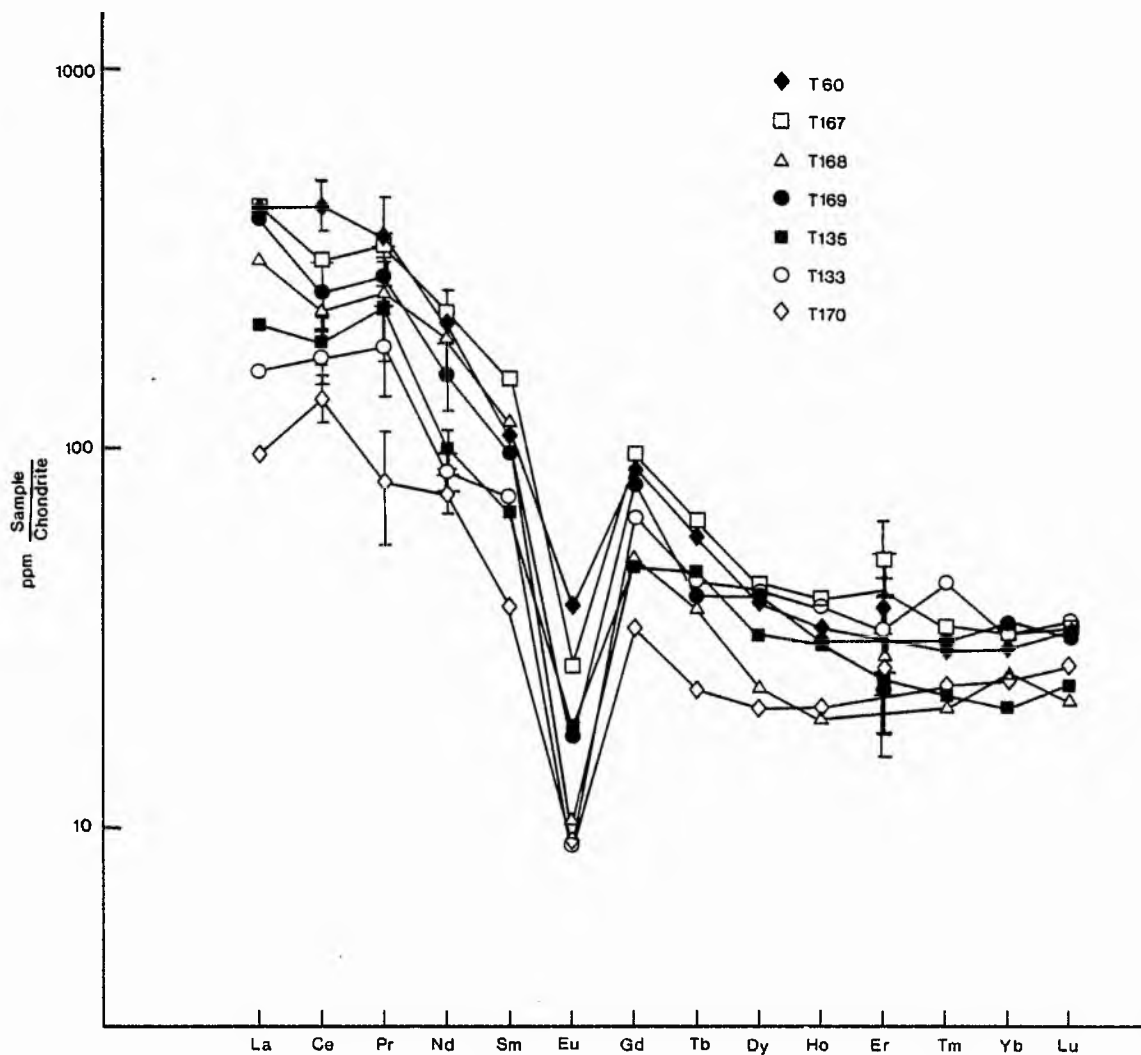


Figure 6.3.5B Plot of chondrite-normalised REE abundances in quartz porphyries of the west-east traverse. Logarithmic scale.

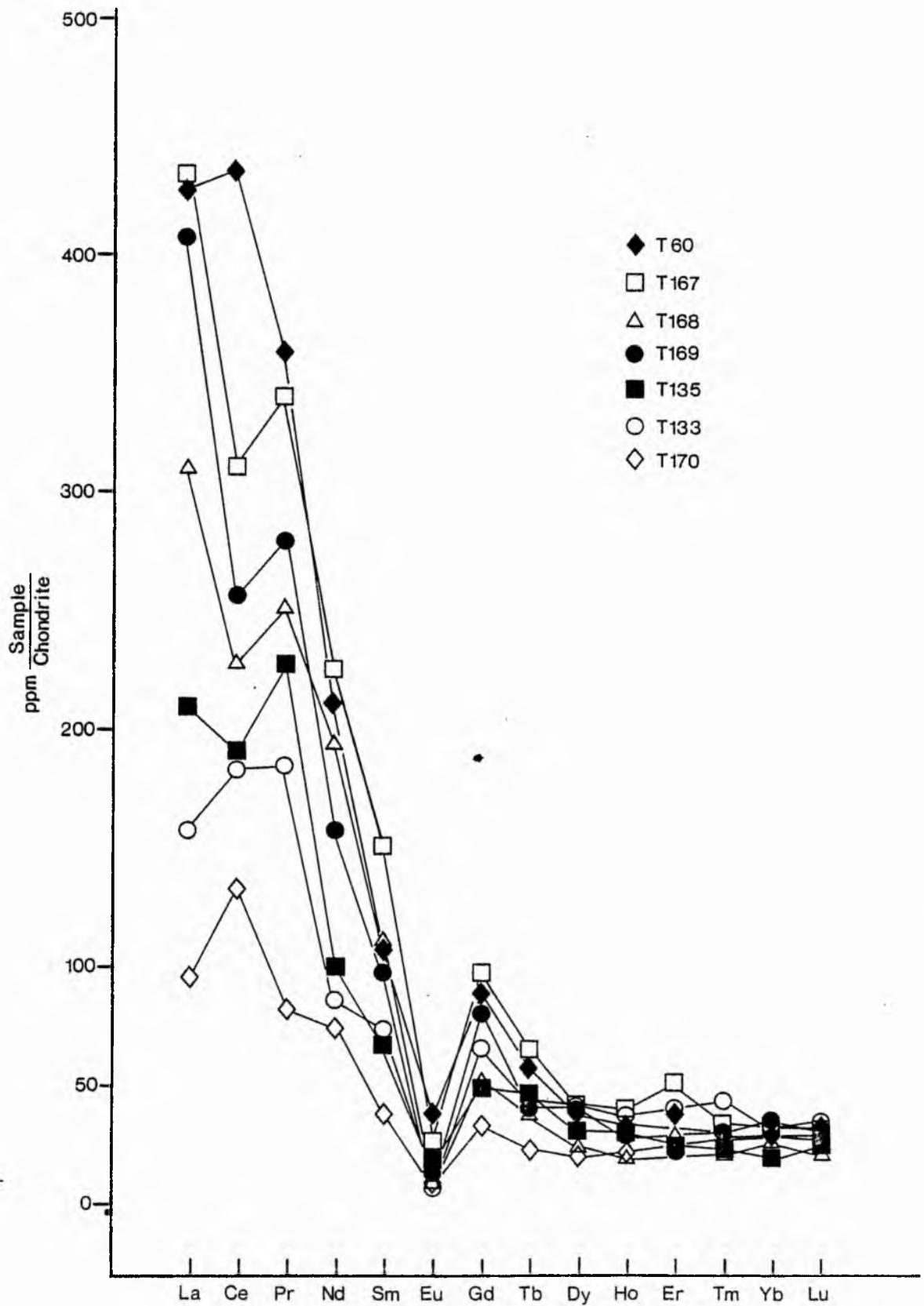


Figure 6.3.5C Plot of chondrite-normalised REE abundances in quartz porphyries of the west-east traverse. Linear scale.

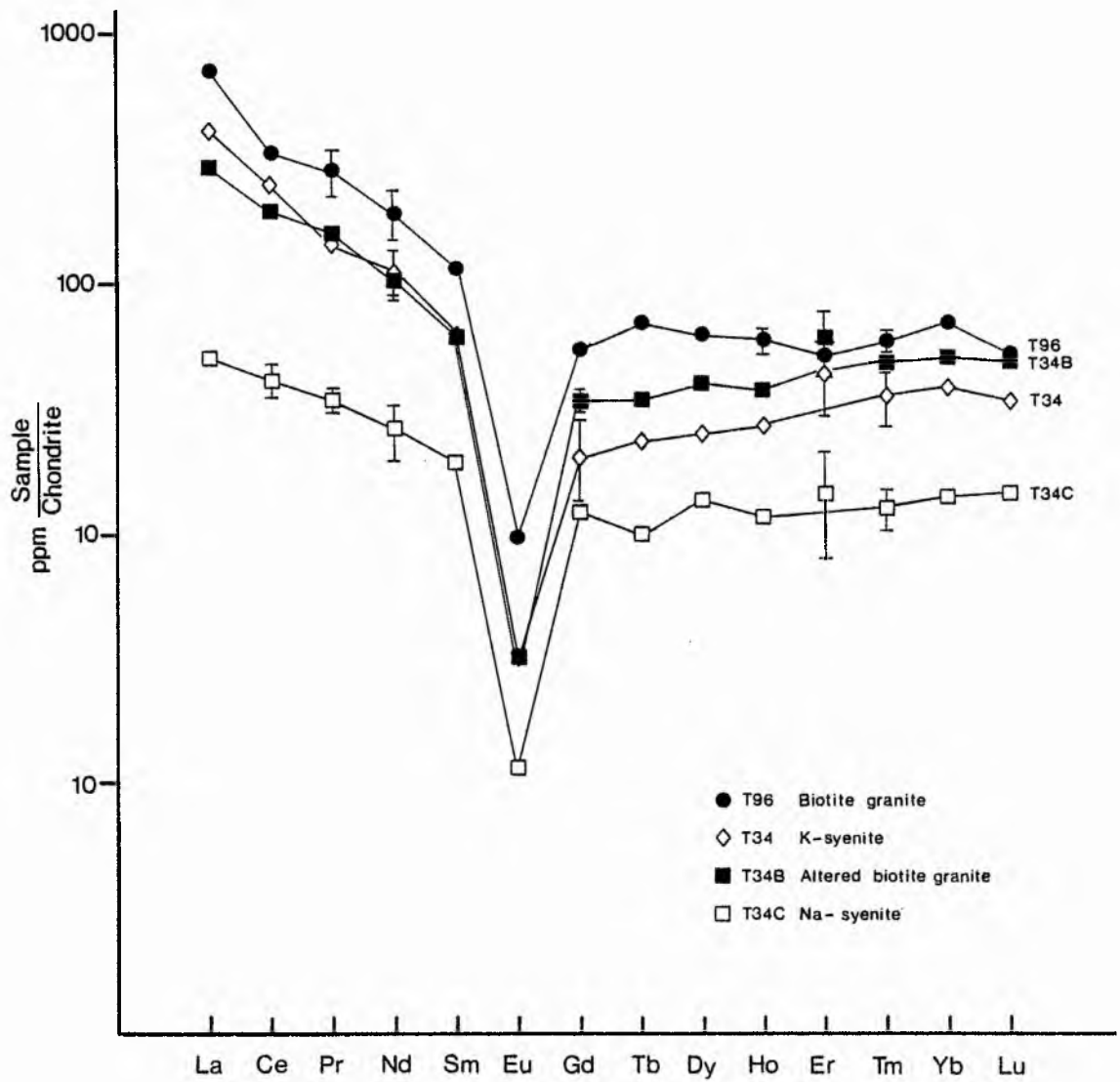


Figure 6.3.5D Plot of chondrite-normalised REE abundances in selected rocks of the south-eastern suite.

are reproduced by the kind permission of A.B. Moyes and their use is gratefully acknowledged by the writer.

Granite porphyry ring-dyke While the Σ REE content of the granite porphyry ring-dyke remains fairly constant, the absolute Eu value is observed to show slight but significant variation between the two samples. Moyes (1979) suggests that local variations in oxygen fugacity observed in the crystallisation history of the pyroxenes of the ring-dyke (this study), and possible natural variations in Eu within the ring-dyke, may have been responsible for the observed variation in the europium values.

Compared with the Kila-Warji quartz syenite porphyry (KW15, Figure 6.3.5A), the granite porphyry shows less

REE but greater Eu anomaly. The greater Eu anomaly is interpreted as signifying that the granite porphyry would be a more fractionated rock in a fractional crystallisation scheme.

In the context of the available REE data from other rocks of the Kila-Warji Complex, a conclusion is reached that the granite porphyry ring-dyke could occupy a transitional position, in a fractionation sequence, between quartz syenite porphyry (KW15) and aegirine granite (KW21) compositions.

The Quartz Porphyries Whole-rock REE abundances for the quartz porphyries of the west-east traverse are shown on chondrite-normalised plots on a logarithmic scale (Figure 6.3.5B) and on a linear scale (Figure 6.3.5C). The following are the key observations:

a) The REE pattern for the pristine (unaltered) rock (T60) is identical to that of the granite porphyry ring-dyke (T5) described earlier.

- b) All the other samples are depleted in Σ REE relative to the pristine rock (T60).
- c) The depletion is particularly noticeable in the LREE group. On a linear scale the LREE depletion relative to the HREE is clearly overwhelming.

Plots of Σ REE and Σ Ce/ Σ Y normalised to T60 against distance to the biotite granite (for locality map ref. Chapter 4), show that the outcrop proximity to the biotite granite contact cannot be correlated easily with the observed REE patterns.

Plots of Σ REE against $\ln \Sigma$ Ce/ Σ Y have been used to try to correlate, if possible, the apparent preferential removal of the LREE, with decreasing REE content. No simple relationship is found although two groups of rocks apparently emerged namely: T60, T167, T169, T170 and T168, T135, T133. The latter group defines a greater slope than the earlier. A plot of $\text{Fe}_2\text{O}_3/\text{FeO}$ against REE is interpreted also as separating the samples into the above two groups. Whereupon Moyes (op. cit.) suggests that the first group displays "a regular variation in their whole-rock REE pattern related directly to the proximity of the biotite granite, whereas" the latter group is "inconsistent in this respect". He also stresses that, "It is indubitable that this latter group have suffered alteration as a result of the granite intrusion, but their pre-existing REE patterns must have already been significantly different to that defined by the 'pristine' rock T60".

After a mathematical modelling of the observed REE changes, Moyes (op.cit.) has arrived at the same conclusion reached in this study, i.e. that a hydrothermal process had taken place in the quartz porphyries investigated. According

to Moyes (op.cit.), however, the exact nature of the causative fluid phase is not known, but is most probably acidic groundwater circulating as a hydrothermal plume at the margins of the cooling granite.

Discussion The conclusion reached by Moyes (op.cit.) on an intermediate position for the Tibchi granite porphyry ring-dyke, between the quartz-syenite porphyry and the aegirine granite of Kila-Warji, is favoured by evidence (this study) from the Ca-rich pyroxene crystallisation history. The tendency towards peralkalinity was evident, as these pyroxenes evolved.

Agreement is reached between the REE study and this study on the question of the suspected hydrothermal alteration in the quartz porphyries. It is perhaps pertinent to mention that to relate the samples directly to the biotite granite contact would be ideal, if the quartz porphyries were indeed magmatically one body of rock with one finite chemical composition. But as the mineral chemistry shows (ref. Ca-rich pyroxene crystallisation history, Chapter 5), the chemistry of the quartz porphyries can only be similar on a broad basis; in detail a magmatic variation in the suite exists which bears little or no relationship to the present position of the samples along the west-east traverse.

Ca-rich pyroxene composition and crystallisation history, combined with the composition and variation in amphibole chemistry, show that if the positions of the samples along the west-east traverse (plus T133) are retained, the order according to degree of increasing fractionation (in parenthesis) would be as follows:

T60 (1)

T135 (7)

T167 (5)

West-east traverse

T168 (2)

T169 (3)

T170 (4)

T133 (6)

Thus the numbers in parenthesis show: a. that the samples along the traverse are not of one finite chemistry since a fractionation trend exists; b. that in their present positions along the traverse, the samples lie in disarray, relative to the fractionation sequence.

The disarray can be accounted for, by the fluidisation mechanism of emplacement of the quartz porphyries, this mechanism being capable of rapid ejection and mechanical mixing of different parts of an evolving magma into an apparently homogeneous mass (Reynolds, 1954). The Tibchi disarray is, however, believed to have been the result of a mechanical mixing on a megascopic, rather than microscopic, scale, hence it is still possible to identify the different 'lithologies' of the quartz porphyry suite.

Plots of ΣREE and $\Sigma\text{Ce}/\Sigma\text{Y}$ normalised to T60 against distance to the biotite granite (Moyes, 1979) failed to show any correlation between the sample proximity to the biotite granite contact and the observed REE patterns because, (a) Normalisation to T60 of all samples implies an assumption that prior to the hydrothermal alteration only one pristine rock (T60) was emplaced. Petrographically, two pristine rocks

(T60, T105) have been established and from mineral chemistry it is clear that each sample was to a certain degree different from every other sample, owing to the existence of a continuous fractionation trend. This existence of a continuous magmatic trend would necessarily place constraints on the initial Σ REE of each sample prior to the hydrothermal alteration.

(b) The disarray along the traverse in the positions of the samples relative to their normal order in the fractionation scheme, caused by fluidised megascopic mixing, makes sample proximity to the biotite granite contact an unworthy term of reference.

Plots of Σ REE against $\ln \Sigma\text{Ce}/\Sigma\text{Y}$ used by Moyes (1979) to try to correlate the apparent preferential removal of the LREE with decreasing REE content, did not show any simple relationship because, Σ REE and $\ln \Sigma\text{Ce}/\Sigma\text{Y}$ were capable of varying independently, the former being controlled by an already existing magmatic trend as well as by the hydrothermal alteration, and the latter by hydrothermal alteration.

Evidence from the amphibole miscibility gap combined with the Ca-rich pyroxene crystallisation history (Chapter 5) shows that if the samples along the traverse (plus T133) were to be divided into two groups, they would fall as follows: T60, T168, T169 which would on hydrothermal alteration produce Al-rich calcic amphiboles and T179, T167, T133, T135 which would give Al-poor sodic-calcic and sodic amphiboles (cf. T60, T167, T169, T170 and T168, T135, T133 by Moyes (1979)).

Locality of suspected metasomatic alteration

Whole-rock REE abundances for the peralkaline sodic syenite (T34C), potassic syenite (T34), antiperthite biotite granite (T34B) and the peraluminous, alkali feldspar biotite

granite (T96) are graphically shown in Figure 6.3.5D. In the REE study, T96 is used to represent the biotite granite pluton and the biotite granite immediately enveloping the locality of suspected metasomatically altered syenites and granite above.

Three key observations are made:

- (a) The LREE and HREE groups are parallel to one another, although Σ REE varies from 885ppm (T96) to 107ppm (T34C);
- (c) A decrease in $\frac{\Sigma\text{Ce}}{\Sigma\text{Y}}$ with decreasing REE is noticeable from T96 to T34B to T34C. For T96 to T34 the above ratio increases.
- (c) On the whole, apparent Eu depletion changes from 0.12 in T96 to 0.07 in T34B, for all the rocks.

Based on the criteria that,

- 1) Granites produced by extensive fractional crystallisation generally show HREE enrichment and a large Eu anomaly, such as in T96;
- 2) Granitic rocks originating from increasing fractional crystallisation show increasing Eu depletion with decreasing Σ REE content as shown by the arrangement, T96 to T34B to T34C. Additionally HREE should show relative increase caused by early crystallisation of biotite and apatite, both of which are rich in LREE.

Moyes (op.cit.) reached the conclusion that the sequence T96 to T34B to T34C "may represent the final residual products of the crystallisation of biotite granite". The T96 to T34 trend representing the potassic phase of the suspected metasomatic alteration is found to run contrary to the above enumerated postulates, hence Moyes (op.cit.) confirmed that

"the proposed potassic trend for samples T96 - T34 could be achieved through REE metasomatic complexing with preferential mobility of the HREE causing the observed increase in the $\frac{\Sigma Ce}{\Sigma Y}$ ratio", and that T96- T34 represents "true metasomatic conditions".

Discussion While the enumerated criteria for REE behaviour in a sequence of fractionally crystallised granitic rocks may be admissible geologically, their application to the T96 - T34B - T34C series (as arranged by Moyes) has not been successful for the following reasons:-

(a) On the critical criterion (no.(2) above), while decreasing ΣREE follows the trend T96 - T34B - T34C, the required increasing Eu depletion follows the order T34B - T34C - T96 with reference to actual values (Table 6.3.5). Clearly this postulate is not applicable in favour of fractional crystallisation. The additional observation that HREE show relative increase in the earlier order, may have been simply fortuitous and cannot be taken to over-ride the main criterion above. Fortunately Moyes (op.cit.) concedes that his REE data are unable to resolve the problem.

There are several reasons evident in various parts of the present study and especially the earlier part of the present chapter, why the order T96 - T34B - T34C cannot represent a fractional crystallisation sequence. In the first instance a syenite (T34C) would be difficult, if not impossible to generate as a final residual product from the fractionation of a very highly evolved biotite granite (T96) by means of fractional crystallisation. The nature and composition of what can be considered the final residual liquid of the biotite granite are believed to reside in the (chilled) marginal

and roof zone microgranite facies already described earlier in this chapter.

The parental (?) basalt T122 Moyes (1979) found T122 consistent with the composition of tholeiitic basalts elsewhere. The slight Eu depletion reported may be overlooked, otherwise the implication would be that T122 had evolved by a small degree of fractionation from a parent liquid not represented in the present erosion level of the Tibchi Complex.

CHAPTER 7SUMMARY, CONCLUSIONS AND PETROGENESIS7.1 Summary and conclusions

Hitherto, the Tibchi Complex was geologically known in outline form only ~~map~~, its petrology was similarly sketchy, while its chemistry had yet to be studied.

The 1:50,000 geological map presented shows that in surface plan the Tibchi Complex is defined by a peripheral granite porphyry ring-dyke which is elliptical in shape and oriented north-south along its major axis. The major and minor axes of the ellipse are 27.3 and 17.4 kilometres respectively. The total surface area within the ring-dyke is 344.5 square kilometres of which roughly two-thirds is enclosed Older Granite basement.

The Complex consists of the following major rock units, in chronological order: a subsided Older Granite basement block, extrusive volcanic rocks, quartz porphyries, granite porphyry ring-dyke and isolated dykes, and a central biotite granite intrusion. The basement block consists of adamellites, while the volcanic sequence comprises basic, intermediate and acid lavas which, together, are subordinate in proportion to the associated pyroclastic rocks. The latter consist of ash-fall tuff, agglomerates and ignimbrites. Ash-fall tuff and rhyolite lavas resting directly on the surface of the subsided basement block represent the first clear exposure of the Jurassic land-surface to the recorded in Nigeria.

Joint-controlled greisen vein development and primary mineralisation in the Complex, are probably comparable only to the most extensive occurrence elsewhere in the Nigerian Younger

Granite province. The following minerals are found: cassiterite, sphalerite, wolfram, pyrite, arsenopyrite, chalcopyrite, chalcantite, native copper, molybdenite, galena and siderite.

A number of miscellaneous rock types with distinctive characteristics, have been found. In many ways these rocks are unusual and have not been previously described in the Nigerian Younger Granite province. These include a hypabyssal rock with phenocrysts of 'fully-ordered' microcline, and a suite of oversaturated and undersaturated peralkaline and peraluminous rocks in metasomatic transitions.

Reconstruction of the structural evolution of the Complex suggests that;

- (a) a surface cauldron subsidence inextricably associated with a caldera is partly preserved;
- (b) the presently exposed surface of the basement enclosed by the ring-dyke, represents approximately the Jurassic land-surface which was intersected by the initial ring-fracture;
- (c) the present erosion level is the critical level in the denudation history of a caldera/ring-dyke association, at which the base of the subsided volcanic pile is exposed relative to the ring-fracture (ring-dyke) framework and the 'central granite stock'.

Minimum down-throw is estimated at 600 metres. It is possible to distinguish pre-caldera and intra-caldera groups of volcanic rocks in the Tibchi and neighbouring complexes through, in addition to existing criteria, structural disconformity between members of the two groups. Pre-caldera volcanism most probably featured a central shield volcano. A fluidisation mechanism is postulated for the regime of intra-

caldera volcanism, with quartz porphyries as feeders to the intra-caldera crystal-rich ignimbrites. The massive character and relative homogeneity, both laterally and vertically, of the fluidised intra-caldera ignimbrites, are peculiar 'lava-like' characters which hitherto had led to the misnomer 'late rhyolites', by previous workers.

It is concluded that the granite porphyry magma was essentially degassed, and that its intrusion was quiescent and fracture-controlled. It is also concluded that the 'central' biotite granite was emplaced eccentrically relative to the centre of the Complex, as defined by the peripheral granite porphyry ring-dyke.

In proposing a structural model for the Tibchi Complex, the principle favoured is that throughout the history of caldera formation and ring-dyke intrusion, magma pressure remains positive, regardless of any reductions that arise at the critical stage where eruption begins and subsidence results. The question of negative magma pressure as a precondition for caldera formation through subsidence is rejected, although it is a brilliant concept for underground cauldron subsidence.

In the pyroclastic rocks the structure of collapsed and uncollapsed pumice vesicles and of distorted and undistorted shards have been documented. The role of lithic fragments and phenocrysts during welding is demonstrated. With care, it is possible to identify extreme compaction and welding producing pseudo-flow textures and rendering the rock liable to misinterpretation as 'flow rhyolite'.

In the basic and intermediate lavas, plagioclase composition and whole-rock chemistry have been used to establish the magmatic sequence as follows:

Olivine tholeiite → Tholeiite → Andesine basalt → Trachyte. In the other rocks, clinopyroxene and fayalite compositions as well as petrography enable the following sequence to be established:

Microferrodiorite → microsyenite → porphyries. Chemical variation diagrams suggest that the above two schemes are linked into a wholesome petrogenetic sequence. However the nature of the relationship between the trachyte of the basalt series and the microferrodiorite and microsyenite of the porphyry series is not yet known because whole-rock data for the microferrodiorite and microsyenite enclaves could not be obtained.

The generally accepted low profile of plagioclase and lime in the granitic members of the Younger Granites, is concluded to be due to the extreme fractionation of plagioclase and apatite in the microferrodiorite and microsyenite stages of the evolutionary sequence. The low magnesium and extreme iron-enrichment, in rocks and rock-forming minerals of the intermediate and acid range of the sequence, is shown to be a function of the prevailing oxygen conditions during the initial stages of fractionation. Thus in the Tibchi Complex initial conditions were of low, fixed oxygen content which enabled iron-enrichment to take place while magnesium was continuously being removed from the system by crystallisation of magnesium-rich mafic phases.

The occurrence of plagioclase-bearing biotite granite facies localised in distribution within the alkali feldspar biotite granite in which discrete plagioclase is virtually absent, is seen as due to contamination, most probably from

the basement rocks. The 'mantling' of the plagioclase thus derived, by alkali feldspar microperthite, is perhaps a result of potassium autometasomatism. In contrast, the mantling of plagioclase by homogeneous alkali feldspar, in the microferrodiorite and microsyenite enclaves, is thought to be due to partial resorption of comagmatic plagioclase accompanied by crystallisation of alkali feldspar and resulting from loss of equilibrium. The term 'anti-rapakivi' is restricted in this study to the alkali feldspar/plagioclase relationship in the primitive enclaves.

The association of mineralisation with the plagioclase-bearing variant of the biotite granite relative to the alkali feldspar variant, is an observation that must await confirmation from other complexes.

Central to the petrology of the Tibchi Complex, is the complication caused by postmagmatic processes. Postmagmatic phenomena recognised include recrystallisation, contact metamorphism, hydrothermal modifications and metasomatic alterations.

Recrystallisation of the pyroclastic rocks near the biotite granite contact, for example, obliterates much of the evidence for welding and of the form of the component shards and pumice fragments, and the rock becomes indistinguishable from ordinary rhyolite.

Contact metamorphism of the basalt series by the biotite granite, has produced a bifacial metamorphic aureole characterised by the albite epidote hornfels facies and the hornblende hornfels facies. The biotite granite must therefore have had a solidus temperature between 500°-600°C.

The hydrothermal modifications of the quartz porphyries is complicated by an intrinsic and subtle magmatic variation in the suite, believed to be caused by the fluidised mechanism of emplacement. This method of emplacement is capable of rapidly ejecting and mechanically mixing different parts of an evolving magma into an apparently homogeneous mass. In the Tibchi Complex mechanical mixing on a megascopic, rather than microscopic, scale, is advocated. Evidence for the megascopic mixing phenomenon comes from the observation that at the zone of the most intense hydrothermal alteration of the quartz porphyries at the biotite granite contact, rocks produced are not of the same lithology, although in all cases anhydrous minerals are totally replaced by amphiboles.

It is concluded that amphiboles found in the hydrothermally altered porphyries are postmagmatic in origin since pristine rocks contain no amphiboles. The type of amphibole produced depends broadly on the composition of the initial pyroxene from which the amphibole has formed. Ferroaugites and less evolved ferrohedenbergites would on reaction give Al-rich calcic amphiboles while the more evolved ferrohedenbergites give Al-poor sodic-calcic and sodic amphiboles.

Structural and petrological evidence jointly relate the hydrothermal alterations observed, to the biotite granite intrusion. For example, the degree of alteration in the quartz porphyries increases as the biotite granite is approached. The restriction of alteration of the granite porphyry ring-dyke to its southern sector is believed to be due to the subsurface displaced position of the 'central' granite, relative to the centre of the Complex, as defined by the ring-dyke.

The petrological concept of the hydrothermal alteration is that an aqueous vapour phase, significantly enriched in normative quartz, and active below the granite solidus temperature, emanated from the biotite granite and pervaded the porphyries. However the action of acidic groundwater circulating as a hydrothermal plume at the margins of the cooling granite may also be involved (Moyes, 1979).

The replacement of biotite by calcite and muscovite in the biotite granite of the Kogo hill area indicates that the fluid phase associated with the (copper) mineralisation, may have been rich in carbon dioxide and fluorine.

The complete Al/Si ordering of the microcline phenocrysts, and the occurrence of a distinctive chlorite after earlier mafic phases, in the unusual hypabyssal rock (T41), are modifications reflecting a hydrothermal overprint. These modifications are caused by influx of an extraneously derived fluid phase, operating most probably more than once and at temperatures undoubtedly less than 600°C, possibly as low as under 400°C.

In the south-eastern suite of oversaturated peralkaline rocks, different feldspar petrographic criteria including the proportion of exsolved K- and Na-phase in the perthite, the morphology and integrity of the perthite-perthite grain boundaries, and (by X-ray) Al/Si ordering, have clearly demonstrated that a sodic-potassic trend exists in the rocks, involving subsolidus re-equilibration.

The sodic phase occupies the higher, and the potassic phase the lower, temperature regions of the transition series. Temperatures estimated from Al/Si ordering in feldspars, iron-

titanium oxide mineralogy, and the thermal stability of amphiboles, separately give values ranging from less than 600°C to less than 400°C. These most probably mark the beginning of the sodic phase, and the end of the potassic phase, respectively. Whole-rock chemistry indicates abnormal enrichments in key major and trace elements. Rare-earth element studies give results inconsistent with fractional crystallisation as a process for the series. From all available evidence, therefore, it is concluded;

- (1) that the sodic syenite (T34C) - potassic syenite (T34) - haematite syenite (T34GR) association, is a metasomatic transition series;
- (2) that the effect of the earlier sodic phase on the biotite granite 'wall rock' was to produce a metasomatic sodic granite (T173);
- (3) that the effect of the superimposition of the potassic phase on the wall-rock already affected by the earlier sodic phase, was to produce the metasomatic antiperthite biotite granite (T34B) and its fine-grained facies (T34BB).

It is concluded that the 'basement screen' is also metasomatically altered. The discrepancy between optical and X-ray data in the plagioclase megacrysts is believed to be due to intense but short-lived metasomatism.

Chemical data are presented for fayalites, pyroxenes, amphiboles, iron-titanium oxide minerals and a selection of biotites and chlorites. Chemical analyses of fayalites, ferrohedenbergites, intergrown magnetite-haematite and chlorite are presented for the first time for the Nigerian Younger Granites. All the mineral species approach as closely as possible the

iron end-members of their respective solid-solution series.

Fayalite compositions range from Fa_{92} to Fa_{99} . The Ca-rich pyroxenes range from ferroaugite through ferrohedenbergites and sodian ferrohedenbergites. On the pyroxene quadrilateral, the Tibchi Ca-rich pyroxenes define two trends namely, a 'quartz porphyry pyroxene trend' and a 'granite porphyry pyroxene trend'. The difference between the two trends is better understood when the acmite component is also considered. The quartz porphyry trend was almost completed under a consistently low Na and Fe^{3+} activities, hence compositions were low in the acmite component. The granite porphyry trend however involved a significant role of the Na and Fe^{3+} components in a way that suggests a modification of the pyroxene trend by increased oxygen fugacity. It is believed that the mere presence of sufficient volatiles in the quartz porphyries (as is most probably the case), was enough to suppress the Na and Fe^{3+} activities in the quartz porphyry trend, even if these components were significantly present in the magma.

If the general pattern of published pyroxene trends can be a guide, the Tibchi Ca-rich pyroxenes (and their host rocks) would be placed among those of tholeiitic affinity, but distinguished as one with a mildly alkaline character. The question of an initial peralkaline parent liquid is put in serious doubt, as peralkalinity is shown by the pyroxene data, to have developed late in already evolved magma.

Amphiboles of the Tibchi Complex consist of calcic, sodic-calcic and alkali groups. Calcic amphiboles consist essentially of hastingsite, hastingsitic hornblende, ferroedenite, ferroactinolitic hornblende and ferroactinolite.

Sodic-calcic amphiboles consist almost exclusively of ferrichterite while alkali amphiboles are mostly arfvedsonites. Occurrence of riebeckite is rare and restricted to special conditions.

Amphiboles of the Tibchi Complex define two divergent trends when the plot of $(\text{Na} + \text{K})_A$ against $(8 - \text{Si})$ for the calcic group, is combined with that of Na_B against $(\text{Na} + \text{K})_A$ for the sodic-calcic and alkali groups. One trend is the ferroactinolite-ferroedenite series, defined by the calcic amphiboles and controlled by the 'edenite substitution'. The other is the ferroactinolite-ferrichterite-alkali amphibole series, defined by the sodic-calcic and alkali amphiboles and controlled by the Na_BNa_A for Ca_B substitution. The compositional divide between the two divergent reaction series lies within the ferroactinolite field and is apparently caused by the difference in the requirement of Al^{IV} and Ca_B in the lattice. The disposition of the two trends is, with regard to the amphiboles that define them, pre-destined by compositions of the initial pyroxenes from which the amphiboles have formed. Initial hydration of the ferroaugite or the less evolved ferrohedenbergite at the onset of the hydrothermal process would result in an Al-rich calcic ferroactinolite, which then initiates the ferroactinolite-ferroedenite trend. On the other hand, the more evolved ferrohedenbergites would give first, an Al-poor Ca-poor ferroactinolite, which then initiates the ferroactinolite-ferrichterite-alkali amphibole series.

The present study favours the proposition by some workers that a miscibility gap between ferroactinolite and ferroedenite does not exist. On the other hand continuous

miscibility between the ferroactinolite-ferroedenite and ferroactinolite-ferrorichterite alkali amphibole series, does not appear practicable.

7.2 Petrogenesis

The origin and evolution of magma(s) parental to rocks of the Nigerian Younger Granites are still controversial.

The following view-points exist:

- (a) Parental syenitic liquids derived directly from the upper mantle, with peralkaline silicic variants formed by 'crustal enrichments' of the syenitic liquids, and the peraluminous biotite granites obtained either as further modifications of the syenitic liquids or as independent derivatives of the 'dioritic' lower crust (van Breemen et al., 1975);
- (b) Parental hornblende fayalite granite liquid derived directly from the upper mantle through partial melting and associated with divergent peralkaline and peraluminous trends through fractional crystallisation, depending on the operating physical conditions (Macleod et al., 1971; Jacobson and Macleod, 1977);
- (c) Parental syenitic and acid magmas from partial melting of crustal and subcrustal rocks (Black and Girod, 1970);
- (d) Mantle-derived basaltic liquid which underwent crystal fractionation, simultaneously causing crustal anatexis from which a second parental acid magma was formed (Turner and Bowden, 1979).

In the Tibchi Complex the question of parental syenitic or hornblende fayalite granite liquid is discounted since, by whatever process, rocks of these compositions have more

primitive precursors. Moreover primary granite magmas cannot be derived from the upper mantle (Wyllie et al., 1976), thus ruling out any possibility elsewhere for the fayalite granite liquid, as postulated in (b) above.

In the Tibchi Complex, there is sufficient evidence for a parental basaltic liquid, presumably from the upper mantle, that evolved through fractional crystallisation. The evolution is of a tholeiitic affinity with mildly alkaline character, perhaps better described as the transitional type. Barberi et al. (1975) have established a transitional basalt-pantellerite sequence of crystallisation, in the Boina Centre (of the Afar rift), Ethiopia. The mechanism of evolution here, according to Barberi et al. (op. cit.), was by early fractionation of olivine and plagioclase, leading to andesine basalts and ferrobasalts, followed by crystallisation of iron-titanium oxide minerals and iron-rich pyroxene, to give over-saturated trachytes. Through the 'plagioclase effect' peralkaline liquids were finally derived from the trachyte members. This scheme fits well with evidence from the Tibchi Complex, except that modal olivine is not found in the early rocks of this Complex. However the sharp decrease in MgO as shown on the Harker diagram, and the disappearance of olivine from the norm, probably have significance equivalent to the early crystallisation of modal olivine.

The scheme is preferred in this study despite the difference in tectonic setting and degree of peralkalinity attained, between the Boina Centre and the Tibchi Complex.

The advantage of the above model is that it clearly accounts for the observed extreme iron-enrichment in the rocks and minerals of the Tibchi Complex and indeed other Nigerian

Younger Granite Complexes, and at the same time demonstrates the development of peralkalinity without invoking a parental peralkaline liquid (which is disapproved, by evidence from the Tibchi Complex). The development of peralkalinity in the Tibchi Complex is in addition fostered by relevant changes in prevailing oxygen fugacity as shown by the pyroxene crystallisation history. The point in time at which oxygen fugacity changes in favour of peralkalinity appears to be structurally controlled. This corresponds to the end of the intra-caldera volcanism, and is associated with the almost complete de-volatilisation of the acid magma. The repeated structural evolutionary sequence of individual complexes favours the repetition of the development of peralkalinity, perhaps with a great deal of precision from complex to complex.

In the neighbouring Ningi-Burra complex, Turner and Bowden (1979) have demonstrated that compositional gaps previously held to separate basalt, trachyte and rhyolite (or their intrusive equivalents) in the Nigerian Younger Granites in general, do not exist, since a full range of intermediate rock types have been sampled. Barberi *et al.* (1975) have suggested that even if such a gap became apparent, it is probably an inherent aspect of the basalt-pantellerite model and accountable by a limited oxygen unbuffered zone within a restricted crystallisation interval, near the transition to the peralkaline field.

Turner and Bowden (1979) suggest that the presence of large volumes of rhyolite and granite required that extensive crustal anatexis took place, in addition to the normal evolution of the basic parent. On account of the absence of any evidence

in the Tibchi Complex to the contrary, this hypothesis is adopted. and on the criteria of Barker et al (1975).

The postmagmatic history of the Tibchi Complex is dominated by the direct or indirect effect of the biotite granite intrusion on earlier rocks, through contact metamorphism, recrystallisation, hydrothermal modification and metasomatic alterations.

By whatever process, there is always an inherent build-up of water in a magmatic sequence of evolution. "Uprise and progressive crystallisation of magma bodies produces H_2O -saturation around margins and in the upper regions of magma chambers" (Maaloe and Wyllie, 1975). As the biotite granite structurally and petrologically marks the end of the evolution of the Tibchi Complex, the build up of water in the magma inevitably has to reach its peak at this stage. Rocks already emplaced become subjected to varied subsolidus modifications as the relatively large biotite granite magma solidifies and the aqueous fluids escape.

If the effect of only one granite intrusion can be that pervasive it is very probable that other complexes with several superposed granitic bodies and earlier volcanic and subvolcanic units, could be even more dramatic. Therefore previously studied areas in which no account has been given of these modifications, probably deserve re-examination. Subsequent studies on other complexes must be conscious of the role of postmagmatic modifications. Only by doing so, can the general magmatic evolution of the province be correlated and better understood.

Metasomatic alterations in which quartz is a stable phase, and often involving its enrichment in normative quantities, as

observed in the siderophyllitic metasomatism of the minor granite porphyry dyke (T22, T23), are greisen-type phenomena related to the biotite granite mineralisation episode. On the other hand, metasomatism involving desilication, as in the south-eastern sector of the Complex, may represent a rare incidence of deep-seated emanations associated with the most remote aspects of Younger Granite magmatism, hitherto undocumented.

REFERENCES

- ABBA, S.I. 1976. Geochemistry and petrology of mineralisation at Ririwai, Gindi Akwati and Dutsen Wai in the Nigerian Younger Granite province. Unpubl. M.Sc. thesis, Ahmadu Bello University, Zaria, Nigeria.
- AJAKAIYE, D.E. 1968. A gravity interpretation of the Liruei Younger Granite ring complex of N. Nigeria. Geol.Mag. 105, 256-263.
- 1970. Gravity measurements over the Nigerian Younger Granite province. Nature 225, 50-52.
- 1974. A gravity profile across the Banke ring complex. Geoexploration, 12, 59-66.
- AKELLA, J. & WINKLER, H.G.F. 1966. Orthorhombic amphibole in some metamorphic reactions. Contr. Mineral. Petrol. 12, 1-12.
- ALEKSIYEV, E.I. 1970. Genetic significance of the REE in the Younger Granites of N. Nigeria and the Cameroons. Geochem.Int. 7, 127-132.
- ANDERSON, E.M. 1936. The Dynamics of the Formation of Cone-sheets, Ring-dykes, and Cauldron-subsidences. Proc.Roy. Soc. Edinburgh 56, 128-157.
- ATKINS, F.B. 1969. Pyroxenes of the Bushveld Intrusion, South Africa. J. Petrology 10, 222-249.
- BADEJOKO, T.A. 1977. The composition and structural state of K-feldspars and their bearing on the evolution of the Younger Granites of Central Nigeria. Unpubl. Ph.D. thesis, University of Ibadan, Nigeria.
- BAILEY, E.B., CLOUGH, C.T. et al. 1924. Tertiary and post-Tertiary geology of Mull, Loch Aline and Oban. Mem. geol. Surv. Scotland.

- BAIN, A.D.N. 1934. The younger intrusive rocks of the Kudu hills, Nigeria. Jl geol. Soc. Lond. 90, 201-239.
- BARBERI, F., FERRARA, G., SANTACROCE, R., TREUIL, M. & VARET, J. 1975. A transitional basalt-pantellerite sequence of fractional crystallisation, the Boina centre (Afar rift, Ethiopia). J. Petrology 16, 22-56.
- BARKER, D.S. & HODGES, F.N. 1977. Mineralogy of intrusions in the Diablo Plateau, northern Trans-Pecos magmatic province, Texas and New Mexico. Bull. geol. Soc. Am. 88, 1428-1436.
- BARKER, F., WONES, D.R., SHARP, W.N. & DESBOROUGH, G.A. 1975. The Pikes Peak Batholith, Colorado Front Range, and a model for the origin of the gabbro-anorthosite-syenite-potassic granite suite. Precambrian Res. 2, 97-160.
- BILLINGS, M.P. 1943. Ring-dikes and their origin. Trans. N.Y. Acad. Sci. 5, 131-144.
- 1945. Mechanics of igneous intrusion in New Hampshire. Am. J. Sci. 243, 40-68.
- BLACK, R. 1963. Note sur les complexes annulaires de Tchouni-Zarniski et de Gouré (Niger). Bull. Bur. Rech. géol. min. Paris 1, 31-45.
- & GIROD, M. 1970. Late Palaeozoic to Recent igneous activity in West Africa and its relationship to basement structure. In CLIFFORD, T.N. & GASS, I.G. (eds.) African magmatism and tectonics. Oliver and Boyd, 185-210.
- BLYTH, F.G.H. 1940. The nomenclature of pyroclastic deposits. Bull. volcan. 6, 145-156.
- BORLEY, G.D. 1963a. Geochemistry of the mafic minerals in some Younger Granites of Nigeria. Unpubl. Ph.D. thesis, University of London.

- BORLEY, G.D. 1963b. Amphiboles from the Younger Granites of Nigeria, Part 1: Chemical classification. Mineral Mag. 33, 358-376.
- BOWDEN, P., BENNETT, J.N., WHITLEY, J.E., & MOYES, A.B. (in press) Rare-earths in Nigerian Mesozoic granites and related rocks. In AHRENS, L.H. (ed.) Origin and distribution of the elements.
- & JONES, J.A. 1978. Mineralisation in the Younger Granite Province of northern Nigeria. MAWAM 3, 179-190.
- & KINNAIRD, J.A. 1978. Younger granites of Nigeria - a zinc-rich tin province. Trans. Instn. Min. Metall. 87: 65-69.
- & TURNER, D.C. 1974. Peralkaline and associated ring-complexes in the Nigeria-Niger province, West Africa. In ~~S~~ØRENSEN, H. (ed.) The Alkaline Rocks, John Wiley & Sons, 330-351.
- , VAN BREEMEN, O., HUTCHISON, J. & TURNER, D.C. 1976. Palaeozoic and Mesozoic age trends for some ring complexes in Niger and Nigeria. Nature 259, 297-299.
- & WHITLEY, J. Rare-earth patterns in peralkaline and associated granites. Lithos 7, 15-21.
- BROWN, G.M. & VINCENT, E.A. 1963. Pyroxenes from the late stages of fractionation of the Skaergaard Intrusion, East Greenland. J. Petrology 4, 175-197.
- BUCHANAN, M.S., MACLEOD, W.N. & TURNER, D.C. 1971. The geology of the Jos Plateau. 2. Younger Granite Complexes. Bull. geol. Surv. Nigeria.
- BUDDINGTON, A.F. & LINDSLEY, D.H. 1964. Iron-Titanium Oxide Minerals and Synthetic Equivalents. J. Petrology 5, 310-357.

- CARMICHAEL, I.S.E. 1960. The pyroxenes and olivines from some Tertiary acid glasses. J. Petrology 1, 309-336.
- 1963. The occurrence of magnesian pyroxenes and magnetite in porphyritic acid glasses. Mineral. Mag. 33, 394-403.
- 1964. The petrology of Thingmuli, a Tertiary volcano in eastern Iceland. J. Petrology 5, 435-460.
- 1967. The iron-titanium oxides of salic volcanic rocks and their associated ferromagnesian silicates. Contr. Mineral. Petrol. 13, 36-64.
- , TURNER, F.J. & VERHOOGEN, J. 1974. Igneous Petrology. McGraw-Hill.
- CHAPMAN, C.A. 1966. Origin of igneous central complexes and formation of ring dikes (abs.). Geol. Soc. Am. Spec. Paper 87, 31.
- 1976. Structural Evolution of the White Mountain Magma Series. Mem. geol. Soc. Am. 146, 281-300.
- CHARLES, R.W. 1977. The phase equilibria of intermediate compositions on the pseudobinary $\text{Na}_2\text{CaMg}_5\text{Si}_8\text{O}_{22}(\text{OH})_2$ - $\text{Na}_2\text{CaFe}_5\text{Si}_8\text{O}_{22}(\text{OH})_2$. Am. J. Sci. 227, 594-625.
- CLOUGH, C.T., MAUFE, H.B., BAILEY, E.B. 1909. The Cauldron-subsidence of Glen Coe and the Associated Igneous Phenomena. Jl geol. Soc. Lond. 65, 611-678.
- DEER, W.A., HOWIE, R.A. & ZUSSMAN, J. 1971. Rock-forming Minerals, vol. Sheet silicates. Longman.
- 1978. Rock-forming Minerals, vol. Single chain silicates. Longman.
- DEMPSTER, A.N. 1956. Draft of Kalato Final Report. Unpublished private report.

- DU TOIT, A.L. 1920. The Karroo dolerites of S. Africa; a study in hypabyssal injection. Trans. geol. Soc. S. Africa. 23, 1.
- ERNST, W.G. 1968. Amphiboles. Springer-Verlag.
- ESCHER, B.G. 1929. On the formation of calderas. Leidshe Geolog. Mededeelingen 3, 183-219.
- FALCONER, J.D. & RAEBURN, C. 1923. The northern tinfields of Bauchi Province Bull. geol. Surv. Nigeria 4.
- FERGUSON, A.K. 1978. The Crystallisation of Pyroxenes and Amphiboles in some Alkaline Rocks and the Presence of a Pyroxene Compositional Gap. Contr. Mineral. Petrol. 67, 11-15.
- FINGER, L.W. 1972. The uncertainty in the calculated ferric iron content of a microprobe analysis. Yb. Carnegie Instn. Washington 71, 600-603.
- FOSTER, M.D. 1960. Interpretation of the Composition of Trioctahedral Micas. U.S. Geol. Surv. Prof. Paper 354-B.
- FYFE, W.S., TURNER, F.J. & VERHOOGEN, J. 1958. Metamorphic reactions and metamorphic facies. Mem. geol. Soc. Am. 73.
- GARY, M., McAFEE, R. & WOLF, C.L. (Eds.). 1974. Glossary of Geology. American Geological Institute, Washington, D.C.
- GIBSON, I.L. & TAZIEFF, H. 1967. Additional theory of origin of fiamme in ignimbrites. Nature 215, 1473-1474.
- GRAPES, R.H. & GRAHAM, C.M. 1978. The actinolite-hornblende series in metabasites and the so-called miscibility gap: A review. Lithos 11, 85-97.
- HAAG, H.L. 1943. Wolfram in Nigeria: with notes on cassiterite, wolfram and columbite zones. Trans. Instn. Min. Metall. 52, 119-183.

- HAGGERTY, S.E. 1976. Opaque mineral oxides in terrestrial igneous rocks. In RUMBLE III, D. (ed.) Oxide Minerals Mineral Soc. Am. Short Course Notes 3, Hg-101 - Hg-300.
- HALLIMOND, A.F. 1943. On the graphical representation of calciferous amphiboles. Am. Mineral. 28, 65-89.
- HARDIE, W.G. 1963. Explosion breccias near Stob Mhic Mhartium, Glen Coe, Argyll, and their bearing on the origin of the nearby flinty crush rock. Trans. geol. Soc. Edinb. 19, 426-438.
- HARKER, A. 1974. Metamorphism. Chapman & Hall.
- HASLAM, H.W. 1968. The Crystallisation of Intermediate and Acid Magmas at Ben Nevis, Scotland. J. Petrology 9, 84-104.
- HEINRICH, E.Wm. 1965. Microscopic identification of minerals. McGraw-Hill.
- HEYS, M.H. 1954. A new review of the chlorites. Mineral. Mag. 30, 277.
- HUTCHISON, C.S. 1974. Laboratory Handbook of Petrographic Techniques. John Wiley & Sons.
- JACOBSON, R.R.E. & MACLEOD, W.N. 1977. Geology of the Liruei, Banke and adjacent Younger Granite ring-complexes. Bull. geol. Surv. Nigeria 33.
- , MACLEOD, W.N. & BLACK, R. 1958. Ring-complexes in the Younger Granite province of Northern Nigeria. Mem. geol. Soc. Lond. 1.
- JENSEN, B.B. 1973. Patterns of trace element partitioning. Geochim. et Cosmochim. Acta 37, 2227-2242.
- KINGSLEY, L. 1931. Cauldron subsidence of the Ossipee Mountains. Am. J. Sci. 22, 139-168.

- KINNAIRD, J.A. 1977. A Geological Investigation of Some Nigerian Jurassic Granites and their Mineralisation. Unpubl. M.Sc. thesis, University of St. Andrews.
- KOGARKO, L.N. 1974. Role of volatiles. In SØRENSEN, H. (ed.) The Alkaline Rocks John Wiley & Sons, 474-488.
- LACROIX, A. 1930. Remarques sur les materiaux de projection des volcans et sur la genese des roches pyroclastiques qu'ils constituent Soc. géol. France 2, 431-472.
- LARSEN, L.M. 1976. Clinopyroxenes and Coexisting Mafic Minerals from the Alkaline Ilimaussaq Intrusion, South Greenland. J. Petrology 17, 258-290.
- LEAKE, B.E. 1978. Nomenclature of amphiboles. Compiled for Subcommittee on amphiboles, I.M.A. Mineral. Mag.
- LINDSLEY, D.H. 1976. Experimental Studies of Oxide Minerals. In RUMBLE III, D. (ed.) Oxide Minerals Mineral. Soc. Am. Short Course Notes, 3, L-61 - L-88.
- , BROWN, G.M. & MUIR, I.D. 1969. Conditions of the ferrowollastonite-ferrohedenbergite inversion in the Skaergaard Intrusion East Greenland. Mineral. Soc. Am. Spec. Paper 2, 193-201.
- & MUNOZ, J.L. 1969. Subsolidus relations along the join hedenbergite-ferrosilite. Am. J. Sci. 267A, 295-234.
- LIU, J.G., KUNIYOSHI, S. & ITO, K. 1974. Experimental studies of the phase relations between greenschist and amphibolite in a basaltic system. Am. J. Sci. 274, 613-632.
- LUTH, W.C. & TUTTLE, O.F. 1969. The hydrous vapour phase in equilibrium with granite and granite magmas. Mem. geol. Soc. Am. 115, 513-548.

- MAALØE, S. & WYLLIE, P.J. 1975. Water content of a granite magma deduced from the sequence of crystallisation determined experimentally with water under-saturated conditions. Contr. Mineral. Petrol. 52, 175-191.
- MACDONALD, G.A. 1972. Volcanoes. Prentice-Hall.
- MACLEOD, W.N., TURNER, D.C. & WRIGHT, E.P. 1971. The Geology of the Jos Plateau 1. General Geology. Bull. geol. Surv. Nigeria 32.
- MANSFIELD, G.R. & ROSS, C.S. 1935. Welded rhyolitic tuffs in southeastern Idaho. Trans. Am. Geophys. Union 16, 308-321.
- MARTIN, R.F. 1969. Effects of fluid composition on structural state of alkali feldspars. Trans. Am. Geophys. Union 50, 350.
- 1972. Controls of ordering and subsolidus phase relations in the alkali feldspars. In MACKENZIE, W.S. & ZUSSMAN, J. (eds.) The feldspars Manchester University Press.
- & BONIN, B. 1976. Water and magma genesis: the association hypersolvus granite - subsolvus granite. Can. Mineral. 14, 228-237.
- & BOWDEN, P. (in preparation). Alkali feldspars as monitors of postmagmatic changes, Ririwai Complex, Nigeria.
- MATHESON, G.I., HERBST, W.A. & HOLT, P.H. 1949. Dynamics of fluid-solid systems. 15th annual chemical engineering symposium: Division of industrial and engineering chemistry, American Chemical Society. Industrial and Engineering Chemistry, 41 (6) 1099-1250.

- MOYES, A.B. 1979. The determination and interpretation of rare-earth element abundances in rocks and minerals from the Younger Granites of Nigeria. Unpubl. Ph D. thesis, University of St. Andrews, Scotland.
- NUEMANN, E.-R. 1976. Compositional relations among pyroxenes, amphiboles and other mafic phases in the Oslo Region plutonic rocks. Lithos 9, 85-109.
- NICHOLLS, J. & CARMICHAEL, I.S.E. 1969. Peralkaline acid liquids: A petrological study. Contr. Mineral. Petrol. 20, 268-294.
- NOLAN, J. 1969. Physical properties of synthetic and natural pyroxenes in the system diopside-hedenbergite-acmite. Mineral. Mag. 37, 216-229.
- OFTEDAHL, C. 1953. Studies on the igneous rock complex of the Oslo region. XIII. The cauldrons. Skrift. Norske Vidensk-Akad. Oslo. 1. Mat.-Nat. Klasse. 3.
- OYAWOYE, M.O. 1968. The geology of the Zarandah ring-complex, N. Nigeria. J. Min. Geol. 3, 33-47.
- OSBORN, E.F. 1959. Role of oxygen pressure in the crystallisation and differentiation of basaltic magma. Am. J. Sci. 257, 609-647.
- PAPIKE, J.J., CAMERON, K.L. & BALDWIN, K. 1974. Amphiboles and pyroxenes: characterisation of other than quadrilateral components and estimation of ferric iron content from microprobe data. Geol. Soc. Am. Abs. Prog. 6, 1053-1
- PARSONS, I. 1978. Feldspars and fluids in cooling plutons. Mineral. Mag. 42, 1-17.
- PITCHER, W.S. 1978. The anatomy of a batholith. Jl geol. Soc. Lond. 135, 157-182.

- POLDERVAART, A. & HESS, H.H. 1951. Pyroxenes in the crystallisation of basaltic magma. J. Geology 59, 472-489.
- REYNOLDS, D.L. 1954. Fluidisation as a geological process, and its bearing on the problem of intrusive granites. Am. J. Sci. 252, 577-614.
- 1956. Calderas and ring-complexes. Geologie Mijnb. 16, 355-379.
- REVERDATTO, V.V., SHARAPOV, V.N. & MELAMED, V.G. 1970. The Controls and Selected Peculiarities of the Origin of Contact Metamorphic Zonation. Contr. Mineral. Petrol. 29, 310-337.
- RIBBE, P.H. 1975. The Chemistry, Structure and Nomenclature of Feldspars. In RIBBE, P.H. (ed.) Feldspar mineralogy Mineral. Soc. Am. Short Course Notes 2, R-1 - R-72.
- RICHEY, J.E. 1928. The Structural relations of the Mourne granites (Northern Ireland). Jl geol. Soc. Lond. 83, 653-688.
- 1932. Tertiary Ring Structures in Britain. Trans. geol. Soc. Glasgow 19, 42-141.
- ROBERTS, J.L. 1963. Source of the Glencoe Ignimbrites. Nature 199, 901.
- 1970. The intrusion of magma into brittle rocks. In NEWALL, G. & RAST, N. (eds.) Mechanism of Igneous Intrusion Gallery press. 201-216.
- ROBSON, G.R. & BARR, K.G. The effect of stress on faulting and minor intrusions in the vicinity of a magma body. Bull. volcan. 27, 315-330.
- ROCKINGHAM, J.E. 1950. Notes on some primary mineralisation at Yeli and Kogo. Rpt. no. 875. Geol. Surv. Nigeria.

- ROCKINGHAM, J.E. 1951. Preliminary report on a lode near Kogo, Tibchi. Rpt. no. 913. Geol. Surv. Nigeria.
- SMITH, J.V. 1974. Feldspar Minerals II. Chemical and Textural properties. Springer-Verlag.
- SPRY, A. 1976. Metamorphic textures. Pergamon press.
- STRECKEISON, A.L. 1967. Classification and Nomenclature of Igneous Rocks. N. Jb. Miner. Abh. 107, 144-214.
- SUNDIUS, N. 1946. The classification of the hornblendes and the solid solution relations in the amphibole group. Arsbok. Sver. geol. Unders. 40, 1-36.
- TAYLOR, H.P. 1977. Water/Rock interactions and the origin of H₂O in granitic batholiths. Jl geol. Soc. Lond. 133, 509-558.
- 1974. The Application of Oxygen and Hydrogen Isotope Studies to Problems of Hydrothermal Alteration and Ore Deposition. Econ. Geol. 69, 843-883.
- TATTAM, C.M. 1941. Wolfram investigation. The Kalato-Kogo District (Tibchi and Yeli Hills). Rpt. no. 702. Geol. Surv. Nigeria.
- TAUBENECK, W.H. 1967. Notes on the Glen Coe Cauldron Subsidence, Argyllshire, Scotland. Bull. geol. Soc. Am. 78, 1295-1316.
- TAZIEFF, H. 1970. Mechanism of ignimbrite eruption. In NEWALL, G. & RAST, N. (eds.) Mechanism of Igneous Intrusion. Gallery Press.
- THORNTON, C.P. & TUTTLE, O.F. 1960. Chemistry of Igneous Rocks 1. Differentiation Index. Am. J. Sci. 258, 664-684.
- TURNER, D.C. 1962. The geology of the Younger Granite ring-complex of the Sara-Fier and Pankshin Hills, Northern Nigeria. Unpubl. Ph.D. thesis. University of London.

- TURNER, D.C. 1968. Volcanic and intrusive structures in the Kila-Warji ring complex, northern Nigeria. Jl. geol. Soc. Lond. 124, 81-89.
- 1972. Structure and tectonic setting of the Younger Granite ring complexes of Nigeria and Southern Niger. Part I: Ring complexes and their component units. Savanna 1, 223-236.
- 1973. Part II: Structural and tectonic patterns in the Younger Granite province. Savanna 2, 51-59.
- 1976. Structure and petrology of the Younger Granite Ring Complexes. In KOGBE, C.A. (ed.) Geology of Nigeria Elizabethan Publishing Co. 143-158.
- & BOWDEN, P. The Ningi-Burra complex, Nigeria: dissected calderas and migratory magmatic centres. Jl. geol. Soc. Lond. 136, 105-119.
- TURNER, F.J. & VERHOOGEN, J. Igneous and metamorphic petrology. McGraw-Hill.
- TUTTLE, O.F. & BOWEN, N.L. 1958. Origin of granite in the Light of experimental studies in the system $\text{NaAlSi}_3\text{O}_8$ - KAlSi_3O_8 - SiO_2 - H_2O . Mem. geol. Soc. Am. 74.
- VAN BEMMELEN, R.W. 1939. The volcano-tectonic origin of Lake Toba (North-Sumatra). IV. Mijnbouw en Geol, 6de Jaar 9, 126-140.
- VAN BREEMEN, O. & BOWDEN, P. 1973. Sequential age trends for some Nigerian Mesozoic granites. Nature Phys. Sci. 242, 9-11.
- , HUTCHISON, J. & BOWDEN, P. 1975. Age and Origin of the Nigerian Mesozoic Granites: A Rb-Sr Study. Contrib. Mineral Petrol. 50, 157-172.

- VINCENT, E.A. & PHILLIPS, R. 1954. Iron-titanium oxide minerals in layered gabbros of the Skaergaard intrusion, East Greenland. Geochemica Acta 6
- VINCENT, P.M. 1970. The evolution of the Tibesti Volcanic Province, eastern Sahara. in CLIFFORD, T.N. & GASS, I.G. (eds.) African magmatism and tectonics. Oliver & Boyd.
- VORMA, A. 1971. Alkali feldspars of the Wiborg rapakivi massif in southeastern Finland. Bull. Comm. Geologique Finlande 246.
- WAGER, L.R. & DEER, W.A. 1939. Geological investigations in East Greenland. Part III. The petrology of the Skaergaard intrusion, Kangerdlugssuak. Medd. Grønland 105, 1-352.
- WALKER, G.P.L. 1963. The Breiddalur central volcano, eastern Iceland. Jl geol. Soc. Lond. 119, 26-63.
- WENTHWORTH, C.K. & WILLIAMS, H. 1932. The classification and terminology of the pyroclastic rocks. Nat. Research Council Bull. 89, 19-53.
- WILLIAMS, H. 1941. Calderas and their origin. Univ. California Bull. Dept. geol. Sci. 25, 239-346.
- 1942. The Geology of Crater Lake National Park, Oregon. Carnegie Instn. Washington Publ. 540.
- WRIGHT, T.L. 1967. The microcline-orthoclase transformation in the contact aureole of the Eldora stock, Colorado, Am. Mineral. 52, 117-136.
- WYLLIE, P.J., HUANG, W-L., STERN, C.R. & MAALØE, S. 1976. Granitic magmas: possible and impossible sources, water contents and crystallisation sequences. Can. J. Earth Sci. 13, 1007-1019.

- YAGI, K. 1966. The system acmite-diopside and its bearing on the stability relations of natural pyroxenes of the acmite-hedenbergite-diopside series. Am. Mineral 51, 978-999.
- YODER, H.S. 1963. Pyroxenes and associated minerals in the crust and mantle. Yb. Carnegie Instn. Washington 62, 84-95.

ACKNOWLEDGEMENT

The lack of geological knowledge about the Tibchi Complex was suggested as an urgent research problem by Professor D.C. Turner to whom the joys and sorrows of this work must first be related. I am thankful to him for the suggestion and his advice in the field. Without a favourable reference from Dr. P. Bowden to the Commonwealth Scholarship Commission, the course of events would have been different. I am grateful to him and I hope I have not let him down. For his subsequent role as my supervisor, I thank him.

My first visit to the Tibchi Complex was with Ben and Anne. I prefer to stick to their first names in appreciation of our first meeting and their friendliness in St. Andrews. Anne went further to type my manuscripts. I appreciate, and here thank her for, her great sense of understanding and patience.

This work was very wide in scope, the list of those to whom I am indebted is necessarily long. I would here simply open my heart to say that it would be impossible to mention everybody by name and that I therefore give this paragraph to all who assisted me in various ways. I shall always remember.

Professor R.F. Martin of McGill University in Canada greatly encouraged me in the 'mid-waters' of this work and further provided X-ray data on the feldspars. I am exceedingly grateful to him, and to his family for hospitality while they were here in Scotland. Both Professor Martin and Dr. M. Barriere of Brest University in France, accompanied me to the Tibchi Complex for on the spot discussions. I am grateful for their advice.

Professor Turner and Dr. Barriere read the initial drafts and made useful criticisms and suggestions. The final stages were closely watched by Dr. J.F. Brown to whom I owe many thanks for making it possible for me to contain myself within a permissible limit.

Dr. W.E. Stephens is thanked for helping out with computing problems and Dr. C.H. Donaldson for discussions and advice on pyroxenes and olivines. Other members of staff have been very kind indeed and I am grateful. I thank the generality of the technical staff for their work and my fellow research workers for their comradeship. My gratitude must go to Professor E.K. Walton, Head of Department, for his generosity at all times.

This work was carried out under a Commonwealth Postgraduate Scholarship awarded by the Commonwealth Scholarship Commission, London. I am indebted to the Commission and very grateful to the Association of Commonwealth Universities, the British Council, and the Overseas Development Ministry. Leave to carry out the work was granted by the Ahmadu Bello University, Zaria, Nigeria under the Study Fellowship scheme. I am exceedingly grateful to the University and would like to thank Professor Kofanski and Professor Kogbe for their patronage.

APPENDIX

(a)

TABLE 4.5

MODAL ANALYSES OF REPRESENTATIVE BIOTITE GRANITES

	<u>T96</u>	<u>T182</u>	<u>T138</u>	<u>T139</u>
Quartz	31.65	32.46	29.15	35.85
Alkali feldspar	63.75	60.37	52.13	45.99
Plagioclase	0.05	0.49	13.00	13.50
Biotite	4.05	4.85	5.44	4.48
Accessories	0.50	1.83	0.27	0.18

Based on the following counts:

T96 = 2000; T182 = 2246; T138 = 3307; T139 = 1693.

T96] Alkali feldspar biotite granite
T182]

T138] Plagioclase-bearing biotite granites of
T139] Kogo hill (mineralised).

(b)

X-RAY DATA ON ALKALI FELDSPARS FROM THE TIBCHI COMPLEX

<u>Porphyries</u>	K-Phase	No. of co-existing phases	N _{or} from a	N _{or} from V	t ₁ ⁰	Δ
T60 clear phenocryst	Orthoclase	2	0.98	0.92	0.44	
T60 Turbid-brown phenocryst	Orthoclase & Intermed. microcline	3	0.98 0.91	0.90 0.94	0.39 0.82	0.59
T135 phenocryst	Intermed. microcline	2	0.90	0.91	0.83	0.71
T135 Matrix	Orthoclase	2	0.96	0.98	0.36	
T167 Phenocryst	Orthoclase	2	0.97	0.95	0.37	
T167 Matrix	Orthoclase	2	0.95	0.98	0.40	
T168 Phenocryst	Orthoclase	2	0.94	0.95	0.35	
T168 Matrix	Orthoclase	2	0.95	0.98	0.37	
TVB Grey-Phenocryst	Orthoclase	2	0.96	0.93	0.47	
TVB Cream Phenocryst	Orthoclase & Intermed. Mic.	3	0.97 0.96	0.95 0.96	0.39 0.84	0.75
T169 Phenocryst	Orthoclase	2	0.94	0.94	0.41	
T170 Phenocryst	Orthoclase & Intermed. Microcline	3	0.94	0.94	0.81	0.74
T133 Phenocryst	Orthoclase	2	0.92	0.92	0.46	
T41 Phenocryst	Maximum Microcline	2	0.92	0.94	1.00	1.00

(c)

South-eastern suite of altered rocks

	K-phase	No. of co-existing phases	N _{or} from a	N _{or} from V	t ₁ ⁰	Δ (or ψ)*
T34C	Orthoclase	2	0.93	0.94	0.44	
T34CA White	Orthoclase	2	0.97	0.99	0.43	
T34CA 'rapakivi'	Intermed. Microcline	2	0.90	0.92	0.77	0.53
T34	Intermed. Microcline	2	0.97	0.98	0.89	0.80
T34G red	Maximum Microcline	2	0.92	0.91	0.92	0.92
T35 Megacryst	Albite	1	0.01	-0.91	0.90	1.19

* For sodic plagioclase

Analyst: Professor R.F. Martin, using the Guinier-Hägg Camera (CuK α , radiation, $\lambda = 1.5405$ A).

ELECTRON MICROPROBE ANALYSES

Microprobe analyses of rock-forming minerals were carried out using the Cambridge Instruments Electron Microprobe Microscan 5, at the University of Edinburgh. Analyses were done by crystal spectrometry, with electron beam spot size of about 1 μ m and a generating potential of 20 KV. Correction procedures were essentially those of Sweatman and Long (1969).

(d)

ESTIMATES OF FERRIC IRON
FROM MICROPROBE DATA OF AMPHIBOLES

By

J.J. Papike

Department of Earth and Space Sciences
State University of New York
Stony Brook, New York 11794

K.L. Cameron

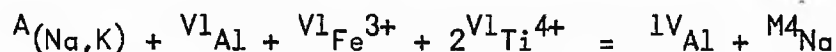
Board of Earth Sciences
University of California
Santa Cruz, California 95064

K. Baldwin

Department of Earth and Space Sciences
State University of New York
Stony Brook, New York 11794

Summary

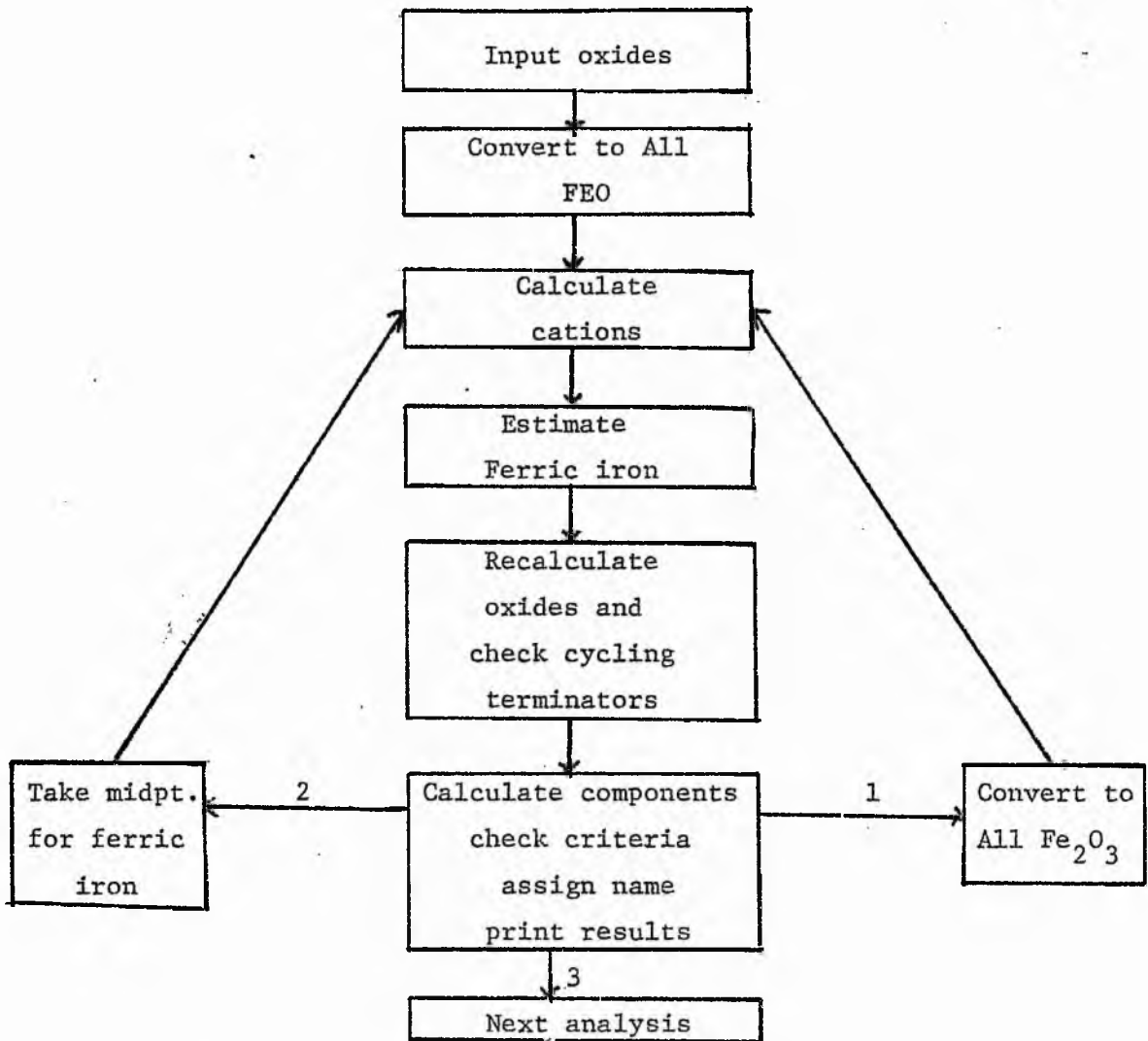
According to Papike et al. (1974) the charge balance equation is as follows:



The programme is run three times on each input of microprobe analysis, once with iron as total FeO, total Fe₂O₃, and a point midway between the minimum value (total FeO), and maximum (total Fe₂O₃) value. Each run is re-iterative, to a limit of 20 cycles. The simplified flow chart is given overleaf and the tests for superior analyses on the page after.

(e)

Simplified Flow Chart (Amphiboles)



(f)

AMPHIBOLES

TESTS FOR SUPERIOR ANALYSES

- 1 THE SUM OF $\text{Si} + \text{Al}^{\text{IV}}$ MUST = 8 ± 0.02 ATOMS PER 23 OXYGENS
- 2 THE OCTAHEDRAL CATIONS ($\text{Mn}, \text{Fe}^{2+}, \text{Fe}^{3+}, \text{Mg}, \text{Ti}, \text{Al}^{\text{VI}}$) MUST SUM TO > 4.98
- 3 EXCESS OCTAHEDRAL CATIONS [THOSE GREATER THAN THE 5.0 ATOMS NECESSARY TO FILL THE M(1), M(2), M(3) SITES] PLUS CALCIUM MUST BE LESS THAN 2.02
- 4 THE M(4) SITE OCCUPANCY MUST = 2.0 ± 0.02
- 5 THE A-SITE OCCUPANCY MUST BE < 1.02
- 6 THE CHARGE BALANCE EQUATION MUST BE BALANCED TO 0.02 OR LESS OF A CHARGE

ADDITIONAL CHEMICAL DATA

Additional analytical data on pyroxenes and amphiboles are supplied on following pages. Ferric iron recalculation is reported throughout the series and the rocks to which the minerals belong may be identified simply by rock sample number except for:

T168SHD = Microferrodiorite enclave in
quartz porphyry T168
and T602X = Microsyenite enclave in
quartz porphyry T60

Other rock sample numbers such as T169, T34C etc. are as used in the text. Ca-rich pyroxenes are prefixed by 'CP' and amphiboles by 'AM'. The species of minerals present in each case are essentially within the range covered by 'representative analyses' in the tables accompanying the text.

CP T168SHD2

OXIDE	P.CENT	FORMULA FOR	4.0 CATIONS
SiO2	48.5430	SI	1.9306
TiO2	0.6510	TI	0.0195
Al2O3	1.1620	AL	0.0545
Fe2O3	2.4455	FE3	0.0732
FeO	21.5364	FE2	0.7163
MNO	0.6440	MN2	0.0217
MGO	6.1380	MG	0.3638
CAO	18.6020	CA	0.7927
NA2O	0.3600	NA	0.0278
K2O	0.0	K	0.0
TOTAL	100.0819	TOTAL	4.0000

CP T168SHD3

OXIDE	P.CENT	FORMULA FOR	4.0 CATIONS
SiO2	48.5450	SI	1.9325
TiO2	0.6060	TI	0.0181
Al2O3	1.2520	AL	0.0588
Fe2O3	2.6998	FE3	0.0809
FeO	21.7156	FE2	0.7230
MNO	0.6730	MN2	0.0227
MGO	5.4870	MG	0.3255
CAO	18.7010	CA	0.7977
NA2O	0.5290	NA	0.0408
K2O	0.0010	K	0.0001
TOTAL	100.2093	TOTAL	4.0000

CP T1151C

OXIDE	P.CENT	FORMULA	FOR	4.0 CATIONS
SI02	48.0140	SI		1.9829
TIO2	0.2880	TI		0.0089
AL2O3	0.2950	AL		0.0144
FE2O3	1.5332	FE3		0.0477
FE0	29.3403	FE2		1.0134
MNO	0.7060	MN2		0.0247
MGO	0.3020	MG		0.0186
CAO	19.0660	CA		0.8437
NA2O	0.5640	NA		0.0452
K2O	0.0110	K		0.0006
TOTAL	100.1195	TOTAL		4.0000

CP T1151D

OXIDE	P.CENT	FORMULA	FOR	4.0 CATIONS
SI02	47.7250	SI		1.9611
TIO2	0.3090	TI		0.0095
AL2O3	0.2790	AL		0.0135
FE2O3	3.6584	FE3		0.1131
FE0	27.4700	FE2		0.9440
MNO	0.7140	MN2		0.0249
MGO	0.3140	MG		0.0192
CAO	19.2270	CA		0.8466
NA2O	0.8520	NA		0.0679
K2O	0.0020	K		0.0001
TOTAL	100.5503	TOTAL		4.0000

(H)

CP T602X44		FORMULA FOR 4.0 CATIONS		FORMULA FOR 4.0 CATIONS	
OXIDE	P. CENT	SI	TI	SI	TI
SI02	48.3210	1.9822	0.0098	48.0610	1.9747
TI02	0.3170	0.0199	0.0310	0.3130	0.0097
AL2O3	0.4120	0.9696	0.0261	0.3520	0.0171
FE2O3	1.0043	0.1000	0.8264	1.5186	0.0470
FE0	28.2612	0.0349	0.0	28.8985	0.9930
MNO	0.7520	0.0	0.0	0.7910	0.0275
MGO	1.6360	4.0000	0.0	1.2370	0.0757
CAO	18.8020	0.0	0.0	18.6810	0.8225
NA2O	0.4390	0.0	0.0	0.4120	0.9328
K2O	0.0	0.0	0.0	0.0	0.0
TOTAL	99.9445	4.0000	4.0000	100.2640	4.0000

CP T602X		FORMULA FOR 4.0 CATIONS		FORMULA FOR 4.0 CATIONS	
OXIDE	P. CENT	SI	TI	SI	TI
SI02	49.6850	2.0091	0.0	48.5280	2.0005
TI02	0.0	0.0053	0.0194	0.0680	0.0021
AL2O3	0.1120	0.9117	0.0244	0.2160	0.0105
FE2O3	0.6381	0.1614	0.8258	0.4800	0.0149
FE0	26.9588	0.0429	0.0	26.5501	0.9153
MNO	0.7110	0.0	0.0	1.0730	0.0375
MGO	2.6790	4.0000	0.0	0.8340	0.0512
CAO	19.0600	0.0	0.0	21.2240	0.9375
NA2O	0.5470	0.0	0.0	0.3820	0.0305
K2O	0.0	0.0	0.0	0.0	0.0
TOTAL	100.3909	4.0000	4.0000	99.3550	4.0000

CP T105QHD1

OXIDE	P.CENT	FORMULA FOR 4.0 CATIONS
SiO2	47.0330	Si 1.9577
TiO2	0.0500	Ti 0.0016
Al2O3	0.7330	Al 0.0360
Fe2O3	2.5814	Fe3 0.0809
FeO	28.4001	Fe2 0.9886
MnO	0.8130	Mn2 0.0287
MgO	0.6840	Mg 0.0424
CaO	18.5800	Ca 0.8287
Na2O	0.4390	Na 0.0354
K2O	0.0	K 0.0
TOTAL	99.3134	TOTAL 4.0000

CP T135HD1D

OXIDE	P.CENT	FORMULA FOR 4.0 CATIONS
SiO2	47.5290	Si 1.9666
TiO2	0.3720	Ti 0.0116
Al2O3	0.5140	Al 0.0251
Fe2O3	2.3333	Fe3 0.0727
FeO	27.3994	Fe2 0.9481
MnO	0.7530	Mn2 0.0264
MgO	1.5310	Mg 0.0944
CaO	18.0680	Ca 0.8011
Na2O	0.5420	Na 0.0435
K2O	0.2010	K 0.0106
TOTAL	99.2426	TOTAL 4.0000

CP T105QH0P

OXIDE	P.CENT	FORMULA FOR 4.0 CATIONS
SiO2	47.9430	Si 1.9789
TiO2	0.0100	Ti 0.0003
Al2O3	0.2850	Al 0.0139
Fe2O3	2.5548	Fe3 0.0794
FeO	28.2771	Fe2 0.9761
MnO	0.8390	Mn2 0.0293
MgO	0.7140	Mg 0.0439
CaO	18.5870	Ca 0.8265
Na2O	0.6450	Na 0.0516
K2O	0.0010	K 0.0001
TOTAL	99.9558	TOTAL 4.0000

CP T135HD2A

OXIDE	P.CENT	FORMULA FOR 4.0 CATIONS
SiO2	48.9000	Si 1.9833
TiO2	0.3470	Ti 0.0106
Al2O3	0.1810	Al 0.0087
Fe2O3	5.5908	Fe3 0.1706
FeO	24.1921	Fe2 0.8206
MnO	0.8160	Mn2 0.0280
MgO	1.2460	Mg 0.0753
CaO	16.9310	Ca 0.7358
Na2O	2.0930	Na 0.1645
K2O	0.0480	K 0.0025
TOTAL	100.3449	TOTAL 4.0000

(1)

CP T11HD2		FORMULA FOR 4.0 CATIONS		FORMULA FOR 4.0 CATIONS	
CXIDE	P.CENT				
SI02	48.4770	SI	1.9961	SI	1.9928
TI02	0.0150	TI	0.0005	TI	0.0003
AL203	0.3190	AL	0.0155	AL	0.0091
FE203	1.4359	FE3	0.0445	FE3	0.0743
FE0	28.6429	FE2	0.9864	FE2	0.8614
MNO	0.8020	MN2	0.0280	MN2	0.0233
MGO	0.9650	MG	0.0592	MG	0.1103
CA0	18.5100	CA	0.8167	CA	0.8588
NA20	0.6660	NA	0.0532	NA	0.0697
K20	0.0	K	0.0	K	0.0
TOTAL	99.8327	TOTAL	4.0000	TOTAL	4.0000

CP T11HD3		FORMULA FOR 4.0 CATIONS		FORMULA FOR 4.0 CATIONS	
CXIDE	P.CENT				
SI02	48.3440	SI	1.5893	SI	1.9998
TI02	0.0210	TI	0.0006	TI	0.0063
AL203	0.3920	AL	0.0190	AL	0.0085
FE203	1.0657	FE3	0.0330	FE3	0.1041
FE0	29.4431	FE2	1.0128	FE2	0.8814
MNO	0.7830	MN2	0.0273	MN2	0.0251
MGO	1.1190	MG	0.0685	MG	0.0907
CA0	18.6160	CA	0.8204	CA	0.7593
NA20	0.3740	NA	0.0298	NA	0.1213
K20	0.0030	K	0.0002	K	0.0035
TOTAL	100.1607	TOTAL	4.0000	TOTAL	4.0000

CP T11HD5		FORMULA FOR 4.0 CATIONS	
CXIDE	P.CENT		
SI02	49.1270	SI	1.9928
TI02	0.0100	TI	0.0003
AL203	0.1910	AL	0.0091
FE203	2.4332	FE3	0.0743
FE0	25.3905	FE2	0.8614
MNO	0.6770	MN2	0.0233
MGO	1.8250	MG	0.1103
CA0	19.7580	CA	0.8588
NA20	0.8860	NA	0.0697
K20	0.0	K	0.0
TOTAL	100.2976	TOTAL	4.0000

CP T135HD1A		FORMULA FOR 4.0 CATIONS	
CXIDE	P.CENT		
SI02	48.9260	SI	1.9998
TI02	0.2040	TI	0.0063
AL203	0.1760	AL	0.0085
FE203	3.3846	FE3	0.1041
FE0	25.7843	FE2	0.8814
MNO	0.7250	MN2	0.0251
MGO	1.4890	MG	0.0907
CA0	17.3360	CA	0.7593
NA20	1.5300	NA	0.1213
K20	0.0680	K	0.0035
TOTAL	99.6229	TOTAL	4.0000

CP T105PXA

OXIDE	P. CENT	FORMULA FOR	4.0 CATIONS
SI02	48.0240	SI	1.9701
TIO2	0.0750	TI	0.0023
AL2O3	0.6170	AL	0.0298
FE2O3	2.3206	FE3	0.0716
FEO	27.8318	FE2	0.9549
MNO	0.9920	MN2	0.0345
MGO	1.1720	MG	0.0717
CAO	18.6250	CA	0.8187
NA2O	0.5000	NA	0.0398
K2O	0.1260	K	0.0066
TOTAL	100.2834	TOTAL	4.0000

CP T105PX

OXIDE	P. CENT	FORMULA FOR	4.0 CATIONS
SI02	48.2710	SI	1.9912
TIO2	0.0120	TI	0.0004
AL2O3	0.4170	AL	0.0203
FE2O3	1.0410	FE3	0.0323
FEO	28.6523	FE2	0.9884
MNO	0.7690	MN2	0.0269
MGO	1.0470	MG	0.0644
CAO	19.0160	CA	0.8405
NA2O	0.4290	NA	0.0343
K2O	0.0260	K	0.0014
TOTAL	99.6801	TOTAL	4.0000

CP T105PXB

OXIDE	P.CENT	FORMULA	FOR	4.0 CATIONS
SiO2	48.0360	SI		1.9720
TiO2	0.0440	TI		0.0014
AL2O3	0.5230	AL		0.0253
FE2O3	2.3537	FE3		0.0727
FeO	26.9790	FE2		0.9238
MNO	0.7020	MN2		0.0244
MGO	1.7610	MG		0.1077
CAO	18.8240	CA		0.8280
NA2O	0.4840	NA		0.0385
K2O	0.1170	K		0.0061
TOTAL	99.7537	TOTAL		4.0000

CP T105PXGV

OXIDE	P.CENT	FORMULA	FOR	4.0 CATIONS
SiO2	48.1100	SI		1.9777
TiO2	0.0440	TI		0.0014
AL2O3	0.5190	AL		0.0252
FE2O3	1.9074	FE3		0.0590
FeO	27.7956	FE2		0.9556
MNO	0.8210	MN2		0.0286
MGO	1.3270	MG		0.0813
CAO	18.8220	CA		0.8291
NA2O	0.4710	NA		0.0375
K2O	0.0900	K		0.0047
TOTAL	99.9069	TOTAL		4.0000

(1)

CP T601HD3A

OXIDE	P.CENT	FORMULA FOR	4.0 CATIONS
SiO2	48.7280	SI	1.9605
TiO2	0.4120	TI	0.0125
AL2O3	0.7250	AL	0.0344
FE2O3	1.8836	FE3	0.0570
FE0	24.6240	FE2	0.8285
MNO	0.6750	MN2	0.0230
MGO	4.6380	MG	0.2781
CAO	17.8290	CA	0.7686
NA2O	0.4630	NA	0.0361
K2O	0.0240	K	0.0012
TOTAL	100.0015	TOTAL	4.0000

CP T601HD3C

OXIDE	P.CENT	FORMULA FOR	4.0 CATIONS
SiO2	47.2660	SI	1.9557
TiO2	0.3390	TI	0.0105
AL2O3	0.4060	AL	0.0198
FE2O3	2.9778	FE3	0.0927
FE0	27.8424	FE2	0.9635
MNO	0.8090	MN2	0.0284
MGO	0.6910	MG	0.0426
CAO	18.9860	CA	0.8418
NA2O	0.5410	NA	0.0434
K2O	0.0310	K	0.0016
TOTAL	99.8891	TOTAL	4.0000

CP T601HD3D

OXIDE	P.CENT	FORMULA FOR	4.0 CATIONS
SiO2	47.7700	Si	1.9506
TiO2	0.3920	Ti	0.0120
Al2O3	0.3760	Al	0.0181
Fe2O3	3.0344	Fe3	0.0932
FeO	27.4325	Fe2	0.9368
MnO	0.7660	Mn2	0.0265
MgO	1.5150	Mg	0.0922
CaO	19.0590	Ca	0.8339
Na2O	0.4580	Na	0.0363
K2O	0.0070	K	0.0004
TOTAL	100.8098	TOTAL	4.0000

CP T602HD4A

OXIDE	P.CENT	FORMULA FOR	4.0 CATIONS
SiO2	48.3210	Si	1.9822
TiO2	0.3170	Ti	0.0098
Al2O3	0.4120	Al	0.0199
Fe2O3	1.0043	Fe3	0.0310
FeO	28.2612	Fe2	0.9696
MnO	0.7520	Mn2	0.0261
MgO	1.6360	Mg	0.1000
CaO	18.8020	Ca	0.8264
Na2O	0.4390	Na	0.0349
K2O	0.0	K	0.0
TOTAL	99.9445	TOTAL	4.0000

SAMPLE AMT170FAM4

SI02	48.60	SI	8.0000
AL203	0.45	AL	0.0881
FE0	34.53	F2	4.7528
FE203	0.10	F3	0.0125
MGO	0.50	MG	0.1229
MNO	1.20	MN	0.1674
TI02	0.27	TI	0.0339
CA0	7.04	CA	1.2412
NA20	2.70	NA	0.8607
K20	0.64	K	0.1338
TOTAL	96.03		15.4132

SAMPLE AMT170FAM5

SI02	48.19	SI	8.0000
AL203	0.65	AL	0.1282
FE0	33.76	F2	4.6876
FE203	1.04	F3	0.1304
MGO	0.41	MG	0.1014
MNO	1.08	MN	0.1526
TI02	0.34	TI	0.0419
CA0	6.53	CA	1.1625
NA20	2.26	NA	0.7288
K20	0.56	K	0.1197
TOTAL	94.84		15.2530

SAMPLE AMT170FAMR

SI02	47.20	SI	7.7663
AL203	1.70	AL	0.3285
FE0	34.80	F2	4.7797
FE203	0.0	F3	0.0
MGO	0.33	MG	0.0808
MNO	0.86	MN	0.1195
TI02	0.92	TI	0.1142
CA0	6.01	CA	1.0575
NA20	3.70	NA	1.2064
K20	1.01	K	0.2110
TOTAL	96.71		15.6639

SAMPLE AMT170FAP3

SI02	48.81	SI	7.9915
AL203	0.63	AL	0.1226
FE0	34.75	F2	4.7582
FE203	0.0	F3	0.0
MGO	0.37	MG	0.0903
MNO	1.12	MN	0.1550
TI02	0.27	TI	0.0331
CA0	7.45	CA	1.3076
NA20	2.51	NA	0.7968
K20	0.55	K	0.1147
TOTAL	96.47		15.3698

SAMPLE AMT115HD6B

SI02	47.14	SI	7.7420
AL203	1.37	AL	0.2652
FE0	34.40	F2	4.7245
FE203	0.0	F3	0.0
MGO	0.36	MG	0.0886
MNO	0.65	MN	0.0903
TI02	1.78	TI	0.2197
CA0	4.81	CA	0.8471
NA20	5.11	NA	1.6261
K20	1.10	K	0.2305
TOTAL	96.72		15.8340

SAMPLE AMT115AM3

SI02	46.90	SI	7.7142
AL203	1.50	AL	0.2905
FE0	33.61	F2	4.6228
FE203	0.0	F3	0.0
MGO	0.40	MG	0.0976
MNO	0.66	MN	0.0918
TI02	2.19	TI	0.2710
CA0	4.87	CA	0.8575
NA20	5.11	NA	1.6299
K20	1.04	K	0.2186
TOTAL	96.28		15.7938

SAMPLE AMT133AM7			
SI02	47.76	SI	7.8809
AL203	1.50	AL	0.2918
FE0	34.31	F2	4.7344
FE203	0.0	F3	0.0
MGO	0.12	MG	0.0300
MNO	0.75	MN	0.1044
TI02	1.27	TI	0.1580
CA0	3.37	CA	0.5960
NA20	5.57	NA	1.7813
K20	1.23	K	0.2585
TOTAL	95.88		15.8352

SAMPLE AMT133AM4			
SI02	47.73	SI	7.8672
AL203	1.44	AL	0.2793
FE0	33.83	F2	4.6641
FE203	0.0	F3	0.0
MGO	0.19	MG	0.0457
MNO	0.70	MN	0.0979
TI02	1.49	TI	0.1842
CA0	3.88	CA	0.6851
NA20	5.35	NA	1.7095
K20	1.24	K	0.2614
TOTAL	95.94		15.7945

(h)

SAMPLE AMT173YAM1
 SI02 49.94 SI
 AL203 1.20 AL
 FE0 27.42 F2
 FE203 5.78 F3
 MGO 0.23 MG
 MNO 1.24 MN
 TI02 0.81 TI
 CAO 0.95 CA
 NA20 7.61 NA
 K20 0.87 K
 TOTAL 96.05

SAMPLE AMT173YAM3
 SI02 49.70 SI
 AL203 1.27 AL
 FE0 27.36 F2
 FE203 5.33 F3
 MGO 0.20 MG
 MNO 1.14 MN
 TI02 0.71 TI
 CAO 1.18 CA
 NA20 7.48 NA
 K20 0.84 K
 TOTAL 95.21

SAMPLE AMT169PH1
 SI02 42.86 SI
 AL203 7.10 AL
 FE0 33.15 F2
 FE203 0.21 F3
 MGO 1.24 MG
 MNO 0.83 MN
 TI02 0.69 TI
 CAO 10.44 CA
 NA20 1.44 NA
 K20 1.18 K
 TOTAL 99.14

SAMPLE AMT173YAM2
 SI02 49.88 SI
 AL203 1.31 AL
 FE0 27.74 F2
 FE203 5.13 F3
 MGO 0.21 MG
 MNO 1.18 MN
 TI02 0.84 TI
 CAO 0.86 CA
 NA20 7.83 NA
 K20 0.88 K
 TOTAL 95.86

SAMPLE AMT173BAM2
 SI02 49.86 SI
 AL203 1.28 AL
 FE0 26.73 F2
 FE203 6.08 F3
 MGO 0.21 MG
 MNO 1.08 MN
 TI02 0.62 TI
 CAO 0.80 CA
 NA20 7.70 NA
 K20 0.83 K
 TOTAL 95.20

SAMPLE AMT169PH2
 SI02 43.01 SI
 AL203 5.83 AL
 FE0 32.42 F2
 FE203 1.05 F3
 MGO 1.10 MG
 MNO 0.95 MN
 TI02 0.24 TI
 CAO 10.59 CA
 NA20 1.37 NA
 K20 0.84 K
 TOTAL 97.28

SAMPLE AMT173BAM1
 SI02 50.00 SI
 AL203 1.17 AL
 FE0 27.59 F2
 FE203 5.59 F3
 MGO 0.23 MG
 MNO 1.04 MN
 TI02 0.67 TI
 CAO 1.32 CA
 NA20 7.42 NA
 K20 0.87 K
 TOTAL 95.84

SAMPLE AMT173FAM3
 SI02 46.38 SI
 AL203 1.38 AL
 FE0 34.57 F2
 FE203 0.0 F3
 MGO 0.42 MG
 MNO 0.92 MN
 TI02 0.68 TI
 CAO 6.35 CA
 NA20 3.43 NA
 K20 0.98 K
 TOTAL 95.10

SAMPLE AMT169PH3
 SI02 43.01 SI
 AL203 5.83 AL
 FE0 32.42 F2
 FE203 1.05 F3
 MGO 1.10 MG
 MNO 0.95 MN
 TI02 0.24 TI
 CAO 10.59 CA
 NA20 1.37 NA
 K20 0.84 K
 TOTAL 97.28

SAMPLE AMT34CBAM2			
SI02	48.68	SI	8.0000
AL203	1.28	AL	0.2484
FEO	28.85	F2	3.9653
FF203	2.28	F3	0.2815
MGO	0.91	MG	0.2231
MNO	2.08	MN	0.2891
TI02	0.50	TI	0.0624
CAO	2.59	CA	0.4570
NA2O	6.55	NA	2.0879
K2O	0.97	K	0.2034
TOTAL	94.69		15.8183

SAMPLE AMT34CYAM1			
SI02	48.60	SI	8.0000
AL203	1.15	AL	0.2241
FEO	31.05	F2	4.2740
FE203	0.79	F3	0.0975
MGO	0.88	MG	0.2166
MNO	2.27	MN	0.3159
TI02	0.46	TI	0.0568
CAO	2.62	CA	0.4622
NA2O	6.49	NA	2.0715
K2O	0.95	K	0.1986
TOTAL	95.26		15.9175

SAMPLE AMT34CBAM1			
SI02	48.60	SI	8.0000
AL203	1.30	AL	0.2512
FEO	31.58	F2	4.3386
FE203	0.0	F3	0.0
MGO	0.97	MG	0.2370
MNO	2.33	MN	0.3248
TI02	0.53	TI	0.0652
CAO	2.79	CA	0.4915
NA2O	6.49	NA	2.0685
K2O	0.93	K	0.1949
TOTAL	95.53		15.9563

SAMPLE AMT34CYAM2			
SI02	48.80	SI	8.0000
AL203	1.12	AL	0.2172
FEO	28.53	F2	3.9108
FF203	3.14	F3	0.3874
MGO	0.91	MG	0.2230
MNO	2.10	MN	0.2920
TI02	0.47	TI	0.0583
CAO	2.42	CA	0.4252
NA2O	6.45	NA	2.0512
K2O	0.95	K	0.1997
TOTAL	94.91		15.7649

SAMPLE AMT34CAYM2			
SI02	47.44	SI	7.9277
AL203	1.49	AL	0.2932
FEO	28.97	F2	4.0487
FF203	0.0	F3	0.0
MGO	2.20	MG	0.5492
MNO	1.58	MN	0.2234
TI02	0.65	TI	0.0816
CAO	3.31	CA	0.5927
NA2O	6.21	NA	2.0138
K2O	1.13	K	0.2418
TOTAL	92.98		15.9719

SAMPLE AMT34CGAM2			
SI02	48.17	SI	7.9386
AL203	1.31	AL	0.2540
FEO	32.09	F2	4.4229
FE203	0.0	F3	0.0
MGO	0.84	MG	0.2076
MNO	2.12	MN	0.2953
TI02	0.67	TI	0.0825
CAO	3.14	CA	0.5550
NA2O	6.18	NA	1.9749
K2O	1.02	K	0.2159
TOTAL	95.54		15.9473

SAMPLE AMT34CGAM1			
SI02	48.73	SI	7.9885
AL203	1.29	AL	0.2491
FEO	32.00	F2	4.3874
FF203	0.0	F3	0.0
MGO	0.86	MG	0.2106
MNO	2.12	MN	0.2942
TI02	0.67	TI	0.0827
CAO	2.75	CA	0.4827
NA2O	6.33	NA	2.0135
K2O	0.98	K	0.2049
TOTAL	95.74		15.9135

SAMPLE AMT169PH5			
SI02	43.97	SI	7.1645
AL203	5.17	AL	0.9929
FEO	32.25	F2	4.3948
FF203	0.0	F3	0.0
MGO	1.47	MG	0.3570
MNO	1.83	MN	0.2526
TI02	0.12	TI	0.0149
CAO	10.23	CA	1.7860
NA2O	1.32	NA	0.4173
K2O	1.47	K	0.3056
TOTAL	97.83		15.6856

SAMPLE AMT34CGAM2			
SI02	48.17	SI	7.9386
AL203	1.31	AL	0.2540
FEO	32.09	F2	4.4229
FE203	0.0	F3	0.0
MGO	0.84	MG	0.2076
MNO	2.12	MN	0.2953
TI02	0.67	TI	0.0825
CAO	3.14	CA	0.5550
NA2O	6.18	NA	1.9749
K2O	1.02	K	0.2159
TOTAL	95.54		15.9473

(q)

SAMPLE	AMT37HS4C	
SI02	41.21	SI
AL203	6.52	AL
FE0	32.26	F2
FE203	0.75	F3
MGO	1.43	MG
MNO	0.74	MN
TI02	0.90	TI
CA0	10.15	CA
NA20	1.70	NA
K20	1.16	K
TOTAL	96.91	

6.8116	
1.2700	
4.4596	
0.0927	
0.3518	
0.1032	
0.1121	
1.7981	
0.5442	
0.2446	
15.7889	

SAMPLE	AMT36A0H6		
SI02	39.79	SI	6.4529
AL203	9.01	AL	1.7226
FE0	25.76	F2	3.4940
FE203	3.51	F3	0.4287
MGO	3.50	MG	0.8458
MNO	0.57	MN	0.0782
TI02	0.29	TI	0.0357
CA0	11.18	CA	1.9422
NA20	1.69	NA	0.5320
K20	1.64	K	0.3395
TOTAL	96.95		15.8715

6.8610	
1.2097	
4.0021	
0.0	
0.8577	
0.0972	
0.1524	
1.7700	
0.6368	
0.2266	
15.8136	

SI	42.76
AL	6.39
F2	29.82
F3	0.0
MG	3.59
MN	0.71
TI	1.26
CA	10.29
NA	2.05
K	1.11
TOTAL	97.99

6.8398	
1.2370	
4.0429	
0.0	
0.8576	
0.1016	
0.1176	
1.7640	
0.6861	
0.2409	
15.8876	

SI	42.19
AL	6.47
F2	25.82
F3	0.0
MG	3.55
MN	0.74
TI	0.96
CA	10.16
NA	2.18
K	1.16
TOTAL	97.25

6.2777	
1.9058	
3.7314	
0.5146	
0.5145	
0.0838	
0.0339	
1.9383	
0.6474	
0.3089	
15.9563	

SI	38.28
AL	9.86
F2	27.20
F3	4.17
MG	2.10
MN	0.60
TI	0.27
CA	11.03
NA	2.04
K	1.49
TOTAL	97.03

SAMPLE	AMT37HS4A	
SI02	42.76	SI
AL203	6.39	AL
FE0	29.82	F2
FE203	0.0	F3
MGO	3.59	MG
MNO	0.71	MN
TI02	1.26	TI
CA0	10.29	CA
NA20	2.05	NA
K20	1.11	K
TOTAL	97.99	

6.9609	
1.1388	
4.4278	
0.0	
0.4350	
0.1231	
0.1051	
1.7835	
0.5570	
0.2237	
15.7549	

SI	42.01
AL	6.00
F2	31.77
F3	0.90
MG	1.79
MN	0.95
TI	0.70
CA	10.16
NA	1.62
K	1.04
TOTAL	96.95

SAMPLE	AMT37HS4H	
SI02	42.19	SI
AL203	6.47	AL
FE0	25.82	F2
FE203	0.0	F3
MGO	3.55	MG
MNO	0.74	MN
TI02	0.96	TI
CA0	10.16	CA
NA20	2.18	NA
K20	1.16	K
TOTAL	97.25	

6.9080	
1.1627	
4.3697	
0.1110	
0.4387	
0.1323	
0.0869	
1.7908	
0.5181	
0.2184	
15.7366	

SI	42.01
AL	6.00
F2	31.77
F3	0.90
MG	1.79
MN	0.95
TI	0.70
CA	10.16
NA	1.62
K	1.04
TOTAL	96.95

SAMPLE	AMT36APH2	
SI02	38.28	SI
AL203	9.86	AL
FE0	27.20	F2
FE203	4.17	F3
MGO	2.10	MG
MNO	0.60	MN
TI02	0.27	TI
CA0	11.03	CA
NA20	2.04	NA
K20	1.49	K
TOTAL	97.03	

6.3826	
1.8400	
3.4962	
0.4441	
0.7684	
0.0781	
0.0156	
1.9750	
0.6168	
0.3027	
15.9196	

SI	38.28
AL	9.86
F2	27.20
F3	4.17
MG	2.10
MN	0.60
TI	0.27
CA	11.03
NA	2.04
K	1.49
TOTAL	97.03

SAMPLE	AMT37HS1A	
SI02	42.52	SI
AL203	5.50	AL
FE0	32.34	F2
FE203	0.0	F3
MGO	1.78	MG
MNO	0.89	MN
TI02	0.95	TI
CA0	10.17	CA
NA20	1.75	NA
K20	1.07	K
TOTAL	97.29	

SAMPLE	AMT37HS1B	
SI02	42.01	SI
AL203	6.00	AL
FE0	31.77	F2
FE203	0.90	F3
MGO	1.79	MG
MNO	0.95	MN
TI02	0.70	TI
CA0	10.16	CA
NA20	1.62	NA
K20	1.04	K
TOTAL	96.95	

SAMPLE	AMT36APH1	
SI02	39.79	SI
AL203	9.73	AL
FE0	26.06	F2
FE203	3.68	F3
MGO	3.21	MG
MNO	0.57	MN
TI02	0.13	TI
CA0	11.49	CA
NA20	1.98	NA
K20	1.48	K
TOTAL	99.12	